The Habitability of Hyperarid Environments:

The Physico-Chemical Dynamics of Water in Extremely Water-Limited Systems

by

Donald M Glaser

A Dissertation Presented in Partial Fulfillment
of the Requirements for the Degree
Doctor of Philosophy

Approved September 2022 by the
Graduate Supervisory Committee:

Hilairy Hartnett, Chair
Ariel Anbar
Everett Shock

ARIZONA STATE UNIVERSITY

December 2022

ABSTRACT

I present results of field and laboratory experiments investigating the habitability of one of Earth's driest environments: the Atacama Desert. This Desert, along the west coast of South America spanning Perú and Chile, is one of the driest places on Earth and has been exceedingly arid for millions of years. These conditions create the perfect natural laboratory for assessing life at the extremes of habitability. All known life needs water; however, the extraordinarily dry Atacama Desert is inhabited by well-adapted microorganisms capable of colonizing this hostile environment.

I show field and laboratory evidence of an environmental process, water vapor adsorption, that provides a daily, sustainable input of water into the near (3 - 5 cm) subsurface through water vapor-soil particle interactions. I estimate that this water input may rival the yearly average input of rain in these soils (~2 mm).

I also demonstrate, for the first time, that water vapor adsorption is dependent on mineral composition via a series of laboratory water vapor adsorption experiments. The results of these experiments provide evidence that mineral composition, and ultimately soil composition, measurably and significantly affect the equilibrium soil water content. This suggests that soil microbial communities may be extremely heterogeneous in distribution depending on the distribution of adsorbent minerals.

Finally, I present changes in biologically relevant gasses (i.e., H_2, CH_4, CO, and CO_2) over long-duration incubation experiments designed to assess the potential for biological activity in soils collected from a hyperarid region in the Atacama Desert. These long-duration experiments mimicked typical water availability conditions in the Atacama Desert; in other words, the incubations were performed without condensed water addition. The

results suggest a potential for methane-production in the live experiments relative to the sterile controls, and thus, for biological activity in hyperarid soils. However, due to the extremely low biomass and extremely low rates of activity in these soils, the methods employed here were unable to provide robust evidence for activity. Overall, the hyperarid regions of the Atacama Desert are an important resource for researchers by providing a window into the environmental dynamics and subsequent microbial responses near the limit of habitability.

ACKNOWLEDGMENTS

I acknowledge the peoples of the Aymara and Quechua: the ancestral and current inhabitants of the land in the Arequipa region of modern Perú where our field work was performed. I also acknowledge the ancestral land of the Akimel O'odham and Pee Posh peoples of the Salt River valley that is currently occupied by Arizona State University. I grew up in the ancestral land of the Puyallup, Suquamish, Nisqually, Skokomish, and Squaxin nations that is occupied by the state of Washington. I acknowledge my privilege to live in these lands and stand with the first nations in their fight for sovereignty within their own lands.

I am extremely fortunate to have an incredibly talented, understanding, and supportive advisor in Hilairy Hartnett. She has worked tirelessly to provide me with the opportunities, support, inspiration, and levity necessary for success. I truly could not have done this without her unwavering support and unflinching optimism. I thank my committee members Ariel Anbar and Everett Shock for their perspective on the big questions in astrobiology, you both have inspired me to think bigger and broader in pursuit of scientific answers.

I would not be where I am today without the help and support of my family. The thanks and gratitude offered here will never suffice. My caring wife Stephanie has stood with me through everything along with our amazing dog, Luna. My mom and dad, Kathy and Mike, never stopped believing in me, especially when I didn't believe in myself. My brother and best friend, Ryan, has always been there for emotional

support as well as technical support with the DIY instrumentation described in this dissertation. My stepmom Shelley, who has always been a model of tenacity and kindness. To my stepbrothers and sisters: Joe & Becky, Jen & Jeff, Jeremy & Miranda, Stephanie & Javier, and Stacy & Zack as well as my nieces and nephews: Donavyn, Gracie, Kadence, Isabella, Elliotte, Vander, Javier, Fable, and Lincoln for surrounding me with happiness and helping with the dishes during Thanksgiving. My grandma Barb, aunt Kim, aunt Deb, Nikki, Kayla, Molly, and Lauren who have always been there for fun and adventure. My incredible in law family: Chuck and Debbie, along with Dan, Sara, Charlie, and Samantha have always been supportive. I want to offer a particular thanks to my MIOLI family, especially Zack, who have always been there to motivate me to move it.

I am extraordinarily grateful to the brilliant and kind friends and colleagues I have met during my time at ASU. To my lab mates over the years in the CaNDy Lab: Josh, Nick, Pilar, Marisol, Elinor, Nikita, and Alexander I am grateful for the scientific insight as well as the 'productively unproductive' time. To the passionate students who worked to build the first AZ AstroBio student research symposium: John, Aleisha, Zoey, Jacob, Brook, Hikaru, and Chanel thank you for your enthusiasm and perseverance. Thank you to the many, many students who helped me with scientific insight or technical know-how: Kris, Kirt, Vince, Jordyn, Mark, Steffen, Damien, Alta, Alexa, James, Chad, and countless more. To the incredible faculty and staff at

ASU for all the help along the way, especially Dr. Throop, Dr. Gordon, Dr. Soignard, Dr. Petuskey, Dr. Cadillo-Quiroz, Dr. Hall, and Dr. Garcia-Pichel.

The work in this dissertation would not have been possible without the help of my incredible collaborators in Arequipa, Perú. Thank you for all the logistical help, especially the people at Universidad Católica San Pablo: Saul Perez-Montaño, Julio Valdivia-Silva, Giovanni Alatrista Góngora, Luis Miguel Carlos Lizarraga Cardenas, Johnathan Wilmer Del Villar Guerra, Ursulo 'Abel' Avelino Yapo, Eloy Condori Mamani, Fernando Mario Cardenas Dias, Maria 'Nelly' Pezo Torres, and Kimberly Huilca Pari.

TABLE OF CONTENTS

Page

CHAPTER Page

APPENDIX Page

LIST OF TABLES

LIST OF FIGURES

Chapter 1

INTRODUCTION

1.1. What is Habitability?

Habitability is an important concept in the field of astrobiology - or more specifically the search for life elsewhere - because if we are to find life elsewhere, we need to know where to look. A habitable environment is an environment capable of hosting life, and there is one factor that determines if an environment is habitable: water (Domagal-Goldman et al., 2016). All known life on Earth needs water, in particular: liquid water, to survive and replicate. Water is one of the only universal necessities of life; therefore, a habitable environment is one that is capable of hosting liquid water. So, ultimately there are two primary factors that determine habitability: *i)* the presence of water and *ii)* the state of water.

1.1.1. The Presence of Water

Water is ubiquitous on Earth, particularly on the surface, which is ~70% covered by water. Earth's water is thought to be primordial, having been created from the first generation of stars that made up the presolar nebula and eventually evolved into our solar system (Hartmann et al., 2017; Izidoro et al., 2013). The specific source of Earth's water (condritic planetisimals vs. comets) is a topic of debate; however, the water ultimately predates the solar system (Izidoro et al., 2013). All the terrestrial planets have water. Venus, Earth (Figure 1.1A), and Mars (Figure 1.1B) have on the order of 0.01 to 0.03 weight percent (mass mass^{-1}; wt%), while Mercury drier: on the order of 0.001 wt% (Izidoro et al., 2013).

These measures of water content are slightly misleading as they are the mass of water compared to the total mass of the planet. For example, Earth's water is concentrated on its surface and, in contrast, Mars' water is more evenly distributed through the mantle (Dong et al., 2022). Water is even more abundant outside the terrestrial planets; as these planets formed and reside beyond the solar system's snow line (e.g., the distance from the sun where all water is in the solid state; Grasset et al., 2017). Of particular interest are the moons of the gas giant planets that are rich in water, notably Europa and Enceladus (Figure 1.1C), both of which are thought to have global oceans below a thick (tens to hundreds of km) ice shell (Grasset et al., 2017; Taubner et al., 2020). Outside the orbit of the gas giants (e.g., in the Kuiper Belt) there is a population of water-rich bodies such as Pluto and the comets. Regions of water ice were recently discovered on the surface of Pluto in 2015 by the NASA New Horizons mission (Figure 1.1D; Stern et al., 2015). Comets are likely the most water-rich bodies in the solar system, and they have been argued to be an important source of water to Earth (Grasset et al., 2017; Izidoro et al., 2013). From hot Mercury to frigid comets, water is seemingly common across our solar system; however, the presence of water alone does not make a world habitable (Domagal-Goldman et al., 2016; O'Brien et al., 2018).

1.1.2. The State of Water

The physical state of water (solid, liquid, or gas) is a key factor because life utilizes water as a solvent to catalyze metabolic (energy-producing) reactions and, in general, gas and solid phase water are poor solvents. An environment needs to have water in the liquid state to be considered habitable and there are two main factors that determine the state of water: temperature and pressure.

1.1.2.1. Habitable Temperatures

The freezing and boiling points of water have been points of reference for temperature for over 200 years, dating back to the 18th century with Daniel Fahrenheit and Anders Celsius (McCaskey, 2020). Liquid water exists between 0 and 100ºC (32 and 212ºF), which to humans is a relatively large range of temperatures. However, Earth is regularly colder than 0ºC, as evidenced by mountain glaciers and the polar ice caps that can reach temperatures as low as -90ºC (Scambos et al., 2018). The air temperature at the surface of Earth has never been recorded higher than 54ºC (El Fadli et al., 2013); however there are localized environments near the surface that regularly exceed 100ºC such as lava flows (Nádudvari et al., 2020) and hydrothermal systems (Li et al., 2018). Temperature is not the only control on the state of water because the freezing and boiling points of water are also a function of pressure.

1.1.2.2. Habitable Pressures

The freezing and boiling points of water are 0 and 100ºC, but only at sea level atmospheric pressure (i.e., 1 atm). Decreased pressure, such as at high elevations, decreases the boiling point of water with the effect of narrowing the temperature 'window' where liquid water can exist. For example, Flagstaff Arizona is at 2,100 m elevation and has roughly 80% of the pressure at sea level, so water in Flagstaff boils at 91ºC. Liquid water, therefore, is not only limited to a range of temperatures, but also a lower boundary of pressure as shown in figure 1.2. The temperature range is limited by the Solid/Solid/Liquid triple point on the lower end (-22ºC) and the supercritical point on the upper end (374ºC). All temperatures lower than -22ºC will result in solid phase water (at most pressures), and all temperatures above 374ºC will result in a gas or supercritical fluid (at most pressures). The

lower boundary for liquid water is limited by the Solid/Liquid/Gas triple point (0.006 atm). Any pressure below the triple point pressure will result in a solid or a gas. There is an upper boundary of pressure for liquid water, however, for most relevant pressures above the triple point there is some range of temperature that thermodynamically favors liquid water. For example, in the atmosphere of Jupiter where the temperature is 25ºC the pressure is roughly 10 atm; at this pressure liquid water is stable from to ~0 to 182ºC (Seiff et al., 1998).

1.1.3. Habitability is…

Water is, arguably, the most important factor for life as we know it and, as such, astrobiologists have focused primarily on defining habitability almost exclusively based on the physical conditions that can host liquid water. The work described in this dissertation focuses on water availability in the driest environments on Earth. Here I investigate environments with habitable temperatures and pressures, but with exceedingly low amounts of water. I use dry environments on Earth as a natural laboratory to approximate other, inaccessible environments of interest, such as Mars, with the goal of understanding the unique availability and dynamics of water in these arid systems and to probe the limits of habitability with respect to water availability.

1.2. Habitability of Arid Environments

1.2.1. What is an Arid Environment?

Roughly one third of Earth's landmass is arid, and these environments are typically thought of as desolate and barren (Chiquoine et al., 2016; Safriel et al., 2005). However, all deserts on Earth are inhabited and have an ecosystem adapted to survive in environments that receive rain infrequently. Deserts are diverse and span all parts of the globe from the

cold deserts of the Antarctic (Figure 1.3A) and Colorado Plateau to the hot deserts of the Sahara (Figure 1.3B) and Australia and even temperate deserts such as the Namib (Figure 1.3C) and Atacama (Figure 1.3D). There are two main factors that make a desert: water input (i.e., precipitation) and water output (i.e., evaporation, transpiration). Using measurements of these two factors one can quantify how dry or arid a desert is using the aridity index (Zomer et al., 2008):

$$AI = \frac{Precipitation}{(Evaporation + Transpiration)}. \quad (1.1)$$

In plain terms, AI tells researchers how much water is gained from rain compared to how much is lost to evaporation and transpiration; for example, an AI of 0.1 (i.e., arid) means that the precipitation water gain is only one tenth the loss due to evaporation and transpiration. Using AI, it is possible to categorize the aridity of all deserts on Earth: dry subhumid ($0.5 \leq AI < 0.65$), semiarid ($0.2 \leq AI < 0.5$), arid ($0.05 \leq AI < 0.2$), and hyperarid (Bastin et al., 2017; Zomer et al., 2008).

1.2.2. Other Challenges for Life in Arid Environments

Earth's arid environments are habitable, yet extreme, environments mainly due to lack of water. There are other factors common in arid environments that make them an even more difficult environment for microbes to colonize, primarily salt and ultraviolet radiation (UV) (Wierzchos et al., 2018). The combination of these factors make most of Earth's drylands considered polyextreme environments (e.g., an environment with more than one factor that limits microbial growth).

The soil in most deserts is high in salt content, which can be >10 times higher compared to temperate soils (Pyle et al., 2019). This is primarily due to the fact that rainwater, in most drylands, evaporates rather than percolating through the soil, allowing salt to accumulate

over geologic time. Microorganisms in arid environments require specific adaptations to accomodate the high salt content. When it rains, the resulting soil pore water can be roughly as salty as seawater (Azua-Bustos et al., 2018; Heinz et al., 2021).

Ultraviolet radiation is harmful to life, particularly UVB (280 – 315 nm) and UVC (100 – 280 nm). Earth's upper atmosphere, including the ozone layer, effectively absorbs all UVC, preventing transmission to the surface. The amount of UVB that reaches the surface depends on several factors including season, latitude, aerosol concentration, and water vapor concentration (Latosińska et al., 2015; Pointing and Belnap, 2012). The low amount of atmospheric water common in drylands results in higher UV flux at the surface due to i) little to no cloud cover (i.e., no UV reflectance from clouds) and ii) low humidity (i.e., no UV absorption from water vapor; (Latosińska et al., 2015; Pei et al., 2019). The surface of drylands, therefore, can be a high UV environment, necessitating biological adaptations for endemic microorganisms.

1.3. Search for Extraterrestrial Life on Arid Worlds

The possibility of the existence of life outside Earth has intrigued humanity likely since before written history. Lucian of Samosata, circa second century CE, published a satirical novel including strange moon creatures; which is commonly cited as the first work of science fiction (Viglas, 2016). The Warlpiri, an indigenous aboriginal community in central Australia, have oral traditions of flying objects from other worlds that are thought to take water from pools and rivers (Saethre, 2007). Both these examples highlight the inherent human desire to imagine and search for life outside Earth.

The scientific search for extraterrestrial life is not new, and has been a key piece of NASA's goals at least since the Viking missions to Mars in the 1970's. Viking I was the first

successful landing on Mars and its payload contained i) a GCMS to measure putative organic carbon and ii) a life detection experiment with radiolabeled organic carbon to assess potential carbon-based respiration in the Martian soil (Levin and Straat, 1976). It is significant that the first successful lander on Mars was equipped to search for life and lends insight into the motivation and mindset of the time. Viking's life detection experiments were ultimately unable to demonstrate active respiration, despite an intriguing false positive that remained a mystery until NASA's Phoenix lander mission in 2008. The false positive was a detection of evolved radioactive CO_2 gas from a radioactive organic carbon addition as expected with a positive detection. However, the Phoenix lander discovered perchlorate, a highly oxidizing species, in the Martian regolith. Our current understanding is that the evolved radioactive CO_2 gas observed in Viking was the result of chemical oxidation of the radioactive organic carbon addition (Navarro-González et al., 2001). The search for life on Mars continues, currently, with NASA's Perseverance rover that is equipped with a robust set of astrobiology-focused instruments, including x-ray fluorescence and Raman spectroscopy, with the expressed goal of searching for biosignatures in the lakebed sediments of Jezero Crater (Hickman-Lewis et al., 2022). In addition, the Perseverance rover is equipped with 43 sample tubes for ultimate return to Earth (Tait et al., 2022).

Mars has been the subject of many scientific exploration missions, mostly due to proximity and a hospitable climate (compared to Venus). Therefore, investigation into arid environments continues to be necessary to inform current and future missions. In addition, research into the habitability of arid environments can be relevant to other worlds such as Luna and Mercury, and may even prove to be necessary in the search for extrasolar life on putative arid exoplanets.

1.4. Dissertation Outline

In this dissertation I present work relevant to the search for life on arid worlds, and investigate the boundaries of habitability with regard to water availability. The work is based on soils from the hyperarid core of the Atacama Desert, which is one of the most extreme environments on Earth due to the extraordinarily dry climate. This dissertation contains three science investigation chapters. The first examines field and laboratory data that reveal a daily cycle of water vapor adsorption in the hyperarid Atacama Desert. The second investigates the role that mineral composition plays in the magnitude of water vapor adsorption. The third explores the potential for microbial metabolic activity under typical, dry (i.e., non-rainfall, non-fog) conditions.

Chapter two of this dissertation investigates an underappreciated source of water in hyperarid environments: water vapor adsorption. Water vapor adsorption is a physico-chemical process that increases soil water content in response to daily changes in temperature. I was able to develop a mathematical model to quantify water vapor adsorption based on soil temperature and relative humidity profile measurements. This work is the first *in situ* observation of water vapor adsorption in the Atacama. Water vapor adsorption represents a small, daily input of water to the soils of the Atacama. The small daily amount of water can be extrapolated to ≥2 mm of rain equivalent per year; roughly the same as the average annual rainfall. This work has implications for the broader understanding of the geochemical conditions of hyperarid environments with potential applications for investigations of water vapor adsorption on Mars and other dry worlds.

Chapter three investigates the physical factors (e.g., temperature, relative humidity, surface area, and mineral composition) that control water vapor adsorption. This is the first

assessment of how soil mineralogy affects water vapor adsorption. I experimentally demonstrated that mineral composition has a measurable effect on the amount of water vapor adsorption per gram soil mass. Using these experimental results I developed a mineral-specific model to predict water vapor adsorption as a function of temperature, relative humidity, and soil surface area. I found that the equilibrium adsorbed water content for each mineral responds differently to changes in temperature, relative humidity, and surface area. These models can be linearly combined to predict water vapor adsorption for mixtures of minerals. This combination of mineral models is able to accurately predict the adsorbed water content of a simple mixture of minerals; suggesting that the water content of more complex mixtures (e.g., soils or regolith) may also be able to be predicted using this method.

Chapter four investigates the potential for microbial activity in the soils of the Atacama Desert. I examined microbial activity, via gas evolution, under typical (i.e., no condensed water) conditions at two sites: a hyperarid site and a semiarid site and hypothesized that the semiarid site would exhibit higher sterile-corrected biological activity, as measured by trace gasses, than the hyperarid site. I performed a set of experiments to measure changes in metabolically-relevant gasses (e.g., H_2, CH_4, CO, and CO_2) under two water availability conditions: dry (i.e., no added water) and humid (i.e., ~100% relative humidity). I hypothesized that sterile-corrected biological activity would be higher in the humid experiment compared to the dry experiment. In the case of most of the gasses - H_2, CO, and CO_2 - I was unable to statistically differentiate the live and sterile samples; meaning there was no measurable biological activity. However, I was able to detect statistically significant CH_4 production in the hyperarid soils in the humid experiment. This result was somewhat

unexpected and provides insight into the environmental differences between the two sites and potentially into how the microbial communities are adapted.

The final chapter summarizes the work presented here, and offers a set of hypotheses for further investigation on the habitability of hyperarid environments. This dissertation provides several new approaches to address questions about water content and water dynamics in extremely water limited systems. There are several tractable avenues of investigation identified in this final chapter regarding the search for signs of life on Mars and arid exoplanets. Arid worlds are likely ubiquitous across the galaxy and may prove to be equally enticing targets of investigation as water-rich worlds. However, more research is necessary to characterize *i)* the potential for life and *ii)* the potential for biosignature production and preservation in these unique, dry environments.

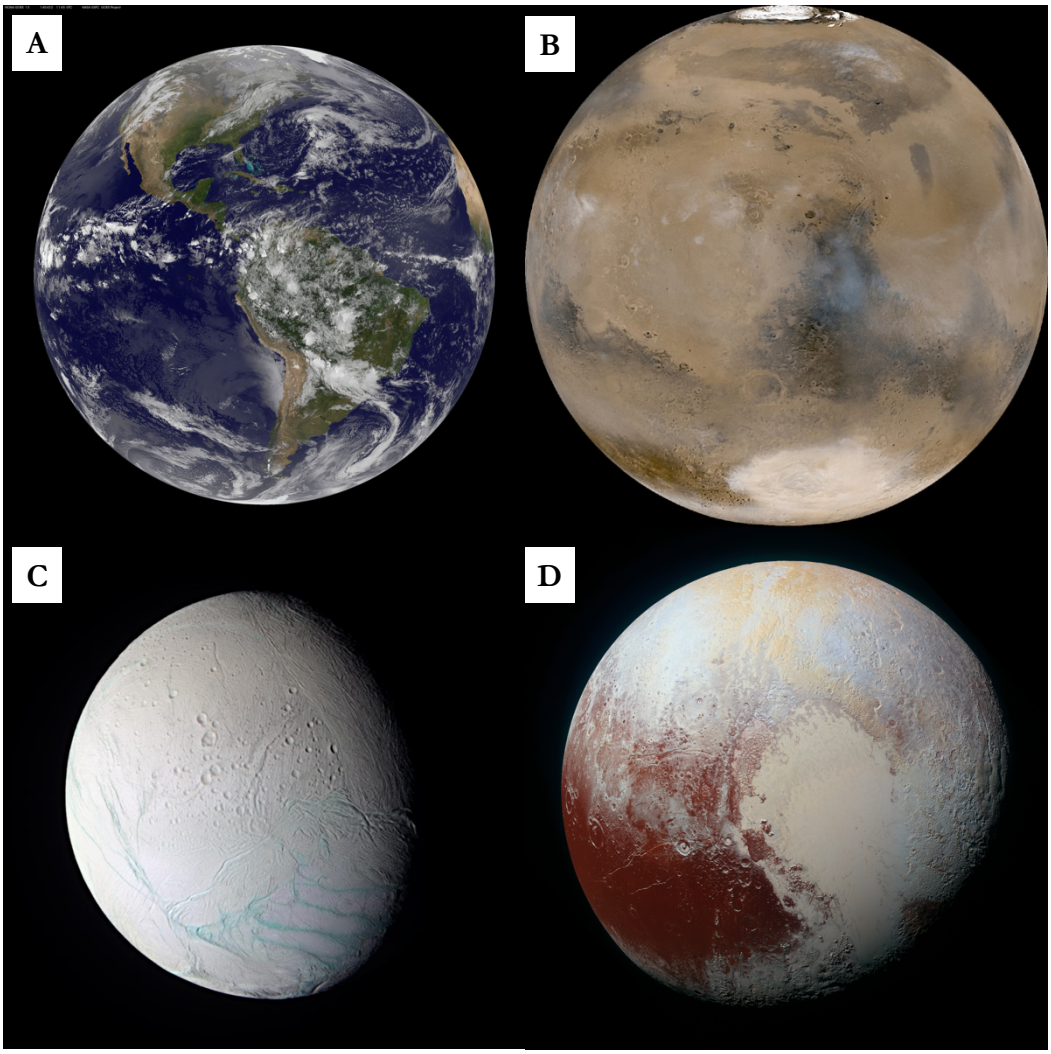

Figure 1.1: Images of several select solar system bodies. **A)** Natural color image of Earth taken by NOAA's Geostationary Operational Environmental Satellite East satellite in 2014. This image shows that much of the surface of Earth is water: from the deep blue ocean and the white clouds to the polar ice sheets. **B)** Natural color image of Mars taken by NASA's Mars Global Surveyor mission in 1999. This image highlights Mars' lack of water and abundance of bare rock and regolith that provides the planet with the moniker of 'the red planet.' The polar sheets in this image are partially solid water but are primarily solid carbon dioxide. **C)** False color image of Enceladus, one of the moons of Saturn taken by NASA's Cassini mission in 2005. The surface of Enceladus is a global water ice sheet covering a global water ocean. **D)** Enhanced color image of Pluto taken by NASA's New Horizon Mission in 2015. This image shows a surface with many complex features, notably the bright white area slightly right and below center. This white region is thought to be solid nitrogen, but there is evidence that there may be water below the surface.

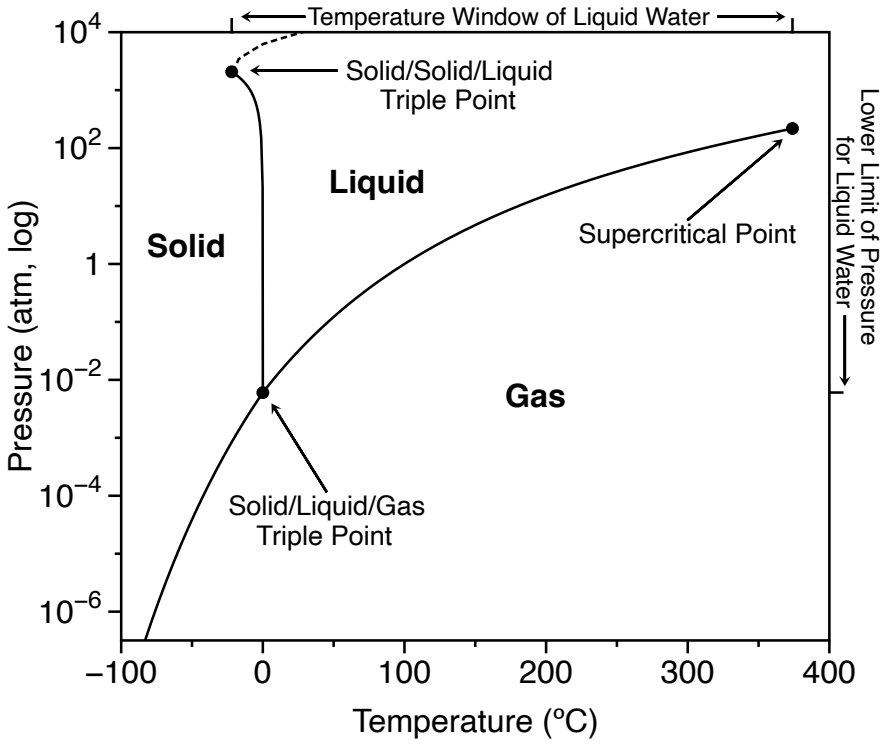

Figure 1.2: Temperature and pressure phase diagram for water. Solid lines are equilibrium curves dividing two phases (noted in bold). Annotated solid points are regions of particular interest within temperature and pressure space. The solid/liquid/gas triple point is the temperature and pressure conditions where solid, liquid, and gas phase water are in thermodynamic equilibrium. The supercritical point is the point where water behaves both as a liquid and a gas at higher temperatures and pressures. The solid/solid/liquid triple point is the pressure and temperature condition where ice I, ice III, and liquid water are in thermodynamic equilibrium. Noted on the upper and right axes are the bounds of liquid water. At temperatures lower than the solid/solid/liquid triple point liquid water is not favored at any pressure. Similarly, at temperatures above the supercritical point liquid water is not favored at any pressure. Liquid water is not favored at pressures below the triple point at any temperature. Here I only consider pressures up to 10^4 atm, and liquid water is possible at that pressure. Diagram modified from Zhang et al. (2015).

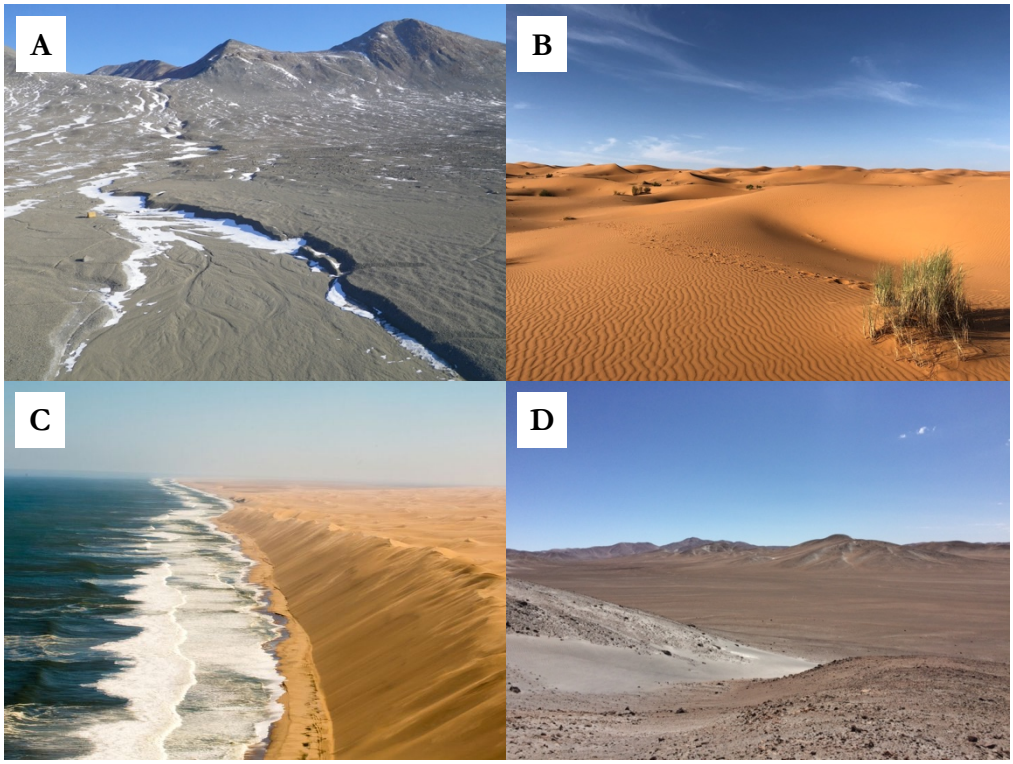

Figure 1.3: Images of several of Earth's notable deserts. **A)** Image of the McMurdo dry valleys in Antarctica from the National Science Foundation's Long Term Ecological Research Network. **B)** Image of sand dunes on the eastern edge of the Sahara Desert in Egypt taken by Greg Gulik. Image used under creative commons license 2.0. **C)** Image of the Atlantic Ocean meeting the sand dunes of the Namib Desert in Namibia taken by Kate Schoenbach via BBC. Image used under creative commons license 2.0. **D)** Image of *Pampas de la Joya* region in the Atacama Desert in Southern Perú taken by Donald Glaser.

CHAPTER 1 REFERENCES

Azua-Bustos, A., Fairén, A. G., González-Silva, C., Ascaso, C., Carrizo, D., Fernández-Martínez, M. Á., Fernández-Sampedro, M., García-Descalzo, L., García-Villadangos, M., Martin-Redondo, M. P., Sánchez-García, L., Wierzchos, J., and Parro, V. (**2018**). Unprecedented rains decimate surface microbial communities in the hyperarid core of the Atacama Desert. *Scientific Reports*, *8*(1). DOI: 10.1038/s41598-018-35051-w

Bastin, J.-F., Berrahmouni, N., Grainger, A., Maniatis, D., Mollicone, D., Moore, R., Patriarca, C., Picard, N., Sparrow, B., Abraham, E. M., Aloui, K., Atesoglu, A., Attore, F., Bassüllü, Ç., Bey, A., Garzuglia, M., García-Montero, L. G., Groot, N., Guerin, G., Laestadius, L., Lowe, A. J., Mamane, B., Marchi, G., Patterson, P., Rezende, M., Ricci, S., Salcedo, I., Diaz, A. S.-P., Stolle, F., Surappaeva, V., and Castro, R. (**2017**). The extent of forest in dryland biomes. *Science*, *356*(6338), 635–638. DOI: 10.1126/science.aam6527

Chiquoine, L. P., Abella, S. R., and Bowker, M. A. (**2016**). Rapidly restoring biological soil crusts and ecosystem functions in a severely disturbed desert ecosystem. *Ecological Applications*, *26*(4), 1260–1272. DOI: 10.1002/15-0973

Domagal-Goldman, S. D., Wright, K. E., Adamala, K., Arina de la Rubia, L., Bond, J., Dartnell, L. R., Goldman, A. D., Lynch, K., Naud, M.-E., Paulino-Lima, I. G., Singer, K., Walter-Antonio, M., Abrevaya, X. C., Anderson, R., Arney, G., Atri, D., Azúa-Bustos, A., Bowman, J. S., Brazelton, W. J., Brennecka, G. A., Carns, R., Chopra, A., Colangelo-Lillis, J., Crockett, C. J., DeMarines, J., Frank, E. A., Frantz, C., de la Fuente, E., Galante, D., Glass, J., Gleeson, D., Glein, C. R., Goldblatt, C., Horak, R., Horodyskyj, L., Kaçar, B., Kereszturi, A., Knowles, E., Mayeur, P., McGlynn, S., Miguel, Y., Montgomery, M., Neish, C., Noack, L., Rugheimer, S., Stüeken, E. E., Tamez-Hidalgo, P., Walker, S. I., and Wong, T. (**2016**). The astrobiology primer v2.0. *Astrobiology*, *16*(8), 561–653. DOI: 10.1089/ast.2015.1460

Dong, J., Fischer, R. A., Stixrude, L. P., Lithgow-Bertelloni, C. R., Eriksen, Z. T., and Brennan, M. C. (**2022**). Water storage capacity of the martian mantle through time. *Icarus*, *385*, 115113. DOI: 10.1016/j.icarus.2022.115113

El Fadli, K. I., Cerveny, R. S., Burt, C. C., Eden, P., Parker, D., Brunet, M., Peterson, T. C., Mordacchini, G., Pelino, V., Bessemoulin, P., Stella, J. L., Driouech, F., Wahab, M. M. A., and Pace, M. B. (**2013**). World Meteorological Organization assessment of the purported world record 58°C temperature extreme at El Azizia, Libya (13 September 1922). *Bulletin of the American Meteorological Society*, *94*(2), 199–204. DOI: 10.1175/BAMS-D-12-00093.1

Grasset, O., Castillo-Rogez, J., Guillot, T., Fletcher, L. N., and Tosi, F. (**2017**). Water and volatiles in the outer solar system. *Space Science Reviews*, *212*(1–2), 835–875. DOI: 10.1007/s11214-017-0407-z

Hartmann, L., Ciesla, F., Gressel, O., and Alexander, R. (**2017**). Disk evolution and the fate of water. *Space Science Reviews*, *212*(1–2), 813–834. DOI: 10.1007/s11214-017-0406-0

Heinz, J., Rambags, V., and Schulze-Makuch, D. (**2021**). Physicochemical parameters limiting growth of Debaryomyces hansenii in solutions of hygroscopic compounds and their

effects on the habitability of Martian brines. *Life*, *11*(11), 1194. DOI: 10.3390/life11111194

Hickman-Lewis, K., Moore, K. R., Hollis, J. J. R., Tuite, M. L., Beegle, L. W., Bhartia, R., Grotzinger, J. P., Brown, A. J., Shkolyar, S., Cavalazzi, B., and Smith, C. L. (**2022**). *In situ* Identification of paleoarchean biosignatures using colocated perseverance rover analyses: Perspectives for *in situ* Mars science and sample return. *Astrobiology*, *22*(9), 1143–1163. DOI: 10.1089/ast.2022.0018

Izidoro, A., de Souza Torres, K., Winter, O. C., and Haghighipour, N. (**2013**). A compound model for the origin of Earth's water. *The Astrophysical Journal*, *767*(1), 54. DOI: 10.1088/0004-637X/767/1/54

Latosińska, J. N., Latosińska, M., and Bielak, J. (**2015**). Towards analysis and predicting maps of ultraviolet index from experimental astronomical parameters (solar elevation, total ozone level, aerosol index, reflectivity). Artificial neural networks global scale approach. *Aerospace Science and Technology*, *43*, 301–313. DOI: 10.1016/j.ast.2015.03.011

Levin, G. V., and Straat, P. A. (**1976**). Labeled release—An experiment in radiorespirometry. *Origins of Life*, *7*(3), 293–311. DOI: 10.1007/BF00926948

Li, L., Zhang, X., Luan, Z., Du, Z., Xi, S., Wang, B., Cao, L., Lian, C., and Yan, J. (**2018**). *In situ* quantitative raman detection of dissolved carbon dioxide and sulfate in deep-sea high-temperature hydrothermal vent fluids. *Geochemistry, Geophysics, Geosystems*, *19*(6), 1809–1823. DOI: 10.1029/2018GC007445

McCaskey, J. P. (**2020**). History of 'temperature': Maturation of a measurement concept. *Annals of Science*, *77*(4), 399–444. DOI: 10.1080/00033790.2020.1817980

Nádudvari, Á., Abramowicz, A., Maniscalco, R., and Viccaro, M. (**2020**). The estimation of lava flow temperatures using landsat night-time Images: Case studies from eruptions of Mt. Etna and Stromboli (Sicily, Italy), Kīlauea (Hawaii Island), and Eyjafjallajökull and Holuhraun (Iceland). *Remote Sensing*, *12*(16), 2537. DOI: 10.3390/rs12162537

Navarro-González, R., McKay, C. P., and Mvondo, D. N. (**2001**). A possible nitrogen crisis for Archaean life due to reduced nitrogen fixation by lightning. *Nature*, *412*(6842), 61–64. DOI: 10.1038/35083537

O'Brien, D. P., Izidoro, A., Jacobson, S. A., Raymond, S. N., and Rubie, D. C. (**2018**). The delivery of water during terrestrial planet formation. *Space Science Reviews*, *214*(1), 47. DOI: 10.1007/s11214-018-0475-8

Pei, L., Min, Q., Du, Y., Wang, Z., Yin, B., Yang, K., Disterhoft, P., Pongetti, T., and Zhu, L. (**2019**). Water vapor near-UV absorption: Laboratory spectrum, field evidence, and atmospheric impacts. *Journal of Geophysical Research: Atmospheres*, *124*(24), 14310–14324. DOI: 10.1029/2019JD030724

Pointing, S. B., and Belnap, J. (**2012**). Microbial colonization and controls in dryland systems. *Nature Reviews Microbiology*, *10*(8), 551–562. DOI: 10.1038/nrmicro2831

Pyle, L. A., Hall, L. M., and Bork, E. W. (**2019**). Soil properties in northern temperate pastures do not vary with management practices and are independent of rangeland health. *Canadian Journal of Soil Science*, *99*(4), 495–507. DOI: 10.1139/cjss-2019-0076

Saethre, E. (**2007**). Close encounters: UFO beliefs in a remote Australian Aboriginal community. *Journal of the Royal Anthropological Institute*, *13*(4), 901–915. DOI: 10.1111/j.1467-9655.2007.00463.x

Safriel, U., Adeel, Z., Niemeijer, D., Puigdefabregas, J., White, R., Lal, R., Winslow, M., Ziedler, J., Prince, S., and Archer, E. (**2005**). Dryland Systems. In *Ecosystems and human well-being: Current state and trends* (pp. 623–662). Island Press.

Scambos, T. A., Campbell, G. G., Pope, A., Haran, T., Muto, A., Lazzara, M., Reijmer, C. H., and van den Broeke, M. R. (**2018**). Ultralow surface temperatures in east Antarctica from satellite thermal infrared mapping: The coldest places on Earth. *Geophysical Research Letters*, *45*(12), 6124–6133. DOI: 10.1029/2018GL078133

Seiff, A., Kirk, D. B., Knight, T. C. D., Young, R. E., Mihalov, J. D., Young, L. A., Milos, F. S., Schubert, G., Blanchard, R. C., and Atkinson, D. (**1998**). Thermal structure of Jupiter's atmosphere near the edge of a 5-μm hot spot in the north equatorial belt. *Journal of Geophysical Research: Planets*, *103*(E10), 22857–22889. DOI: 10.1029/98JE01766

Stern, S. A., Bagenal, F., Ennico, K., Gladstone, G. R., Grundy, W. M., McKinnon, W. B., Moore, J. M., Olkin, C. B., Spencer, J. R., Weaver, H. A., Young, L. A., Andert, T., Andrews, J., Banks, M., Bauer, B., Bauman, J., Barnouin, O. S., Bedini, P., Beisser, K., Beyer, R. A., Bhaskaran, S., Binzel, R. P., Birath, E., Bird, M., Bogan, D. J., Bowman, A., Bray, V. J., Brozovic, M., Bryan, C., Buckley, M. R., Buie, M. W., Buratti, B. J., Bushman, S. S., Calloway, A., Carcich, B., Cheng, A. F., Conard, S., Conrad, C. A., Cook, J. C., Cruikshank, D. P., Custodio, O. S., Dalle Ore, C. M., Deboy, C., Dischner, Z. J. B., Dumont, P., Earle, A. M., Elliott, H. A., Ercol, J., Ernst, C. M., Finley, T., Flanigan, S. H., Fountain, G., Freeze, M. J., Greathouse, T., Green, J. L., Guo, Y., Hahn, M., Hamilton, D. P., Hamilton, S. A., Hanley, J., Harch, A., Hart, H. M., Hersman, C. B., Hill, A., Hill, M. E., Hinson, D. P., Holdridge, M. E., Horanyi, M., Howard, A. D., Howett, C. J. A., Jackman, C., Jacobson, R. A., Jennings, D. E., Kammer, J. A., Kang, H. K., Kaufmann, D. E., Kollmann, P., Krimigis, S. M., Kusnierkiewicz, D., Lauer, T. R., Lee, J. E., Lindstrom, K. L., Linscott, I. R., Lisse, C. M., Lunsford, A. W., Mallder, V. A., Martin, N., McComas, D. J., McNutt, R. L., Mehoke, D., Mehoke, T., Melin, E. D., Mutchler, M., Nelson, D., Nimmo, F., Nunez, J. I., Ocampo, A., Owen, W. M., Paetzold, M., Page, B., Parker, A. H., Parker, J. W., Pelletier, F., Peterson, J., Pinkine, N., Piquette, M., Porter, S. B., Protopapa, S., Redfern, J., Reitsema, H. J., Reuter, D. C., Roberts, J. H., Robbins, S. J., Rogers, G., Rose, D., Runyon, K., Retherford, K. D., Ryschkewitsch, M. G., Schenk, P., Schindhelm, E., Sepan, B., Showalter, M. R., Singer, K. N., Soluri, M., Stanbridge, D., Steffl, A. J., Strobel, D. F., Stryk, T., Summers, M. E., Szalay, J. R., Tapley, M., Taylor, A., Taylor, H., Throop, H. B., Tsang, C. C. C., Tyler, G. L., Umurhan, O. M., Verbiscer, A. J., Versteeg, M. H., Vincent, M., Webbert, R., Weidner, S., Weigle, G. E., White, O. L., Whittenburg, K., Williams, B. G., Williams, K., Williams, S., Woods, W. W., Zangari, A. M., and Zirnstein, E. (**2015**). The Pluto system: Initial results from its exploration by New Horizons. *Science*, *350*(6258), aad1815. DOI: 10.1126/science.aad1815

Tait, K. T., McCubbin, F. M., Smith, C. L., Agee, C. B., Busemann, H., Cavalazzi, B., Debaille, V., Hutzler, A., Usui, T., Kminek, G., Meyer, M. A., Beaty, D. W., Carrier, B. L., Haltigin, T., Hays, L. E., Cockell, C. S., Glavin, D. P., Grady, M. M., Hauber, E.,

Marty, B., Pratt, L. M., Regberg, A. B., Smith, A. L., Summons, R. E., Swindle, T. D., Tosca, N. J., Udry, A., Velbel, M. A., Wadhwa, M., Westall, F., and Zorzano, M.-P. (**2022**). Preliminary planning for Mars sample return (MSR) curation activities in a sample receiving facility (SRF). *Astrobiology*, *22*(S1), S-57-S-80. DOI: 10.1089/ast.2021.0105

Taubner, R.-S., Olsson-Francis, K., Vance, S. D., Ramkissoon, N. K., Postberg, F., de Vera, J.-P., Antunes, A., Camprubi Casas, E., Sekine, Y., Noack, L., Barge, L., Goodman, J., Jebbar, M., Journaux, B., Karatekin, Ö., Klenner, F., Rabbow, E., Rettberg, P., Rückriemen-Bez, T., Saur, J., Shibuya, T., and Soderlund, K. M. (**2020**). Experimental and simulation efforts in the astrobiological exploration of exooceans. *Space Science Reviews*, *216*(1), 9. DOI: 10.1007/s11214-020-0635-5

Viglas, K. (**2016**). The placement of Lucian's novel true history in the genre of science fiction. *Interlitteraria*, *21*(1), 158. DOI: 10.12697/IL.2016.21.1.13

Wierzchos, J., Casero, M. C., Artieda, O., and Ascaso, C. (**2018**). Endolithic microbial habitats as refuges for life in polyextreme environment of the Atacama Desert. *Current Opinion in Microbiology*, *43*, 124–131. DOI: 10.1016/j.mib.2018.01.003

Zomer, R. J., Trabucco, A., Bossio, D. A., and Verchot, L. V. (**2008**). Climate change mitigation: A spatial analysis of global land suitability for clean development mechanism afforestation and reforestation. *Agriculture, Ecosystems & Environment*, *126*(1–2), 67–80. DOI: 10.1016/j.agee.2008.01.014

Chapter 2

WATER VAPOR ADSORPTION PROVIDES DAILY, SUSTAINABLE WATER TO SOILS OF THE HYPERARID ATACAMA DESERT

2.1. Abstract

Water is necessary for all life on Earth. Water is so critical that organisms have developed strategies to survive in hyperarid environments. These regions with extremely low water availability are also unique analogs in which to study the physio-chemical conditions of extraterrestrial environments such as Mars. We have identified a daily, sustainable cycle of water vapor adsorption (WVA) and desorption that measurably affects soil water content in the hyperarid region of the Atacama Desert in southern Perú. We pair field-based soil temperature and relative humidity soil profiles with laboratory simulations to provide evidence for a daily WVA cycle. Using our WVA model, we estimate that one adsorptive period – one night – increases soil water content by 0.2 - 0.3 mg g^{-1} of soil (~30 μm rainfall). We can plausibly rule out other water inputs during our field campaign that could account for this water input, and we provide evidence that this WVA cycle is driven by solar heating and maintained by atmospheric water vapor. WVA may also serve to retain water from infrequent rain events in these soils. If the water provided by WVA in these soils is bioavailable, it could have significant implications for the microorganisms endemic to hyperarid environments.

2.2. Introduction

Water is necessary for all known life on Earth. However, life has developed strategies to survive all sorts of environments from freshwater lakes and tropical rainforests to hypersaline lakes and hyperarid deserts. In the search for life elsewhere, NASA has pursued a 'follow the water' strategy to investigate the most probable targets for life contingent on the presence of liquid water. Our nearest neighbors in the solar system are dry, inhospitable places. Yet scientists have been searching over the past several decades for life on these dry planets.

Mars is an extraordinarily dry planet, having lost virtually all its surface water ~1 Ga through interaction with the solar wind (Kite, 2019; Terada et al., 2009). Water on modern Mars, though scarce, is almost entirely present as ice located in the polar caps and in the subsurface of higher latitudes (Piqueux et al., 2019). Smaller non-ice reservoirs of water include *i)* atmospheric vapor (~20 – 160 ppmv; Fedorova et al., 2021; Savijärvi et al., 2015) *ii)* ephemeral deliquescent brines (Rennó et al., 2009; Toner and Catling, 2018); and *iii)* regolith adsorbed vapor (~0.5 – 1.5 weight percent [wt%]; Beck et al., 2010; Steele et al. 2017). Recent work has also incited a robust debate as to the presence of hypersaline lakes in the subsurface below the southern polar cap (Lauro et al., 2021; Smith et al., 2021).

Hyperarid environments (defined as an aridity index, the ratio of evapotranspiration to rain, of ≤0.05; Bastin et al., 2017) are one of the best terrestrial analogs from which to understand the physical and chemical conditions on Mars and, eventually, arid exoplanets. The hyperarid, ecological region of the Atacama Desert, which spans Perú and Chile, is one of the driest environments on Earth and is a reasonably accessible place that mimics aspects of Martian conditions (Houston and Hartley, 2003; Narvaez-Montoya et al., 2022). Water

inputs to the Atacama soils are rare and meager (~2 mm yr^{-1}) due to the rain shadow effect from the Andes (Houston and Hartley, 2003). Rain and fog events occur between ~1 and 10 times per year on average, respectively (McKay et al., 2003; Valdivia-Silva et al., 2012a). Despite the infrequency of rain and fog events, viable cells are found in the top tens of cm in these soils (Navarro-Gonzalez et al., 2003; Schulze-Makuch et al., 2018; Valdivia-Silva et al., 2011). Little is known about the relationship between water input and microbial activity or microbial growth in these environments, except that – counter intuitively – major inputs of water (e.g., during *El Niño* events) can negatively affect the microbial community by driving certain microbial species locally-adapted to hyperarid conditions to extinction, and favoring a select minority capable of tolerating osmotic-shock and hypersaline brines (Azua-Bustos et al., 2018).

Water Vapor Adsorption (WVA) is a phenomenon that increases soil water content (SWC) through van der Waals-type attraction between water molecules and soil particles (Figure 2.1; see also Agam and Berliner, 2006). The WVA process occurs when the ambient atmospheric relative humidity (RH) is higher than the RH of the soil pore space (Agam and Berliner, 2006). Soil WVA has been studied extensively in agricultural settings, particularly in arid and semiarid environments (Agam and Berliner, 2004; Kosmas et al., 1998, 2001; Verhoef et al., 2006). It has been shown to provide biologically-relevant amounts of water and induce microbial respiration in semiarid environments (McHugh et al., 2015). There are only a few direct measurements of WVA reported in hyperarid environments (Kaseke et al., 2012b; Kool et al., 2021); and, to our knowledge, no measurements have been made in the Atacama Desert. Here we present field observations and laboratory simulation data along with an empirical model demonstrating the presence of a RH-driven WVA cycle in the

hyperarid soils of the Atacama Desert. We developed a simple diffusion-advection-reaction model to interpret our field measurements; the model quantifies *i*) the rates of WVA and desorption and *ii*) the effect of adsorption on SWC. We compare the amount of water cycled by WVA with estimates of water input by rain and fog in this hyperarid region. We also compare our WVA estimates with those in other hyperarid environments. This work adds to our understanding of the total water budget of the near subsurface in hyperarid environments. It may also inform the search for microenvironments of water availability on Mars and, eventually, on dry exoplanets.

2.3. Materials & Methods

2.3.1. Field Methods

2.3.1.1. Site

We performed field measurements and collected samples in a hyperarid region (aridity index ≤ 0.003; Zomer et al., 2008) of the Atacama Desert in Southern Perú known as *Pampas de la Joya*, previously described by Valdivia-Silva et al. (2011). We characterized two sites, ~1 km apart, located near ~16.7ºS, 72.1ºW in a hilly desert landscape (Figure 2.2 A-D). The Mar de Quartz (MDQ) site is in a flat basin or playa (Figure 2.2C). The Los Halitos (LH) site is located on a nearby hillside, roughly 5 m above the playa (Figure 2.2D). Recent, nearby studies show relatively deep water tables of 50 – 150 m (Graber et al., 2021) and ~200 m (Vera et al., 2021), indicating limited groundwater influence at the surface.

2.3.1.2. Soil Collection

We collected duplicate soil samples (~2 m apart) at each site in October 2017. The top 5 cm (~300 g) of surface soil was collected using a plastic hand spade and placed in a new,

polyethylene zip-top bag. Samples were shipped back to the laboratory within 2 weeks and stored in the dark at 22ºC prior to analysis and experimentation.

2.3.1.3. Soil Temperature & Relative Humidity

We measured soil temperature (T) and RH using a custom-designed and built sensor array. The sensor arrays were allowed to equilibrate in the soil for ~36 h prior to data analysis (Supplemental Figure A.1). Collection of T and RH data occurred from Oct. 1 to Oct. 10, 2017, at MDQ, and from Sep. 29 to Oct. 4 2017, at LH. The T and RH array was built from ½" PVC tubing (1.5 cm ID, 2.1 cm OD) with six discrete chambers; one at each depth [i.e., 0, 2.5, 5, 10, 20, and 30 cm] to prevent air mixing between soil depths (Figure A.2). The PVC has a thermal conductivity similar to that of dry, sandy soil (e.g., 0.12 – 0.25 W m^{-1} K^{-1}; Dashora et al., 2005; Robertson, 1988), so the sensors experience conditions similar to the adjacent soil. Two, 2 cm-diameter holes were placed 180º apart for air equilibration between the outer soil and the inside of the array chambers. Tyvek® 1442R polyethylene membranes (Dupont®: Wilmington, DE, USA) were glued over the holes to prevent soil particles from entering the chambers while allowing air and water vapor to equilibrate across the membrane. A plastic polymer putty was used to separate the chambers due to its thermal insulation properties. Temperature and RH were measured using Honeywell® HIH7000 series capacitance sensors (Charlotte, NC, USA). The data from the sensors were collected and stored using an arduino® pro-trinket microprocessor with an adafruit™ microSD card breakout board. Coding and wiring schematics are available in a github repository[1]. Reported measurements at each depth were calculated as the mean of 10 readings (500 ms apart) every 20 min.

[1] https://github.com/donnyglaser/Soil_TRH_SensorArray

2.3.1.3.a. Sensor Calibration & Accuracy

The HIH sensors were calibrated prior to deployment. To calibrate temperature, the sensor was placed in an environmental chamber (Lab-Line® model 850), allowed to stabilize for ≥ 30 min, and temperature recorded using a Fluke 52II meter with an LT-22N thermocouple probe. A four-point calibration was performed with 10 sensor measurements at each temperature (i.e., 12.5, 17, 24, and 32°C; Figure A.3). The HIH sensor's temperature calibration had $r^2 = 0.99994$; residuals for all calibration temperatures were <0.15ºC (Figure A.3). To calibrate relative humidity, the sensor was placed in a sealed glass chamber with a saturated salt solution buffer (Rockland, 1960). Humidity was allowed to stabilize for ≥24 hr with each of four buffers (LiCl, 12%RH; $Mg(NO_3)_2$, 52%RH; NaCl, 75%RH; and H_2O, 100%RH;) and 10 measurements were recorded (Figure A.4). The HIH sensor's relative humidity calibration had $r^2 = 0.99959$; residuals for all calibration values of relative humidity were <1.5%RH (Figure A.4).

2.3.1.3.b. Sensor Precision

We assessed the typical precision of the HIH sensor using data compiled from 6 depths, over ~11 days at the MDQ site. We evaluated the standard deviation (SD) of repeated measures from the HIH sensor for temperature (binned over 10 degrees; Table A.1) and relative humidity (binned over 20%RH; Table A.2) to get a sense of the precision of the measurements. The average SD on the temperature reading was 0.008ºC and the maximum SD was 0.08ºC; there is no relationship between temperature and SD indicating the sensors are equally precise across the entire range of observations. The average SD for relative humidity was 0.008%RH and the maximum SD was 0.1%RH. There is a weak correlation between SD and RH, suggesting values at high RH are somewhat less precise than

measurements at low RH. However, the maximum observed SD (± 0.1%RH) is similar to the manufacturer reported precision (± 0.04%RH), indicating that the sensor is behaving nominally.

2.3.2. Laboratory Methods

2.3.2.1. Soil Characterization

Soil samples were sieved to 2 mm to remove gravel and cobbles and the <2 mm, fine-earth, fraction was used for characterization (Soil Survey Staff, 2014). We prioritized the fine-earth fraction because WVA is surface area-dependent (Leão and Tuller, 2014; Tuller and Or, 2005) and surface area decreases exponentially with increasing mean particle diameter (Allen, 2013). The soil particle size distribution was measured on a 40 g dry weight subsample using the hydrometer method (Day, 1965). Soil pH and conductivity were measured on a 1:2 (mass:mass) soil:deionized water (18.2 MΩ·cm water; Barnstead, Van Nuys, CA, USA) slurry using a HACH HQ30d (Loveland, CO, USA) multimeter with PHC201 and CDC401 probes, respectively. Extractable soil anions and cations were determined on filtered (0.2 μm, Supor©; Pall: Port Washington, NY, USA) subsamples of the 1:2 soil:deionized water mixture on Dionex DX600 (anions: Dionex IonPac AS11 analytical and IonPac AG11 guard columns) and DX120 (cations: Dionex IonPac CS12A analytical and IonPac SG11 guard columns) ion chromatographs, respectively according to methods from Shock et al. (2010). A calibration curve from 0.1 ppm to 10 ppm, periodic blanks (deionized water; 1 blank: 5 samples), and standards of known concentration were measured over the course of each sequence to ensure accurate ion concentration measurements. Bulk soil carbon and nitrogen content were determined in triplicate on dried, ground (i.e., 4 minutes in a ball-mill) soil samples. Briefly, soil subsamples treated with and without HCl

fumigation (12 M, 8 h) were used to determine organic and total carbon content, respectively. Milled, acidified/un-acidified soil was combusted using a Costech ECS 4010 (Valencia, CA, USA) elemental analyzer with a thermal conductivity detector (Hedges and Stern, 1984). Inorganic carbon was determined as the difference between total carbon and organic carbon. Specific surface area was determined from Brunauer-Emmett-Teller (BET) isotherm analysis using N_2 adsorption in a Micromeritics® Tristar II model 3020 (Norcross, GA, USA) according to published methods (Bhambhani et al., 1972; Kaiser and Guggenberger, 2003); surface area samples were dried at 70ºC under a gentle nitrogen stream to drive off excess water vapor prior to analysis. Mineral abundances were determined by powder x-ray Diffractometry (XRD) using a Bruker D8 (parameters: 5º - 65º 2θ, 0.02º steps, 2 s per step, Cu K-α radiation; Madison, WI, USA) on soil samples ground to <20 μm using a McCrohn mill according to methods in Środoń et al. (2001). The resulting spectra were interpreted using "powdR", an R library that calls the USGS's RockJock spectral database and optimizes fit by minimizing the weighted least squares residual error (Butler and Hillier, 2021; Eberl, 2003). Bulk soil porosity was calculated from helium pycnometry volume measurements on an AccuPyc 1330 (Micromeritics, Norcross, GA, USA) using methods similar to Tamari (2004).

2.3.2.2. Simulation Experiments

We performed laboratory incubations designed to simulate field conditions at a depth of 10 cm in the Atacama soils and measured the effect of changes in T at fixed RH on SWC (Figure A.5). Temperature was controlled using a Lab-Line® model 850 environmental chamber (Thermo Fisher: Waltham, MA, USA). The chamber maintains T to within ± 0.3ºC and was used without a T ramp. Soil samples were placed into an air-tight

polymethylmethacrylate enclosure (Mart® Microbiology B.V.; Lichenvoorde, NL) with a beaker containing ~30 mL of a saturated LiCl solution to buffer at ~12%RH (Figure A.6; Rockland, 1960). Prior to starting the experiment, the soil was dried at 50ºC to a constant mass (i.e., stable to ± 1.0 mg). A lower drying temperature was chosen to eliminate all water (section 2.3.2.3.) without the risk of mineral dehydration (i.e., Strydom et al., 1995). Dry, <2 mm soil from each site (124 g for MDQ and 70 g for LH) in an 8-cm glass petri dish was placed into the air-tight enclosure and the environmental chamber was cycled between 12ºC (night conditions) and 35ºC (day conditions) for 16 h and 8 h intervals, respectively, to simulate the T changes observed in the field (Figure A.5). The starting condition was 35ºC; and after 8 hours, soil was removed from the enclosure and mass determined on a Mettler Toledo model XS204 analytical balance (Columbus, OH, USA). The soil sample was then put back into the enclosure and cycled to the next T setting. Enclosure T and RH were measured using a 1-sensor version of the field array setup described in section 2.3.1.3. We modified the software to enable a higher data sampling rate and report the mean of 20 measurements (500 ms apart) every 5 min. The experiment was performed over a 4-day period. A control mass (75 g) consisting of a polyethylene petri dish packed tightly with pyrite grains and sealed with electrical tape was incubated alongside the Atacama soils to assess the magnitude of changes in mass on a low surface area object of similar mass.

2.3.2.3. Soil Water Extraction and Validation

Soil water was extracted from the experimental soils using a cryogenic trapping method similar to that presented by Koeniger et al. (Figure A.7; 2011). In brief, soil water was extracted after incubation for 48 hours under night conditions (12ºC, 12% RH). The soil (85 g) was placed into a 60 mL glass serum bottle (Wheaton®: Rockwood, TN, USA) connected

to a 12 mL Exetainer® (Labco: Lampeter, UK) with 1/16" stainless-steel capillary tubing. The serum bottle was placed in a liquid nitrogen bath for ~5 min, then the headspace was removed using a vacuum pump to reduce the pressure ~25 kPa, gauge (Figure A.7A). The serum bottle was removed from the liquid nitrogen and allowed to warm to room temperature for ~15 min. To extract the water vapor adsorbed to the soils, the serum bottle was placed in a 90ºC water bath and the connected exetainer immersed in an adjacent liquid nitrogen bath, facilitating transfer of water vapor from the soil into the exetainer (Figure A.7B). Over the course of 2 hours ~20 mg of clear liquid was transferred from the serum bottle to the exetainer. The resulting extract in the exetainer was analyzed using Fourier Transform Infrared Spectroscopy (FT-IR) on a Bruker® IFS 66v/S (Madison, WI, USA) and compared to deionized water. A similar extraction of soil incubated at 50ºC for 48 h failed to produce any measurable liquid; indicating that this soil was in fact dry.

2.4. Results

2.4.1. Field Results

2.4.1.1. Soil Temperature & Relative Humidity

The surface T at MDQ (Figure 2.3A) and LH (Figure 2.4A) exhibit a strong diurnal pattern ranging from an average of ~10ºC at night to an average of ~45ºC during the day. The peak in surface T occurs between 11:50 and 13:35 (solar time). The sensors at depth show a similar diurnal pattern; however, the amplitude decreases with depth and the timing of the peak in T is delayed by ~5 h at the 20 cm depth. The 30 cm sensor shows a relatively stable T of ~25ºC.

The surface RH at MDQ (Figure 2.3B) shows a strong diurnal pattern from ~60% RH at night to ~10%RH during the day. The shallowest sensor (2.5 cm) shows a daily pattern of

~20%RH at night, a sharp peak of ~40%RH around 09:00, and ~10%RH during the day. The RH sensors at all greater depths (5 – 30 cm) show almost no diurnal pattern and RH is roughly constant (±4%RH) over the entire day at ~25%RH (Figure 2.4B). Relative humidity at LH (Figure 2.4B) is comparable to MDQ; however, nighttime surface RH at LH (~40%RH) is lower than during the same period at MDQ (~60%RH).

The overall shapes and patterns in surface RH occur at both sites, but the magnitude and timing can vary. For example, the daytime RHs at both sites are similar at roughly 10%RH. There is a sharp, pronounced peak (~70%RH) in RH at ~07:30, just as T begins to increase. This same feature is evident at both sites, but is less pronounced, at MDQ. The 2.5 cm sensor at LH has an RH peak at 9:00 but the LH peak is smaller than the MDQ peak. Relative humidity increases slowly from daytime values of 10%RH at ~17:00 to nighttime values of 40 – 60%RH at 21:00.

2.4.2. Laboratory Results

2.4.2.1. Soil Characterization

Soil was analyzed in two fractions: bulk soil (all size fractions) and a <2 mm fraction. Bulk soil contains 17 wt% gravel (>2 mm fraction) and 83 wt% non-gravel (<2 mm fraction) at MDQ, and 13 wt% gravel and 87 wt% non-gravel at LH. In addition, LH had large (10 – 20 cm diameter) cobbles that were not sampled; the grain size difference between the two sites was noticeable by eye due to the presence of the large cobbles at LH. The texture of the <2 mm fraction at both sites is broadly a sandy loam (80 wt% sand, 15 wt% loam, and 5 wt% clay: Table 2.1). The MDQ soil has a slightly lower sand fraction and a higher silt fraction compared to LH. Both sites have similar, circumneutral pH (~6.5; Table 2.1). Soil conductivity at both sites is relatively high; with conductivity of ~3 mS cm^{-1} and ~6 mS cm^{-1},

respectively (Table 2.1). Solid phase soil total carbon contents at both sites are similarly low at 0.2 mg g^{-1} (0.02 wt%); organic carbon was ~80 wt% of total carbon (e.g., 0.15 mg g^{-1}; Table 2.1). Solid phase soil total nitrogen content is 0.17 mg g^{-1} (0.017 wt%) and 0.34 mg g^{-1} (0.034 wt%) at MDQ and LH, respectively (Table 2.1). In general, replicate samples at the same site show high variability for most chemical analyses. The porosity of the MDQ soil was 0.52 and lower than that at LH, 0.66 (Table 2.1). The most abundant extractable major ions are Na^+, Cl^-, Ca^{2+}, and SO_4^{2-}, and concentrations are of the order of tens of mg kg^{-1} dry soil. (Table A.3). Fitted MDQ and LH XRD spectra were created using the "powdR" R library with weighted least squares residual error of 0.12 and 0.07, respectively. Anhydrite is the most abundant mineral at MDQ and actinolite is the dominant mineral at LH (Figure A.8). Both sites have roughly the same proportion of non-feldspar silicates (~45 wt%). The LH soil has the same proportion of feldspar and non-feldspar silicates (~45 wt%) while MDQ has relatively lower feldspar abundance (~10 wt%; Figure A.8). Evaporitic minerals were present at relatively higher proportions at MDQ (~20 wt%) than at LH (~10 wt%).

2.4.2.2. Simulated Atacama Soil Experiment

The results of the soil experiments are changes in soil mass as a function of T measured over the course of 80 hours. Temperature ranged from 11 to 13ºC at night and 32 to 35ºC during the day; RH was held at a fairly constant ~12%RH (± 2.7%RH) at all times (Figure A.5). The large, sharp peaks in RH at 09:00 is due to the air-tight enclosure being opened and exposed to the ambient lab conditions for soil mass measurement; the peak decreases to target conditions within an hour.

Soil mass changes from the initial dry mass during the experiment were ~180 mg (~1.5 mg g^{-1}) for Mar de Quartz and ~69 mg (~1.0 mg g^{-1}) for Los Halitos. For soils from both

locations, the first time interval corresponded to a large positive change in mass, roughly 1 mg g^{-1} for Mar de Quartz and 0.5 mg g^{-1} for Los Halitos (Figure 2.5). Starting from the second interval and continuing to the end of the experiment, soil mass increased during the nighttime (12ºC) intervals and decreased during the daytime (35ºC) intervals for soils from both sites. The control does not show the same magnitude of changes or the same pattern as the two soil samples. The control gains a total of ~0.2 mg g^{-1} in mass over the experiment, an order of magnitude less than the soil samples.

2.4.2.3. Soil Water Extraction & Validation

Cryogenic extraction of 85 g soil yielded 22.6 mg of a clear liquid. The liquid exhibited FTIR absorption features at 1650 cm^{-1} and 3370 cm^{-1} that were similar to the peaks present in a deionized water standard (Figure A.9). Results of a residual analysis show little difference ($\leq$ 0.005 AU [absorbance units]) between the peaks for the liquid extracted from the soil and a water standard in the two regions of interest (Figure A.9B).

2.5. Discussion

Here we develop a diffusion-advection-reaction model to interpret the soil absolute humidity profiles as a two-part linear approximation from which we calculate water vapor flux via diffusion, and a reaction term that we interpret as WVA.

2.5.1. Subsurface Temperature, Relative Humidity, and Absolute Humidity in the Pore Space

Absolute humidity ($[H_2O_{(g)}]$), as compared to RH, is the concentration of water per unit volume and is not commonly measured directly. Absolute humidity is calculated using modeled saturation partial pressure of water that is an exponential function of T. The RH sensor measurements are calibrated in units of pressure, and it is necessary to convert to

water concentration. We calculate [$H_2O_{(g)}$] using an entropy maximization framework developed by Koutsoyiannis (2012) based on RH, assuming ideal gas conditions. We observe that RH from 5 to 30 cm depth is relatively stable (±4%RH) over a diurnal cycle while T varies from ~10 to 45ºC at the 5 cm depth. Considering this, and the fact that [$H_2O_{(g)}$] is a function of both T & RH, we infer that [$H_2O_{(g)}$] must be driven almost entirely by T in the subsurface, where our measured RH is nearly constant. Figure 2.6A shows [$H_2O_{(g)}$] as a function of T for both sites at 5 cm depth. This indicates that there is a moderately strong positive correlation between T and [$H_2O_{(g)}$] that follows contours of fixed RH. Conversely, figure 2.6B shows [$H_2O_{(g)}$] as a function of RH, and there is little to no correlation as the data array vertically with RH. This suggests the effect of RH on [$H_2O_{(g)}$] in these soils is negligible.

The stability of RH over the course of the day at 5 cm depth (and down to 20 cm due to the diurnal T fluctuations) suggests the presence of some process that maintains roughly constant RH. It is plausible that deliquescent salts may buffer the RH of the pore space. In order for salts to buffer at the low RH values observed (~20%RH in MDQ and ~10%RH in LH) they must have a low deliquescent relative humidity (DRH); examples include LiCl, certain other chlorides, chlorates, or perchlorates. We were unable to detect the presence of any salts with low DRH, based on x-ray diffraction. However, they could be present at abundances <3 wt%. Recent work has shown the colligative effects of salt mixtures on deliquescence, with the effect of reducing DRH relative to pure minerals (Dupas-Langlet et al., 2013; Gough et al., 2014; Toner and Catling, 2018). So, mixtures of salts could potentially buffer the RH we observe at MDQ and LH. However, common-ion effects can increase DRH and counteract the colligative effects of salt mixtures (Allan et al., 2016). Thus, RH

control by deliquescence will depend on the specific salts present; however, it is plausible that low abundance salts could be present, buffering the subsurface RH.

Our ion chromatography results for soil extracts (Tables A.3 & A.4) may be consistent with salt-buffered RH in the soils. The LH site has lower RH at 5 cm depth (~10%RH) and a higher salt concentration (6.29 mS cm^{-1}) compared to the MDQ site (~20%RH; 3.03 mS cm^{-1}). In addition, LH has a higher abundance of Cl^- (57.0 mg kg^{-1}) compared MDQ (7.1 mg kg^{-1}). Further work would be required to positively identify salts present at trace levels in these soils. It is also plausible that the WVA process itself maintains the constant RH at depth. In this case, the soil particle surfaces may act as a source and sink for water vapor, which has the effect of maintaining stable RH in the pore space.

Surface T peaks between 11:50 and 13:35 (solar time), which is ~45 min earlier than previous similar observations of surface temperature in the Atacama (McKay et al., 2003). Another point to note in our observations of soil T is the delay in timing of the peak T at 20 cm relative to the peak T at the surface. Modeled soil temperatures as a function of depth and time (Gao et al., 2010; see their equation 4c) predict that T at 20 cm should peak ~6 hr after the peak surface T; our observations show a delay of ~5 hr. These observations may be the result of non-conductive heat sources; for example, the lack of water in these soils leads to reduced latent heat. More research is needed to investigate the energy balance of these soils and its effect on water inputs.

2.5.2. WVA Model

A 1-D mass transport, diffusion-advection-reaction, model (WVA model) was developed to interpret the field data and is available in its entirety in a github repository[2]. Using the field-collected soil T & RH profiles as input parameters (described in section 2.3.1.3.) we calculate WVA:

$$\frac{\partial[H_2O_{(g)}]}{\partial t} = Diff + Adv + Rxn, \quad (2.1)$$

where $[H_2O_{(g)}]$ is water vapor concentration, t is time, Diff is diffusive transport, Adv is advective transport, and Rxn is the reaction term. Each term in equation 2.1 has units of μmol cm^{-3} s^{-1}, i.e., a change in $[H_2O_{(g)}]$ per time. We assume that advective transport though the soil is negligible and that $[H_2O_{(g)}]$ is in pseudo steady state on timescales of tens of minutes or more; therefore, we can simplify equation 2.1 as:

$$0 = Diff + Rxn, \quad (2.2)$$

and balance the diffusive component against the reaction component. We use Fick's second law of diffusion to define diffusive transport:

$$Diff = D\frac{\partial^2[H_2O_{(g)}]}{\partial z^2} = \frac{dJ}{dz}, \quad (2.3)$$

where D is the diffusion coefficient in units of m^2 s^{-1}, $\frac{\partial^2[H_2O_{(g)}]}{\partial z^2}$ is the second derivative of $[H_2O_{(g)}]$ with respect to depth (z), and J is the water vapor diffusive flux.

[2] https://github.com/donnyglaser/SoilProfile_DiffusionReaction_Model

2.5.2.1. Water Vapor Diffusive Flux

A gradient of $[H_2O_{(g)}]$ with respect to depth will drive diffusive transport of water vapor from high concentration to low concentration. Here we use Fick's first law of diffusion to solve for the water vapor flux (J):

$$J = -D \times \frac{\partial[H_2O_{(g)}]}{\partial z}. \quad (2.4)$$

To solve this equation, we calculate $\frac{\partial[H_2O_{(g)}]}{\partial z}$, in units of μM cm^{-1} (μmol cm^{-4}), using a linear regression to approximate the $[H_2O_{(g)}]$ vs. depth profiles described in section 2.5.2.2. Most of the $[H_2O_{(g)}]$ vs. depth profiles exhibit a two-part nature due to the presence of a $[H_2O_{(g)}]$ minimum or maximum (Figure 2.7). We consider the flux of the upper (J_{up}) and lower (J_{lo}) portions of the profile separately and then calculate the change in J (dJ; Equation 2.5) to obtain the reaction term (Rxn), which we interpret as WVA (Equation 2.6); i.e.,

$$dJ = -J_{up} + J_{lo}, \quad (2.5)$$

and

$$WVA = -Rxn = \frac{dJ}{dz}, \quad (2.6)$$

where dz is the combined depth of the upper and lower portions of the profile (Figure A.10). Here we use the convention that positive WVA is adsorption ($[H_2O_{(g)}]$ minimum) and negative WVA is desorption ($[H_2O_{(g)}]$ maximum). Overall, the WVA model allows us to calculate the WVA rate and allows the estimation of changes in SWC.

2.5.2.2. Profile Identification and Simplification

All $[H_2O_{(g)}]$ profiles were classified as either *i)* $[H_2O_{(g)}]$ minimum, *ii)* $[H_2O_{(g)}]$ maximum, or *iii)* constant (Figure 2.7). The details of this classification scheme are described in the supplemental materials (Section A.1). Each $[H_2O_{(g)}]$ minimum and $[H_2O_{(g)}]$ maximum-type

profile was simplified into upper and lower spatial regions that can be approximated by linear regression. This is because the upper and lower regions have slopes of opposite sign and must be linearized separately to calculate dJ and thus, WVA.

2.5.2.3. Diffusion Coefficient

The diffusion coefficient, D, is a function of porosity and T which we calculate (in units of $cm^2\ s^{-1}$), according to:

$$D = 0.073\left[\frac{(S-0.1)}{0.9}\right]^2\left[\frac{T}{273}\right]^{1.75}, \quad (2.7)$$

where S is bulk soil porosity and T is temperature in Kelvin (e.g., Jabro, 2009; Troeh et al., 1982). To calculate S, in units of $cm^3\ cm^{-3}$ we use:

$$S = \frac{V_p}{V_t}; \quad (2.8)$$

where V_p is the pore volume and V_t is the total volume of the soil. We assume constant porosity as a function of depth for each site (Table 2.1). We calculate separate diffusion coefficients for the upper and lower profiles (D_{up} & D_{lo}) because T differs significantly in the two regions of the profile at different times of day (Figure A.10). Temperature is calculated by interpolating the two nearest data points between the surface and the reaction point (T_{up}) and between the reaction point and the reaction bottom (T_{lo}; see Figure A.10 & A.16 – A.20). The average upper and lower T (T_{up} & T_{lo}) calculated is equal to T in equation 2.7 and is used to solve for the upper and lower diffusion coefficient (D_{up} & D_{lo}), respectively.

2.5.2.4. WVA Model Output

The output of the WVA model generates values of WVA rate ($\mu mol\ cm^{-3}\ s^{-1}$) that we present over time (Figure 2.8). Values are positive during periods of WVA (i.e., $[H_2O_{(g)}]$ minimum) and negative during periods of water vapor desorption (i.e., $[H_2O_{(g)}]$ maximum).

Trends in WVA rate are similar for both sites. The WVA rate begins positive at ~0.0002 μmol cm^{-3} s^{-1} from midnight until ~7:00. From ~7:00 to ~9:00, there is a marked increase in WVA rate to ~0.0003 observed on most days. Negative WVA values reach a minimum between -0.0007 and -0.0015 μmol cm^{-3} s^{-1} between 11:00 and 12:00, after which there is a gradual trend toward more positive values of WVA rate. Water vapor adsorption rates switch back to positive values of ~0.0003 μmol cm^{-3} s^{-1} at ~17:00, gradually decreasing to ~0.0002 μmol cm^{-3} s^{-1} at midnight.

We integrated WVA rate (μmol cm^{-3} s^{-1}) over time to produce a change in WVA over a specific time interval (μmol cm^{-3}). We then summed all the changes in WVA over the course of a day to produce cumulative WVA, representing the net adsorption or desorption of water in the soils (Figure 2.9). Positive cumulative WVA indicates net adsorption. Over the duration of observation at MDQ (10 days), we calculate a slightly negative cumulative WVA of -4.4 μmol cm^{-3} indicating a minimal loss of water over this period. At LH, we calculate a slightly negative cumulative WVA of -3.5 μmol cm^{-3}, indicating a similarly negligible water loss over the observation period (4 days). Our observational period is too short to make overall generalizations of long-term WVA.

2.5.2.5. Soil Water Content

Changes in soil water content, the amount of H_2O associated with the soil particles (mg g^{-1}), can be estimated from WVA (μmol cm^{-3}) by dividing by soil density (g cm^{-3}). This method cannot determine absolute SWC but can assess relative changes in SWC over the adsorption or desorption periods. At MDQ, we calculate average changes in SWC of 0.19 and -0.17 mg g^{-1} for the adsorption and desorption periods, respectively (Table 2.2). Similarly, we calculate average changes in SWC of 0.20 and -0.22 mg g^{-1} at LH for the

adsorption and desorption periods, respectively (Table 2.2). These changes in SWC are in very good agreement with the changes in SWC observed independently in the simulation experiment (Section 2.5.3.2; Table 2.2). The similar magnitudes of adsorption and desorption indicate SWC is in rough steady state over the course of several days with no appreciable net loss of water from the soil (or gain to the soil). These changes in SWC are localized to the upper and lower profile regions of the soil, typically the top 10 – 20 cm (Figure A.10). An increase in SWC of 0.20 mg g^{-1} over the top 10 cm of soil would equate to 20 – 30 μm of rain equivalent per day from WVA.

2.5.3. Laboratory Simulations of Water Vapor Adsorption

2.5.3.1. Soil Characteristics

Soil water content changes in response to changes in T in our laboratory simulations (Figure 2.5) indicate that MDQ soils have higher steady state (they reach a higher asymptotic plateau) water retention compared to LH soils (i.e., 1.5 and 1.0 mg g^{-1} soil, respectively). This is most likely due to the higher BET surface area of MDQ soils (~1.05 m^2 g^{-1} soil) compared to LH soils (~0.47 m^2 g^{-1} soil; Table 2.1). Organic carbon is a highly adsorptive species capable of adsorbing ≥300 times the water observed in this experiment (Liu et al., 2017). However, both samples in this experiment have very low organic carbon content (~0.16 mg g^{-1}; ~0.016 wt%), discrediting the idea that organic carbon content could be driving either *i*) the overall WVA process, or *ii*) the differences in steady state water retention between MDQ and LH. The difference in steady state water retention could also be due to the significant differences in mineralogy for the two sites. (Figure A.8). For example, the high evaporite content at MDQ could enhance WVA (or perhaps deliquescence); alternatively, the high

feldspar content at LH could contribute to reduced WVA. We know of no published work that specifically explores the role of mineralogy in WVA.

2.5.3.2. Changes in Soil Water Content

The results of the laboratory simulation show a reasonably regular oscillation in mass after an initial equilibration time (~24 hr) for both MDQ and LH soils (see Figure A.11). We interpret this as evidence that the experiment reached a state where the increases and decreases in mass were roughly the same for cold and hot periods, respectively. In other words, water vapor adsorption/desorption adds and removes roughly equal amounts of water into and out of the soil in our experiment (Table 2.2). The increase in mass is most parsimoniously interpreted as adsorption of water to the soil grains when T is low. Similarly, mass decreases when T is increased and water is desorbed into the vapor phase. Our experiments generated an average increase (trough-to-peak) in SWC of 0.25 ± 0.06 mg g^{-1} for MDQ and 0.34 ± 0.16 mg g^{-1} for LH (Table 2.2). All SWC increases for both samples are significantly different from zero. These results are in quite reasonable agreement with our WVA model-derived estimates of SWC increase of 0.19 and 0.20 mg g^{-1} for MDQ and LH, respectively (Table 2.2). The excellent agreement in SWC between the field and lab results suggests our field observations are evidence for measurable WVA.

2.5.4. Evidence for Water Vapor Adsorption in Hyperarid Soils

We have provided several lines of *in situ* and laboratory evidence to support a daily WVA and desorption cycle in the soils of one of Earth's driest environments, the Atacama Desert.

2.5.4.1. WVA Modeling

The output of the WVA model (Figure 2.8) shows periods of positive WVA rate (i.e., between ~17:00 and ~9:00) at both field sites. In addition, our WVA model shows periods of negative WVA between ~9:00 and ~17:00 at both sites. We assert that a positive WVA rate is a measure of water vapor moving from the pore space and adsorbing to soil particles, thus increasing SWC (Figure 2.1). Conversely, a negative WVA rate corresponds to water desorbing from soil particles and moving into the pore space, thus decreasing SWC (Figure 2.1). Figure A.12A shows a [$H_2O_{(g)}$] minimum-type profile with the directionality of diffusive water vapor transport indicated. At 5 cm depth, [$H_2O_{(g)}$] should increase over time, as water vapor is supplied from the top and bottom. This would result in a relatively straight [$H_2O_{(g)}$] profile if diffusion were the only process acting in these soils. However, this is not what we observe; the [$H_2O_{(g)}$] minimum-type profile is stable over 12 - 16 hours. This indicates a reaction, or some other physical process is removing water vapor from the pore space to maintain the [$H_2O_{(g)}$] minimum in the profile. Figure A.12B shows a [$H_2O_{(g)}$] maximum-type profile with the direction of diffusive water vapor transport shown. Like the [$H_2O_{(g)}$] minimum-type profiles, the [$H_2O_{(g)}$] should change over time if diffusion were the only process acting on pore space water vapor. We observe [$H_2O_{(g)}$] maximum-type profiles that are stable for 4 – 5 hours, indicating a reaction process that is adding water vapor to the pore space during this time.

2.5.4.2. Laboratory Experiments

The results of an 80-hour simulation experiment show both increases and decreases in SWC inversely related to increases and decreases in T (Figure 2.5). These results are consistent in directionality and magnitude with the modeled field results. In both cases we

observe increased SWC during nighttime (12ºC) conditions and decreased SWC during daytime (35ºC) conditions. Cryogenic extraction of a liquid with FTIR characteristics similar to those of water from the simulation soils provides strong evidence that the cause of increased mass during the nighttime conditions is water (Figure A.9).

2.5.4.3. Differences Between Surface and Subsurface Relative Humidity

Agam & Berliner (2006) state that WVA occurs when surface RH is greater than soil pore RH. We observe daily periods of several hours in duration (at both sites) where RH at the surface is greater than RH at 2.5 cm depth (Figure A.13). These periods occur for roughly 16 hours a day, between ~17:00 and ~9:00. Similarly, Kaseke et al. (2012a) state that WVA occurs due to a gradient of $[H_2O_{(g)}]$ where the surface concentration is greater than the soil pore concentration. We observed these types of $[H_2O_{(g)}]$ gradients from ~17:00 to ~9:00 (see Section 2.5.5.2 and Figure 2.10). Both observations agree and suggest long periods during the night when conditions are favorable for WVA.

2.5.4.4. Other Water Inputs

Water vapor adsorption is not the only water input into these soils. Excluding rain; fog, dew, and deliquescence are all potential sources of water in the Atacama. However, several lines of evidence preclude these water inputs at the time of our field measurements, leaving us to conclude that WVA may be the primary water source (excluding rain) to these soils during our observations.

2.5.4.4.a. Fog

Fog deposition occurs when the atmospheric water content is at saturation (~100%RH) and water droplets condense onto suspended solid particles that then settle out of the

atmosphere to be deposited onto the soils (Agam and Berliner, 2006; Jacobs et al., 2002). Fog was observed during our campaign, but prior to measurements. During the duration of study at both sites, no fog was observed and the highest observed RH at the surface was 81 and 74%RH at MDQ and LH, respectively. This supports the claim that there were no fog events during the study at either site, indicating that fog is not necessary to support the WVA water cycle described here.

2.5.4.4.b. Dew

Dew deposition is a non-rainfall water input where water condenses directly onto the soil surface. Agam & Berliner (2006) describe the conditions for dew deposition as being when the soil surface T is at or below the dewpoint. Generally, dew is rare on soil or mineral surfaces in arid regions and requires a complex biological surface for formation and growth (Agam and Berliner, 2006; Tomaszkiewicz et al., 2015), so dew would not be expected, but we also can attempt to rule out dew formation using our data . Our study was not designed to measure surface T. However, using data from a Peruvian 10 m meteorological station located ~45 km away from the field sites (16.34ºS, 72.15ºW) in a similarly hyperarid region, we have determined that our surface sensor is well within the surface layer as opposed to the mixed layer. The surface layer is the air layer nearest the surface where air is highly influenced by the surface (e.g., frictional drag, heat conduction, and evaporation; Stull, 2015); we generally observe a significant difference between the 10 m meteorological air T and our measured surface air T (Figure A.14). During the day, the air is ≥10ºC cooler than the surface, indicating that our surface sensor may be a reasonable proxy for soil surface T due to radiative heating. In general, the dewpoint is much lower than the surface T, virtually precluding dew deposition. We compared our surface T values to the dewpoint T (section

A.3.) and demonstrate that the vast majority of the surface T measurements are much greater than the dewpoint (Figure A.15). There are, however, several brief periods of time at both sites where the surface air T cools to within 5ºC of the dewpoint. Thus, we cannot completely preclude the presence of dew deposition; however, if any dew deposition occurred at our sites, it is most likely only for a short duration between 7:00 and 8:00. There was no visible evidence of dew observed in the field.

2.5.4.4.c. Deliquescence

Deliquescence is the phenomenon whereby hygroscopic minerals absorb and condense water vapor out of the atmosphere and on to mineral surfaces, typically salts, creating a super saturated brine (Davila et al., 2008; Gough et al., 2016; Guo et al., 2019). Deliquescence is a function of *i)* mineral type, *ii)* T, and *iii)* RH. Each mineral absorbs water from the atmosphere at or above its unique DRH for a given T. Our analysis of the powder XRD spectra using MDI® Jade precludes the presence of typical, environmentally relevant deliquescent minerals, with DRH <75%, such as $CaCl_2$, KF, $MgCl_2$, $CaNO_3$, and $MgNO_3$ (Figure A.22). We cannot strictly conclude the absence of these minerals; only that if they are present, they must be considered trace mineral components.

Both MDQ and LH are rich in soluble salts as evidenced by soil conductivities of 3.03 and 6.29 mS cm^{-1}, respectively; however, the predominant ions are different for the two sites (Tables A.3 & A.4). The extractable ions are primarily Ca^{2+} and SO_4^{2-} at MDQ and Na^+ and Cl^- at LH (Tables A.3 & A.4). Powder XRD analysis identified anhydrite ($CaSO_4$) at both sites, but at higher abundance at MDQ (Figure A.8). Halite (NaCl) was not identified by powder XRD at either site, despite the high concentration of Na^+ and Cl^-, particularly at LH. It is possible halite (or the above-mentioned deliquescent minerals) was only present as thin

rinds; more investigation is needed on the salt environment and deliquescent capabilities of these soils. We note, our ion chromatography analysis did not detect perchlorate (ClO_4^-), which is a highly deliquescent ion.

The field results cannot completely preclude deliquescence; however, near the [$H_2O_{(g)}$] minimum/maximum depth (i.e., 3 – 5 cm) relative humidity is very stable. Increases in SWC due to deliquescence require changes in RH, because changes in RH are the only driver of deliquescence and its opposite process: efflorescence. It is possible that trace amounts of deliquescent salts could buffer the pore space RH; further research is needed to deconvolve WVA and deliquescence in these soils. There may be short periods where deliquescence can occur at the surface, i.e., when RH shifts from low to high. In contrast, the RH at depth is stable at ≤50%RH, ruling out deliquescence for most naturally occurring salts (e.g., NaCl and $NaNO_3$). Our laboratory simulation experiments show increases and decreases in SWC despite a constant, buffered RH (similar to field conditions). The observed increases and decreases in SWC in the laboratory simulation thus rule out deliquescence as a potential mechanism because the experimental RH was constant. Deliquescence could explain the initial increase in SWC in our experiments; however, since the RH remains constant, deliquescence cannot explain the subsequent decreases/increases in SWC.

2.5.5. Water Vapor Adsorption as a Water Input

2.5.5.1. Evidence for a Sustainable Diurnal Water Cycle

Over the course of our observations at MDQ (~10 days), we observed [$H_2O_{(g)}$] minimum-type profiles for 160 h of a total 238 h (67%; Figure 2.8A). At LH (~4 days), we observed [$H_2O_{(g)}$] minimum-type profiles for 67 h of a total 120 h (56%; Figure 2.8B). These

results indicate that the WVA cycle is sustainable through water vapor recharge over the duration of observation.

2.5.5.2. Observed Input of Water into Soils is from Atmospheric Water Vapor

The difference in [$H_2O_{(g)}$] between two layers of air determines the diffusive movement of water between the layers (i.e., 'Fickian' diffusion). Comparison of our T, RH, and [$H_2O_{(g)}$] data collected at depth to 10 m air data from a nearby meteorological station (Figure A.21) reveals differences in [$H_2O_{(g)}$] between our 2.5 cm measurement and the 10 m air measurements (Figure 2.10). Negative values indicate higher [$H_2O_{(g)}$] in the air, and a gradient favoring a downward movement of water. Over the course of our observations, we observe that the [$H_2O_{(g)}$] difference between the overlying air and 2.5 cm is negative for 158 h of the total 238 h (66%) at MDQ and 74 h of 120 h (62%) at LH, indicating water movement from the overlying air into the soil. When comparing [$H_2O_{(g)}$] difference and WVA rate, we show an interesting negative correlation (Figure 2.10). This provides further evidence that water vapor is moving from the overlying air into the soil and onto the soil surfaces between ~16:00 and ~8:00. The opposite process is occurring – water vapor moving from the soil surfaces and out of the soil – during midday.

We observe net movement of water into the soil from the air as well as upward movement of water from depth in the soil. This has two main implications. First that the soil is capable of absorbing water from the atmosphere. Second, that deeper subsurface water can move upward toward the soil surface and be influenced by the diurnal T cycle. The WVA cycle observed here may work to retain and recycle water in the top 10 – 20 cm of soil; it also may help to store water from the very infrequent rain and fog events in this region. This is an enticing thought in the search for the habitable hyperarid environments, as

an efficient water retention process could serve to sustain putative organisms for long periods of time between events of condensed water addition (e.g., rain or fog).

2.5.6. Relevance as a Martian Analog

It is intriguing that many of the behaviors of water vapor observed in the Atacama are seen on present-day Mars. Fischer et al. (2019) reported that water vapor underwent regular diurnal cycles at the *Phoenix* and *Mars Science Laboratory/Curiosity Rover* sites, with [$H_2O_{(g)}$] being 4 to 40 times higher during the day than at night. They argued these diurnal cycles were driven by interaction with the regolith, but ruled out frost deposition/sublimation, instead favoring adsorption or deliquescence (Fischer et al., 2019). At the *Phoenix* landing site, ephemeral liquid brines were observed (Rennó et al., 2009), and Fischer et al. (2019) suggested more favorable conditions for brine formation may exist in the subsurface, which is where we find WVA occurring in Atacama soils. Given that other environments can stimulate biological activity through WVA (McHugh et al., 2015), and the direct evidence for the presence of microbes in Atacama soils (Navarro-Gonzalez et al., 2003; Schulze-Makuch et al., 2018; Valdivia-Silva et al., 2011), it seems possible that WVA contributes at least partially to the habitability of Atacama soils. Taken together, it seems reasonable to conclude that future missions to Mars could fruitfully investigate the subsurface RH and water cycle.

2.6. Summary & Implications

2.6.1. Summary

We have provided evidence for an active WVA cycle in the hyperarid soils of the Atacama Desert. This WVA cycle has the capacity to measurably increase SWC during the night and early morning hours. In support of this interpretation, we provide five pieces of

evidence indicating a sustainable cyclic increase and decrease in SWC through WVA summarized in the following subsections.

2.6.1.1. Water Vapor Adsorption and Soil Water Content are Driven by Changes in the $[H_2O_{(g)}]$ of the Subsurface Pore Space

The day and night $[H_2O_{(g)}]$ profiles in figure 2.7 show $[H_2O_{(g)}]$ minimum and $[H_2O_{(g)}]$ maximum-type profiles that are stable for several hours. The $[H_2O_{(g)}]$ profiles require water vapor to be moved into or out of the soil pore space to maintain the observed profiles. We assert that WVA is the necessary reaction and the results of our WVA model are consistent with this interpretation.

2.6.1.2. Laboratory Simulations Support WVA Model Interpretations

We performed soil incubation experiments under simulated Atacama day/night conditions. These experiments show gravimetrically measurable changes in soil mass in response to changes in T at fixed RH, and that mass change is due to adsorbed water – as evidenced by FTIR spectroscopy. This demonstration of WVA provides robust evidence for changes in subsurface SWC in the field solely in response to changes in T.

2.6.1.3. Other Sources of Water Can Be Reasonably Ruled Out

Rain and fog in this environment are well established but rare events. We can also practically rule out the presence of other non-rainfall water inputs such as fog and dew at the time of our investigation. Surface T during the study never fell below the dewpoint, which is necessary for dew formation. We can confidently assert that any relevant minerals that deliquesce at RH <75% are a very minor constituent as the XRD spectra are not consistent with the presence of deliquescent minerals. Therefore, deliquescence is unlikely to

measurably affect bulk SWC especially at depth. The laboratory simulations show increases in SWC at low RH (12%RH), and no known naturally occurring minerals deliquesce at or below 12%RH. In addition, the laboratory simulations showed increases and decreases of water at stable RH. This is inconsistent with deliquescence as changes in RH are required for deliquescence or efflorescence.

2.6.1.4. Atmospheric Water Vapor is the Source of Adsorbed Water

The results of our WVA model and assessment of regional 10 m meteorological [$H_2O_{(g)}$] data indicate a net movement of water into the soils and onto soil surfaces from the overlying atmosphere during the night and early morning. This is limited to a brief observational window but indicates a mechanism for hyperarid soils to gain or retain water from the atmosphere.

2.6.2. Implications

The WVA process described here provides an additional mechanism for daily water input (albeit small) and retention in a hyperarid region of the Atacama Desert. Given that our profiles indicate that WVA occurs over the top 10 - 20 cm of the soil, our observed increases in SWC of 0.2 mg g^{-1} day^{-1} amount to 20 - 30 μm of rain equivalent. For context, similar measurements have been made in the Namib Desert that range from 200 - 8300 μm of rain equivalent per day (Kaseke et al., 2012b; Kool et al., 2021). If this process occurs at this magnitude every day (20 - 30 μm), it could account for a very significant amount of water – equivalent to or greater than the mean annual rainfall of 2 mm and, perhaps, as much as a factor of 5 more than rainfall. This suggests that WVA may be an important and underappreciated water input in the hyperarid regions of the Atacama.

Previously, rain and fog were thought to be the only relevant water inputs to this system. Water vapor adsorption has been shown to supply sufficient water to induce microbial activity in semiarid systems (McHugh et al., 2015); but, it remains to be determined if WVA can provide biologically-relevant amounts of water in this hyperarid region. If so, it would provide compelling evidence for the habitability of these soils between rain and fog events. The WVA described here is almost entirely driven by heating from the sun and small amounts of ambient atmospheric water vapor. This provides an interesting prospect for astrobiologists searching for microenvironments of habitability (i.e., refugia) on other past or present arid worlds.

Table 2.1: Soil texture and chemistry data for the Mar de Quartz and Los Halitos sites. Each value is the mean of measurements for two replicate samples with one standard deviation in parentheses.

Parameter	Mar de Quartz	Los Halitos
Sand (%)	79.5 (±0.3)	84 (±0.1)
Silt (%)	16.8 (±1.55)	11 (±0.1)
Clay (%)	3.8 (±1.25)	5 (±0.0)
pH	6.46 (±0.190)	6.54 (±0.115)
Conductivity (mS cm^{-1})	3.03 (±0.525)	6.29 (±0.220)
Total Carbon (mg g^{-1})	0.20 (±0.010)	0.16 (±0.025)
Inorganic Carbon (mg g^{-1})	0.04 (±0.005)	0.01 (±0.010)
Organic Carbon (mg g^{-1})	0.17 (±0.015)	0.15 (±0.010)
Total Nitrogen (mg g^{-1})	0.17 (±0.025)	0.34 (±0.000)
BET Surface Area (m^2 g^{-1})	1.06 (±0.055)	0.473 (±0.0210)
Density (g cm^{-3})	1.38 (±0.001)	0.97 (±0.001)
Porosity (mL mL^{-1})	0.516*	0.655*

*One measurement only

Table 2.2: Change in SWC at both sites based on field data and lab simulation results. Values are the mean of all observations ± 1 standard deviation.

		Change in Soil Water Content (mg g^{-1})			
Site	Observation	Adsorption		Desorption	
Mar de Quartz	Field[a]	0.19	(±0.02)	-0.17	(±0.03)
	Simulation[c]	0.25	(±0.08)	-0.15	(±0.05)
Los Halitos	Field[b]	0.20	(±0.07)	-0.22	(±0.03)
	Simulation[c]	0.34	(±0.07)	-0.28	(±0.03)

[a] n = 10; [b] n = 4; [c] n = 3

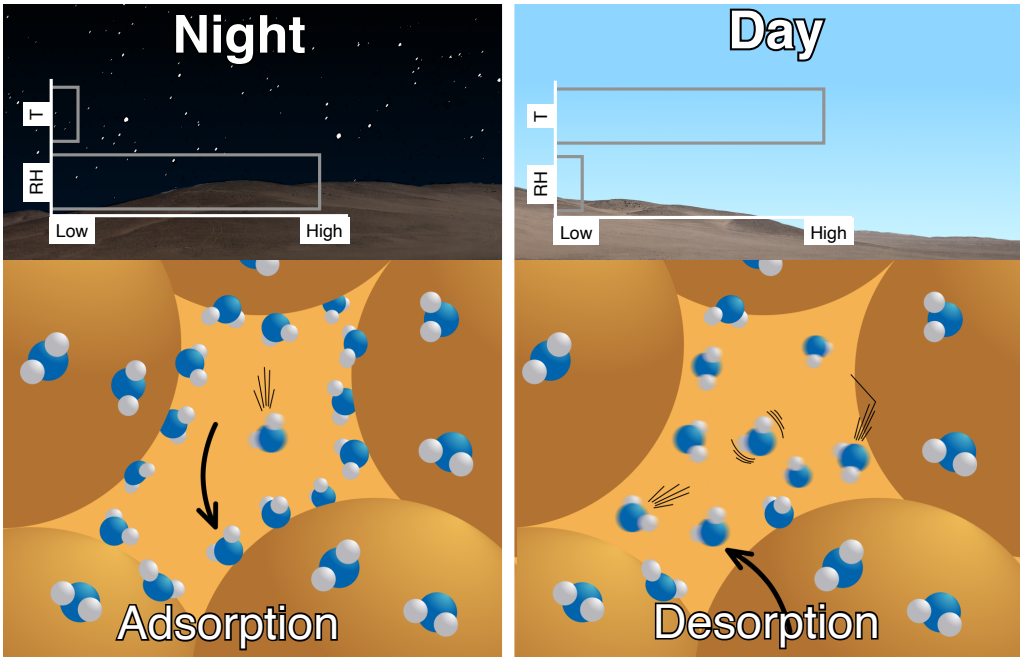

Figure 2.1: Conceptual diagram of water vapor adsorption and desorption in response to environmental conditions in the Atacama Desert. Upper panels show representative surface temperature (T) and relative humidity (RH) conditions during the night and day. Lower panels are a cartoon of water molecules (blue and white) in a soil matrix (dark tan spheres) with open pore space (light orange area in middle). Water molecules are either free in the pore space as [$H_2O_{(g)}$] (blurred) or adsorbed onto the soil surface (sharp). During the night (left panels), T is low, and most water molecules do not have enough energy to escape the surface adsorptive attraction (i.e., adsorbed water molecules). During the day (right panels), T is high, and most water molecules have sufficient energy to escape the surface attraction to enter the soil pore space (i.e., desorbed water molecules).

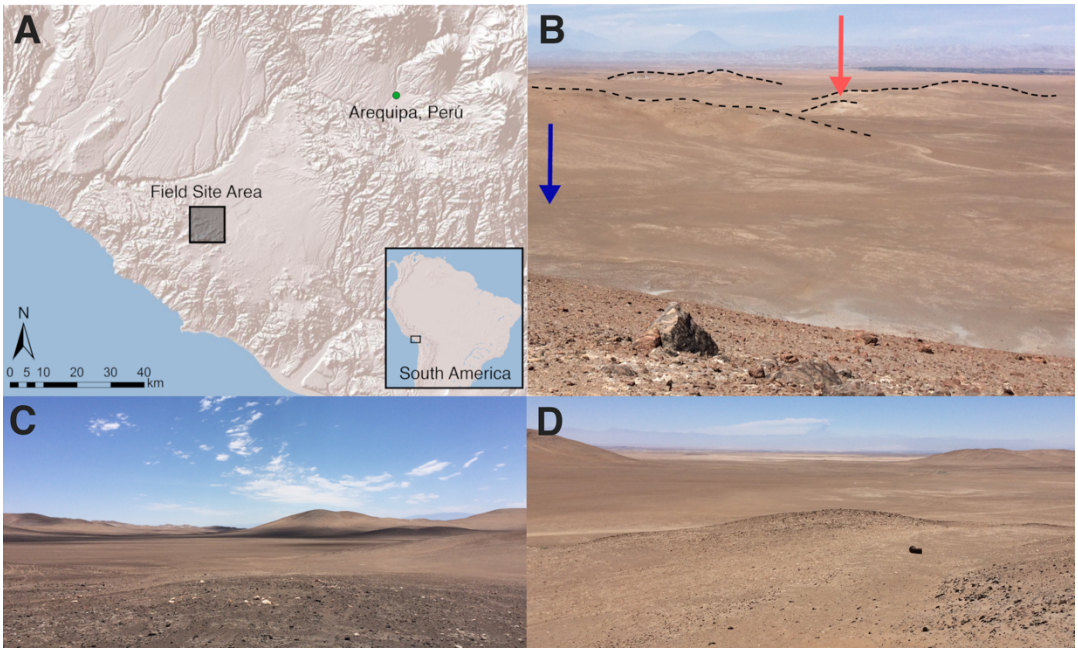

Figure 2.2: Map and photographs of the *Pampas de la Joya* field sites. **A)** Overview map of the field area in southern Perú with the city of Arequipa noted with a green dot for geographical context. **B)** Overview photo of the field site showing Mar de Quartz (playa site; blue arrow) and Los Halitos (hillside site; red arrow) from a nearby hill facing ENE; note Misti volcano at center-left of the horizon. Black dashed lines emphasize the relief (~10 m) in the landscape. **C)** Photograph of the Mar de Quartz site facing NW. **D)** Photograph of the Los Halitos site facing NNE. Photo credits: Donald M Glaser.

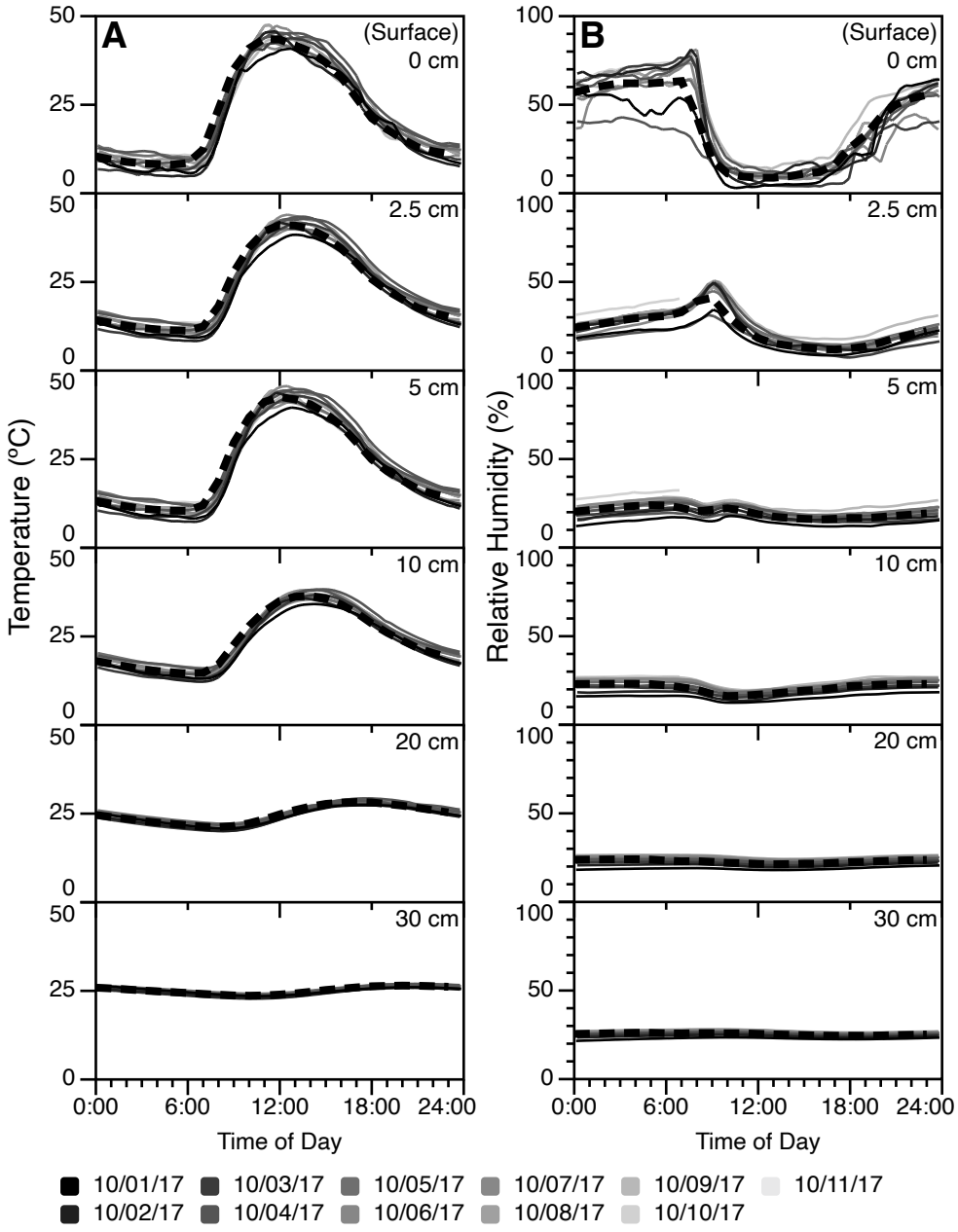

Figure 2.3: Soil **A)** temperature and **B)** relative humidity at the Mar de Quartz site as a function of time. Each panel shows multiple 24 hr time series (thin lines) from a single depth arranged from 0 cm (surface) in the top panel down to 30 cm in the bottom panel. Thick black dashed line is an hourly average of all days. Each panel within **A** and **B** have the same Y-axis scale for direct comparison between panels. The gray-scale gradient distinguishes different days from the earliest date (black line, Oct 1) to the latest date (lightest gray, Oct 11). Both T and RH are relatively constant day to day, with the most variation observed in the surface RH.

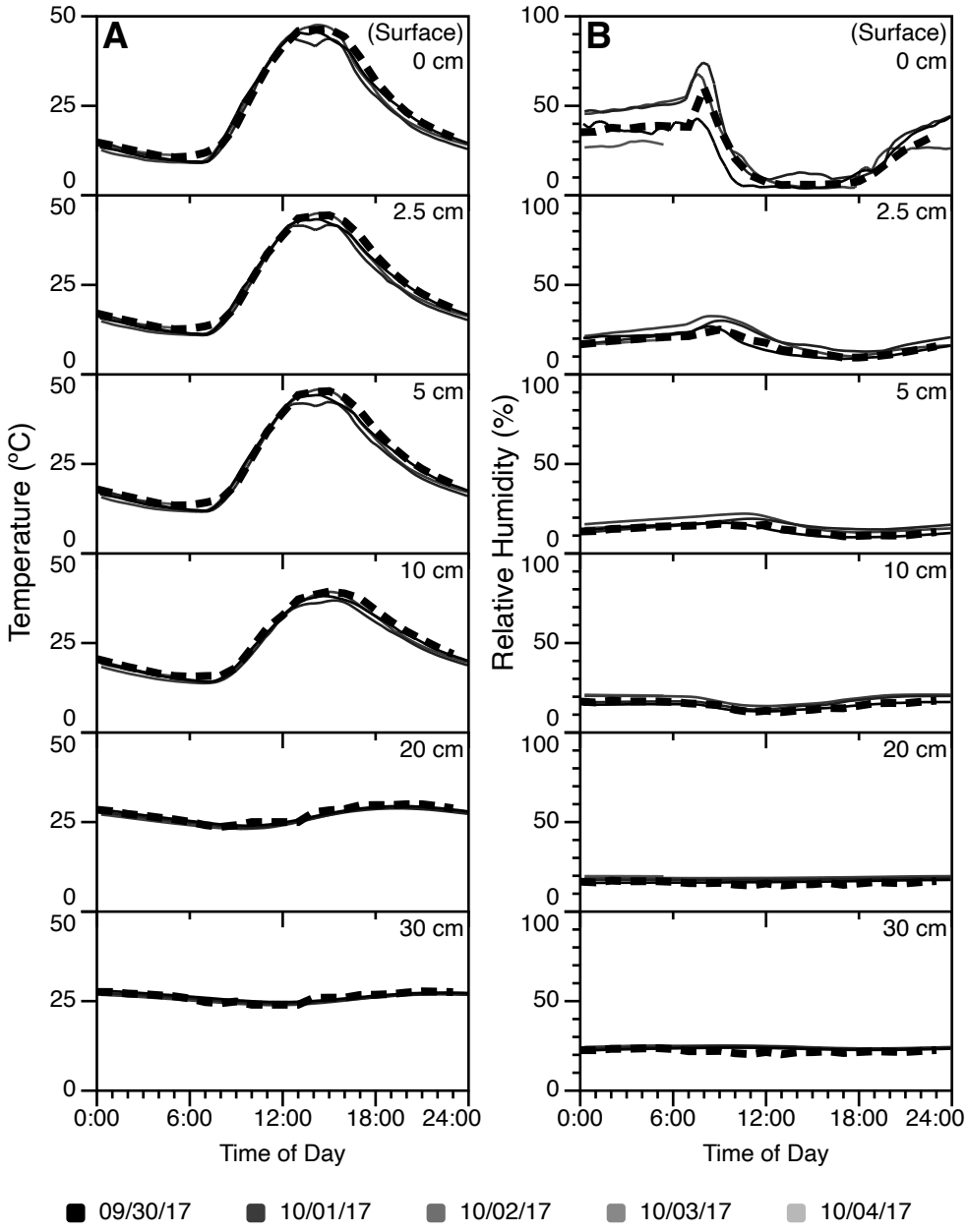

Figure 2.4: Soil **A)** temperature and **B)** relative humidity at the Los Halitos site as a function of time. Each panel shows multiple 24 hr time series (thin lines) from a single depth arranged from 0 cm (surface) in the top panel down to 30 cm in the bottom panel. Thick black dashed line is an hourly average of all days. Each panel within **A** and **B** have the same Y-axis scale for direct comparison between panels. The gray-scale gradient distinguishes different days from the earliest date (black line, Sep 30) to the latest date (lightest gray, Oct 4). Both T and RH are relatively constant day to day, with the most variation observed in the surface RH.

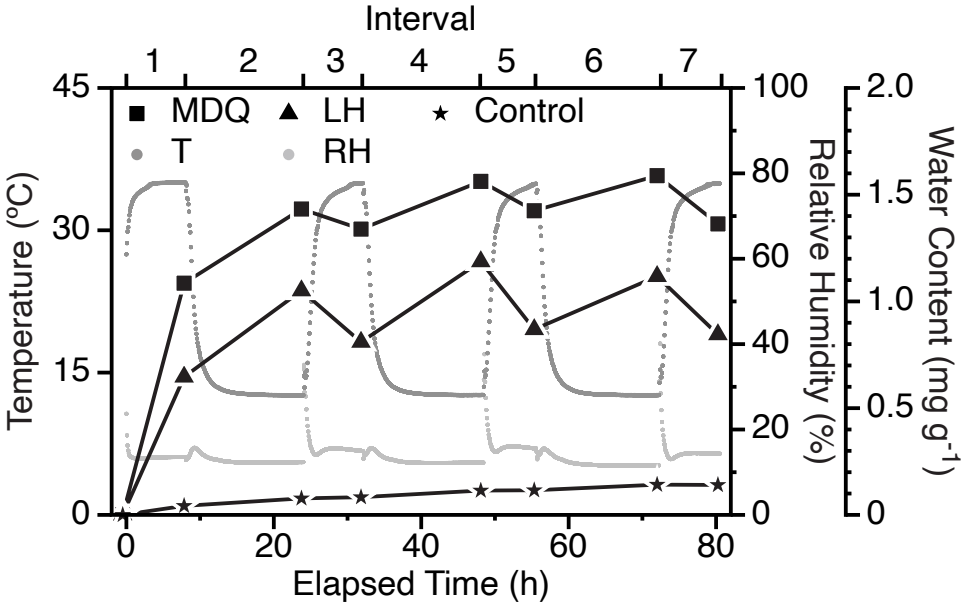

Figure 2.5: Change in mass during the simulation experiment as a function of time for soil samples from Mar de Quartz, Los Halitos, and a control. Left Y-axis (small, dark grey points) is enclosure temperature in ºC. First right Y-axis (small, light grey points) is enclosure relative humidity in %. Right most Y-axis is sample soil water content for Mar de Quartz (black squares), Los Halitos (black triangles), and control (black stars). Water content was calculated by comparing sample mass to dry mass. Samples were incubated for 82 hr and T changed from 12 to 35ºC on a 16:8 h cycle to simulate night/day conditions. Relative humidity was buffered at ~12%RH. Sharp deviations in RH at the beginning of each interval are due to opening of the enclosure to measure the samples. Upper X-axis ticks show points when the chamber temperature was changed to create the simulated night and day intervals. We observe increases in water content after intervals of cool conditions (12ºC; nighttime) and decreases in water content after intervals of hot conditions (35ºC; daytime). The control gains a small amount of water over the experiment, but at a much smaller magnitude compared to the soil samples; the control does not show decreases in water content during the hot intervals.

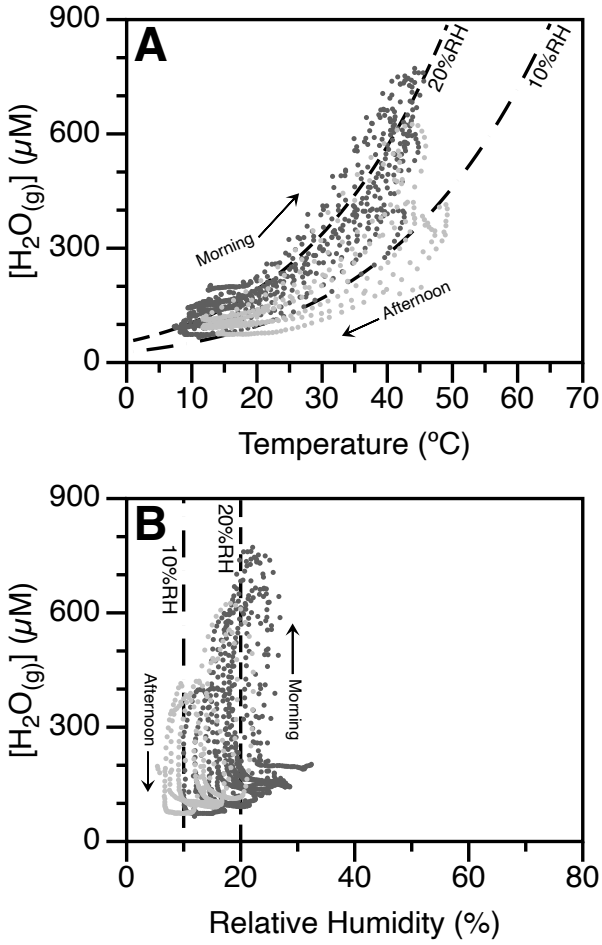

Figure 2.6: Absolute humidity ($[H_2O_{(g)}]$) for all days at 5 cm depth in the soil pore space as a function of **A)** temperature and **B)** relative humidity at Mar de Quartz (dark grey) and Los Halitos (light grey). Black dashed lines are contours of constant RH at 10% (long dash) and 20% (short dash). The RH contours in panel A are calculated using the entropy maximization framework described in section 4.1 (i.e., Koutsoyiannis, 2012). There is a moderately strong positive correlation between $[H_2O_{(g)}]$ and T that follows the RH contours (Panel A). Hysteresis in the curves is evident as a function of time such that $[H_2O_{(g)}]$ increases over the course of the mornings and decreases in the afternoons in a clockwise loop (noted by arrows). There is no relationship between $[H_2O_{(g)}]$ and RH as the data align almost vertically (Panel B); counterclockwise hysteresis over the day is noted. These data suggest that diurnal changes in the subsurface can be driven primarily by changes in temperature as heat is conducted through the soil column and RH is nearly constant.

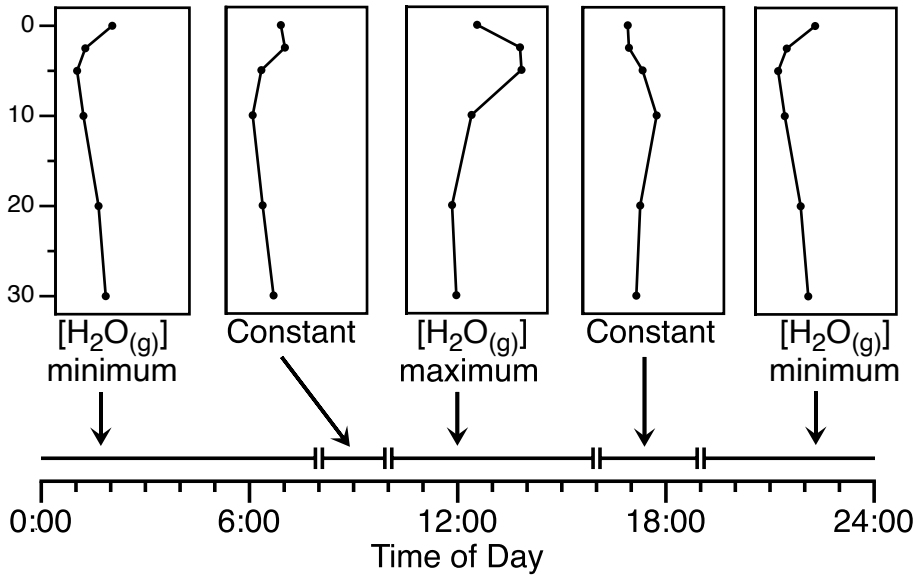

Figure 2.7: Representative $[H_2O_{(g)}]$ profiles and their approximate time periods over the course of a day. Vertical axis (in cm) and horizontal axis (in μM) are the same for all five panels.

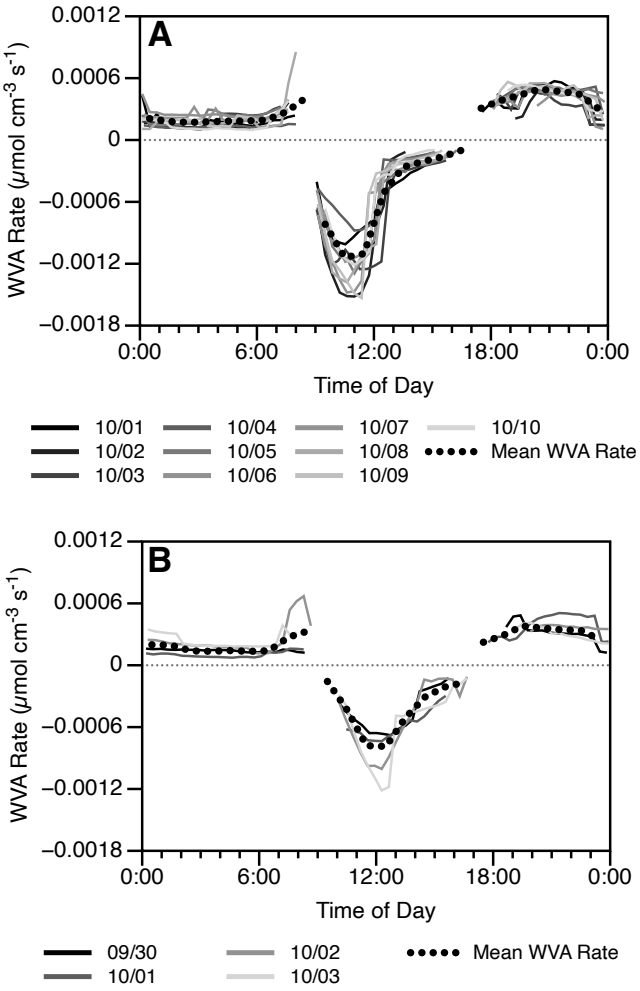

Figure 2.8: Results of WVA model showing WVA rate over time at **A)** Mar de Quartz from Oct. 1 (black) to Oct. 10 (light grey) and **B)** Los Halitos from Sep.30 (black) to Oct 3 (light grey). Thick black dotted line shows the hourly mean WVA rate for all days. Positive WVA rate indicates periods where water vapor is removed from the soil pore space (adsorption). Both sites show similar patterns of WVA rate with time. Panel **A** shows steady adsorption (~0.0002 μmol cm^{-3} s^{-1}) from midnight to 7:00, with a slight increase in adsorption (~0.0004 μmol cm^{-3} s^{-1}) at ~8:00. At ~9:00 WVA rate switches from positive to negative (desorption) and sharply decreases from ~-0.0008 to ~-0.0012 μmol cm^{-3} s^{-1} at ~11:00. WVA rate increases until ~17:00 when WVA rate switches from negative back to positive at ~0.0004 μmol cm^{-3} s^{-1} slowly decreasing to ~0.0002 μmol cm^{-3} s^{-1} at midnight. Panel **B** (Los Halitos) shows a similar pattern as **A** (Mar de Quartz), however, there are much less data from which to make definitive interpretations. This shows a daily cycle of water vapor adsorption and desorption.

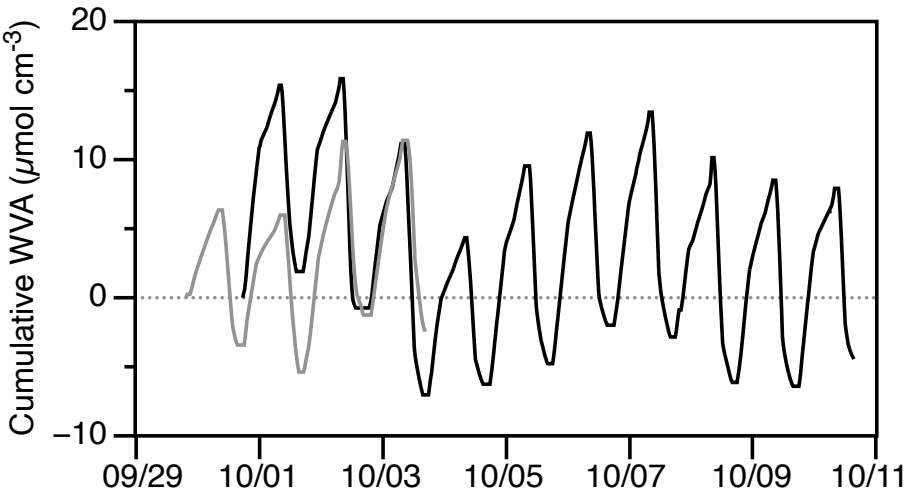

Figure 2.9: Cumulative WVA, i.e., total water added/removed from the soil column per unit area, at Mar de Quartz (black) and Los Halitos (grey). Positive cumulative WVA indicates net adsorption (increased soil water content), and negative cumulative WVA indicates net desorption (decreased soil water content). Cumulative WVA at MDQ and LH indicate minimal water loss (3.5 – 4.4 μmol cm^{-3}) over the study period.

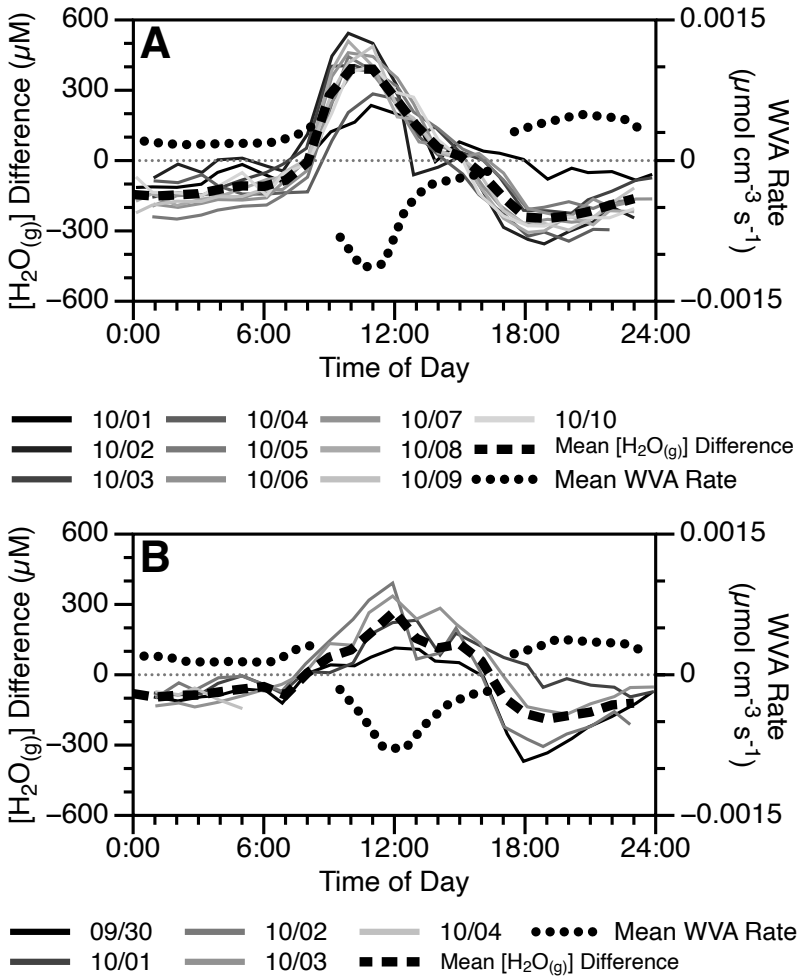

Figure 2.10: $[H_2O_{(g)}]$ difference calculated from a nearby 10 m meteorological station $[H_2O_{(g)}]$ data and our observed 2.5 cm $[H_2O_{(g)}]$ data at **A)** Mar de Quartz from Oct. 1 (thin black) to Oct. 11 (thin light grey) and **B)** Los Halitos from Sep.30 (thin black) to Oct 3 (thin light grey). Thick black dashed line shows the hourly mean $[H_2O_{(g)}]$ difference for all days. Positive $[H_2O_{(g)}]$ differences indicate lower $[H_2O_{(g)}]$ in the 10 m air compared to at 2.5 cm depth, suggesting water vapor movement out of the soil. Negative values suggest water vapor movement from the air into the soil. Thick black dotted line shows the mean WVA rate from Figure 8. In general, $[H_2O_{(g)}]$ differences are negative from ~16:00 to ~8:00 (16 h) and positive from ~8:00 to ~16:00 (8 h). Comparing $[H_2O_{(g)}]$ difference with WVA rate shows that when water is moving into soil (~16:00 to ~8:00) we observe a positive WVA rate indicating that water is being adsorbed to the soil. This implies atmospheric recharge of water vapor into the soil during the night, and a loss of water vapor from the soil to the atmosphere during the day.

CHAPTER 2 REFERENCES

Agam, N., and Berliner, P. R. (**2004**). Diurnal water content changes in the bare soil of a coastal desert. *Journal of Hydrometeorology*, *5*(5), 922–933. DOI: 10.1175/1525-7541(2004)005<0922:DWCCIT>2.0.CO;2

Agam, N., and Berliner, P. R. (**2006**). Dew formation and water vapor adsorption in semi-arid environments—A review. *Journal of Arid Environments*, *65*(4), 572–590. DOI: 10.1016/j.jaridenv.2005.09.004

Allan, M., Taylor, L. S., and Mauer, L. J. (**2016**). Common-ion effects on the deliquescence lowering of crystalline ingredient blends. *Food Chemistry*, *195*(15), 2–10. DOI: 10.1016/j.foodchem.2015.04.063

Allen, T. (**2013**). *Particle size measurement*. Springer.

Azua-Bustos, A., Fairén, A. G., González-Silva, C., Ascaso, C., Carrizo, D., Fernández-Martínez, M. Á., Fernández-Sampedro, M., García-Descalzo, L., García-Villadangos, M., Martin-Redondo, M. P., Sánchez-García, L., Wierzchos, J., and Parro, V. (**2018**). Unprecedented rains decimate surface microbial communities in the hyperarid core of the Atacama Desert. *Scientific Reports*, *8*(1). DOI: 10.1038/s41598-018-35051-w

Bastin, J.-F., Berrahmouni, N., Grainger, A., Maniatis, D., Mollicone, D., Moore, R., Patriarca, C., Picard, N., Sparrow, B., Abraham, E. M., Aloui, K., Atesoglu, A., Attore, F., Bassüllü, Ç., Bey, A., Garzuglia, M., García-Montero, L. G., Groot, N., Guerin, G., Laestadius, L., Lowe, A. J., Mamane, B., Marchi, G., Patterson, P., Rezende, M., Ricci, S., Salcedo, I., Diaz, A. S.-P., Stolle, F., Surappaeva, V., and Castro, R. (**2017**). The extent of forest in dryland biomes. *Science*, *356*(6338), 635–638. DOI: 10.1126/science.aam6527

Beck, P., Pommerol, A., Schmitt, B., and Brissaud, O. (**2010**). Kinetics of water adsorption on minerals and the breathing of the Martian regolith. *Journal of Geophysical Research*, *115*(E10), E10011. DOI: 10.1029/2009JE003539

Bhambhani, M. R., Cutting, P. A., Sing, K. S. W., and Turk, D. H. (**1972**). Analysis of nitrogen adsorption isotherms on porous and nonporous silicas by the BET and αs methods. *Journal of Colloid and Interface Science*, *38*(1), 109–117. DOI: 10.1016/0021-9797(72)90226-3

Butler, B. M., and Hillier, S. (**2021**). powdR: An R package for quantitative mineralogy using full pattern summation of X-ray powder diffraction data. *Computers & Geosciences*, *147*, 104662. DOI: 10.1016/j.cageo.2020.104662

Dashora, P., Gupta, G., and Dashora, J. (**2005**). Thermal conductivity, diffusivity and heat capacity of plasticized polyvinyl chloride. *Indian Journal of Pure and Applied Physics*, *43*(2), 132–136.

Davila, A. F., Gómez-Silva, B., de los Rios, A., Ascaso, C., Olivares, H., McKay, C. P., and Wierzchos, J. (**2008**). Facilitation of endolithic microbial survival in the hyperarid core of the Atacama Desert by mineral deliquescence: Deliquescence and microbial survival. *Journal of Geophysical Research: Biogeosciences*, *113*(G1). DOI: 10.1029/2007JG000561

Day, P. R. (**1965**). Hydrometer method of particle size analysis. *Methods of Soil Analysis. Agronomy*, *9*, 562–566.

Dupas-Langlet, M., Benali, M., Pezron, I., Saleh, K., and Metlas-Komunjer, L. (**2013**). Deliquescence lowering in mixtures of NaCl and sucrose powders elucidated by modeling the water activity of corresponding solutions. *Journal of Food Engineering*, *115*(3), 391–397. DOI: 10.1016/j.jfoodeng.2012.10.042

Eberl, D. (**2003**). *User guide to RockJock-A program for determining quantitative mineralogy from X-ray diffraction data* (No. 2331–1258). US Geological Survey.

Fedorova, A., Montmessin, F., Korablev, O., Lefèvre, F., Trokhimovskiy, A., and Bertaux, J. (**2021**). Multi-annual monitoring of the water vapor vertical distribution on Mars by SPICAM on Mars express. *Journal of Geophysical Research: Planets*, *126*(1). DOI: 10.1029/2020JE006616

Fischer, E., Martínez, G. M., Rennó, N. O., Tamppari, L. K., and Zent, A. P. (**2019**). Relative humidity on Mars: New results from the Phoenix TECP sensor. *Journal of Geophysical Research: Planets*, 2019JE006080. DOI: 10.1029/2019JE006080

Gao, Z., Horton, R., and Liu, H. P. (**2010**). Impact of wave phase difference between soil surface heat flux and soil surface temperature on soil surface energy balance closure. *Journal of Geophysical Research*, *115*(D16), D16112. DOI: 10.1029/2009JD013278

Gough, R. V., Chevrier, V. F., and Tolbert, M. A. (**2014**). Formation of aqueous solutions on Mars via deliquescence of chloride–perchlorate binary mixtures. *Earth and Planetary Science Letters*, *393*, 73–82. DOI: 10.1016/j.epsl.2014.02.002

Gough, R. V., Chevrier, V. F., and Tolbert, M. A. (**2016**). Formation of liquid water at low temperatures via the deliquescence of calcium chloride: Implications for Antarctica and Mars. *Planetary and Space Science*, *131*, 79–87. DOI: 10.1016/j.pss.2016.07.006

Graber, A., Santi, P., and Meza Arestegui, P. (**2021**). Constraining the critical groundwater conditions for initiation of large, irrigation-induced landslides, Siguas River Valley, Peru. *Landslides*, *18*(12), 3753–3767. DOI: 10.1007/s10346-021-01767-6

Guo, L., Gu, W., Peng, C., Wang, W., Li, Y. J., Zong, T., Tang, Y., Wu, Z., Lin, Q., Ge, M., Zhang, G., Hu, M., Bi, X., Wang, X., and Tang, M. (**2019**). A comprehensive study of hygroscopic properties of calcium- and magnesium-containing salts: Implication for hygroscopicity of mineral dust and sea salt aerosols. *Atmospheric Chemistry and Physics*, *19*(4), 2115–2133. DOI: 10.5194/acp-19-2115-2019

Hedges, J. I., and Stern, J. H. (**1984**). Carbon and nitrogen determinations of carbonate-containing solids. *Limnology and Oceanography*, *29*(3), 657–663. DOI: 10.4319/lo.1984.29.3.0657

Houston, J., and Hartley, A. J. (**2003**). The central Andean west-slope rainshadow and its potential contribution to the origin of hyper-aridity in the Atacama Desert. *International Journal of Climatology*, *23*(12), 1453–1464. DOI: 10.1002/joc.938

Jabro, J. D. (**2009**). Water vapor diffusion through soil as affected by temperature and aggregate size. *Transport in Porous Media*, *77*(3), 417–428. DOI: 10.1007/s11242-008-9267-z

Jacobs, A. F. G., Heusinkveld, B. G., and Berkowicz, S. M. (**2002**). A simple model for potential dewfall in an arid region. *Atmospheric Research*, *64*(1–4), 285–295. DOI: 10.1016/S0169-8095(02)00099-6

Kaiser, K., and Guggenberger, G. (**2003**). Mineral surfaces and soil organic matter. *European Journal of Soil Science*, *54*(2), 219–236. DOI: 10.1046/j.1365-2389.2003.00544.x

Kaseke, K. F., Mills, A. J., Brown, R., Esler, K. J., Henschel, J. R., and Seely, M. K. (**2012**a). A method for direct assessment of the "non rainfall" atmospheric water cycle: Input and evaporation from the soil. *Pure and Applied Geophysics*, *169*(5–6), 847–857. DOI: 10.1007/s00024-011-0328-9

Kaseke, K. F., Mills, A. J., Esler, K., Henschel, J., Seely, M. K., and Brown, R. (**2012**b). Spatial variation of "non-rainfall" water input and the effect of mechanical soil crusts on input and evaporation. *Pure and Applied Geophysics*, *169*(12), 2217–2229. DOI: 10.1007/s00024-012-0469-5

Kite, E. S. (**2019**). Geologic Constraints on Early Mars Climate. *Space Science Reviews*, *215*(1), 10. DOI: 10.1007/s11214-018-0575-5

Koeniger, P., Marshall, J. D., Link, T., and Mulch, A. (**2011**). An inexpensive, fast, and reliable method for vacuum extraction of soil and plant water for stable isotope analyses by mass spectrometry: Vacuum extraction of soil and plant water for stable isotope analyses. *Rapid Communications in Mass Spectrometry*, *25*(20), 3041–3048. DOI: 10.1002/rcm.5198

Kool, D., Agra, E., Drabkin, A., Duncan, A., Fendinat, P. P., Leduc, S., Lupovitch, G., Nambwandja, A. N., Ndilenga, N. S., Nguyễn Thị, T., Poodiack, B., Sagi, L., Shmuel, Y., Maggs-Kölling, G., Marais, E., Pinshow, B., Turner, J. S., and Agam, N. (**2021**). The overlooked non-rainfall water input sibling of fog and dew: Daily water vapor adsorption on a !Nara hummock in the Namib Sand Sea. *Journal of Hydrology*, *598*, 126420. DOI: 10.1016/j.jhydrol.2021.126420

Kosmas, C., Danalatos, N. G., Poesen, J., and van Wesemael, B. (**1998**). The effect of water vapour adsorption on soil moisture content under Mediterranean climatic conditions. *Agricultural Water Management*, *36*(2), 157–168. DOI: 10.1016/S0378-3774(97)00050-4

Kosmas, C., Marathianou, M., Gerontidis, S., Detsis, V., Tsara, M., and Poesen, J. (**2001**). Parameters affecting water vapor adsorption by the soil under semi-arid climatic conditions. *Agricultural Water Management*, *48*(1), 61–78. DOI: 10.1016/S0378-3774(00)00113-X

Koutsoyiannis, D. (**2012**). Clausius–Clapeyron equation and saturation vapour pressure: Simple theory reconciled with practice. *European Journal of Physics*, *33*(2), 295–305. DOI: 10.1088/0143-0807/33/2/295

Lauro, S. E., Pettinelli, E., Caprarelli, G., Guallini, L., Rossi, A. P., Mattei, E., Cosciotti, B., Cicchetti, A., Soldovieri, F., Cartacci, M., Di Paolo, F., Noschese, R., and Orosei, R. (**2021**). Multiple subglacial water bodies below the south pole of Mars unveiled by new MARSIS data. *Nature Astronomy*, *5*(1), 63–70. DOI: 10.1038/s41550-020-1200-6

Leão, T. P., and Tuller, M. (**2014**). Relating soil specific surface area, water film thickness, and water vapor adsorption. *Water Resources Research*, *50*(10), 7873–7885. DOI: 10.1002/2013WR014941

Liu, L., Tan, S. (Johnathan), Horikawa, T., Do, D. D., Nicholson, D., and Liu, J. (**2017**). Water adsorption on carbon—A review. *Advances in Colloid and Interface Science*, *250*, 64–78. DOI: 10.1016/j.cis.2017.10.002

McHugh, T. A., Morrissey, E. M., Reed, S. C., Hungate, B. A., and Schwartz, E. (**2015**). Water from air: An overlooked source of moisture in arid and semiarid regions. *Scientific Reports*, *5*(1). DOI: 10.1038/srep13767

McKay, C. P., Friedmann, E. I., Gómez-Silva, B., Cáceres-Villanueva, L., Andersen, D. T., and Landheim, R. (**2003**). Temperature and moisture conditions for life in the extreme arid region of the Atacama Desert: Four years of observations including the El Niño of 1997–1998. *Astrobiology*, *3*(2), 393–406. DOI: 10.1089/153110703769016460

Narvaez-Montoya, C., Torres-Martínez, J. A., Pino-Vargas, E., Cabrera-Olivera, F., Loge, F. J., and Mahlknecht, J. (**2022**). Predicting adverse scenarios for a transboundary coastal aquifer system in the Atacama Desert (Peru/Chile). *Science of The Total Environment*, *806*, 150386. DOI: 10.1016/j.scitotenv.2021.150386

Navarro-Gonzalez, R., Rainey, F., Molina, P., Bagaley, D., Hollen, B., de la Rosa, J., Small, A., Quinn, R., Grunthaner, F., Caceres, L., Gomez-Silva, B., and McKay, C. (**2003**). Mars-like soils in the Atacama Desert, Chile, and the dry limit of microbial life. *Science*, *302*(5647), 1018–1021. DOI: 10.1126/science.1089143

Piqueux, S., Buz, J., Edwards, C. S., Bandfield, J. L., Kleinböhl, A., Kass, D. M., Hayne, P. O., The MCS, and THEMIS Teams. (**2019**). Widespread shallow water ice on Mars at high latitudes and midlatitudes. *Geophysical Research Letters*, *46*(24), 14290–14298. DOI: 10.1029/2019GL083947

Rennó, N. O., Bos, B. J., Catling, D., Clark, B. C., Drube, L., Fisher, D., Goetz, W., Hviid, S. F., Keller, H. U., Kok, J. F., Kounaves, S. P., Leer, K., Lemmon, M., Madsen, M. B., Markiewicz, W. J., Marshall, J., McKay, C., Mehta, M., Smith, M., Zorzano, M. P., Smith, P. H., Stoker, C., and Young, S. M. M. (**2009**). Possible physical and thermodynamical evidence for liquid water at the Phoenix landing site. *Journal of Geophysical Research*, *114*. DOI: 10.1029/2009JE003362

Robertson, E. C. (**1988**). Thermal properties of rocks. *USGS Open-File Report 88-441*, 106. DOI: 10.3133/ofr88441

Rockland, L. B. (**1960**). Saturated salt solutions for static control of relative humidity between 5° and 40°C. *Analytical Chemistry*, *32*(10), 1375–1376. DOI: 10.1021/ac60166a055

Savijärvi, H. I., Harri, A.-M., and Kemppinen, O. (**2015**). Mars science laboratory diurnal moisture observations and column simulations: MSL diurnal moisture. *Journal of Geophysical Research: Planets*, *120*(5), 1011–1021. DOI: 10.1002/2014JE004732

Schulze-Makuch, D., Wagner, D., Kounaves, S. P., Mangelsdorf, K., Devine, K. G., de Vera, J.-P., Schmitt-Kopplin, P., Grossart, H.-P., Parro, V., Kaupenjohann, M., Galy, A.,

Schneider, B., Airo, A., Frösler, J., Davila, A. F., Arens, F. L., Cáceres, L., Cornejo, F. S., Carrizo, D., Dartnell, L., DiRuggiero, J., Flury, M., Ganzert, L., Gessner, M. O., Grathwohl, P., Guan, L., Heinz, J., Hess, M., Keppler, F., Maus, D., McKay, C. P., Meckenstock, R. U., Montgomery, W., Oberlin, E. A., Probst, A. J., Sáenz, J. S., Sattler, T., Schirmack, J., Sephton, M. A., Schloter, M., Uhl, J., Valenzuela, B., Vestergaard, G., Wörmer, L., and Zamorano, P. (**2018**). Transitory microbial habitat in the hyperarid Atacama Desert. *Proceedings of the National Academy of Sciences*, *115*(11), 2670–2675. DOI: 10.1073/pnas.1714341115

Shock, E. L., Holland, M., Meyer-Dombard, D., Amend, J. P., Osburn, G. R., and Fischer, T. P. (**2010**). Quantifying inorganic sources of geochemical energy in hydrothermal ecosystems, Yellowstone National Park, USA. *Geochimica et Cosmochimica Acta*, *74*(14), 4005–4043. DOI: 10.1016/j.gca.2009.08.036

Smith, I. B., Lalich, D. E., Rezza, C., Horgan, B. H. N., Whitten, J. L., Nerozzi, S., and Holt, J. W. (**2021**). A solid interpretation of bright radar reflectors under the Mars south polar ice. *Geophysical Research Letters*, *48*(15). DOI: 10.1029/2021GL093618

Soil Survey Staff. (**2014**). *Kellogg soil survey laboratory methods manual* (42 version 5). US Department of Agriculture, Natural Resources Conservation Service.

Srodoń, J., Drits, V. A., McCarty, D. K., Hsieh, J. C. C., and Eberl, D. D. (**2001**). Quantitative X-Ray diffraction analysis of clay-bearing rocks from random preparations. *Clays and Clay Minerals*, *49*(6), 514–528. DOI: 10.1346/CCMN.2001.0490604

Steele, L. J., Balme, M. R., and Lewis, S. R. (**2017**). Regolith-atmosphere exchange of water in Mars' recent past. *Icarus*, *284*, 233–248. DOI: 10.1016/j.icarus.2016.11.023

Strydom, C. A., Hudson-Lamb, D. L., Potgieter, J. H., and Dagg, E. (**1995**). The thermal dehydration of synthetic gypsum. *Thermochimica Acta*, *269–270*, 631–638. DOI: 10.1016/0040-6031(95)02521-9

Stull, R. (**2015**). *Practical Meteorology: An algebra-based survey of atmospheric science*. University of British Columbia. https://doi.library.ubc.ca/10.14288/1.0300441

Tamari, S. (**2004**). Optimum design of the constant-volume gas pycnometer for determining the volume of solid particles. *Measurement Science and Technology*, *15*(3), 549–558. DOI: 10.1088/0957-0233/15/3/007

Terada, N., Kulikov, Y. N., Lammer, H., Lichtenegger, H. I. M., Tanaka, T., Shinagawa, H., and Zhang, T. (**2009**). Atmosphere and water loss from early Mars under extreme solar wind and extreme ultraviolet conditions. *Astrobiology*, *9*(1), 55–70. DOI: 10.1089/ast.2008.0250

Tomaszkiewicz, M., Abou Najm, M., Beysens, D., Alameddine, I., and El-Fadel, M. (**2015**). Dew as a sustainable non-conventional water resource: A critical review. *Environmental Reviews*, *23*(4), 425–442. DOI: 10.1139/er-2015-0035

Toner, J. D., and Catling, D. C. (**2018**). Chlorate brines on Mars: Implications for the occurrence of liquid water and deliquescence. *Earth and Planetary Science Letters*, *497*, 161–168. DOI: 10.1016/j.epsl.2018.06.011

Troeh, F. R., Jabro, J. D., and Kirkham, D. (**1982**). Gaseous diffusion equations for porous materials. *Geoderma*, *27*(3), 239–253. DOI: 10.1016/0016-7061(82)90033-7

Tuller, M., and Or, D. (**2005**). Water films and scaling of soil characteristic curves at low water contents: Scaling of characteristic curves. *Water Resources Research*, *41*(9). DOI: 10.1029/2005WR004142

Valdivia-Silva, J. E., Navarro-González, R., Fletcher, L., Pérez-Montaño, S., Condori-Apaza, R., Ortega-Gutiérrez, F., and McKay, C. (**2012**). Climatological characteristics in the extreme hyper-arid region of Pampas de La Joya, Peru. Astrobiological approach in four years of observation: 2004–2008. *International Journal of Astrobiology*, *11*(01), 25–35. DOI: 10.1017/S1473550411000292

Valdivia-Silva, J. E., Navarro-González, R., Ortega-Gutierrez, F., Fletcher, L. E., Perez-Montaño, S., Condori-Apaza, R., and McKay, C. P. (**2011**). Multidisciplinary approach of the hyperarid desert of Pampas de La Joya in southern Peru as a new Mars-like soil analog. *Geochimica et Cosmochimica Acta*, *75*(7), 1975–1991. DOI: 10.1016/j.gca.2011.01.017

Vera, A., Pino-Vargas, E., Verma, M. P., Chucuya, S., Chávarri, E., Canales, M., Torres-Martínez, J. A., Mora, A., and Mahlknecht, J. (**2021**). Hydrodynamics, hydrochemistry, and stable isotope geochemistry to assess temporal behavior of seawater intrusion in the La Yarada aquifer in the vicinity of Atacama Desert, Tacna, Peru. *Water*, *13*(22), 3161. DOI: 10.3390/w13223161

Verhoef, A., Diaz-Espejo, A., Knight, J. R., Villagarcía, L., and Fernández, J. E. (**2006**). Adsorption of water vapor by bare soil in an olive grove in southern Spain. *Journal of Hydrometeorology*, *7*(5), 1011–1027. DOI: 10.1175/JHM556.1

Zomer, R. J., Trabucco, A., Bossio, D. A., and Verchot, L. V. (**2008**). Climate change mitigation: A spatial analysis of global land suitability for clean development mechanism afforestation and reforestation. *Agriculture, Ecosystems & Environment*, *126*(1–2), 67–80. DOI: 10.1016/j.agee.2008.01.014

Chapter 3

MINERAL COMPOSITION AFFECTS WATER VAPOR ADSORPTION IN UNSATURATED SOILS

3.1. Introduction

Water vapor adsorption (WVA) is a process that occurs in unsaturated soils in all types of environments on Earth. However, WVA is particularly important in arid environments because adsorbed water may be the only measurable type of water available for many months of the year due to the scarcity of rain, fog, and dew (Agam and Berliner, 2006; Amer, 2019; Kosmas et al., 2001). Water vapor adsorption is a physico-chemical process whereby gas-phase water molecules adhere to the surface of a solid by van der Waals-type forces in soils (Agam and Berliner, 2006). This adsorption of water molecules to the surfaces of the soil grains has the effect of increasing soil water content; the magnitude of which can be quite significant, on the order of 100 mg of water per gram soil, or more (Verhoef et al., 2006).

Traditionally, in the soil science literature, WVA is considered to be independent of the chemical makeup of the surface substrate and almost completely driven by surface area, along with temperature (T) and relative humidity (Leão and Tuller, 2014). Organic carbon and clays are generally thought to represent the vast majority of surface area in soils and thus have been the primary targets of studies quantifying WVA because WVA is a surface area-driven process (Allen, 2013; Arthur et al., 2015; Liu et al., 2017). The chemical engineering

literature, in contrast, suggests that WVA may not be solely driven by surface area, but can also be affected by the surface chemistry of the adsorbant; these are typically an engineered substrate such as carbon nanotubes or metal-organic frameworks where surface functional groups play a role in adsorption (AbdulHalim et al., 2017; Fletcher et al., 2007).

The planetary science literature on WVA is more limited, and yet, WVA is clearly of interest for this community. Water vapor adsorption has been invoked on Mars as a sink of atmospheric water to balance atmospheric water in climate models (Beck et al., 2010; Houben, 1999). Water vapor adsorption may also prove to be relevant to future NASA missions on Mars or Luna as a source of water for *in situ* resource utilization. For exoplanets and outer solar system bodies, WVA might be an important aspect of planetary habitability, particularly for dry planets. Recent work provides evidence for differences in WVA from two proximal hyperarid Mars-analog sites with different amounts of WVA that cannot be explained by differences in surface area or organic content (i.e., chapter 2; Glaser et al., 2022). The different magnitudes of WVA for these two sites introduces the possibility that the surface chemistry of the soils (i.e., mineral composition) may play an important role in WVA, consistent with observations from the chemical engineering literature.

Here I provide results from a comprehensive set of experiments providing first-of-their-kind data on steady-state water absorption onto pure minerals as a function of T, RH, and surface area. I use these results to inform an empirical, regression-based model that predicts WVA for a given soil as a function of its mineral composition. I selected minerals that are ubiquitous on Earth and across the solar system to demonstrate these differences in equilibrium water vapor adsorption. My results show that in addition to RH and T (environmental variables) it is necessary to consider both the surface area and mineral

composition (substrate variables) in assessing water vapor adsorption. This work provides an experimentally based method to predict WVA across many different soil types. These results are important to understand the total water budget of arid environments on Earth and, perhaps, on Mars, Luna, and other arid worlds.

3.2. Materials and Methods

3.2.1. Experimental Design

I measured equilibrium adsorbed water content (AWC) by incubating five representative minerals (olivine, anorthite, quartz, serpentine, and calcite), each at two grain sizes (nominally 180 - 2000 μm, and <180 μm), over a range of environmentally relevant temperatures (10 to 35ºC) and relative humidity (11 to 75%RH) until the samples reached a stable, constant mass.

3.2.1.1. Environmental Conditions

The incubations were performed in air-tight polymethymethacrylate enclosures (Mart® Microbiology B.V.; Lichenvoorde, NL) placed in a Lab-Line® model 850 environmental chamber (Thermo Fisher; Waltham, MA, USA) capable of maintaining T to within ± 0.3ºC. Relative humidity was maintained in each enclosure using a series of saturated salt solutions - (LiCl, KCH_3COO, $Mg(NO_3)_2$, and NaCl) to buffer RH nominally at 11, 24, 52, and 75%RH, respectively. The solutions were prepared with 18.2 MΩ·cm deionized water. Temperature and RH were measured using Honeywell® HIH7000 series capacitance sensors (Charlotte, NC, USA) and the data stored using an arduino® mega microprocessor with an adafruit™ microSD card breakout board. Measurements were collected every 5 min and are the mean of 20 readings measured 500 ms apart. Coding and wiring schematics for the sensors are

referenced in chapter 2. The reported nominal T and RH measurements for each incubation are the mean of the chamber conditions recorded 4 hr prior to mass measurements.

3.2.1.2. Mineral Mass Measurement

Sample masses were determined after ≥36 hr of incubation using a Mettler Toledo model XS204 analytical balance (Columbus, OH, USA). In brief, samples were removed from the incubation enclosure and placed, individually, into sealed dishes to reduce water equilibration with ambient laboratory RH prior to measurement. The sealed dishes were placed into an insulated container (i.e., a cooler; at the experimental T) to reduce thermal equilibration prior to measurement. Mineral samples were removed from the container and dish and quickly measured three times in a random order to prevent bias (within ~20 minutes, given the amount of time it took to make and record the measurements). Mineral samples were dried at 55ºC to constant mass (i.e., ± 1.0 mg) prior to the experiments; this relatively low drying T was used to ensure all calculated water is adsorbed rather than mineral bound (Strydom et al., 1995). I report water content values as AWC, the difference between the water content at the incubation condition and the initial 55ºC ambient RH "dry condition." A matrix of sixteen T (10, 18, 26, and 35ºC) and RH (11, 24, 52, and 75%RH) combinations were used to assess the equilibrium AWC over a broad range of environmentally relevant conditions. Incubations began with the lowest humidity condition and were performed from low to high RH. All four T conditions were evaluated (from high T to low T) prior to moving to the next RH condition. This ordering was designed so that, as much as possible, the amount of AWC increased across the incubation conditions.

3.2.2. Sample Preparation and Verification

Natural olivine, anorthite, quartz, and calcite mineral samples were acquired in bulk, as an assortment of sizes ranging from large pebbles to small cobbles (roughly 5 - 15 cm in diameter), from Ward's Scientific (Rochester, NY, USA). Similarly sized natural serpentine was acquired from a local mineral store (Everything Just Rocks; Tempe, AZ, USA). Minerals were prepared as two different grain size fractions by first crushing until the samples could pass through a 2 mm sieve using a series of rock crushers (jaw, cone, disk). The rock crushers were cleaned prior to use with compressed air and a brush to remove any previous rock fragments, within feasibility. A subsample of the <2 mm fraction was ground in a ball-mill for 5 minutes and then sieved to <180 μm. The sample fraction that passed through both sieves was collected as the small grain size fraction and the portion that was <2 mm and >180 μm was collected as the large grain size fraction. Each fraction was split (using the quartering method; ~8 - 35 g; e.g., Schumacher et al., 1990) into 3 replicate samples and placed in a pre-weighed polyethylene petri dish prior to the experiment.

Prior to incubation, mineral composition was determined by powder x-ray diffraction (XRD) using a Bruker D8 diffractometer (run parameters: 5º to 65º 2θ, 0.02º steps, 2 s per step, Cu K-α radiation; Madison, WI, USA) on samples ground to <20 μm using a McCrohn mill according to methods similar to Srodoń et al. (2001). Sample XRD spectra were compared manually to library spectra of pure minerals for verification of mineral identity. Specific surface area (SSA) for each mineral sample was determined using Brunauer-Emmett-Teller (BET) isotherm analysis using N_2 adsorption in a Micromeritics® Tristar II model 3020 according to standard methods (Bhambhani et al., 1972; Kaiser and

Guggenberger, 2003). Samples were dried at 90ºC under a gentle nitrogen stream for ≥12 hr prior to BET analysis to remove water because water is a contaminant in the BET method.

3.2.3. Benchmark Experiments to Determine Model Accuracy

Two different sample types were prepared to assess the validity of this approach and the accuracy of the mathematical models. The first type is a prepared mineral mixture made from the three of the five pure minerals (section 3.2.2) and the second type is a natural soil collected from the Atacama Desert in southern Perú.

3.2.3.1. Simple Mineral Mixture

A composite mineral mixture (essentially a soil-mimic) was prepared as a verification benchmark to ground-truth the adsorbed water vapor model. The mixture was composed of three minerals in roughly equal proportions: the large grain size serpentine (29 weight percent, wt%), small grain size olivine (38 wt%), and small grain size calcite (33 wt%). It was prepared by physically mixing the minerals until it appeared to be homogeneous. The mixture was split (by a modified quartering method) into three replicate samples (~20 g each) and placed in petri dishes for incubation. The replicate samples of the soil-composite were incubated at 52%RH and 25ºC for ≥48 hr. The water content results from this composite sample were compared to model predictions of AWC for a mixture of this composition.

3.2.3.2. Complex Natural Soil

Natural soil samples were collected from two sites, Mar de Quartz (MDQ) and Los Halitos (LH), within the hyperarid core of the Atacama Desert in *Pampas de la Joya*. Soils from these sites were previously described by Glaser et al. (2022). Powder XRD was

performed on the bulk samples as described in section 3.2.2 and mineral composition was determined using the "powdR" R library described in section 2.3.2.1. In brief, these samples were prepared for incubation by removing particles ≥2 mm using a sieve in the field. The <2 mm fraction (≥100 g sample) was incubated under three different water availability conditions: high (50 - 60%RH, 25ºC), medium (12%RH, 13ºC), and low (16%RH, 34ºC) and mass was determined after ≥48 hr of incubation. Notably, these soils are low in organic carbon content (~0.01 wt%) as shown in table 2.1 and Glaser et al. (2022); and as such are good representative soils for other arid regions and environments of astrobiological interest.

I hypothesize that higher resolution data, compared to bulk analysis, will yield AWC estimates that are significantly more accurate. To test this hypothesis I prepared soil separate samples. Soils were split into two size fractions (large and small grain size) using a 180 μm sieve, similar to the preparation of the mineral samples described in section 3.2.2. Mineral composition and surface area were measured on each of the soil size fractions using XRD and BET analyses, respectively.

3.3. Results

3.3.1. Chamber Conditions

Chamber T and RH conditions were measured every 5 minutes throughout the duration of incubations. The mean of 4 hr of RH and T data preceding each mass measurement are reported as the nominal RH and T for that condition. A summary of the measured experimental chamber T conditions is shown in figure 3.1 organized by each RH buffer. In general, the mean chamber T has higher variation at lower T; however, all mean chamber Ts are ± 1ºC from the set point (with a range of ± 2ºC). A summary of the measured experimental chamber RH conditions is shown in figure 3.2 organized by T set point. Most

mean chamber RHs are ± 3%RH from the nominal buffered value (with a range of ± 6%RH). The exception is experiment 9, where I observe a mean RH within 3%RH of the buffered value, but with a relatively high range (± 20%RH). In summary, the mean measured chamber conditions reasonably matched the target conditions.

3.3.2. Mineral Composition and Surface Area

Mineralogy of the natural samples was verified using XRD which shows reasonable agreement between the expected and measured mineral composition (Figure 3.3). For anorthite, quartz, and calcite; pure mineral spectra were available for comparison (Graf, 1961; Levien et al., 1980; Wenk et al., 1980). In the case of olivine and serpentine, which are mineral groups and not specific minerals, the closest fitting pure spectra was used: forsterite for olivine and lizardite for serpentine (Mellini, 1982; Nord et al., 1982). Mean SSA for all minerals ranges from 0.03 to 5.31 $m^2 g^{-1}$ in the large grain size and from 1.2 to 9.2 $m^2 g^{-1}$ in the small grain size (Table 3.1). The increase in SSA from the large grain size to the small grain size for any given mineral was between 1.5 to 40 times, with most minerals showing ~2 times increase.

3.3.3. Mass Measurements

3.3.3.1. Initial Dry Mass

Prior to incubation, the mass of each sample dish was determined; values ranged from 4.42 to 4.80 g. Total dry mass (i.e., the sample + the dish) was determined after incubation at 55ºC. Several measurements were collected with ≥36 hr between each, until the measurement stabilized at what I call the equilibrium mass. Total dry mass measurements for all minerals ranged from 11.59 to 42.63 g (Table C.1). Subtracting the dish mass from the

total dry mass yields the dry sample mass. The dry sample mass ranged from 6.88 to 38.22 g. These two values (total dry mass and dry sample mass), along with the incubation mass, are needed to calculate equilibrium water mass and water content. Water mass is calculated as:

$$Water\ mass = \frac{Incubation\ mass - Total\ dry\ mass}{1000}, \quad (3.1)$$

where both the equilibrium mass (see section 3.3.3.2) and total dry mass include the dish mass and soil mass. Any mass should exclusively be adsorbed water in units of mg. Adsorbed water content is calculated as:

$$AWC = \frac{Water\ mass}{Dry\ sample\ mass}, \quad (3.2)$$

where water mass is in mg H_2O and dry sample mass is in g of soil, yielding AWC in units of mg H_2O g^{-1} soil.

3.3.3.2. Incubation Equilibrium Mass

Mineral samples were measured at least three times (3 - 5 times) under each set of RH and T conditions to ensure adsorbed water content equilibrium (see section 3.2.1.1). Equilibrium mass measurements (dish + sample) ranged from 11.60 to 42.68 g, and calculated adsorbed water mass ranged from 2.28 to 375.20 mg, yielding adsorbed water content that ranged from 0.09 to 24.09 mg g^{-1}. Here I focus on the mass-normalized water content (mg H_2O g^{-1} soil) because this value allows comparison across the fairly large range of dry sample masses among all samples.

I observe a range of water content of 0.09 to 4.71 mg g^{-1} for olivine (Figure 3.4), 0.20 to 4.65 mg g^{-1} for anorthite (Figure 3.5), 0.84 to 24.09 mg g^{-1} for serpentine (Figure 3.6), 0.51 to 14.67 mg g^{-1} for quartz (Figure 3.7), and 1.18 to 11.80 mg g^{-1} for calcite (Figure 3.8). Each range in AWC is illustrated as a series of histograms organized by the categorical variables of

RH, T, and grain size to show differences in AWC under a range of different conditions. In general, all minerals show *i)* increasing water content with increasing nominal RH, *ii)* decreasing water content with increasing T, and *iii)* increasing water content with decreasing grain size. The notable exception to this pattern is calcite, where there is little difference between the water content of the large and small grain size samples.

3.3.3.3. Mass of Benchmark Experiment Samples

The three replicate subsamples of the composite mineral mixture had mean dry weights (with petri dish) of 22.4654, 28.3394, and 27.2440 g. The three replicate subsamples were incubated 6 times (≥48 hr each) under target conditions of 52%RH and 25ºC and mass measurement results are shown in table C.2.

The two natural soil samples, MDQ and LH, had mean dry weights (with petri dish) of 159.0012 and 107.5969 g, respectively. The two samples were incubated under three different water availability conditions (high, medium, and low) and the mass measurement results are shown in table C.3.

3.4. Discussion

Here I aim to quantify the AWC of different mineral samples under a range of grain sizes and environmental conditions, with the goal of developing a predictive understanding of AWC in unsaturated, low carbon, heterogeneous soils. I use the experimental dataset to generate a multi-dimensional regression model that allows me to predict AWC across a range of RH, T, SSA. The multiple regression model is built upon (and consistent with) relationships derived from lower-dimensional, 1D-(i.e., AWC as a function of RH, T, or SSA) and 2D-models (i.e., AWC as a function of any two variables: RH, T, and/or SSA). See

figures C.1 – C.45 for a graphical depiction of the lower dimensional models. The following briefly outlines the 1D, linear relationships from which I build the multiple regression models. In brief, AWC has an exponential relationship with RH:

$$AWC \propto RH^2. \tag{3.3}$$

I transformed the RH data as RH^2 to yield a quasi-linear relationship between AWC and RH^2 with $r^2 > 0.75$ (Figure 3.9 A&B). This correlation is the same for both 1D and 2D models for AWC as a function of RH. The AWC exhibits linear relationships with both T and SSA, (AWC is negatively correlated with T and positively correlated with SSA; Figure 3.9 C&D). The relationships for AWC with respect to RH, T, and SSA are similar across all minerals and variables. The scale (i.e., slope) of the relationship, however, is dependent on the mineral as well as on RH, T, and SSA. The majority of the 1D models have $r^2 > 0.75$. A small number (36 of 300) of the 1D T and 1D SSA models showed little to no correlation ($r^2 < 0.3$) with AWC. This is mostly (24 of 36) found for the AWC vs. SSA data and results from the unexpected SSA measurements for calcite, where the small grain size samples have an unexpectedly lower SSA compared to the large grain size samples. This results in a relatively flat relationship (i.e., low r^2) for AWC as a function of SSA in the case of calcite (e.g., Figure C.30). I also evaluated multiple regressions among two parameters (e.g., any two of T, RH, or SSA). All the 2D models for all the minerals have $r^2 > 0.82$, indicating that accounting for any two of the three independent variables yields a moderately strong relationship. Indeed, stronger than the 1D models alone.

3.4.1. Mineral Specific, Three-Dimensional Adsorbed Water Content Model

Because AWC is ultimately a function of multiple parameters, I use a multiple linear regression approach (essentially a weighted linear combination model) to calculate AWC

based on all three independent variables (i.e., RH, T, and SSA) for each mineral. This model demonstrates *i)* similar shapes and trends to those observed in the 1D and 2D models and *ii)* reasonably accurate estimates of low water content. I evaluated regression equations with an intercept coefficient (*c*), i.e.,

$$AWC = (a \times RH^2) + (b \times T) + (d \times SSA) + c, \quad (3.4)$$

and without an intercept coefficient, i.e.,

$$AWC = (a \times RH^2) + (b \times T) + (d \times SSA). \quad (3.5)$$

In each case, a, b, and d are the weighted contributions of each variable. Both equations show similar residuals, as summarized by root mean square error (RMSE) (Table C.4). Therefore, I opt for the most parsimonious model (i.e., equation 3.5) considering Occam's razor.

The multiple regression model generates planes of AWC in 3D space (i.e., y = RH, x = T, z = SSA). The AWC contours are a surface (compared to a 2D model where the AWC contours are lines). The overall shape of the 3D model varies somewhat among the different minerals; however, the general trends are the same. The general patterns indicate that AWC increases with increasing RH and increasing SSA, and that AWC decreases with increasing T. This is intuitive, in that cooler, wetter environmental conditions allow more water to absorb and higher surface area per gram allows more absorbed water per gram.

The initial 3D models generally underestimated AWC at the very lowest water contents (i.e., RH <20%, T >30ºC), and in a few cases the model predicted negative AWC. This outcome is inherently absurd, so I calculated a scaling factor *(f)* based on mean model residuals that acts to increase modeled AWC at low RH and high T. The scaling factor is a simple multiplier on RH and T:

$$f = \frac{\Delta_m}{(100^2 - RH^2) \times T}, \quad (3.6)$$

where Δ_m is the mean residual under the lowest water availability conditions (i.e., LiCl buffer [RH = 11%RH] and T = 35ºC), 100^2 is the upper boundary for RH^2. Thus, the correction is largest at low RH and high T, and minimal at high RH and low T. Using this method, I observe the following: *i)* the overall trend and shape of the model is not significantly changed from the 1D and 2D models, *ii)* the RMSE is not significantly increased, and *iii)* the model accurately reproduces AWC in the low water content region. Therefore the addition of the scaling factor *(f)* serves to correct underestimates of AWC at low water availability without sacrificing overall accuracy. The overall form of the final 3D model equation is:

$$AWC = (a \times RH^2) + (b \times T) + (d \times SSA) + (f \times (100^2 - RH^2) \times T). \quad (3.7)$$

The 3D AWC model outcome for the five different minerals as a function of RH and T, displayed as 2D slices at two different grain sizes is compared to measured AWC and shown in figures 3.10 – 3.14. The details of the model coefficients (a, b, d, and f) for all minerals are presented in table C.5.

All minerals (with the exception of anorthite) show a similar pattern for contours of AWC as a function of RH and T. In general, the lowest AWC occurs at high T and low RH, and the highest AWC occurs at low T and high RH. An increase in SSA (i.e., a decrease in grain size) increases AWC across the entire range of RH and T. Anorthite exhibits a slightly different trend relative to the other minerals, with the lowest AWC at low T and low RH. This result is unexpected and is likely due to the relatively small differences in AWC as a function of T at low RH that are difficult for the model to fit. Overall, I observe similar trends between AWC and RH, T, and SSA for all minerals.

3.4.1.1 Model Residuals

Model residuals are the difference between the modeled (i.e., calculated) values of AWC and the measured AWC values. They provide a measure of the accuracy of the model. I calculate model residuals as:

$$Model\ residual = AWC_{meas} - AWC_{mod}, \quad (3.8)$$

where AWC_{meas} is the measured AWC value and AWC_{mod} is the modeled value. A histogram of model residuals for each mineral is presented as panel c of figures 3.10 – 3.14; in all cases the model residual is much smaller than the range in values for AWC. The models for olivine and anorthite AWC have RMSE <0.30 mg g^{-1}. The models for serpentine, quartz and calcite have slightly higher RMSE, between 0.48 and 0.56 mg g^{-1}. Overall (across the entire range of RH, T, and SSA), the 3D model for each mineral reasonably represents the measured data (within ~0.5 mg g^{-1}). In the following discussion of the results of these models, I will report the model's uncertainty as the RMSE for a given mineral.

3.4.2. Effect of Mineral Composition on Equilibrium Adsorbed Water Content

Here I use the models to demonstrate the similarities and differences in equilibrium AWC - at the same RH, T, and SSA - among olivine, anorthite, quartz, serpentine, and calcite at 18 points over the range of RH, T, and SSA.

3.4.2.1 Common Igneous Minerals: Olivine, Anorthite, and Quartz

Olivine, anorthite, and quartz represent the three endmembers of Bowen's reaction series and are therefore reasonably representative of igneous minerals ranging from mafic (i.e., olivine and anorthite) to felsic (quartz), and from Mg-rich (olivine), to Ca-rich (anorthite), to Si-rich (quartz). Olivine ($[Mg,Fe]_2SiO_4$) is ubiquitous in the solar system; it is

found in Earth's upper mantle (Green and Ringwood, 1967; Peslier and Bizimis, 2015), on Mars' surface (Hamilton and Christensen, 2005; Lane and Christensen, 2013), and in several meteorite populations such as chondrites (Mason, 1963) and pallasites (Ohtani, 1983). Anorthite ($CaAl_2Si_2O_8$) is a feldspar mineral, which is the most abundant mineral type on Earth's surface (Hecker et al., 2010). Anorthite itself is rare on Earth's surface, but abundant in the Lunar highlands and thus has relevance for planetary systems (Anbazhagan and Arivazhagan, 2010). Quartz (SiO_2) is the result of fractional crystallization, which requires active geodynamic processes and volcanism (Frost et al., 2016). Therefore, quartz is ubiquitous on Earth's surface in granitic rocks and many sediments, but is relatively rare across the solar system.

Overall, olivine and anorthite have similar adsorbed AWC (at conditions of 25%RH, 30ºC, and 1.5 m^2 g^{-1}) with AWC of 0.8 and 0.9 mg g^{-1}, respectively, and 2.5 and 2.6 mg g^{-1} (at conditions of 75%RH, 10ºC, 3.5 m^2 g^{-1}), respectively, (Figure 3.15). Quartz, in contrast, generally has higher adsorbed water content compared to olivine and anorthite at high humidity, low T, low SSA (e.g., RH >60%, T <18ºC, and SSA <1.6 m^2 g^{-1}). For example (conditions of 75%RH, 10ºC, and 1.5 m^2 g^{-1}), quartz has twice the adsorbed water content of 4.1 mg g^{-1} compared to 1.6 and 1.8 mg g^{-1} for olivine and anorthite, respectively. However, in the relatively low AWC region of low RH, high T, and high SSA (conditions of 25%RH, 30ºC, and 3.5 m^2 g^{-1}), quartz, olivine and anorthite all have similar AWC of 2.1, 1.8, and 1.8 mg g^{-1}, respectively. These patterns suggest high-Si minerals may have a higher affinity for adsorbed water compared to low-Si minerals, with the notable exception of low RH, high T, and high SSA conditions.

3.4.2.2. Olivine and Serpentine: Minerals Related by Weathering

Serpentine is a clay mineral that is a weathering product of olivine described by the following chemical reaction:

$$3Mg_2SiO_4 + 3H_2O \rightarrow Mg_3Si_2O_5(OH)_4 + Mg(OH)_2. \quad (3.9)$$

I have written the reaction using the Mg endmembers, but most naturally occurring olivine and serpentine is a mixture of Mg and Fe bearing minerals (Sun and McDonough, 1989). Serpentine has a higher adsorbed water content than olivine at low SSA and mid to high RH (<2.6 $m^2\ g^{-1}$ and >45%RH; Figure 3.16). The region of high SSA and low RH is the only set of conditions where olivine has higher AWC than serpentine. For example, serpentine has an AWC of 1.0 mg g^{-1} (at 25%RH, 30ºC, 3.5 $m^2\ g^{-1}$), while olivine has ~2 times higher AWC of 1.8 mg g^{-1} under the same conditions. Under high RH conditions, serpentine has a much higher water content, however, under arid conditions (i.e., low RH) olivine likely has higher AWC over the range of T. This outcome may be a result of the vastly different ranges of SSA covered by the different minerals. Future experiments should include a wider range of SSA for all minerals, nonetheless, these results provide an interesting implication for the habitability of arid worlds, in that mineral types have different equilibrium AWC.

3.4.2.3. Calcite: An Evaporite Mineral

Calcite, a polymorph of calcium carbonate, is a ubiquitous mineral on Earth. It is primarily created biogenically (Nelson Eby, 2016); however, large amounts of calcite are precipitated abiotically at ocean spreading ridges as a result of the reducing conditions of serpentinization (Chen et al., 2020). I observe a unique distribution of the AWC of calcite across RH, T, and SSA, but is most similar to quartz in terms of adsorbed water content under most conditions (Figure 3.17). The unique AWC of calcite is likely due to sample

preparation constraints, discussed in the next paragraph. Overall, I observe that calcite is somewhat unique, in terms of AWC, among the minerals of this study, but not extraordinarily different from quartz.

The calcite samples had an unexpectedly narrow distribution of surface area, presumably because the sample preparation wasn't adequate to generate a better grain size distribution. The large grain samples have a similar or, indeed, higher SSA than the nominally small grain size samples. Both grain size subsamples were sourced from the same calcite sample: a palm-sized, consolidated sample that was crushed and sieved into the two grain size fractions. This limits the ability to interpolate the data because the two grain size fractions are so similar as to be effectively the same. My confidence in extrapolation outside of the measured surface areas is low for calcite because the model is informed by a very small range of SSA.

3.4.3. Soil Water Content Prediction for Mineral Mixtures

Here I introduce a new method to predict the AWC of a soil at a given T and RH, knowing only the mineralogy mass fraction and the surface area (or grain size). I assert that mixtures of minerals will behave similarly to the pure mineral samples. I can then test to see if the AWC of a mineral mixture can be predicted as a set of additive model equations for each of its mineral constituents using:

$$AWC_{mix} = \sum X_m \times AWC_m(RH, T, SSA_m), \quad (3.10)$$

where AWC_{mix} is the AWC of the mineral mixture, X_m is the mass fraction of the mineral in the soil, AWC_m is the AWC model of the mineral, T and RH are the temperature and relative humidity conditions, SSA_m is the surface area of the mineral, and m is the index of the representative mineral (e.g., olivine, anorthite, quartz, serpentine, calcite). In this way complex soil mixtures can be simplified into the mass fraction of their mineral constituents

and the AWC of the soil can be predicted. At this time, I have experimental ground truthing for five minerals (olivine, anorthite, quartz, serpentine, and calcite) and I can approximate a soil mixture, very roughly, as a combination of these five minerals.

3.4.3.1. Benchmark I: Simple, Composite Mineral Mixture

I prepared a soil-like mineral mixture composed of three of the pure minerals (olivine, serpentine, and calcite) used in this experiment to demonstrate whether the AWC of mineral mixtures can be predicted using the models developed here. The measured and predicted AWC values for the mineral mixture shown in figure 3.18 reveal that the model predicts AWC (within its own uncertainty: ~30%), and with residuals of 3 - 15% of the measured AWC value. Model uncertainty is constrained using the RMSE values for each mineral; averaging over the five minerals results in a mean uncertainty of ~30%. This is likely an overestimation of uncertainty but is effective for assessing the validity and accuracy of this approach and overall model performance. The relatively low residuals of 3 - 15% offer strong support for my assertion that mineral mixtures adsorb water in an additive way that scales with the mass fraction of their constituents as shown in equation 3.10.

3.4.3.2. Benchmark II: Complex Natural Soil

Here I predict the AWC of two natural soils with a relatively complex mixture of minerals. This is perhaps the most rigorous test of this approach and model because the five basis minerals are likely a moderate to poor representation of the mineralogical diversity of a natural soil. The two soil samples, MDQ and LH, were collected from the same environment, ~1 km apart and have marked differences in mineral composition (chapter 2; Tables 3.2 and 3.3). The work in this study was designed using minerals that are reasonably

representative of five broad classes of minerals: olivine (an ultramafic silicate), anorthite (a feldspar or mafic silicate), quartz (a felsic silicate), serpentine (a clay weathering product), and calcite (a precipitate). The mineral composition, and how the minerals were binned into the five broad mineral categories, of MDQ and LH are shown in tables 3.2 and 3.3, respectively.

I use the mineral-specific models described here to calculate AWC for MDQ and LH and compare them to the measured AWC as well as to three published soil water content models (Leão and Tuller, 2014; Resurreccion et al., 2011; Tuller and Or, 2005).

Most existing AWC models are based on soil matric potential (the potential energy of a soil matrix with regard to water) or RH. First, I use a previously described model based on RH, T, and SSA (here known as model A):

$$AWC = \left(\frac{AV_w}{6\pi RTln\left(\frac{P}{P_0}\right)}\right), \tag{3.11}$$

where A is the Hamaker constant (-6 x 10^{-20} J), V_w is the molecular volume of water (1.8068 x 10^{-5} m^3 mol^{-1}), R is the gas constant (8.31446 J mol^{-1} K^{-1}), T is temperature in K, and P/P_0 is relative humidity (Pa Pa^{-1}; Leão and Tuller, 2014; Tuller and Or, 2005). Second, Resurreccion et al. (2011) described a modified version of an earlier soil water content model by Campbell and Shiozawa (1992) based on matric potential and clay content (here known as model B):

$$AWC = \frac{log\left(\frac{\psi}{\psi_{ref}}\right)}{10.75\left(f_c^{-0.8}\right)} \times \frac{10^6}{\rho_s}, \tag{3.12}$$

where ψ is the matric potential (in m H_2O), ψ_{ref} is the reference soil water matric potential (-$10^{4.91}$ m H_2O), f_c is the clay fraction (g g^{-1}), ρ_s is soil density (kg m^{-3}), and 10^6 is the conversion factor for volumetric to gravimetric water content. Matric potential is a measure

of water's potential energy within a soil matrix and is a function of RH and T following the Kelvin equation:

$$\psi = \frac{100RT}{M_w g} ln\left(\frac{P}{P_0}\right), \quad (3.13)$$

where M_w is the molar mass of water (0.018 kg mol^{-1}), g is the acceleration due to gravity (9.81 m s^{-2}), and 100 is a conversion factor between m and cm. Finally, Resurreccion et al. (2011) described a similar soil water content model as 3.13, but based on SSA rather than clay mass fraction (here known as model C):

$$AWC = \frac{log\left(\frac{\psi}{\psi_{ref}}\right)}{1631(SSA^{-0.96})} \times \frac{10^6}{\rho_s}, \quad (3.14)$$

where SSA is the specific surface area (m^2 g^{-1}).

These three AWC models will be compared to the model described here: equations 3.7 and 3.10. Here I calculate AWC using two approaches: bulk and separate. The bulk approach uses the bulk soil properties (mineral abundance and SSA) and environmental conditions (RH and T) to calculate AWC using the model coefficients (Table C.5) and equations 3.7 and 3.10. The separate approach is similar, but the soil is physically split into two subsamples (large and small grain; described in section 3.2.3.2), and soil properties are measured on each of the soil separates and resulting AWC is multiplied by the mass fraction of the separates and summed between the subsamples:

$$AWC_{tot} = X_l AWC_l + X_s AWC_s, \quad (3.15)$$

where AWC_{tot} is the calculated AWC of the bulk soil, X_l is the mass fraction of the large grain subsample, AWC_l is the AWC of the large grain subsample, X_s is the mass fraction of the small grain subsample, and AWC_s is the AWC of the small grain subsample.

3.4.3.2.a. Adsorbed Water Content Predictions for Mar de Quartz

Mar de Quartz is a site within the hyperarid core of the Atacama Desert - a Mars analog (Shen, 2020; Valdivia-Silva et al., 2012b) - described previously by Glaser et al. (chapter 2; 2022). The site sits on the lower floor of a playa landscape mixed with low-laying hills. Measured AWC for MDQ is 3.5, 1.6, and 1.4 mg g^{-1} under high (50-60%RH, 25ºC), medium (12%RH, 13ºC), and low (16%RH, 35ºC) water availability conditions, respectively. MDQ mineral abundances and classification used for model input are shown in table 3.2 and soil properties are in table 3.4. The model results of the bulk and separate approaches are shown in comparison to the measured AWC and models A, B, and C in figure 3.19. The bulk and separate approaches underestimate AWC in all cases and predict AWC for the high (2.0 and 1.7 mg g^{-1}), medium (0.4 and 0.5 mg g^{-1}), and low (0.2 and 0.4 mg g^{-1}) water availability conditions. Table 3.5 shows a summary of the residuals for all models. The bulk approach and model B both show similar accuracy (residuals of ~30 - 90%) with the model underestimating and model B overestimating AWC by similar magnitudes across all water availability conditions. The separate approach is an improvement in prediction compared to the bulk approach in the medium and low water availability conditions. However, under the high water availability conditions the bulk approach has a lower residual; this result is unexpected and warrants further investigation.

3.4.3.2.b. Adsorbed Water Content Predictions for Los Halitos

Los Halitos, similar to MDQ, is located in the hyperarid core of the Atacama Desert; however, LH is located on a hill ~5-10 m above the playa floor (Glaser et al., 2022). Measured AWC for LH is 2.3, 1.2, and 0.9 mg g^{-1} under high (50-60%RH, 25ºC), medium (12%RH, 13ºC), and low (16%RH, 35ºC) water availability conditions, respectively. Los

Halitos mineral abundances and classification used for model input are shown in table 3.3 and soil properties are in table 3.4. The model results of the bulk and separate approaches are shown in comparison to the measured AWC and models A, B, and C in figure 3.20. The bulk and separate approaches underestimate AWC in all cases and predict AWC for the high (1.5 and 1.9 mg g^{-1}), medium (0.2 and 0.5 mg g^{-1}), and low (0.2 and 0.2 mg g^{-1}) water availability conditions. Table 3.6 shows a summary of the residuals for all models. All models, excluding model B, underestimate LH AWC. The bulk and separate approaches perform at least as accurately (residuals of ~20 to 90%) as models A (residuals of ~90%) and C (residuals of ~80 to 90%) over all water availability conditions. The separate approach shows an improvement in accuracy over the bulk approach in all cases. Model B overestimates LH AWC by at least an order of magnitude under all water availability conditions.

3.4.3.2.c. Overall Model Accuracy Assessment

This model performs as accurately, or better compared to the three previously published soil AWC models. In general, this model is more accurate under high water availability with mean residual of -37% compared to -78% under low water availability. The model is slightly more accurate with mean residuals of -57% for LH compared to -67% for MDQ. Also, the separate model has slightly lower mean residuals (-56%) compared to the bulk model (-69%). These mean residuals are better than for both models A and C; where the residuals are all <-80%. Model B estimates AWC for MDQ quite well with residuals of 38, 44, and 72% for the high, medium, and low water availability conditions, respectively (Table 3.5). However, model B vastly overestimates AWC for LH with residuals of >200% under all water availability conditions (Table 3.6). Considering the variability of residuals for model B

between the two soil samples, I assert that the model described here is the most consistently accurate of the considered AWC models.

This model also can predict differences in AWC between the two natural soils. These soils were collected reasonably close to each other (~1 km), however I observe differences in mineralogy and surface area and, ultimately, AWC. This result suggests that mineral and physical heterogeneities in soils can have profound effects on the water budget, perhaps on a micro scale.

In all but one case the separate approach was an improvement in estimation over the bulk approach. However, the improvement in accuracy is limited in most cases (~10% of the measured value). These results suggest that a bulk approach, while low resolution, is capable of estimating AWC in natural soils to within a factor of 2 in most cases.

3.4.4. Model Limitations

The mineral-specific set of models to predict AWC as a function of RH, T, and SSA have shown *i)* mineralogy must be considered in estimates of AWC and *ii)* mineral mixtures behave in an additive fashion with respect to AWC. However, the model is somewhat limited in its capacity to approximate AWC for natural soils. This may be due to several factors: *i)* mineral oversimplification and misrepresentation or *ii)* surface area non-linearity. Here I discuss each of these factors in detail.

3.4.4.1. Mineral Oversimplification and Misrepresentation

Experimental constraints required that I choose a limited set of minerals. Thus, I was not able to measure all the minerals present in the natural soils. I prioritized a broad set of distinct minerals with relevance both for the Atacama and for planetary science applications,

generally. Since there is no other pure mineral AWC data in the literature, to my knowledge, I assert that this set of minerals is an adequate foundational dataset for future research. Overall, it may be premature to use this technique to predict AWC for unknown materials because minerals may adsorb water in a way that is inconsistent with chemically and mineralogically similar minerals. This is consistent with my attempt to use the five AWC mineral models to describe a system that has ~15 minerals (MDQ and LH) because it is likely that there are minerals in the natural soil that behave differently than the five described minerals. The minerals chosen for this study may not be representative, with regards to AWC, of their entire class of minerals and it is likely that five well-described minerals are insufficient to represent a complex soil. More work is needed to create AWC models for other minerals to accurately designate minerals into AWC classes and, ultimately, predict AWC. This effort will likely have the effect of reducing the model uncertainty for a given soil if there is a larger array of representative mineral categories.

3.4.4.2. Surface Area Non-Linearity

This study was limited to a tractable number of experimental samples. Therefore, I was not able to create an additional grain size and measure another surface area for each mineral. The number of surface area bins (2) for each mineral is potentially a significant limitation of this study. I extrapolate linearly above and below the basis dataset, which may not be appropriate for some, if not all, minerals. Linearity is a reasonable, *a priori* expectation, however, it is necessary to investigate this with more experimental data. Ideally, there would be four different surface area bins for each mineral. This would allow a more robust interpretation of the linearity (or non-linearity) of AWC as a function of surface area for each mineral.

3.5. Summary and Implications

3.5.1. Summary

I measured equilibrium AWC for five different minerals at two grain sizes over an environmentally relevant range of RH and T. These measurements were used to inform a mineral-specific, 3D model to predict AWC as a function of RH, T, and SSA. I developed 3D models to predict AWC as a function of RH, T, and SSA. These models accurately predicted AWC for pure minerals over a range of RH (10 - 75%RH), T (5 - 35ºC), and SSA (~0.5 - 5 $m^2 g^{-1}$). All minerals show reasonable agreement between the measured and modeled values, as evidenced by the relatively small RMSE (0.22 - 0.55 mg g^{-1}).

3.5.1.1. Mineralogy Plays a Role in Equilibrium AWC

The 3D models developed for each mineral are unique, as evidenced by the model coefficients (Table C.5), and indicate that AWC scales differently with RH, T, and SSA for each described mineral. These models allow comparison between minerals at the same conditions. For example, figure 3.15 shows that at high RH and low T, there are significant differences in AWC between olivine and quartz at both low (1.5 $m^2 g^{-1}$) and high (3.5 $m^2 g^{-1}$) surface area. These findings are novel and suggest potentially significant differences in soil AWC between soils with differing mineralogy.

3.5.1.2. Adsorbed Water Content of Complex Soil Mixtures is a Linear Combination of the Constituent Minerals

Adsorbed water content for a mixture of minerals appears to behave as a linear combination, by mass fraction, of the AWC for the mixture's mineral constituents. Using a roughly 1:1:1 mixture of olivine:serpentine:calcite I find the model prediction is within

~10% of the measured AWC value for the mixture. In addition, I modeled the AWC of a complex, natural soil by simplifying the natural soil into representative mineral groups that could be represented by the minerals characterized in this study. The model predictions of the complex natural soil are within 17 - 90% of the measured AWC values. These results are as accurate, or up to a factor of 6 more accurate, compared to previously published AWC models.

3.5.2. Implications

Soil water content, especially in arid environments, is a key factor for microbial activity. Many hyperarid environments go months, if not years, without condensed water input (rain or fog) and, therefore, WVA may be an important water source. Previous work has shown that water from WVA is sufficient to stimulate respiration in some microorganisms (McHugh et al., 2015), suggesting that WVA can provide bioavailable water. This work provides the first model that can predict AWC from RH, T, and SSA for specific minerals. For planetary systems where we don't have good measures of soil water content, these models might allow us to make informed estimates and could provide an additional constraint on AWC.

Mineralogy varies greatly across arid environments on Earth. This work provides evidence that the microenvironment of unsaturated soils may provide bioavailable water at different rates based on mineralogy. Heterogeneities in soil mineral composition may result in heterogeneities in soil water content considering the differences in AWC between MDQ and LH presented here. This work can be applied to Mars, or to any other arid worlds of astrobiological relevance. Based on my results and considering the low RH on Mars (~0 – 50%RH), regions with high olivine abundance may have higher AWC compared to regions

high in clay minerals. For example, under conditions of 10%RH and 5ºC with a surface area of 3 m^2 g^{-1}, this model predicts an AWC value of 1.5 mg g^{-1} for olivine and 1.0 mg g^{-1} for serpentine. Considering this, high surface area olivine deposits could be important targets in the search for life or biosignatures, particularly on Mars. These regions with higher AWC are prime targets for in depth rover investigations and potentially for a return sample mission. More speculatively, these regions could be a high priority target for future missions that require water collection via *in situ* resource utilization.

Table 3.1: BET Surface area data, in $m^2 g^{-1}$, summarized by mineral and grain size. Error is one standard deviation of three duplicate samples.

Mineral	Grain Size	Surface Area
Olivine	Large	0.29 ± 0.031
	Small	1.61 ± 0.775
Anorthite	Large	0.03 ± 0.037
	Small	1.23 ± 0.316
Quartz	Large	1.94 ± 0.126
	Small	3.70 ± 0.287
Serpentine	Large	5.31 ± 0.398
	Small	9.17 ± 0.491
Calcite	Large	3.79 ± 0.153
	Small	3.12 ± 0.139

Table 3.2: Mineral abundances (in wt%) for the natural soil sample MDQ. Representative category shows the general class I used to approximate AWC using the model.

Representative Category	Mineral	XRD Abundance Measurements			Representative Category Abundance Estimation		
		Bulk	Large Grain	Small Grain	Bulk	Large Grain	Small Grain
Mafic (Olivine)	Actinolite	9.0	0.0	15.2	12.1	2.1	19.9
	Biotite	0.0	0.0	0.0			
	Lepidocrocite*	0.0	0.0	0.0			
	Magnetite*	3.1	2.1	4.8			
	Sillimanite	0.0	0.0	0.0			
	Tourmaline*	0.0	0.0	0.0			
Feldspar Felsic (Anorthite)	Andesine	11.7	13.0	13.3	28.5	24.3	29.4
	Anorthite	6.2	6.5	7.5			
	Anorthoclase	8.3	0.0	0.0			
	Buddingtonite	0.0	4.2	0.0			
	Bytownite	2.3	0.6	3.2			
	Labradorite	0.0	0.0	5.3			
	Microcline	0.0	0.0	0.0			
	Oligoclase	0.0	0.0	0.0			
Felsic (Quartz)	Chert	0.0	0.0	0.0	32.2	50.0	12.6
	Opal	8.3	0.0	11.4			
	Quartz	9.0	9.4	1.2			
	Tridymite	14.9	40.6	0.0			
Weathering Product Clay (Serpentine)	Chlorite	6.4	5.6	8.7	6.4	5.6	15.1
	Clinoptilolite*	0.0	0.0	6.4			
	Dickite	0.0	0.0	0.0			
	Mordenite*	0.0	0.0	0.0			
	Natrolite*	0.0	0.0	0.0			
Precipitate/Evaporite (Calcite)	Anhydrite	11.0	8.8	12.6	16.7	12.5	20.2
	Bassanite	5.8	3.7	7.5			

**These minerals are not captured well by the representative minerals with regards to structure and formation history*

Table 3.3: Mineral abundances (in wt%) for the natural soil sample LH. Representative category shows the general class I used to approximate AWC using the model.

Representative Category	Mineral	XRD Abundance Measurements			Representative Category Abundance Estimation		
		Bulk	Large Grain	Small Grain	Bulk	Large Grain	Small Grain
Mafic (Olivine)	Actinolite	0.0	0.0	0.0	15.8	0.0	13.5
	Biotite	4.0	0.0	0.0			
	Lepidocrocite*	3.5	0.0	0.0			
	Magnetite*	0.0	0.0	0.0			
	Sillimanite	0.0	0.0	3.6			
	Tourmaline*	8.2	0.0	9.9			
Feldspar Felsic (Anorthite)	Andesine	0.0	0.0	0.0	18.3	21.9	10.3
	Anorthite	0.0	0.0	0.0			
	Anorthoclase	0.0	0.0	0.0			
	Buddingtonite	0.0	0.0	0.0			
	Bytownite	4.6	5.5	0.0			
	Labradorite	0.0	0.0	6.6			
	Microcline	7.5	9.2	3.7			
	Oligoclase	6.3	7.3	0.0			
Felsic (Quartz)	Chert	4.3	5.3	0.0	33.0	53.2	0.0
	Opal	7.2	2.7	0.0			
	Quartz	0.0	3.4	0.0			
	Tridymite	21.6	41.8	0.0			
Weathering Product Clay (Serpentine)	Chlorite	0.0	3.9	0.0	0.0	3.9	16.5
	Clinoptilolite*	0.0	0.0	0.0			
	Dickite	0.0	0.0	7.2			
	Mordenite*	0.0	0.0	6.1			
	Natrolite*	0.0	0.0	3.2			
Precipitate/Evaporite (Calcite)	Anhydrite	22.3	9.9	36.5	24.6	9.9	39.6
	Bassanite	2.3	0.0	3.2			

**These minerals are not captured well by the representative minerals with regards to structure and formation history*

Table 3.4: Surface area values for MDQ and LH bulk and soil separates fractions.

Sample	Grain Size	Mass Fraction	BET Surface Area ($m^2 g^{-1}$)
MDQ	Bulk (all)	-	1.06
	Large	0.477	1.09
	Small	0.523	1.27
LH	Bulk (all)	-	0.47
	Large	0.532	0.58
	Small	0.468	1.80

Table 3.5: Measured and modeled AWC values for MDQ at three water availability conditions. Residuals are the difference between the modeled and measured AWC value where positive residual is a model overestimation of AWC.

AWC Value	High		Medium		Low	
	AWC (mg g^{-1})	Residual (%)	AWC (mg g^{-1})	Residual (%)	AWC (mg g^{-1})	Residual (%)
Measured AWC	3.5 ± 0.142	-	1.6 ± 0.013	-	1.4 ± 0.031	-
This Model (bulk approach)	2.0 ± 0.187	-43	0.3 ± 0.000	-79	0.15 ± 0.000	-89
This Model (separate approach)	1.7 ± 0.124	-52	0.5 ± 0.000	-66	0.38 ± 0.000	-73
Model A	0.35 ± 0.026	-90	0.24 ± 0.0145	-85	0.24 ± 0.015	-82
Model B	4.9 ± 0.35	38	2.3 ± 0.144	44	2.4 ± 0.144	72
Model C	0.46 ± 0.033	-87	0.22 ± 0.014	-86	0.23 ± 0.014	-84

Table 3.6: Measured and modeled AWC values for LH at three water availability conditions. Residuals are the difference between the modeled and measured AWC value where positive residual is a model overestimation of AWC.

AWC Value	High		Medium		Low	
	AWC (mg g^{-1})	Residual (%)	AWC (mg g^{-1})	Residual (%)	AWC (mg g^{-1})	Residual (%)
Measured AWC	2.3 ± 0.119	-	1.2 ± 0.035	-	0.86 ± 0.012	-
This Model (bulk approach)	1.5 ± 0.055	-36	0.2 ± 0.000	-86	0.18 ± 0.000	-79
This Model (separate approach)	1.9 ± 0.063	-17	0.5 ± 0.000	-55	0.24 ± 0.000	-72
Model A	0.16 ± 0.010	-93	0.11 ± 0.005	-91	0.11 ± 0.005	-87
Model B	8.6 ± 0.527	278	4.0 ± 0.206	249	4.3 ± 0.198	397
Model C	0.30 ± 0.019	-87	0.14 ± 0.007	-88	0.15 ± 0.007	-82

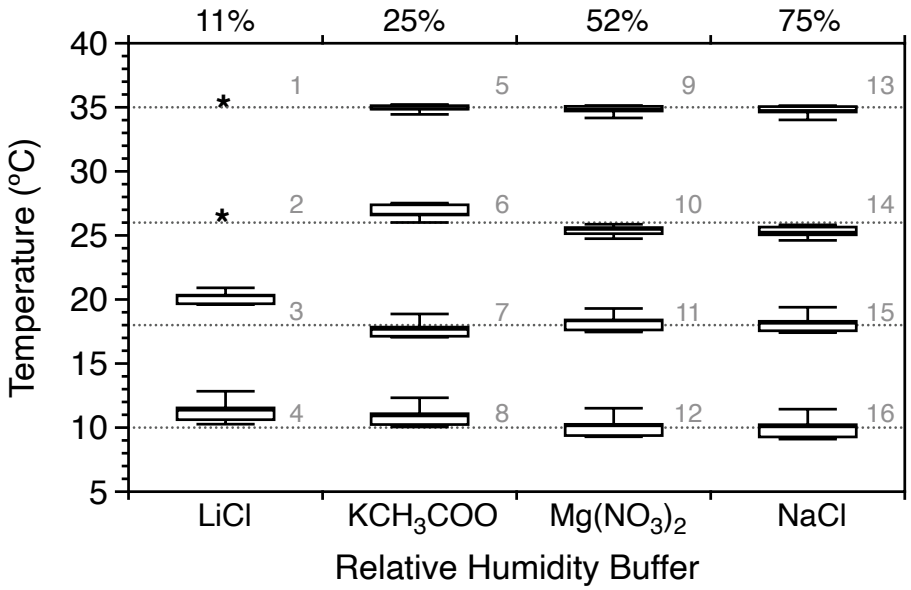

Figure 3.1: Reported chamber temperature for each experiment, organized by relative humidity buffer. Relative humidity buffers are organized along the x-axis from low- to high-RH (i.e., LiCl: 11%RH, KCH_3COO: 25%RH, $Mg(NO_3)_2$: 52%RH, and NaCl: 75%RH). Temperature is presented as box plots where box boundaries show the 25th, and 75th percentile (box or IQR), the line across each box is the 50th percentile (median), and whiskers indicate the range of the data. Each incubation experiment has ≥290 T & RH observations. Dotted horizontal lines show the set, or target, T for each experiment. Gray numbers beside the box and whisker plot are the incubation number; incubations were performed in ascending order. In general, mean chamber T has higher variation at lower T; however, all mean chamber temperatures are ± 1ºC from the set point with a range of ± 2ºC.

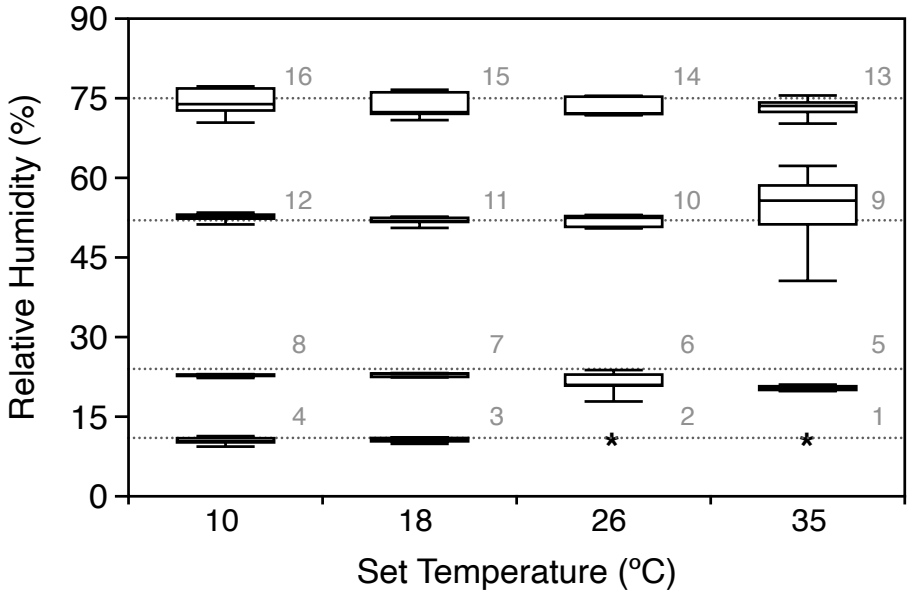

Figure 3.2: Reported chamber relative humidity for each incubation plotted at the nominal set temperature. Similar to figure 3.1, box and whiskers show the 25th, 50th, and 75th percentile (box or IQR) and the range of the data (whiskers). Each experiment has ≥290 T & RH observations. Dotted horizontal lines show the set, or target, RH for each experiment as designated by the buffer. Gray numbers beside the box and whisker plot are the experiment number; experiments were performed in ascending order. Most mean chamber RHs are ± 3%RH from the set point with a range of ± 6%RH. The exception is experiment 9, where I observe a mean RH within 3%RH of the set point, but with a relatively high range of ± 20%RH.

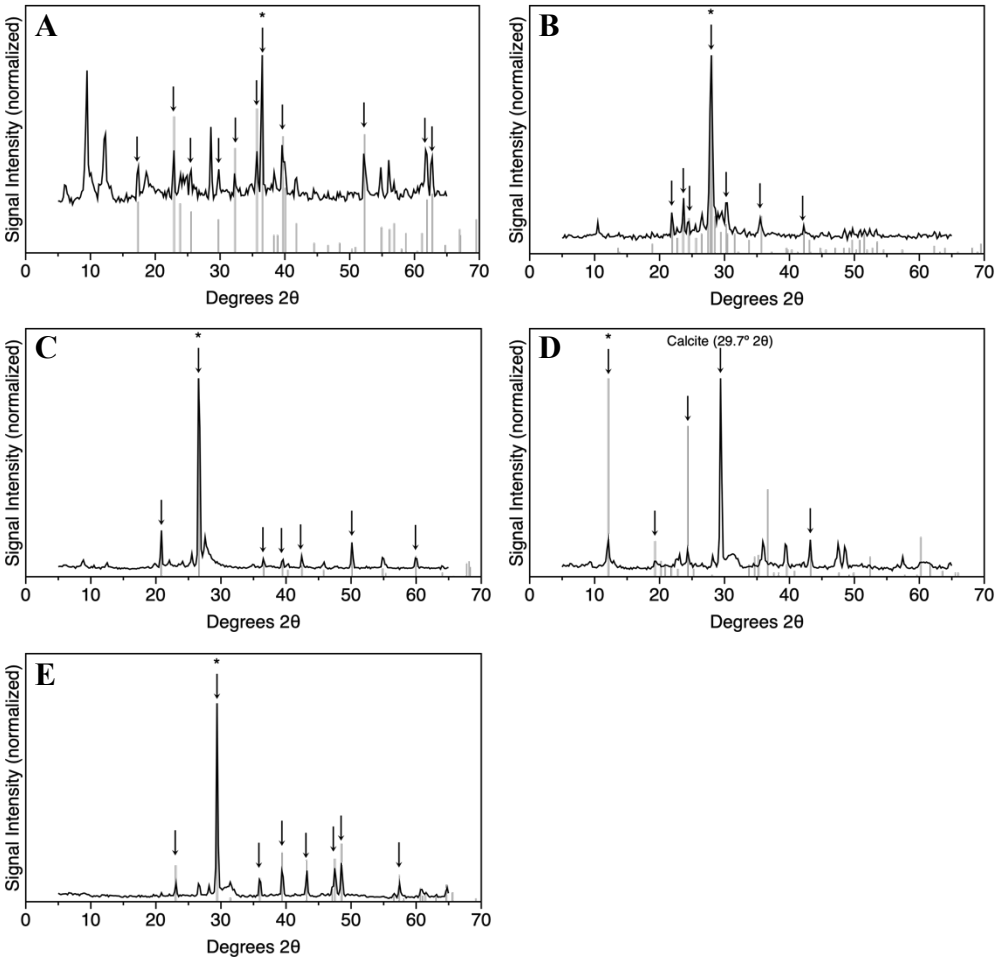

Figure 3.3: Powder XRD spectra from sample minerals (black) compared to pure mineral standard peaks (gray). Arrows show agreement between sample and standard spectra used for identification. Asterisk identifies the strongest peak in standard spectra used to normalize the signal intensity. **A)** olivine sample and forsterite standard (Nord et al., 1982). **B**) anorthite sample and anorthite standard (Wenk et al., 1980). **C**) quartz sample and quartz standard (Levien et al., 1980). **D**) serpentine sample and lizardite standard (Mellini, 1982). **E**) calcite sample and calcite standard (Graf, 1961).

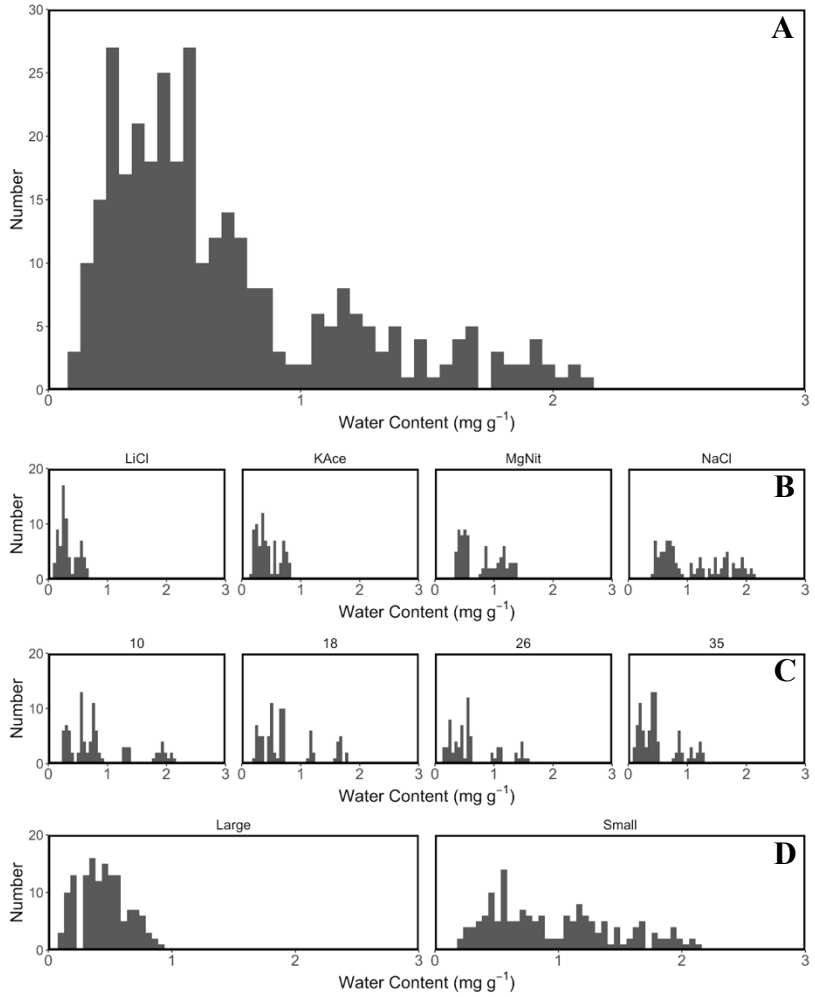

Figure 3.4: Adsorbed water content histograms for olivine. X axis is water content from low to high. Panel **A)** shows all water content data, while following panels show water content divided by **B)** RH buffer, **C)** T, and **D)** grain size. Bin width is 0.08 mg g^{-1} for all panels. Panel B is organized by increasing RH from left to right (LiCl = 11%RH, KAce = 25%RH, MgNit = 52%RH, and NaCl = 75%RH).

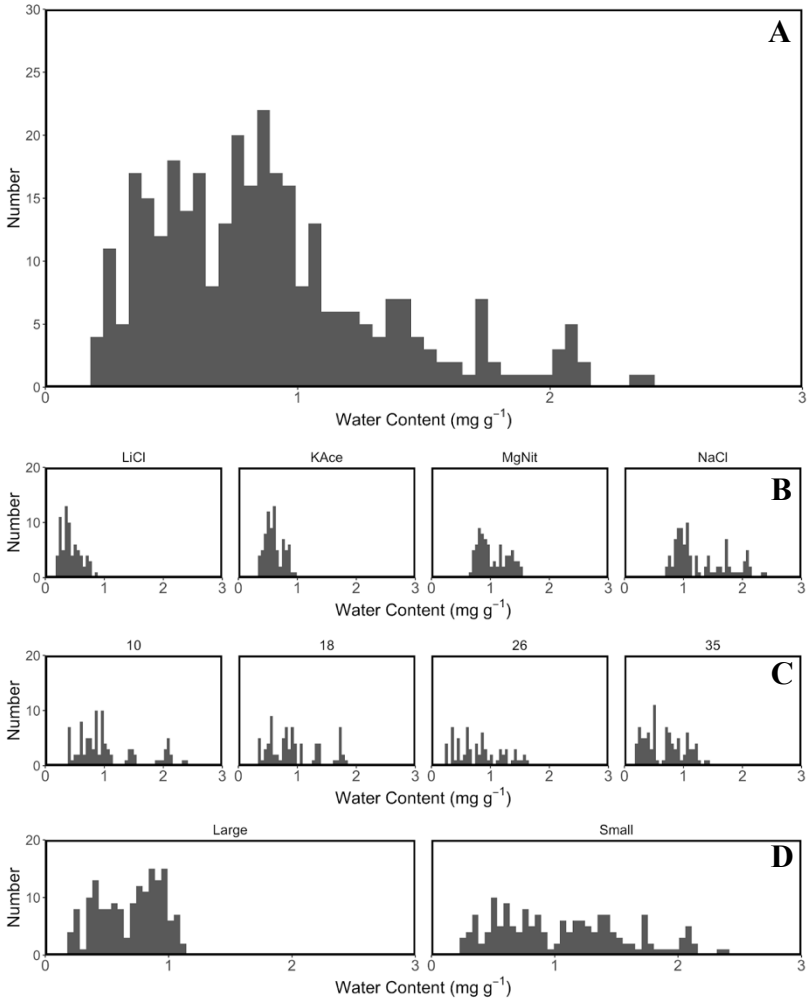

Figure 3.5: Adsorbed water content histograms for anorthite. Panel **A)** shows all water content data, while following panels show water content divided by **B)** RH buffer, **C)** T, and **D)** grain size. Bin width is 0.08 mg g^{-1} for all panels. Panel B is organized by increasing RH from left to right (LiCl = 11%RH, KAce = 24%RH, MgNit = 52%RH, and NaCl = 75%RH).

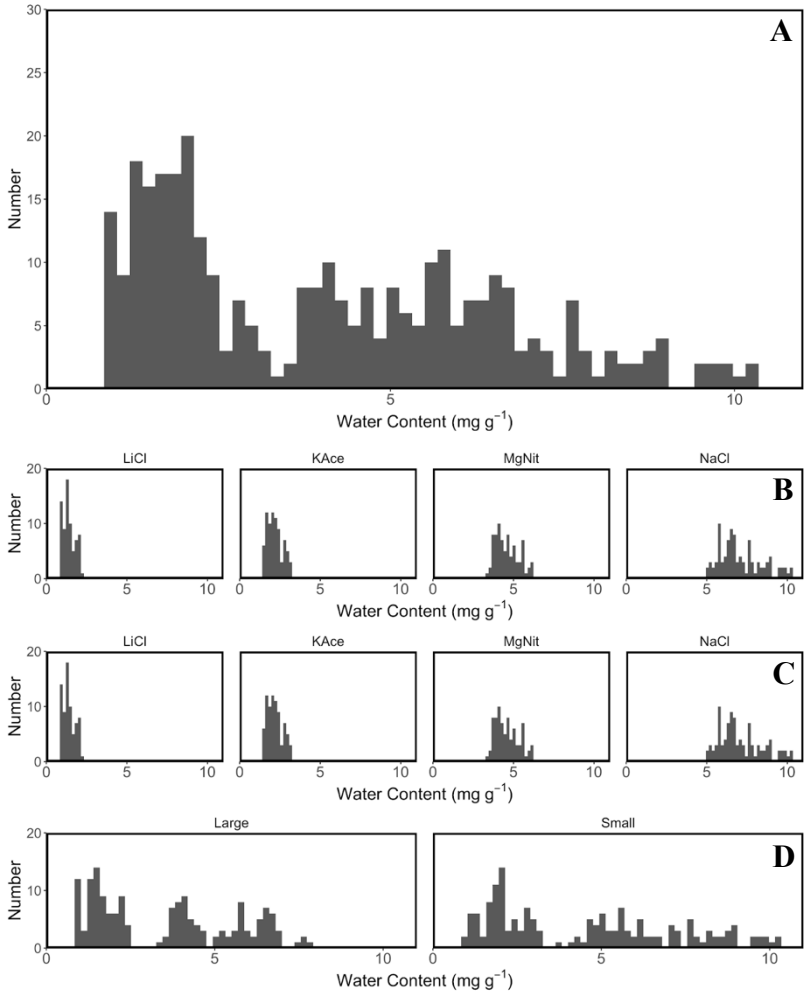

Figure 3.6: Adsorbed water content histograms for serpentine. Panel **A)** shows all water content data, while following panels show water content divided by **B)** RH buffer, **C)** T, and **D)** grain size. Bin width is 0.42 mg g^{-1} for all panels. Panel B is organized by increasing RH from left to right (LiCl = 11%RH, KAce = 24%RH, MgNit = 52%RH, and NaCl = 75%RH).

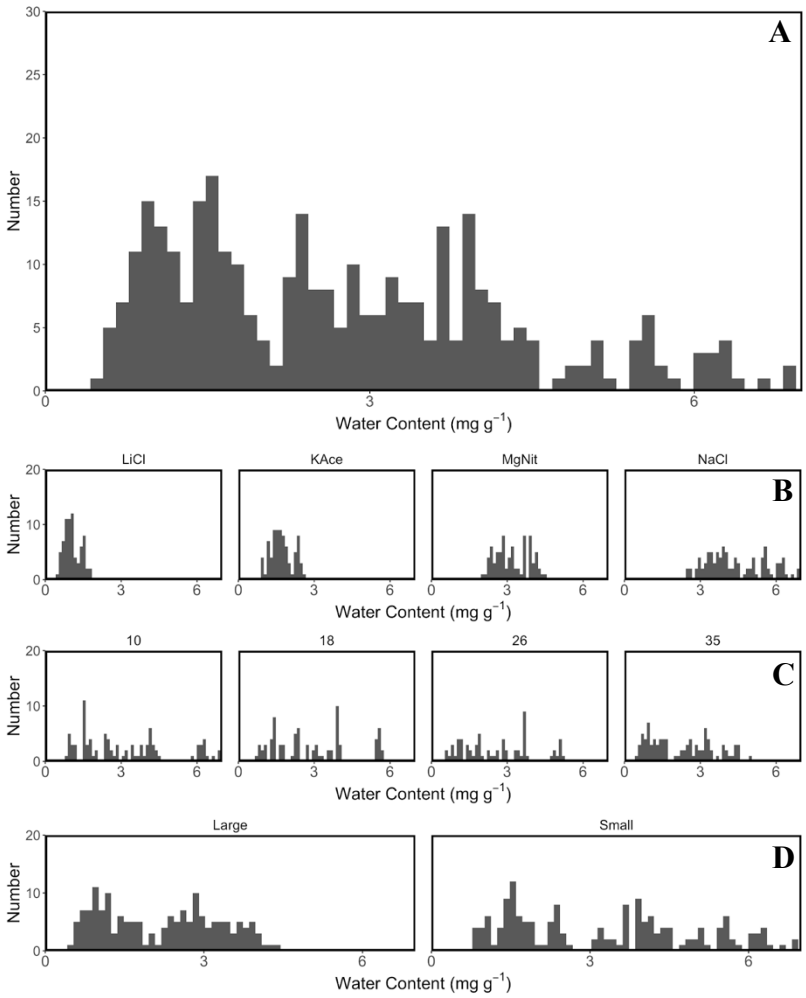

Figure 3.7: Adsorbed water content histograms for quartz. Panel **A)** shows all water content data, while following panels show water content divided by **B)** RH buffer, **C)** T, and **D)** grain size. Bin width is 0.25 mg g^{-1} for all panels. Panel B is organized by increasing RH from left to right (LiCl = 11%RH, KAce = 24%RH, MgNit = 52%RH, and NaCl = 75%RH).

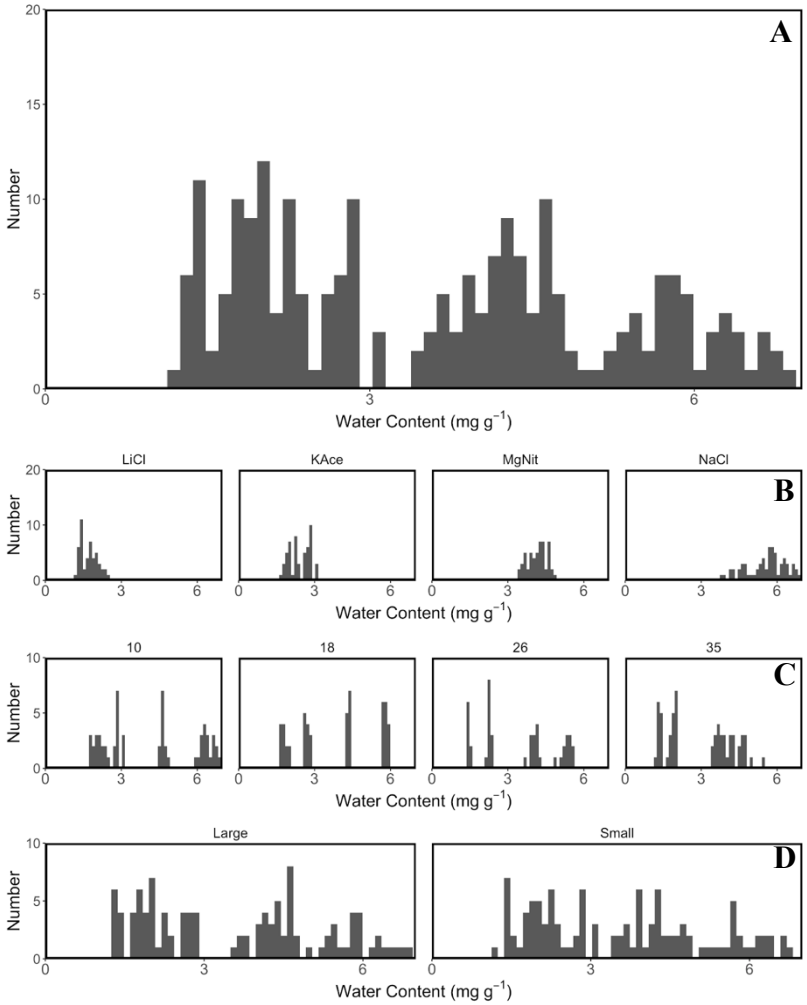

Figure 3.8: Adsorbed water content histograms for calcite. Panel **A)** shows all water content data, while following panels show water content divided by **B)** RH buffer, **C)** T, and **D)** grain size. Bin width is 0.20 mg g^{-1} for all panels. Panel B is organized by increasing RH from left to right (LiCl = 11%RH, KAce = 24%RH, MgNit = 52%RH, and NaCl = 75%RH). Note that large and small grain sizes have similar surface area.

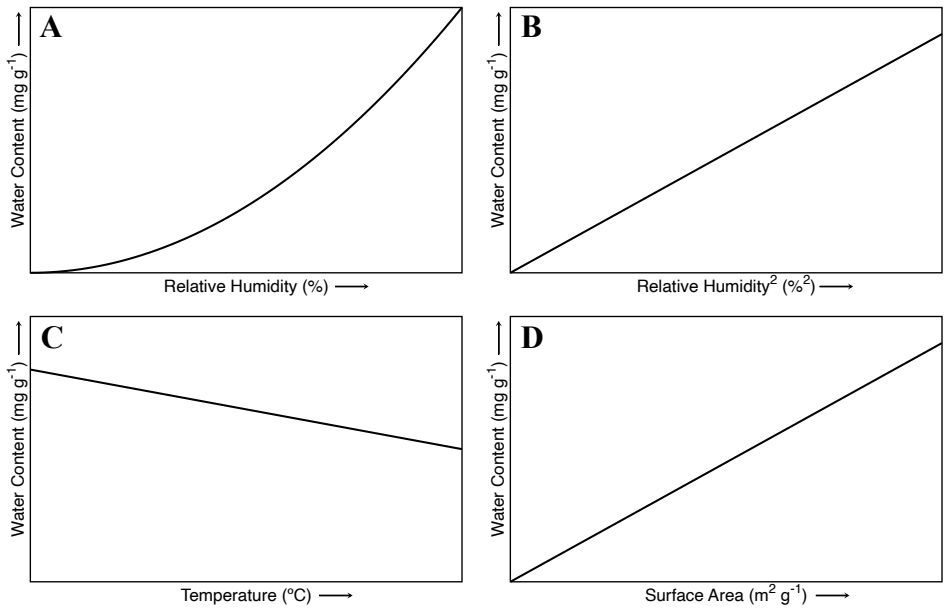

Figure 3.9: Representative one-dimensional trends of AWC with respect to: **A)** relative humidity, **B)** relative humidity squared, **C)** temperature, and **D)** specific surface area. Relative humidity shows a positive exponential relationship with AWC and relative humidity squared shows a positive linear relationship with AWC (n = 4). Temperature shows a negative linear relationship with AWC (n = 4). There are only two bins of surface area for each mineral (n = 2) that show a positive relationship, and I assume a liner relationship.

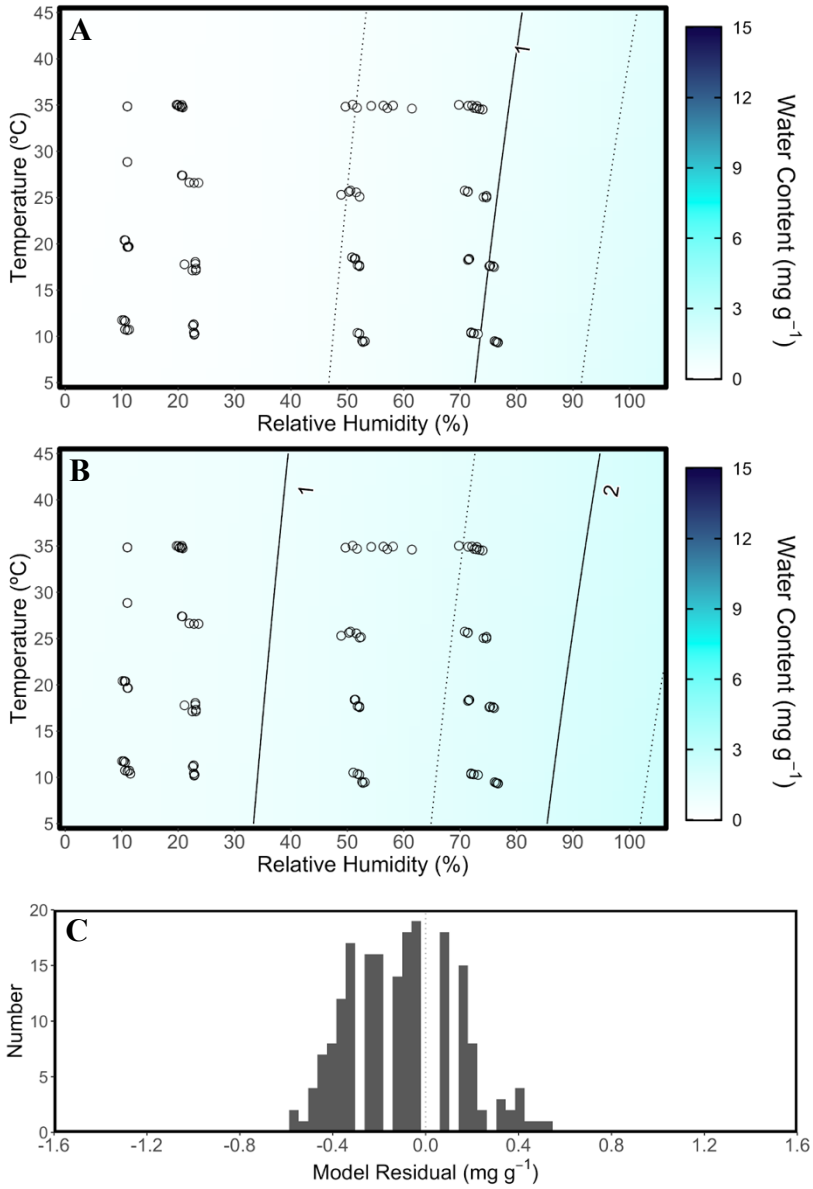

Figure 3.10: Measured (points) and modeled (contours) AWC for olivine at **A)** large grain size (SSA = 0.3 m^2 g^{-1}) and **B)** small grain size (1.6 m^2 g^{-1}). Both the measured and modeled water content use the same color scale. Panel **C)** shows the distribution of the model residuals for both SSAs. The RMSE of the distribution is 0.22 mg g^{-1}.

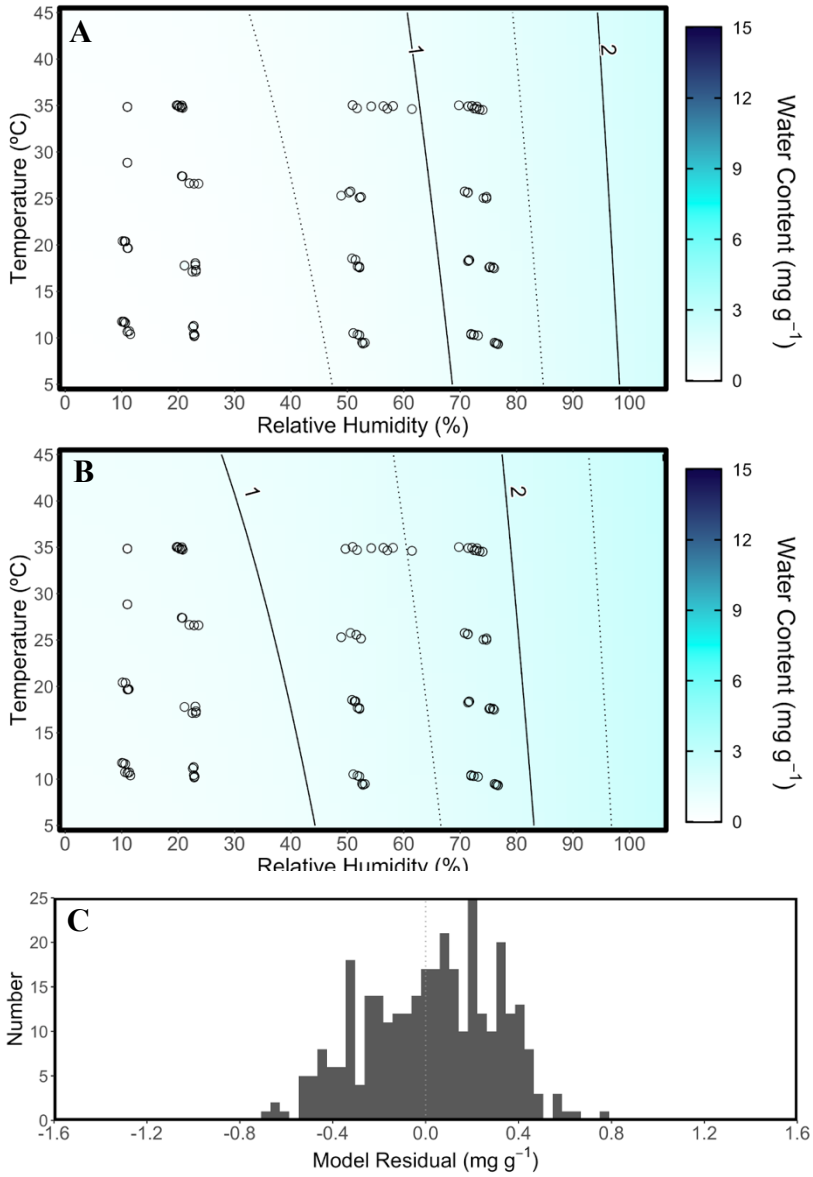

Figure 3.11: Measured (points) and modeled (contours) AWC for anorthite at **A)** large grain size (SSA = 0.03 m^2 g^{-1}) and **B)** small grain size (1.2 m^2 g^{-1}). Both the measured and modeled water content use the same color scale. Panel **C)** shows the distribution of the model residuals for both SSAs. The RMSE of the distribution is 0.28 mg g^{-1}.

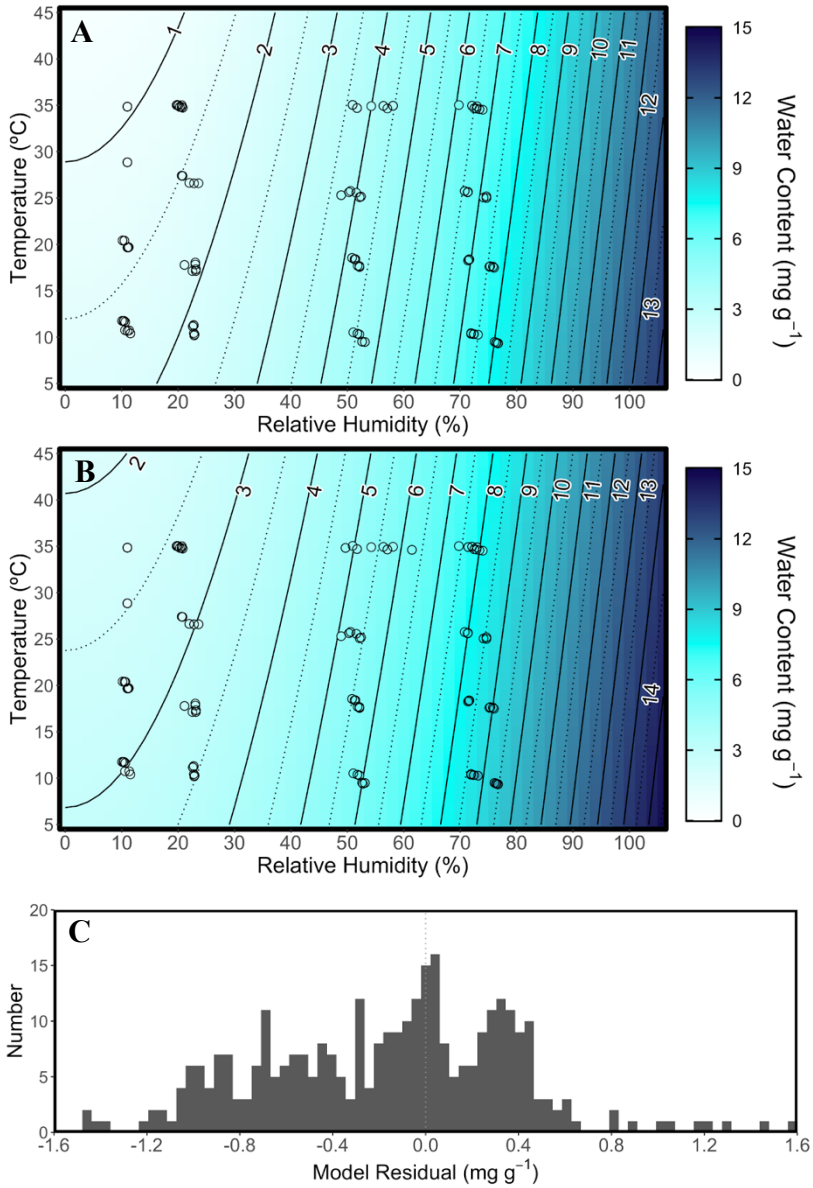

Figure 3.12: Measured (points) and modeled (contours) AWC for serpentine at **A)** large grain size (SSA = 5.2 m^2 g^{-1}) and **B)** small grain size (9.2 m^2 g^{-1}). Both the measured and modeled water content use the same color scale. Panel **C)** shows the distribution of the model residuals for both SSAs. The RMSE of the distribution is 0.55 mg g^{-1}.

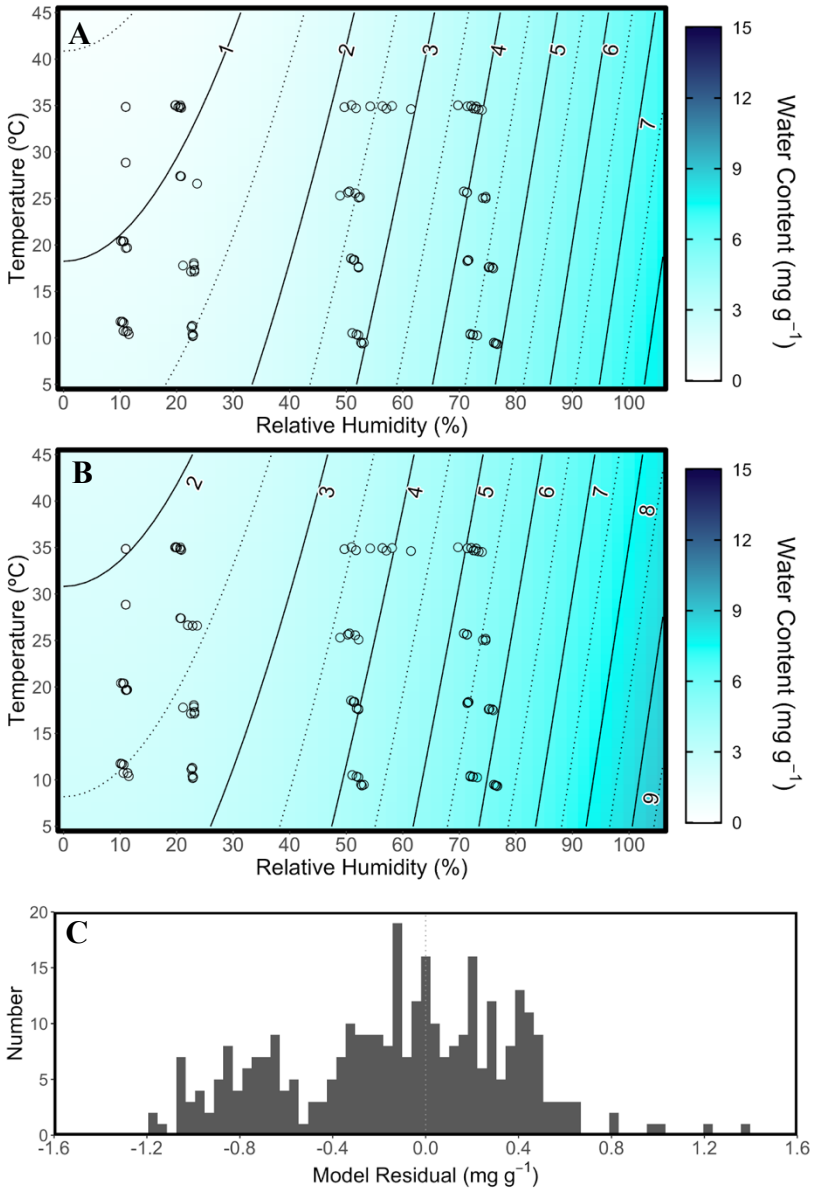

Figure 3.13: Measured (points) and modeled (contours) AWC for quartz at **A)** large grain size (SSA = 1.9 m^2 g^{-1}) and **B)** small grain size (3.7 m^2 g^{-1}). Both the measured and modeled water content use the same color scale. Panel **C)** shows the distribution of the model residuals for both SSAs. The RMSE of the distribution is 0.50 mg g^{-1}.

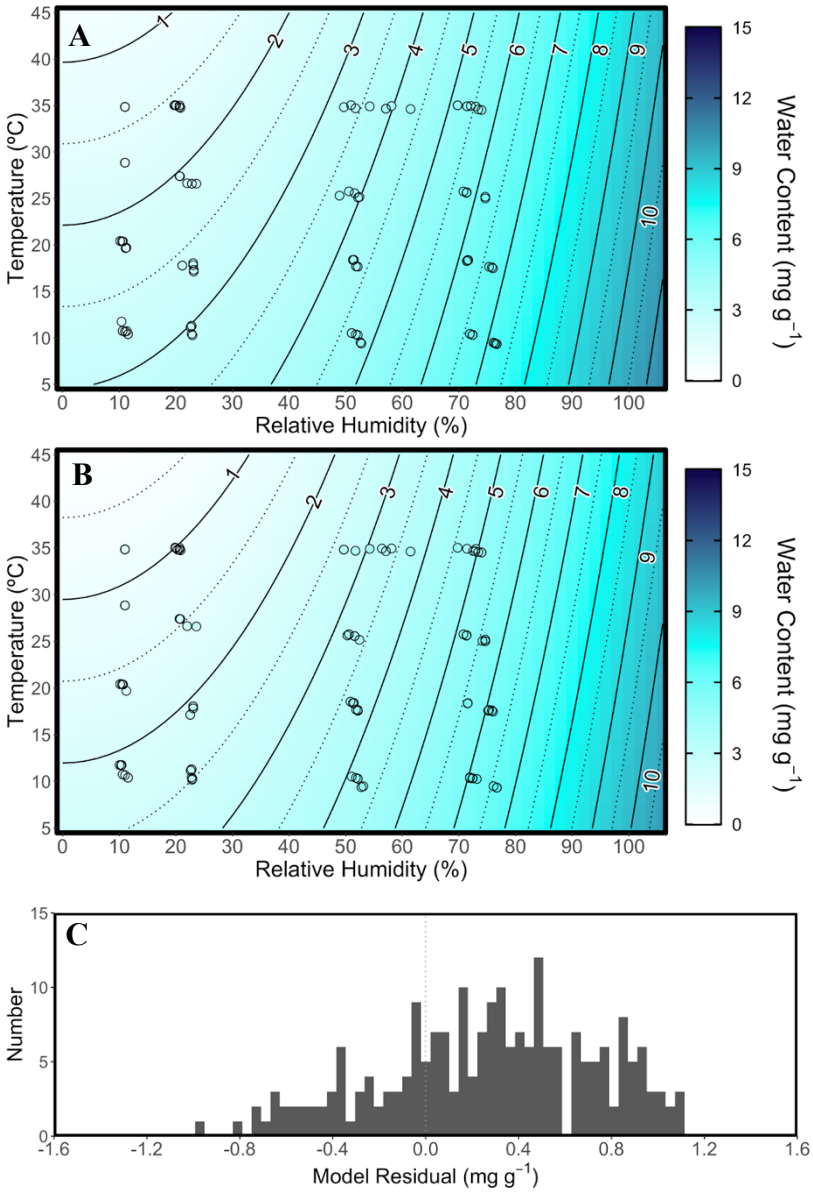

Figure 3.14: Measured (points) and modeled (contours) AWC for calcite at **A)** large grain size (SSA = 3.8 m^2 g^{-1}) and **B)** small grain size (3.1 m^2 g^{-1}). Both the measured and modeled water content use the same color scale. Panel **C)** shows the distribution of the model residuals for both SSAs. The RMSE of the distribution is 0.53 mg g^{-1}.

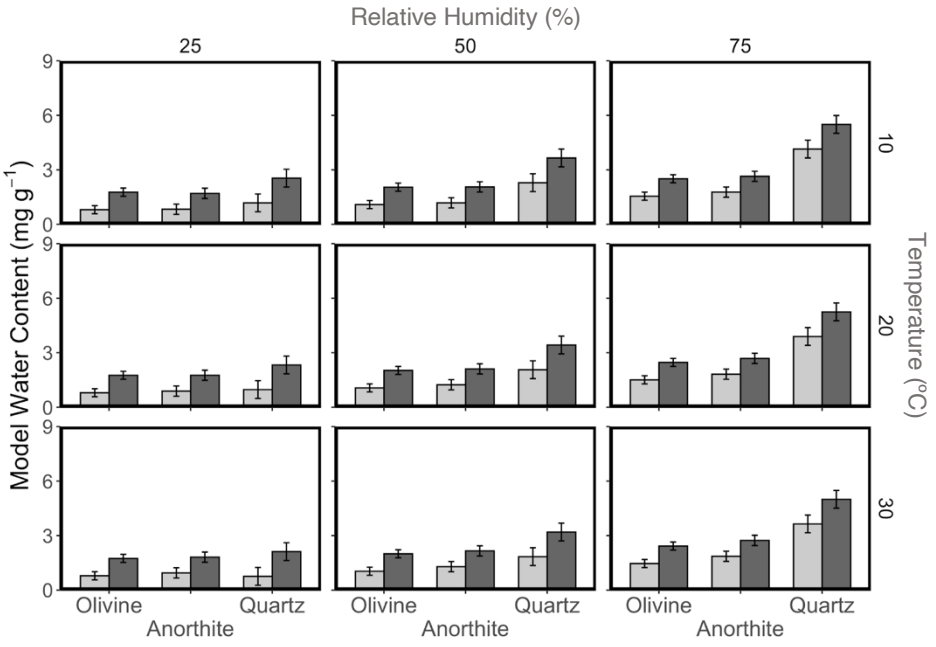

Figure 3.15: Modeled AWC for olivine, anorthite, and quartz at three RH (columns; 25, 50, & 75%RH), three T (rows; 10, 20, & 30ºC), and two SSA (colors; 1.5: light gray & 3.5 m^2 g^{-1}: dark gray). Error bars are model RMSE for the given mineral.

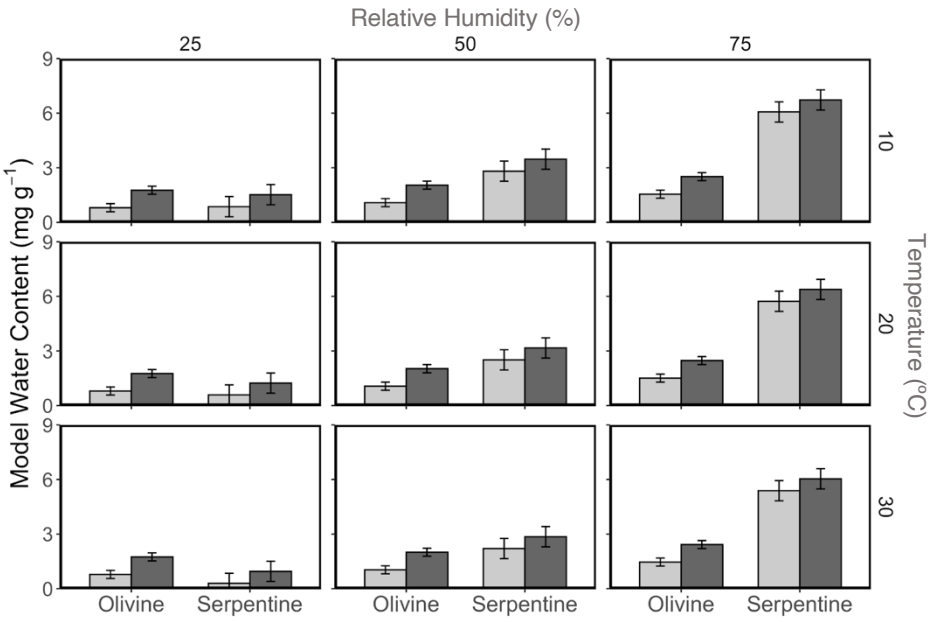

Figure 3.16: Model AWC for olivine and serpentine at three RH (columns; 25, 50, & 75%RH), three T (rows; 10, 20, & 30ºC), and two SSA (colors; 1.5: light gray & 3.5 m^2 g^{-1}: dark gray). Error bars are model RMSE for the given mineral.

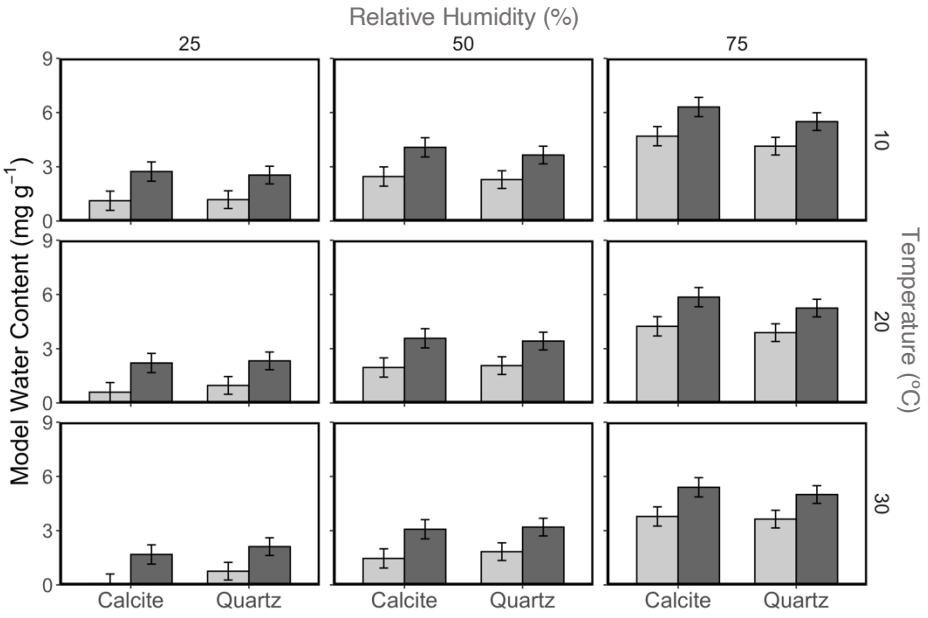

Figure 3.17: Model AWC for calcite and quartz at three RH (columns; 25, 50, & 75%RH), three T (rows; 10, 20, & 30ºC), and two SSA (colors; 1.5: light gray & 3.5 m^2 g^{-1}: dark gray). Error bars are model RMSE for the given mineral.

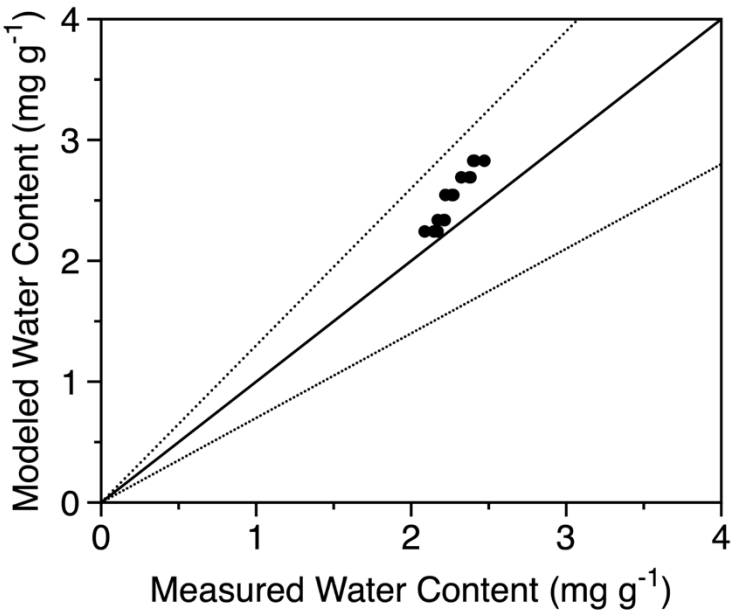

Figure 3.18: Measured and modeled AWC for the three mineral mixture sample replicates. The solid line is a 1:1 line and shows where the model is in agreement with laboratory measurements. The dotted lines show the model uncertainty (± 30%). These data are the results of six incubation periods where T is between 24.7 and 24.8ºC and RH is between 46 and 56%RH. The points lie within the field of uncertainty, indicating the model is reasonably estimating the measured AWC values. The points slightly deviate from the 1:1 line at higher RH (56%RH; upper right most points), but are in relatively good agreement at lower RH (46%RH; lower left most points). The model residuals range from -0.07 to -0.43 mg g^{-1}. Overall, this demonstrates the effectiveness of this approach of AWC estimation.

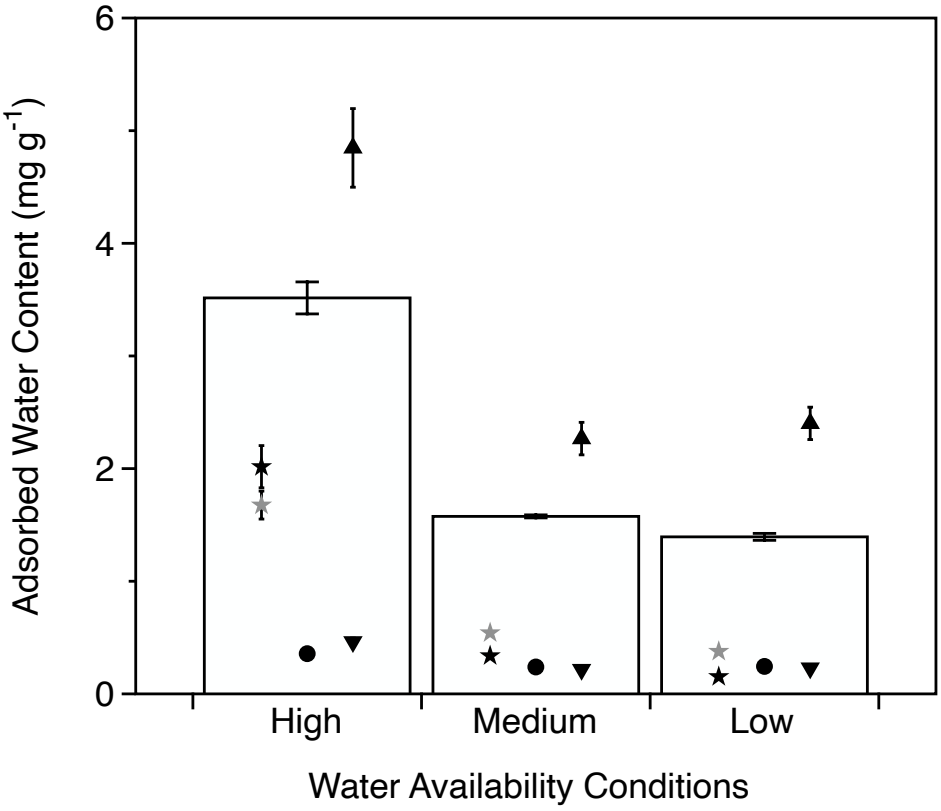

Figure 3.19: Measured (bar) and modeled (points) AWC for the MDQ natural soil. The different AWC models are: this model (stars), model A (dot), model B (upward triangle), and model C (downward triangle). The two approaches for the model are shown by color with black (bulk) and gray (separate). Error bars of measured data represent measurement uncertainty (1 standard deviation) and error bars on points represent propagated error from measurement uncertainty.

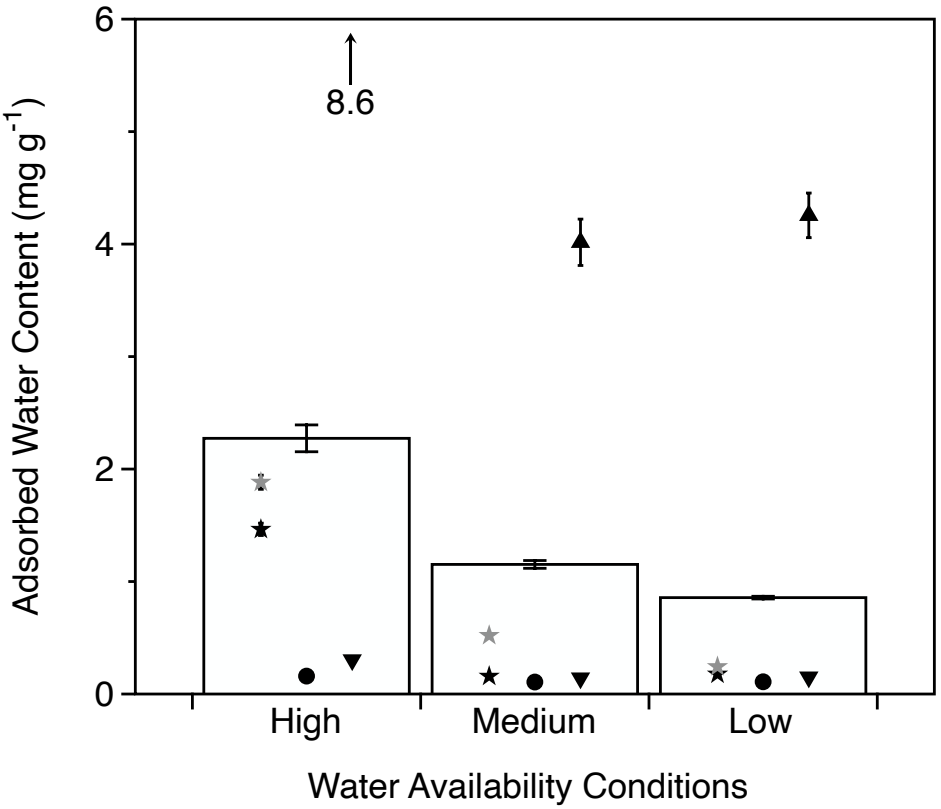

Figure 3.20: Measured (bar) and modeled (points) AWC for the LH natural soil. The different AWC models are: this model (stars), model A (dot), model B (upward triangle), and model C (downward triangle). The model C point for high water availability conditions is off the axis (as noted) at 8.6 mg g^{-1}. The two approaches for the model are shown by color with black (bulk) and gray (separate). Error bars of measured data represent measurement uncertainty (1 standard deviation) and error bars on points represent propagated error from measurement uncertainty.

CHAPTER 3 REFERENCES

AbdulHalim, R. G., Bhatt, P. M., Belmabkhout, Y., Shkurenko, A., Adil, K., Barbour, L. J., and Eddaoudi, M. (**2017**). A fine-tuned metal–organic framework for autonomous indoor moisture control. *Journal of the American Chemical Society*, *139*(31), 10715–10722. DOI: 10.1021/jacs.7b04132

Agam, N., and Berliner, P. R. (**2006**). Dew formation and water vapor adsorption in semi-arid environments—A review. *Journal of Arid Environments*, *65*(4), 572–590. DOI: 10.1016/j.jaridenv.2005.09.004

Allen, T. (**2013**). *Particle size measurement*. Springer.

Amer, A. M. (**2019**). Soil moisture adsorption capacity and specific surface area in relation to water vapor pressure in arid and tropical soils. *Eurasian Journal of Soil Science*, *8*(4), 289–297. DOI: 10.18393/ejss.580889

Anbazhagan, S., and Arivazhagan, S. (**2010**). Reflectance spectra of analog anorthosites: Implications for lunar highland mapping. *Planetary and Space Science*, *58*(5), 752–760. DOI: 10.1016/j.pss.2009.12.002

Arthur, E., Tuller, M., Moldrup, P., Jensen, D. K., and De Jonge, L. W. (**2015**). Prediction of clay content from water vapour sorption isotherms considering hysteresis and soil organic matter content: Clay content prediction from water vapour sorption. *European Journal of Soil Science*, *66*(1), 206–217. DOI: 10.1111/ejss.12191

Beck, P., Pommerol, A., Schmitt, B., and Brissaud, O. (**2010**). Kinetics of water adsorption on minerals and the breathing of the Martian regolith. *Journal of Geophysical Research*, *115*(E10), E10011. DOI: 10.1029/2009JE003539

Bhambhani, M. R., Cutting, P. A., Sing, K. S. W., and Turk, D. H. (**1972**). Analysis of nitrogen adsorption isotherms on porous and nonporous silicas by the BET and αs methods. *Journal of Colloid and Interface Science*, *38*(1), 109–117. DOI: 10.1016/0021-9797(72)90226-3

Campbell, G., and Shiozawa, S. (**1992**). Prediction of hydraulic properties of soils using particle-size distribution and bulk density data. *Indirect Methods for Estimating the Hydraulic Properties of Unsaturated Soils*, 317–328.

Chen, Y., Han, X., Wang, Y., and Lu, J. (**2020**). Precipitation of calcite veins in serpentinized harzburgite at Tianxiu hydrothermal field on Carlsberg ridge (3.67°N), northwest Indian ocean: Implications for fluid circulation. *Journal of Earth Science*, *31*(1), 91–101. DOI: 10.1007/s12583-020-0876-y

Fletcher, A. J., Uygur, Y., and Thomas, K. M. (**2007**). Role of surface functional groups in the adsorption kinetics of water vapor on microporous activated carbons. *The Journal of Physical Chemistry C*, *111*(23), 8349–8359. DOI: 10.1021/jp070815v

Frost, C. D., Frost, B. R., and Beard, J. S. (**2016**). On silica-rich granitoids and their eruptive equivalents. *American Mineralogist*, *101*(6), 1268–1284. DOI: 10.2138/am-2016-5307

Glaser, D. M., Hartnett, H. E., Finn, D. R., Perez-Montaño, S., Cadillo-Quiroz, H., and Desch, S. (**2022**). Water Vapor Adsorption Provides Daily, Sustainable Water to Soils of

the Hyperarid Atacama Desert. *Astrobiology*, *22*(10), 1222–1238. DOI: 10.1089/ast.2021.0171

Graf, D. L. (**1961**). Crystallographic tables for the rhombohedral carbonates. *American Mineralogist*, *46*(11–12), 1283–1316. DOI: 10.1007/BF03176144

Green, D. H., and Ringwood, A. E. (**1967**). The genesis of basaltic magmas. *Contributions to Mineralogy and Petrology*, *15*(2), 103–190. DOI: 10.1007/BF00372052

Hamilton, V. E., and Christensen, P. R. (**2005**). Evidence for extensive, olivine-rich bedrock on Mars. *Geology*, *33*(6), 433. DOI: 10.1130/G21258.1

Hecker, C., der Meijde, M. van, and van der Meer, F. D. (**2010**). Thermal infrared spectroscopy on feldspars—Successes, limitations and their implications for remote sensing. *Earth Science Reviews*, *103*(1–2), 60–70. DOI: 10.1016/j.earscirev.2010.07.005

Houben, H. (**1999**). The martian diurnal water cycle. *Advances in Space Research*, *23*(9), 1587–1590. DOI: 10.1016/S0273-1177(99)00174-X

Kaiser, K., and Guggenberger, G. (**2003**). Mineral surfaces and soil organic matter. *European Journal of Soil Science*, *54*(2), 219–236. DOI: 10.1046/j.1365-2389.2003.00544.x

Kosmas, C., Marathianou, M., Gerontidis, S., Detsis, V., Tsara, M., and Poesen, J. (**2001**). Parameters affecting water vapor adsorption by the soil under semi-arid climatic conditions. *Agricultural Water Management*, *48*(1), 61–78. DOI: 10.1016/S0378-3774(00)00113-X

Lane, M. D., and Christensen, P. R. (**2013**). Determining olivine composition of basaltic dunes in Gale Crater, Mars, from orbit: Awaiting ground truth from Curiosity. *Geophysical Research Letters*, *40*(14), 3517–3521. DOI: 10.1002/grl.50621

Leão, T. P., and Tuller, M. (**2014**). Relating soil specific surface area, water film thickness, and water vapor adsorption. *Water Resources Research*, *50*(10), 7873–7885. DOI: 10.1002/2013WR014941

Levien, L., Prewitt, C. T., and Weidner, D. J. (**1980**). Structure and elastic properties of quartz at pressure. *American Mineralogist*, *65*(9–10), 920–930.

Liu, L., Tan, S. (Johnathan), Horikawa, T., Do, D. D., Nicholson, D., and Liu, J. (**2017**). Water adsorption on carbon—A review. *Advances in Colloid and Interface Science*, *250*, 64–78. DOI: 10.1016/j.cis.2017.10.002

Mason, B. (**1963**). Olivine composition in chondrites. *Geochimica et Cosmochimica Acta*, *27*(10), 1011–1023. DOI: 10.1016/0016-7037(63)90062-0

McHugh, T. A., Morrissey, E. M., Reed, S. C., Hungate, B. A., and Schwartz, E. (**2015**). Water from air: An overlooked source of moisture in arid and semiarid regions. *Scientific Reports*, *5*(1). DOI: 10.1038/srep13767

Mellini, M. (**1982**). The crystal structure of lizardite 1T: hydrogen bonds and polytypism. *American Mineralogist*, *67*(5–6), 587–598.

Nelson Eby, G. (**2016**). *Principles of environmental geochemistry*. Waveland Press, Inc.

Nord, A. G., Annersten, H., and Filippidis, A. (**1982**). The cation distribution in synthetic Mg–Fe–Ni olivines. *American Mineralogist*, *67*(11–12), 1206–1211.

Ohtani, E. (**1983**). Formation of olivine textures in pallasites and thermal history of pallasites in their parent body. *Physics of the Earth and Planetary Interiors*, *32*(2), 182–192. DOI: 10.1016/0031-9201(83)90138-3

Peslier, A. H., and Bizimis, M. (**2015**). Water in Hawaiian peridotite minerals: A case for a dry metasomatized oceanic mantle lithosphere. *Geochemistry, Geophysics, Geosystems*, *16*(4), 1211–1232. DOI: 10.1002/2015GC005780

Resurreccion, A. C., Moldrup, P., Tuller, M., Ferré, T. P. A., Kawamoto, K., Komatsu, T., and de Jonge, L. W. (**2011**). Relationship between specific surface area and the dry end of the water retention curve for soils with varying clay and organic carbon contents: SOIL WATER CHARACTERISTIC CURVE. *Water Resources Research*, *47*(6). DOI: 10.1029/2010WR010229

Schumacher, B. A., Shines, K. C., Burton, J. V., and Papp, M. L. (**1990**). Comparison of Three Methods for Soil Homogenization. *Soil Science Society of America Journal*, *54*(4), 1187–1190. DOI: 10.2136/sssaj1990.03615995005400040046x

Shen, J. (**2020**). Phospholipid biomarkers in Mars-analogous soils of the Atacama Desert. *International Journal of Astrobiology*, *19*(6), 505–514. DOI: 10.1017/S1473550420000294

Srodoń, J., Drits, V. A., McCarty, D. K., Hsieh, J. C. C., and Eberl, D. D. (**2001**). Quantitative X-Ray diffraction analysis of clay-bearing rocks from random preparations. *Clays and Clay Minerals*, *49*(6), 514–528. DOI: 10.1346/CCMN.2001.0490604

Strydom, C. A., Hudson-Lamb, D. L., Potgieter, J. H., and Dagg, E. (**1995**). The thermal dehydration of synthetic gypsum. *Thermochimica Acta*, *269–270*, 631–638. DOI: 10.1016/0040-6031(95)02521-9

Sun, S. -s., and McDonough, W. F. (**1989**). Chemical and isotopic systematics of oceanic basalts: Implications for mantle composition and processes. *Geological Society, London, Special Publications*, *42*(1), 313–345. DOI: 10.1144/GSL.SP.1989.042.01.19

Tuller, M., and Or, D. (**2005**). Water films and scaling of soil characteristic curves at low water contents: Scaling of characteristic curves. *Water Resources Research*, *41*(9). DOI: 10.1029/2005WR004142

Valdivia-Silva, J. E., Navarro-González, R., Rosa, J. de la, and McKay, C. P. (**2012**). Decomposition of sodium formate and L- and D-alanine in the Pampas de La Joya soils: Implications as a new geochemical analogue to Martian regolith. *Advances in Space Research*, *49*(5), 821–833. DOI: 10.1016/j.asr.2011.12.012

Verhoef, A., Diaz-Espejo, A., Knight, J. R., Villagarcía, L., and Fernández, J. E. (**2006**). Adsorption of water vapor by bare soil in an olive grove in southern Spain. *Journal of Hydrometeorology*, *7*(5), 1011–1027. DOI: 10.1175/JHM556.1

Wenk, H. R., Joswig, W., Tagai, T., Korekawa, M., and Smith, B. K. (**1980**). The average structure of An 62–66 labradorite. *American Mineralogist*, *65*(1–2), 81–95.

Chapter 4

THE SEARCH FOR BIOLOGICAL ACTIVITY VIA TRACE GASSES UNDER TYPICAL WATER AVAILABILITY CONDITIONS IN SOILS FROM THE HYPERARID ATACAMA DESERT

4.1. Introduction

Microorganisms are highly adaptable and have evolved to survive in virtually all the harshest environments explored on Earth. Microorganisms colonize wide arrays of extreme environments: hot and acidic (Shock et al., 2010), dark and freezing (Bendia et al., 2018; Chan-Yam et al., 2019), 2 km below in the seafloor (Trembath-Reichert et al., 2017), and in hyperarid soils (Navarro-Gonzalez et al., 2003; Schulze-Makuch et al., 2018). There is an abundance of evidence that life can be found in - nearly - every explored corner of the planet with the exception of unique hydrothermal ponds in Ethiopia (Belilla et al., 2019). To survive in these harsh environments, microorganisms need to adapt and develop strategies to mitigate the effects of the environment to survive and reproduce.

Arid environments (i.e., deserts; defined as areas where evaporation > precipitation) are of particular importance as they represent roughly one third of all the landmass on Earth (Chiquoine et al., 2016; Safriel et al., 2005). Many types of life, ranging from microorganisms to plants and animals, have adapted to desert environments; for example, the saguaro cactus of the Sonoran Desert (in the US and Mexico) is emblematic of a rugged plant capable of living in a particularly dry environment. However, the harshness of the Sonoran pales in

comparison to the hyperarid regions of the Atacama Desert in Perú and Chile. The Atacama Desert is orders of magnitude drier than the Sonoran Desert, receiving an average of just ~2 mm of rain per year compared to ~190 mm in the southwest United States. The driest year on record in the Sonoran Desert was 2002; and the desert received about ~70 mm of rainfall. This is roughly the same amount that the Atacama received over the nearly ten years between 2008 and 2017 (~75 mm); notably that period included two of the wettest years on record in the Atacama (Azua-Bustos et al., 2018). The hyperarid regions of the Atacama, therefore, do not have plants and only the most well-adapted microorganisms are capable of colonization in what is thought to be near the limit of habitability (Azua-Bustos et al., 2012; Hall et al., 2012). The limit of habitability (here I am investigating habitability with respect to water availability) is a loosely defined term, theoretical in nature, that implies there is a dichotomic amount of environmental water that divides habitable and uninhabitable environments. We do not know how much water represents the limit of habitability, but we do know that even the driest environments on Earth are inhabited (Chan-Yam et al., 2019; Jacobson et al., 2015; Schulze-Makuch et al., 2018).

Many researchers have provided evidence for microbial colonization in the driest regions of the Atacama (Jones et al., 2018; Navarro-Gonzalez et al., 2003; Schulze-Makuch et al., 2018). We can infer a plethora of survival strategies; for example spore formation (Dose et al., 2001), endolithic structures (Vítek et al., 2016), and hypolithic distribution (Azúa-Bustos et al., 2011). From genomic data researchers have inferred the presence of many unique metabolic reactions such as trace gas scavenging that may provide an advantage for extremophilic microbes (Lynch et al., 2014).

The timing of biological activity may be another adaptation and survival strategy for hyperarid microorganisms. The paradigm of this environment is that many of the microorganisms are capable of sporulation, a process whereby the organism enters a dormant-like state, in response to harsh conditions, with little to no activity (Azua-Bustos et al., 2012; Schulze-Makuch et al., 2018). This state persists until the harsh conditions subside such as (in the case of the Atacama) rain or fog events that provide sufficient water for spores to germinate and for active cells to metabolize, grow, and reproduce. We have yet to determine the possibility of biological activity for the endemic microbial communities during typical conditions (i.e., without rain or fog) of water availability.

Rain and fog events are the primary source of condensed water in hyperarid environments. There is, however, evidence for potentially bioavailable, non-condensed water, in the form of water vapor adsorption (WVA), in these hyperarid soils as well (Glaser et al., 2022). Water vapor adsorption is an exceedingly small amount of water, roughly 1 - 3 monolayers of adsorbed water atoms at the surface of soil particles. However, the WVA process occurs nightly and provides a reliable, albeit very small, source of water (Glaser et al., 2022). It is possible that microorganisms have access to this small amount of water and may be able to support low levels of metabolic activity for maintenance energy between rain events. This chapter investigates the potential for biological activity under typical Atacama Desert conditions (i.e., without the presence of condensed water) by performing laboratory simulation experiments to measure changes in biologically relevant gas phase metabolites over time.

4.1.1. Target Gas Phase Metabolites

Life uses many different chemical species as metabolites that support the organism's energetic needs. Here I focus on four gas-phase metabolites (hydrogen, methane, carbon monoxide, and carbon dioxide) that can be used diagnostically to assess putative biologic activity.

4.1.1.1. Hydrogen-Based Metabolisms

Some chemolithoautotrophic soil microbes utilize H_2 as both an energy source and an electron source (Conrad, 1996). This energy source combined with an inorganic carbon source (CO_2) and catalyzed by a hydrogenase enzyme can fix carbon using this simplified reaction:

$$2H_2 + CO_2 \rightarrow 'CH_2O' + H_2O, \quad (4.1)$$

where 'CH_2O' is shorthand for organic carbon with a 1:2:1 ratio of carbon, hydrogen, and oxygen (i.e., biomass; Conrad, 1996; Lynch et al., 2014). Hydrogen can also be consumed, aerobically, in a partial reaction, creating energy to be used in other coupled reactions:

$$2H_2 + O_2 \rightarrow 2H_2O. \quad (4.2)$$

In both cases, I hypothesize that decreases in hydrogen concentration over time can be reasonably indicative of hydrogen-based biological activity since hydrogen is a reactant in these biological reactions.

4.1.1.2. Methane-Based Metabolisms

Methane is relatively common in biologically mediated reactions and there are reactions that both consume and produce methane.

4.1.1.2.a. Methanogenesis

Methanogenesis is a category of reactions that produce methane from either organic or inorganic carbon sources (Angel et al., 2011; Lyu et al., 2018; Serrano-Silva et al., 2014). The simplified reaction for methanogenesis from inorganic carbon (i.e., hydrogenotrophy) is written as:

$$CO_2 + 4H_2 \rightarrow CH_4 + 2H_2O. \quad (4.3)$$

Methanogenesis from an organic source is written as a simplified reaction:

$$CH_3COO^- + H^+ \rightarrow CH_4 + CO_2; \quad (4.4)$$

where I consider acetate as the substrate (Angel et al., 2011; Pan et al., 2016; Penning and Conrad, 2006).

4.1.1.2.b. Methanotrophy

Methanotrophy is a series of metabolic reactions that consume methane; the aerobic oxidation of methane is, simplified as:

$$CH_4 + 2O_2 \rightarrow CO_2 + 2H_2O. \quad (4.5)$$

In contrast to the case of hydrogen, the use of methane to assess biological activity is complex since methane can be both a reactant and a product in biological reactions. Changes in methane concentration over time may indicate biological activity, but quantification of the magnitude of biological activity is difficult since it is difficult to disentangle methanogenesis and methanotrophy. I hypothesize that any changes (increase or decrease) in methane over time can be reasonably indicative of methane-based biological activity.

4.1.1.3. Carbon Monoxide

Carbon monoxide is a reduced metabolite that is utilized similarly as H_2, the primary difference being that CO, is an electron source, energy source, and a carbon source (Conrad, 1996). Consumption of CO (or H_2) is also known as trace gas scavenging (Conrad, 1996; Ji et al., 2017). Most CO reactions are utilized as an energy and electron source similar to the half reaction:

$$CO + H_2O \rightarrow CO_2 + 2H^+ + 2e^-, \quad (4.6)$$

where the produced protons are utilized by a proton pump and the electrons are shuttled by electron transfer cofactors such as NADP. I hypothesize that decreases in carbon monoxide over time are reasonably indicative of CO-based biological activity.

4.1.1.4. Carbon Dioxide

Lastly, I highlight carbon dioxide, which is ubiquitous in biological reactions, both as a reactant such as in autotrophic photosynthesis:

$$CO_2 + H_2O \rightarrow 'CH_2O' + O_2, \quad (4.7)$$

and as a product such as in heterotrophic respiration and can be simplified as:

$$'CH_2O' + O_2 \rightarrow CO_2 + H_2O. \quad (4.8)$$

Similar to methane, carbon dioxide is both a reactant and product in biological reactions. I hypothesize that changes in carbon dioxide over time is a reasonable indication of biological activity. However, similar to the case of methane, quantification of biological rates may be impossible due to the entanglement of autotrophy and heterotrophy. I hypothesize that changes (increase or decrease) in carbon dioxide over time can be reasonably indicative of CO_2-based biological activity.

4.1.2. Rationale

Measurement of the four highlighted gas species will thus provide an assessment of the presence of a variety of metabolisms in these soils, both qualitatively (i.e., metabolic type) and quantitatively (i.e., metabolic rate). Hypothetically, there is a lower limit of water necessary to sustain life, in particular active life, which we can consider as the edge of habitability with respect to water availability. Evidence of biological activity under typical conditions would serve to change the paradigm of microbial life in hyperarid environments and would serve to broaden our definition of the edge of habitability under arid conditions (Schulze-Makuch et al., 2018; Wilhelm et al., 2018).

Here I consider measurement of four gas-phase analytes under typical hyperarid conditions (i.e., no condensed water addition) to assess biological activity: H_2, CH_4, CO, and CO_2. Each of these analytes can be interpreted as a product or reactant of a metabolic process and therefore changes in concentration of these analytes would be a strong indication of biological activity. I attempted to measure changes in biologically relevant gas phase metabolites *in situ* in the Atacama Desert with uninterpretable results, due to no discernable difference from the atmospheric background. The null results of the field experiments were attributed to *i)* chamber design flaws, *ii)* field instrumentation accuracy, and *iii)* difficulties with field logistics. Considering the *in situ* difficulties, soil samples were collected to replicate the experiment in a laboratory simulation to address and control the difficult factors from the field experiments. The experiments and results described in this chapter are the results of the laboratory simulation.

4.2. Materials & Methods

4.2.1. Site Description & Sample Collection

I performed field work in the Atacama Desert of Southern Perú, in September and October of 2017, and established field sites along a 55 km transect of an aridity gradient ranging from hyperarid to semiarid (Figure 4.1). The hyperarid end member of the aridity gradient was collected from the core of the Atacama Desert in a region known as *Pampas de la Joya* (~16.7ºS, 72.1ºW) and the semiarid end member was collected from a desert steppe-like environment in the rural outskirts of Arequipa, Perú (~16.4ºS, 71.7ºW). *Pampas de la Joya* is in a double rain shadow from the coastal mountains to the west and the Andes mountains to the east. This region receives an average of ~2 mm of rain per year, but often goes a full year without any measurable rain. There are rare fog events that can deposit small amounts of water, but, overall the environment is exceedingly dry. Arequipa, in contrast, is situated in the foothills of the Andean altiplano at an elevation of ~2300 m and receives ~100 mm of rain per year, mostly in the summer rainy season. The two sites are only separated by roughly 55 km, however, the aridity index (a ratio of precipitation to evaporation) gradient is steep ranging from <0.003 at *Pampas de la Joya* to 0.2 at Arequipa (Zomer et al., 2008).

Duplicate 300 g soil samples were collected, between 2 and 5 cm depth, from each site in October 2017 using a clean plastic spade and a clean sealable plastic bag. The plastic bag containing the soil sample was triple bagged to prevent contamination during transport. After transport, the soil was stored at room temperature in the dark prior to experimentation.

4.2.1.1. Soil Characterization

Gravel and cobble sized materials were removed from the soil prior to analysis using an ethanol cleaned 2 mm sieve and the resulting fine-earth fraction was used for both soil characterization and water addition experiments. Soil characterization was similar to that reported in chapter 2. Soil texture was determined using the hydrometer method to calculate sediment settling rates on 40 g of dry sample vigorously agitated in 5 weight percent (mass $mass^{-1}$; wt%) sodium hexametaphosphate solution (Day, 1965). Soil pH and conductivity were determined using a 1:2 (mass:mass) soil:deionized water mixture using a HACH HQ30d (Loveland, CO, USA) multimeter with PHC201 and CDC401 probes, respectively. Soil carbon and nitrogen were determined, with and without HCl fumigation, via high temperature combustion using a Costech ECS 4010 elemental analyzer on triplicate samples according to standard methods for low carbon soils (Hedges and Stern, 1984).

4.2.2. Experimental Design

I designed two experiments: dry (~5%RH air) and humid (~100%RH air) to simulate typical Atacama conditions (i.e., dry) and high humidity conditions, respectively, to assess biological activity as a function of water availability. Here, I consider water availability and adsorbed water (as described in chapters 2 & 3) as interchangeable terms since there is a clear relationship between relative humidity, adsorbed water, and soil water content (i.e., chapters 2 & 3). These experiments occurred serially with the dry experiment preceding the humid to reduce the manipulation and water contamination of the samples. This prevented the 'humid' experiment from influencing the dry experiment. Each experiment was incubated for 1248 hr (52 days) with eight headspace gas samples collected. The dry experiment had slightly different collection time points (0, 6, 12, 24, 72, 168, 576, 1248 hr)

compared to the humid experiment (0, 6, 18, 42, 114, 282, 618, 1248 hr); this was due to logistical issues with sampling. This sample design was intended to capture gas fluxes (changes over time) and ensure that changes during the first week of the incubation are captured in high temporal resolution.

4.2.2.1. Sample Preparation

Roughly 40 g of soil was added to autoclaved 60 mL serum bottles (Wheaton; NJ, USA); samples were prepared in a biosafety cabinet using 70% ethanol and UVC sterilized tools. I prepared 10 replicate bottles of intact soil from the hyperarid site for incubation along with 7 sterilized controls. Sterile controls consisted of hyperarid soils that were sterilized by baking the soils in a muffle furnace at 400ºC for 24 hr. Similarly, I prepared 5 bottles of intact soil from the semiarid site for incubation along with 5 sterile controls. All serum bottles were sealed using a blue butyl rubber stopper (Chemglass; NJ, USA) and aluminum crimp seals. In addition to the live and sterile samples; seven empty, negative control bottles were included to assess the seal of the bottles.

The sample bottles were prepared for the experiment by placing two 21-gauge needles (BD; NJ, USA), each equipped with a stopcock valve, through the stopper (Figure E.1A). Each valve was opened, and one valve (the inlet) was attached to a small, motorized pump that added air, at 1 L min^{-1} to the bottle from a 5 L jar filled with either drierite desiccant (dry experiment) or deionized water (humid experiment; Figure E.1B). A humidity sensor within the jar ensured that the output air was ±3%RH from target humidity. This system was allowed to flow for two minutes with gentle hand agitation of the soil to homogenize the sample bottle headspace. After two minutes an initial (0 hr) gas sample was collected; once all the 0 hr samples were collected, the sample bottles were placed in the dark at room

temperature (i.e., 22ºC) for the duration of the incubation. The headspace pressure of the bottle was nominally the same as atmospheric pressure (~1 atm).

4.2.2.2. Gas Sample Collection

Headspace gas samples were collected via 60 mL syringe (BD; NJ, USA) and stored in Cali-5-Bond foil gas sampling bags (Calibrated Instruments; MD, USA) prior to measurement. This was necessary because the number of samples collected (34) necessitated more time to measure on the gas chromatographs (~4 days) than the sampling process (~30 min). Prior to gas sample collection, each bag was flushed with UHP N_2 (99.999%) and evacuated three times. As an additional precaution to prevent gas bag leakage, each bag was observed to maintain vacuum for ≥24 hr prior to gas sample collection indicating a stable bag.

At each time point a headspace gas sample of 16 mL was collected using a 60 mL syringe and then placed in a sample collection bag. After gas sample collection, 16 mL of laboratory air was added back to maintain constant pressure (nominally 1 atm) within the sample bottle. Laboratory air samples were collected prior to and after sampling each day to quantify each atmosphere addition to the samples.

4.2.2.3. Gas Chromatography

Gas samples were measured as soon as possible after collection (typically within two weeks of collection). Quantification of the four analytes necessitated the use of two different gas chromatographs, one equipped with a reducing compound photometer (GC-RCP) and one with a flame ionization detector (GC-FID). The GC-RCP is tuned to detect H_2 and CO. The GC-FID has a methanizer and is tuned to detect CH_4 and CO_2. The gas samples were

measured serially, first by GC-RCP then by GC-FID. This procedure minimized the potential for gas leaks, specifically for H_2, as H_2 is a small molecule that is notoriously difficult to store in sample containers. Samples were injected into each instrument using a 250 μL (Hamilton; NV, USA) or 5 mL (SGE; Vic, AU) glass, gas-tight syringe for GC-RCP or GC-FID, respectively. For injection onto the GC-RCP, a small amount of deionized water was used in the syringe to occupy the dead space in the needle; this reduces carry over between samples and atmospheric contamination. For injection on the GC_FID, the syringe was first flushed with UHP N_2 prior to sample removal from the storage bag to prevent carry over and atmospheric contamination. Each instrument was calibrated on every measurement day, and blanks and check standards were measured roughly every 9 - 15 injections to identify possible instrument drift. A 5.5 ppm H_2 standard and 10 ppm CO standard (Praxair: Tempe, AZ, US) were used for GC-RCP calibration; and a 50 ppm CH_4 standard and 5000 ppm CO_2 standard (Praxair: Tempe, AZ, US) were used for GC-FID calibration. All reported concentration values are the results of 3 replicate injections. Duplicate sample measurements were performed once per day to ensure the reproducibility of measurements.

4.3. Results

4.3.1. Soil Characteristics

Overall, the two sites are similar in many measured parameters. Both the hyperarid and semiarid soils are generally a sandy loam texture with roughly 80% sand and 20% silt with minimal clay (Table 4.1). Both sites have circumneutral pH. The sites have different soil conductivity; the hyperarid site has a higher conductivity, 3.05 mS cm^{-1}, compared to 1.10 mS cm^{-1} at the semiarid site. The sites also differ in total carbon and organic carbon. The

hyperarid site has lower total carbon (0.020 wt%) and organic carbon (0.017 wt%) than the semiarid site (0.090 wt% and 0.081 wt%) for total carbon and organic carbon, respectively. Both sites have low inorganic carbon contents, 0.003 wt% for the hyperarid site and below detection at the semiarid site. Similarly, both sites have low nitrogen contents, 0.017 wt% and 0.013 wt% in the hyperarid and semiarid sites, respectively.

4.3.2. Gas Phase Measurements

4.3.2.1. Hydrogen

Hydrogen concentration measurements, ranging from 500 ppb to 20 ppm, over the course of 52 days in both experiments and for both sites are shown in figure 4.2. In both the dry (Figure 4.2A&B) and the humid experiments (Figure 4.2C&D), H_2 concentrations increase and decrease slightly over the course of the experiment; however, after 1248 hr most samples have roughly the same H_2 concentration they had at 0 hr. In contrast, the humid experiment (Figure 4.2C&D) exhibits very little change in H_2 concentration over the course of the experiments, with a few exceptions. There are a few samples with higher H_2 concentration at 42 hr and one with an increase in concentration at 282 hr. However, similar to the dry experiment, the concentrations at 0 and 1248 hr are roughly the same.

4.3.2.2. Methane

Methane concentration measurements for both sites and both experiments are shown in figure 4.3. In the dry experiment (Figure 4.3A&B), both sites show a general increase in concentration over the experiment duration. With the increase in concentration over time, there is also a large increase in the variability between samples and the range in concentration of the samples. Similar to H_2, there may be a hint of two sample populations: one high and

one low at 572 hr, however, the difference between the populations is much less distinct than in the case of H_2. The humid experiment (Figure 4.3C&D) shows little dynamics over the duration of the experiment, and concentrations are roughly the same at 0 and 1248 hr.

4.3.2.3. Carbon Monoxide

Carbon monoxide concentration measurements for both sites and both experiments are shown in figure 4.4. In the dry experiment (Figure 4.4A&B), both sites show two distinct populations at 1248 hr: less than or more than 6 ppm. The population greater than 6 ppm shows a steady increase in concentration from 72 hr to 1248 while the other population shows a roughly steady concentration over the same time period. The humid experiment (Figure 4.4C&D) shows a similar pattern to the dry experiment, the only noticeable difference being a generally lower concentration from 0 to 42 hr.

4.3.2.4. Carbon Dioxide

Carbon dioxide concentration measurements for both sites and both experiments are shown in figure 4.5. In the dry experiment (Figure 4.5A&B), both sites show a relatively constant concentration over the duration of the experiment. In the humid experiment (Figure 4.5C&D), the semiarid site shows some distinct sharp increases in two cases; these are likely outliers as the concentration sharply decreases to nominal levels on the next time point.

4.4. Discussion

4.4.1. Cumulative Gas Production

The time series data can reveal overall trends in gas concentrations, however, to accurately quantify the changes in an analyte over time, and compare across treatments, it is

necessary to convert from concentration to total moles in the bottle. This is necessary to correct for the atmosphere addition after the sample collection at each time point. The correction is a simple addition:

$$n_f = n_i + (n_a - n_s), \tag{4.9}$$

where n_f is the final number of moles, n_i is the initial number of moles, n_a is the number of moles of gas contributed by the atmosphere addition, and n_s is the number of moles removed due to sampling. To calculate these values, I employed the ideal gas law:

$$n = \frac{P \times \left(\frac{c}{10^6}\right) \times V}{R \times T} \times 10^6, \tag{4.10}$$

where n is the number of moles of analyte (μmol), P is pressure (0.996 atm), c is the measured concentration (ppm), V is volume (L), R is the gas constant (0.082057 L atm mol^{-1} K^{-1}), and T is temperature (K). To calculate each of the four values of n, I first calculate n_i using the measured concentration c, the bottle headspace volume, V, and the lab temperature at the time of sampling, T. Each sample bottle has a different headspace volume calculated using the total bottle volume, the sample porosity, and the mass of the soil sample. Each day of sampling, the lab temperature was recorded from an alcohol thermometer (Ward's Scientific; NY, USA). The added moles (n_a) were calculated using the atmosphere concentration (c), 16 mL (atmosphere addition volume) for V, and the lab temperature, T. The sampled moles (n_s) were calculated using the sample concentration for c, 16 mL (sample volume) for V, and the lab temperature for T. This process results in an initial and final number of moles for each time point. In simple terms, I subtract the final number of moles (at the previous time point) from the initial number of moles (at the current time point) to quantify the change in the number of moles between the two time points. I calculate the change in the number of moles between time points as:

$$\Delta n = n_i(t = k) - n_f(t = k-1)\,, \tag{4.11}$$

where k is the index term of timepoints (i.e., the kth timepoint).

4.4.1.1. Hydrogen

I hypothesize that if a hydrogen-based metabolism is active, hydrogen should be consumed (net negative cumulative production) over the experiment considering the reactions of equations 1 and 2 (Figure E.2A). In both cases, H_2 is a reactant, and H_2 concentrations should decrease over time. At the same time, hydrogen should not change in the sterile and negative control bottles.

4.4.1.1.a. Dry Conditions

A timeseries of cumulative H_2 production in the dry experiment for both sites is shown in figure 4.6 A&B. Both sites exhibit increasing H_2 concentrations until 168 hr; whereby cumulative H_2 production decreases to near zero by the end of the experiment. The hyperarid site (Figure 4.6A) shows a slight hint that there are two groups of results with one set of bottles that have positive H_2 production and one set with negative H_2 production. The semiarid site bottles all behaved similarly where cumulative H_2 at 1248 hr is between -0.02 and 0.02 μmol. The cumulative hydrogen production for both sites is displayed as a box and whisker plot in figure 4.6C&D to better compare treatment groups at the end of the experiment. I observe slightly positive H_2 production in the live (0.0028 μmol) and sterile (0.0066 μmol) hyperarid soils and slightly negative H_2 production in the live (-0.0020 μmol) and sterile (-0.0059 μmol) semiarid soils; however, in both cases the differences are not significantly different from zero. To determine the plausibility of hydrogen-based biological activity, it is necessary that the live and sterile treatment populations be significantly different

from each other. In both the case of the hyperarid and semiarid soils the results of a students' t test show that there are no significant differences ($p \geq 0.05$) between the live and sterile treatments (Table 4.2). Therefore, I adopt the null hypothesis that there is no measurable hydrogen-based biological activity under dry conditions.

4.4.1.1.b. Humid Conditions

A timeseries of cumulative H_2 production in the humid experiment for both sites is shown in figure 4.7A&B. Both sites show little H_2 production over the experiment duration. The hyperarid soil bottles (Figure 4.7A) shows interesting peaks in H_2 production at 42 hr that decrease back to nominal levels at 114 hr. There is a single bottle that has a significant increase to ~0.018 μmol at 282 hr, and the bottle remains above ~0.01 μmol until the end of the experiment. The semiarid soil bottles (Figure 4.7B) show little to no changes in cumulative H_2 production over the experiment duration. The cumulative hydrogen production for both sites is displayed as a box and whisker plot in figure 4.7C&D to better compare treatment groups at the end of the experiment. I observe slightly positive H_2 production in the live (0.0030 μmol) and sterile (0.0013 μmol) hyperarid soils as well as the live (0.00047 μmol) and sterile (0.0028 μmol) semiarid soils. The live and sterile treatments are all significantly different from zero, except for the live semiarid soils, however the magnitudes of all mean H_2 production values are exceedingly small. The values are likely significant from zero only due to the small range in measured values. To determine the plausibility of hydrogen-based biological activity, it is necessary that the live and sterile treatment populations be significantly different from each other. The semiarid live and sterile treatments are statistically similar and the hyperarid live and sterile treatments are significantly different (Table 4.2).

The finding in the hyperarid soils is interesting and warrants further scrutiny. The hydrogen production in the live and sterile hyperarid soils are significantly different, however, the live treatment and negative control bottles are statistically similar. This suggests that either *i)* diffusion or *ii)* the atmosphere additions may explain the H_2 production observed in the live hyperarid bottles. It is more likely that the atmosphere addition corrections, described in section 4.4.1, were not able to adequately account for the change in total moles due to measurement inaccuracies in *i)* volume, *ii)* pressure, or *iii)* temperature. In addition, I observe H_2 production in the live hyperarid bottles. This is contrary to my hypothesis of hydrogen consumption (i.e., trace gas scavenging) as an indication of biological activity. Considering these important caveats, it is necessary to adopt the null hypothesis of no measurable hydrogen-based biological activity under humid conditions.

4.4.1.2. Methane

The hypothesis for methane-based metabolism is more nuanced than for hydrogen. Because methane can both be produced and consumed, it is necessary to have additional context to assess the plausibility of biologic activity. Methane production in methanogenesis is coupled with H_2 and CO_2 consumption, so any methane production from methanogenesis should coincide with 1:1 consumption of CO_2 and 1:4 consumption of H_2 (see equation 4.2; Figure E.2B). Thus, in order to conclude there is biological production of methane I expect to see CH_4 production along with consumption of both H_2 and CO_2.

4.4.1.2.a. Dry Conditions

A timeseries of cumulative CH_4 production in the dry experiment for both sites is shown in figure 4.8A&B. Both sites show similar magnitudes of CH_4 production over the

experiment duration, particularly between 576 and 1248 hr. The cumulative CH_4 production for both sites is displayed as a box and whisker plot in figure 4.8C&D to better compare treatment groups after the experiment. There is positive production in all cases. I observe CH_4 production in the live (0.020 μmol) and sterile (0.041 μmol) hyperarid soils as well as the live (0.030 μmol) and sterile (0.025 μmol) semiarid soils. The live and sterile treatments are all significantly different from zero. To determine the plausibility of methane-based biological activity, it is necessary that the live and sterile treatment populations be significantly different from each other. The results of a students' t test shows that both pairs of live and sterile bottles are statistically similar (Table 4.3). Therefore, I fail to reject the null hypothesis, and I determine that there is no measurable methane-based biological activity in the dry experiment.

4.4.1.2.b. Humid Conditions

A timeseries of cumulative CH_4 production in the humid experiment for both sites is shown in figure 4.9A&B. Both sites show similar trends over time of cumulative CH_4 production. In the hyperarid site between 618 and 1248 hr it is clear that the highest production bottles are live treatment samples (Figure 4.9A). The cumulative CH_4 production for both sites is displayed as a box and whisker plot in figure 4.9C&D to better compare treatment groups after the experiment. I observe CH_4 production in the live (0.0069 μmol) and sterile (0.0037 μmol) hyperarid soils as well as the live (0.0062 μmol) and sterile (0.0061 μmol) semiarid soils. The live and sterile treatments are all significantly different from zero indicating net production over the experiment. To determine the plausibility of methane-based biological activity, it is necessary that the live and sterile treatment populations be significantly different from each other. In the case of the semiarid soil, the live and sterile

treatments are statistically similar. However, in the hyperarid soil, the live production is statistically different when compared to both the sterile and negative controls (Table 4.3). This result allows me to reject the null hypothesis and suggests the plausibility of methane-based biological production in the humid treatment which I discuss in depth in section 4.4.2.

4.4.1.3. Carbon Monoxide

Carbon monoxide, similar to hydrogen, is a reduced gas that is utilized by microorganisms as an electron and energy source. Therefore, I expect carbon monoxide concentrations to decrease over time if there is biological activity (net negative cumulative production; Figure E.2C). Similarly, I expect the sterile and negative controls to remain near zero cumulative production.

4.4.1.3.a. Dry Conditions

A timeseries of cumulative CO production in the dry experiment for both sites is shown in figure 4.10A&B. Both sites show a similar trend of increasing CO production over the experiment duration, particularly after 168 hr. There is clear separation over time between the live and other bottles in both soils, with the live bottles having a higher cumulative production. The cumulative CO production for both sites is displayed as a box and whisker plot in figure 4.10C&D to better compare treatment groups after the experiment. There is positive production in all cases. I observe CO production in the live (0.021 μmol) and sterile (0.0016 μmol) hyperarid soils as well as the live (0.017 μmol) and sterile (0.0082 μmol) semiarid soils. All treatments are significantly different from zero. To determine the plausibility of carbon monoxide-based biological activity, it is necessary that the live and sterile treatment populations be significantly different from each other. The results of a

students' t test shows that both pairs of live and sterile bottles are significantly different from each other (Table 4.4). The difference between the live and sterile treatments is interesting and would suggest a biological mechanism, however, my hypothesis for CO metabolism is a net negative cumulative production over time. This unexpected observation of CO production is discussed later in this section.

4.4.1.3.b. Humid Conditions

A timeseries of cumulative CO production in the humid experiment for both sites is shown in figure 4.11A&B. Similar to the dry experiment, both sites show a trend of increasing CO production over the experiment duration, particularly after 282 hr. Again, there is clear separation over time between the live and other bottles in both soils, with the live bottles having a higher cumulative production. The cumulative CO production for both sites is displayed as a box and whisker plot in figure 4.11C&D to better compare treatment groups after the experiment. There is positive production in all cases and the magnitudes are similar to the dry experiment. The CO production in the live (0.019 μmol) and sterile (0.0061 μmol) hyperarid soils as well as the live (0.015 μmol) and sterile (0.0098 μmol) semiarid soils. All treatments are significantly different from zero. The results of a students' t test shows that both pairs of live and sterile bottles are significantly different from each other (Table 4.4). The differences between live and sterile treatments are intriguing, however, they require a high level of scrutiny which are detailed in the next section.

4.4.1.3.c. Plausible Carbon Monoxide Production in Soils?

Cumulative carbon monoxide production over the experiment duration is certainly an unexpected result, as I did not account for this scenario in either my hypothesis (net negative

cumulative CO production) or the null hypothesis (no net cumulative CO production). Carbon monoxide production results have been observed previously and are not interpreted to be a reaction mediated by microorganisms (Conrad and Seiler, 1985; Gödde et al., 2000). Carbon monoxide production in soils is attributed to two main abiotic oxidation processes: chemical and photo. These two processes are correlated with soil organic content. In the case of my experiments, the mechanism of CO production is likely chemical as the samples were stored in the dark during incubation, precluding photooxidation. Conrad and Seiler (1985) describe similar results (from fine-grained soils) where chemical oxidation, via a radical autoxidation mechanism, of organic matter produced CO in sterile controls (Nanni et al., 1980). Considering that the cumulative CO production observed here (~0.02 μmol) is many orders of magnitude lower than the available organic carbon content (~80 mmol), it is plausible that the CO source is abiotic oxidation of a small fraction of the organic carbon pool. I also observed a slightly higher (not significant) CO production in the semiarid samples, which is in agreement with previous observations that the magnitude of CO production is correlated with soil organic content (Conrad and Seiler, 1985; Gödde et al., 2000)

Notably, I do not observe equivalent CO production in the sterile controls as would be expected with an abiotic reaction. This is very likely due to the method of sterilization, i.e., heating to 400ºC in a muffle furnace, which is sufficient to thermally oxidize the soil organic carbon to CO_2. Therefore, the sterile controls samples did not have a pool of organic carbon to oxidize, which is in agreement with my interpretation of abiotic chemical oxidation. Considering my results and previous observations it is likely that the cumulative CO production observed here is abiotic due to chemical oxidation (Conrad and Seiler, 1985).

4.4.1.4. Carbon Dioxide

Carbon dioxide as a metabolite is ubiquitous in biological reactions and the two most predominant metabolisms in the biosphere either consume (primary production; equation 4.7) or produce (heterotrophy; equation 4.8) CO_2. In fact, CO_2 is involved in most other metabolic reactions noted here including equations 4.1, 4.3, 4.4, 4.5, and 4.6. Measurement of CO_2 concentrations over time is used in many systems to indicate the relative magnitudes of primary production and respiration. For example, decreasing CO_2 indicates that rates of primary production > heterotrophy and vice versa. Alone, changes in CO_2 are not especially diagnostic, but it is indicative of biological activity (Figure E.2D). However, changes in CO_2 can provide important additional context for other metabolites: in this case H_2, CH_4, and CO.

4.4.1.4.a. Dry Conditions

Cumulative CO_2 production over time in the dry experiment is shown in figure 4.12A&B. Note that the cumulative production observed in CO_2 is roughly two orders of magnitude higher than the other analytes, likely due to the relatively higher ambient CO_2 concentrations. Both sites show a similar trend of roughly constant CO_2 production over the experiment duration, with a slight hint of an increase between 576 and 1248 hr. The cumulative CO_2 production for both sites is displayed as a box and whisker plot in figure 4.12C&D to better compare treatment groups after the experiment. I observe CO_2 production in the live (0.71 μmol) while the sterile controls show little to no production (0.040 μmol) in the hyperarid soils. The semiarid soils show similar results in the live (0.69 μmol) and sterile (0.053 μmol) treatments. In both cases, the sterile controls are statistically similar to zero and the live treatments are significantly different from zero. To determine the

plausibility of carbon dioxide-based biological activity, it is necessary that the live and sterile treatment populations be significantly different from each other. The results of a students' t test shows that the semiarid live and sterile bottles are statistically similar (Table 4.5). The hyperarid live and sterile bottles are statistically significant from each other, however, the live and negative control are statistically similar (Table 4.5). This suggests there is an abiotic explanation for the CO_2 production observed in the live hyperarid soils: likely unaccounted for variations during the atmosphere correction.

4.4.1.4.b. Humid Conditions

Cumulative CO_2 production over time in the dry experiment is shown in figure 4.13A&B. There is a negative control that had a sharp decrease of ~5 μmol in the first interval (6 hr), which is highly abnormal (Figure 4.4C). The anomalous control has a CO_2 concentration, at 0 hr, three times higher than the next most concentrated negative control (Figure E.3). This behavior is likely due to sampling errors and contamination during the 0 hr timepoint. Considering these factors, I have chosen to omit the anomalous negative control from discussion. Similarly, there is a live sample that shows anomalously high CO_2 concentrations at 6 hr as annotated in figure 4.5E. This single measurement is the most concentrated in either experiment and is roughly 50% higher than the next most concentrated measurement (Figure E.4). Considering this I have decided to omit this single live sample from the CO_2 analysis, as the high concentration is likely from contamination from sampling.

Both sites show a similar trend of roughly constant CO_2 production over the experiment duration. The cumulative CO_2 production for both sites is displayed as a box and whisker plot in figure 4.13C&D to better compare treatment groups after the experiment. The CO_2

production in the humid experiment shows an opposite trend than the dry; where sterile controls (0.97 μmol) have higher production than the live (0.055 μmol) in the hyperarid soil. The semiarid soils show slight CO_2 consumption (negative production) in both the case of the live (-0.017 μmol) and sterile (-0.16 μmol) bottles. In the semiarid soils, both the live and sterile bottles are statistically similar to zero; and in the hyperarid soils the live bottles are similar to zero whereas the sterile bottles are significantly different from zero (Table 4.5). The results of a students' t test shows that the semiarid live and sterile bottles are statistically similar (Table 4.5). Conversely, the hyperarid live and sterile bottles are significantly different from each other (Table 4.5). This indicates the plausibility of carbon dioxide-based biological activity in the hyperarid soils, and I will consider these results collectively along with the H_2, CH_4, and CO results to assess biological activity.

4.4.2. Putative Microbial Activity in Atacama Soils

The most informative analyte that shows significant, metabolically plausible changes in the live samples but not in the controls is methane in the hyperarid soil during the humid water availability experiment (see section 4.4.1.2.b). Here I investigate the differences in plausible biological methane production across the two water availability conditions (i.e., dry and humid) and the two sites (i.e., hyperarid and semiarid; Figure 4.14). I also consider the observed CH_4 production in concert with the production (or consumption) of the other three analytes (H_2, CH_4, and CO). To do this, it is necessary to sterile-correct the live production using the sterile control production. This has the effect of accounting for and correcting any abiotic reactions that may be occurring. I calculate the difference between live and sterile, as sterile-corrected production, by subtracting the mean sterile production from each live production value:

$$CP_i = cumulative\ live\ production_i - mean_{sterile}, \quad (4.12)$$

where CP_i is the sterile-corrected production and i is the measurement index (i.e., a list of i sterile-corrected production values).

4.4.2.1. Methane Production as a Function of Water Availability

The significant methane production observed in the hyperarid soil under humid conditions is interesting and it is reasonable to expect that biological activity will increase with water availability. Putative biological methane production (i.e., sterile-corrected production) for the dry and humid conditions is shown in figure 4.15. The differences in plausible metabolic methane production between the experimental conditions are not significant ($p > 0.05$) due to the large range in values, particularly in the dry experiment. The range in values decreases noticeably between the dry and humid experiments. Since these experiments were performed serially (first dry, then humid), it is possible that improved experimental and analytical techniques significantly reduced the range of values. Overall, there may be a difference between the experimental conditions, however, the statistical insignificance between the dry and humid methane production prevents any definitive interpretation. Here I fail to reject the null hypothesis and conclude that water availability shows no effect on the magnitude of methane production in hyperarid soils.

4.4.2.2. Methane Production as a Function of Soil Climate

It is reasonable to expect that any measurable activity will be higher at the semiarid site as, presumably, there is more biomass at this site. However, I observe a noticeably higher putative biological methane production at the hyperarid site compared to the semiarid site; and the results of a student's t test confirm the difference is significant ($p < 0.05$; Figure

4.16). This counterintuitive observation deserves further investigation. Microbiological techniques, such as 16s rRNA sequencing, characterizing the microbial community in these soils could provide necessary context for these results. However, these soils are difficult to extract cells from due to low cell concentrations; anecdotally, I was only able to extract ~20 ng of DNA from roughly 40 g of hyperarid soil (unpublished results). This amount of DNA is almost insufficient for PCR amplification. I, however, can form a hypothesis for future work based on these results.

4.4.2.3. Simultaneous Methanogenesis and Methanotrophy

There are many examples of environments where methanogenesis and methanotrophy have been documented to coexist, typically at the interface of anoxic and oxic environments (Serrano-Silva et al., 2014; Wendlandt et al., 2010). Here I explain my assertion that there is not simultaneous methanogenesis and methanotrophy.

The effort to disentangle methanogenesis and methanotrophy has been ongoing for decades, primarily to constrain global climate change models as CH_4 is an important greenhouse gas (O'Connor et al., 2010). Using the data collected here, I can consider simultaneous CH_4 production and consumption using H_2 and CO_2. There are two cases I can consider: methanogenesis from inorganic or organic sources.

First, I consider methanogenesis from inorganic sources as summarized in equation 4.3, and when this reaction is combined with equation 4.5, I can write the net reaction as:

$$O_2 + 2H_2 \rightarrow 2H_2O. \quad (4.13)$$

Therefore, if there were simultaneous inorganic methanogenesis and methanotrophy occurring, I would expect to see net consumption (negative production) of H_2 as shown in equation 4.13. Hydrogen production in the hyperarid soils of the humid experiment is

shown in figure 4.7C and using equation 4.13 I calculate a sterile-corrected hydrogen production shown in figure 4.17A. Here I observe slightly positive production, roughly 0.0017 μmol. This result does not support the interpretation of simultaneous inorganic methanogenesis and methanotrophy as I would expect hydrogen consumption as opposed to an increase, as observed.

Lastly, I consider methanogenesis from organic sources (e.g., equation 4.4). Combining this reaction with methanotrophy yields the net reaction as:

$$CH_3COO^- + H^+ + 2O_2 \rightarrow 2CO_2 + 2H_2O. \quad (4.14)$$

In this case, if methanogenesis and methanotrophy are occurring simultaneously, I would expect net production of CO_2 as shown in equation 4.14. Carbon dioxide production of the hyperarid soils in the humid experiment is shown in figure 4.13C; and using equation 4.12 I can calculate sterile-corrected carbon dioxide production which is shown in figure 4.17B. Here I observe negative production (consumption) with a median of -0.92 μmol. Similar to the case of H_2, this result does not support the interpretation of simultaneous organic methanogenesis and methanotrophy because I expect CO_2 production.

4.4.2.4. Observed Methane Production Rates

The putative biological methane production observed in the hyperarid soils during the humid experiment is a median 6.9 nmol. Here I will compare the production of other known CH_4 producing environments to the CH_4 produced in this experiment to test the plausibility of a biological origin of CH_4. Angel et al. (2011) performed similar laboratory incubation experiments with arid biological soil crust samples. They observe CH_4 production in their analogous experiments at a rate of 200 nmol g^{-1} dry weight over a 42 day incubation period which simplifies to 4.8 nmol day^{-1} g^{-1} dry weight (Angel et al., 2011). In comparison, the CH_4

production observed in these experiments is 0.003 nmol day^{-1} g^{-1} dry weight, which is roughly three orders of magnitude lower than reported by Angel et al. (2011). It is expected that my experiments would be lower due to the differences in *i)* microbial communities and *ii)* water availability. I did not characterize the microbial community of these soils, but similar hyperarid Atacama soils have been characterized to be low in overall biomass and community diversity (Fernández-Martínez et al., 2019; Schulze-Makuch et al., 2018). Biological soil crusts in comparison are relatively high in biomass and have diverse microbial communities (Garcia-Pichel et al., 2003). The experiments performed by Angel et al. (2011) also contained liquid water addition, which would likely have the effect of increased production compared to my experiments without condensed water. Considering the differences in sample and experimental water addition my CH_4 production rates are plausibly biological in origin. Dryland systems, in general, are thought to be net sinks (consumption > production) of atmospheric methane; therefore my finding necessitates further investigation (Singh et al., 1998).

4.4.3. Hypothesis for Future Work

I expect that the microbial community in the hyperarid site is well-adapted to surviving long periods of time, sometimes more than a year, without measurable water input. This lack of water creates high evolutionary pressure to adapt and exploit any available water resources. High humidity events, such as fog, occur roughly 10 times per year in the hyperarid regions of the Atacama (McKay et al., 2003; Valdivia-Silva et al., 2012a). I hypothesize that the microbial community is adapted to take advantage of these conditions and methanogenesis, while a relatively low energy production metabolism, may be sufficient for biological maintenance requirements between rain events (Borch et al., 2010; Serrano-

Silva et al., 2014). This result is not unprecedented, as there are observations on hydrogenotrophic methanogenesis in oxic, desert soils (Angel et al., 2011).

Conversely, at the semiarid site, the water availability conditions are slightly less extreme. There is, therefore, not as great a pressure to adapt. The semiarid site, outside Arequipa, Perú, is similar in aridity to the Phoenix, Arizona area (though the temperatures are more moderate in Arequipa), receiving several rain events per year. The rain events in Arequipa, as in Phoenix, are typically associated with large, monsoon-like conditions that produce large amounts of water in a brief period of time. I therefore hypothesize that microorganisms at the semiarid site are not adapted to metabolize under fog-like conditions. Endemic microbes present at the semiarid site may be able to meet all their metabolic needs without resorting to methanogenesis. It may be more advantageous for the semiarid microbes to 'wait' for a rain event and use aerobic heterotrophy, rather than use methanogenesis during a fog event. This hypothesis requires investigation into the microbial populations at both sites in order to identify genes that encode enzymes associated with methanogenesis such as methyl-coenzyme M reductase or acetyl CoA synthase (Berghuis et al., 2019; Serrano-Silva et al., 2014). Presence of these genes in the hyperarid site and absence in the semiarid site would reinforce the results found here. It is also possible to perform similar experiments, but with isotope tracers such as D_2 ($^2H_2$) and $^{13}CO_2$. This approach would be able to identify the mechanism of methane production by measuring the δ^2H and $\delta^{13}C$ of the resulting methane using isotope ratio mass spectrometry (Douglas et al., 2017). Measurement of $^{13}CH_4$, CH_3D, or any other methane isotopologues would be strong evidence of biological activity.

4.5. Summary & Implications

4.5.1. Summary

The experiments described here were designed to assess the presence of metabolic activity in soils collected from the Atacama Desert across a rainfall gradient. Specifically, the biological production or consumption of hydrogen, methane, carbon monoxide, and carbon dioxide as a function of water availability in soils representing two different climate conditions. Admittedly, it was difficult to determine the biogenicity of biological signals with any certainty.

4.5.1.1. CO Production is Likely Abiotic Chemical Oxidation

Carbon monoxide production, as shown in figures 4.10C&D and 4.11C&D, was an unexpected result of the experiments. The production of CO in the live treatments is likely due to abiotic chemical oxidation, a process attributed to an autooxidation mechanism (Conrad and Seiler, 1985; Gödde et al., 2000). Further investigation is necessary to distinguish simultaneous biological CO consumption from abiotic CO production.

4.5.1.2. Fog or High Humidity may Stimulate Methane Production in Hyperarid Sites

This study shows reasonably plausible evidence that the hyperarid soils in the Atacama Desert may be capable of biological methane production under high humidity conditions (Figure 4.9C). This is in reasonable agreement with previous studies of desert soils that exhibit biological production of methane, even in a highly oxidized environment such as an unsaturated soil (Angel et al., 2011). My observations suggest the microbes of the hyperarid Atacama Desert may plausibly exploit rare fog events for energy production through

methanogenesis. Further investigation with genomic or isotope tracer approaches is necessary to support this interpretation.

4.5.2. Implications

The experiments described here were designed to assess microbial activity in arid soils with little manipulation, particularly without the addition of condensed water. These conditions are quite extreme and are, most likely, the most rigorous approach to identify microbial activity under typical hyperarid conditions. Even the conditions of the humid experiment are relatively extreme. They do not add condensed water, but rather only increase humidity similar to a fog event, however, in the case of the experiment there was no condensed water as is typically deposited during fog events.

4.5.2.1. High Humidity Events Stimulate Methanogenesis in Hyperarid Environments

These results provide reasonable evidence for fog-induced methanogenesis in the hyperarid Atacama Desert. If these results could be confirmed as microbial activity, it suggests that the microbes of the Atacama Desert may be more active than previously thought; as the current paradigm is microbial dormancy between rain events (Schulze-Makuch et al., 2018). Moreover, because the experiment did not provide condensed water, it is plausible that any high humidity (roughly above 95%RH) event - not just fog - could stimulate the production observed here.

The results described here may prove to be important to the carbon cycle in drylands, particularly in hyperarid deserts. Over a third of Earth's landmass is considered drylands, and roughly a quarter of the drylands area is hyperarid (Chiquoine et al., 2016; Safriel et al., 2005; Zomer et al., 2008). Despite the low rates reported here, the large area of hyperarid

environments may prove to be an important source or sink of carbon, particularly in the face of global warming. These results may also provide important context for the search for life elsewhere, as these results suggest that Earth-like microbes may be capable of active metabolism at water availabilities lower than previously thought.

Table 4.1. Hyperarid and semiarid soil properties. All results are the average of two duplicate sample measurements.

Parameter	Hyperarid	Semiarid
Sand (wt%)	79.5 ± 0.3	78.3 ± 0.9
Silt (wt%)	16.75 ± 1.55	21.7 ± 0.9
Clay (wt%)	3.75 ± 1.25	0 ± 0
pH	6.46 ± 0.19	6.7 ± 0
Conductivity (mS $cm^{-1)}$	3.05 ± 0.55	1.1 ± 0.2
Total Carbon (wt%)	0.02 ± 0.001	0.0895 ± 0.0065
Organic Carbon (wt%)	0.0165 ± 0.0015	0.0805 ± 0.0075
Inorganic Carbon (wt%)	0.00305 ± 0.00035	BDL ± 0.005
Total Nitrogen (wt%)	0.0165 ± 0.0025	0.0125 ± 0.0005

BDL: Below detection limit

Table 4.2. Summary of cumulative hydrogen production across the two variables. Median production is in units of μmol. Comparison values are the results of a students' t test comparing to other treatments or to zero.

Experiment	Site	Treatment	Median Production	Comparison			
				Live	Sterile	Negative	Zero
Dry	Hyperarid	Live	0.0028	1	0.991	0.052	0.176
		Sterile	0.0066	–	1	0.174	0.460
		Negative[d]	-0.0054	–	–	1	0.174
Dry	Semiarid	Live	-0.0020	1	0.926	0.822	0.105
		Sterile	-0.0059	–	1	0.822	0.518
		Negative[d]	-0.0054	–	–	1	0.174
Humid	Hyperarid	Live	0.0030	1	0.041*****	0.054	0.002*****
		Sterile	0.0013	–	1	0.826	0.010*****
		Negative[h]	0.0013	–	–	1	0.009*****
Humid	Semiarid	Live	0.0005	1	0.111	0.614	0.207
		Sterile	0.0028	–	1	0.075	0.002*****
		Negative[h]	0.0013	–	–	1	0.009*****

*****Statistically significant ($p < 0.05$)

[d][h] There was only one set of negative controls per experiment. They are separated for ease of comparison to live and sterile treatments.

Table 4.3. Summary of cumulative methane production across the two variables. Median production is in units of μmol. Comparison values are the results of a students' t test comparing to other treatments or to zero.

Experiment	Site	Treatment	Median Production	Comparison			
				Live	Sterile	Negative	Zero
Dry	Hyperarid	Live	0.0204	1	0.159	0.506	0.002*****
		Sterile	0.0144	–	1	0.076	0.001*****
		Negative[d]	0.0273	–	–	1	0.006*****
Dry	Semiarid	Live	0.0295	1	0.376	0.761	0.007*****
		Sterile	0.0250	–	1	0.297	0.039*****
		Negative[d]	0.0273	–	–	1	0.006*****
Humid	Hyperarid	Live	0.0069	1	0.025*****	0.000*****	0.000*****
		Sterile	0.0037	–	1	0.015*****	0.017*****
		Negative[h]	-0.0015	–	–	1	0.469
Humid	Semiarid	Live	0.0062	1	0.964	0.006*****	0.016*****
		Sterile	0.0061	–	1	0.002*****	0.006*****
		Negative[h]	-0.0015	–	–	1	0.469

*****Statistically significant ($p < 0.05$)

[d][h] There was only one set of negative controls per experiment. They are separated for ease of comparison to live and sterile treatments.

Table 4.4. Summary of cumulative carbon monoxide production across the two variables. Median production is in units of μmol. Comparison values are the results of a students' t test comparing to other treatments or to zero.

Experiment	Site	Treatment	Median Production	Comparison			
				Live	Sterile	Negative	Zero
Dry	Hyperarid	Live	0.0205	1	0.000*****	0.000*****	0.000*****
		Sterile	0.0016	–	1	0.002*****	0.010*****
		Negative[d]	0.0078	–	–	1	0.001*****
Dry	Semiarid	Live	0.0173	1	0.000*****	0.000*****	0.000*****
		Sterile	0.0081	–	1	0.767	0.002*****
		Negative[d]	0.0078	–	–	1	0.001*****
Humid	Hyperarid	Live	0.0185	1	0.000*****	0.000*****	0.000*****
		Sterile	0.0061	–	1	0.477	0.000*****
		Negative[h]	0.0053	–	–	1	0.000*****
Humid	Semiarid	Live	0.0147	1	0.124	0.000*****	0.000*****
		Sterile	0.0098	–	1	0.022*****	0.003*****
		Negative[h]	0.0053	–	–	1	0.000*****

*****Statistically significant ($p < 0.05$)

[d][h] There was only one set of negative controls per experiment. They are separated for ease of comparison to live and sterile treatments.

Table 4.5. Summary of cumulative carbon dioxide production across the two variables. Median production is in units of μmol. Comparison values are the results of a students' t test comparing to other treatments or to zero.

Experiment	Site	Treatment	Median Production	Comparison			
				Live	Sterile	Negative	Zero
Dry	Hyperarid	Live	0.7074	1	0.016*****	0.952	0.006*****
		Sterile	0.0395	–	1	0.101	0.919
		Negative[d]	0.4002	–	–	1	0.085
Dry	Semiarid	Live	0.6901	1	0.128	0.823	0.065
		Sterile	0.0525	–	1	0.186	0.754
		Negative[d]	0.4002	–	–	1	0.085
Humid	Hyperarid	Live	0.0548	1	0.015*****	0.029*****	0.611
		Sterile	0.9696	–	1	0.002*****	0.012*****
		Negative[h]	-0.5030	–	–	1	0.040*****
Humid	Semiarid	Live	-0.0167	1	0.569	0.181	0.406
		Sterile	-0.1644	–	1	0.076	0.526
		Negative[h]	-0.5030	–	–	1	0.040*****

*****Statistically significant ($p < 0.05$)

[d][h] There was only one set of negative controls per experiment. They are separated for ease of comparison to live and sterile treatments.

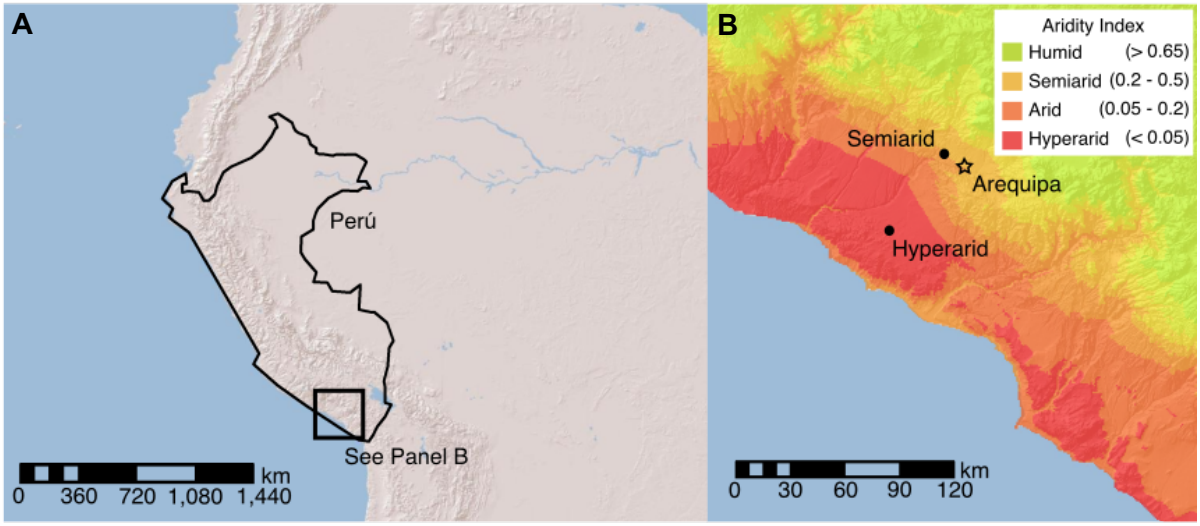

Figure 4.1. Maps of the two field sites and surrounding region. **A)** Terrain relief map of the western coast of South America centered on Perú (outlined). **B)** Terrain relief map with aridity index overlay of field sites with Arequipa noted for context (Zomer et al., 2008). Hyperarid site has mean AI of < 0.01 and semiarid site has mean AI of 0.2.

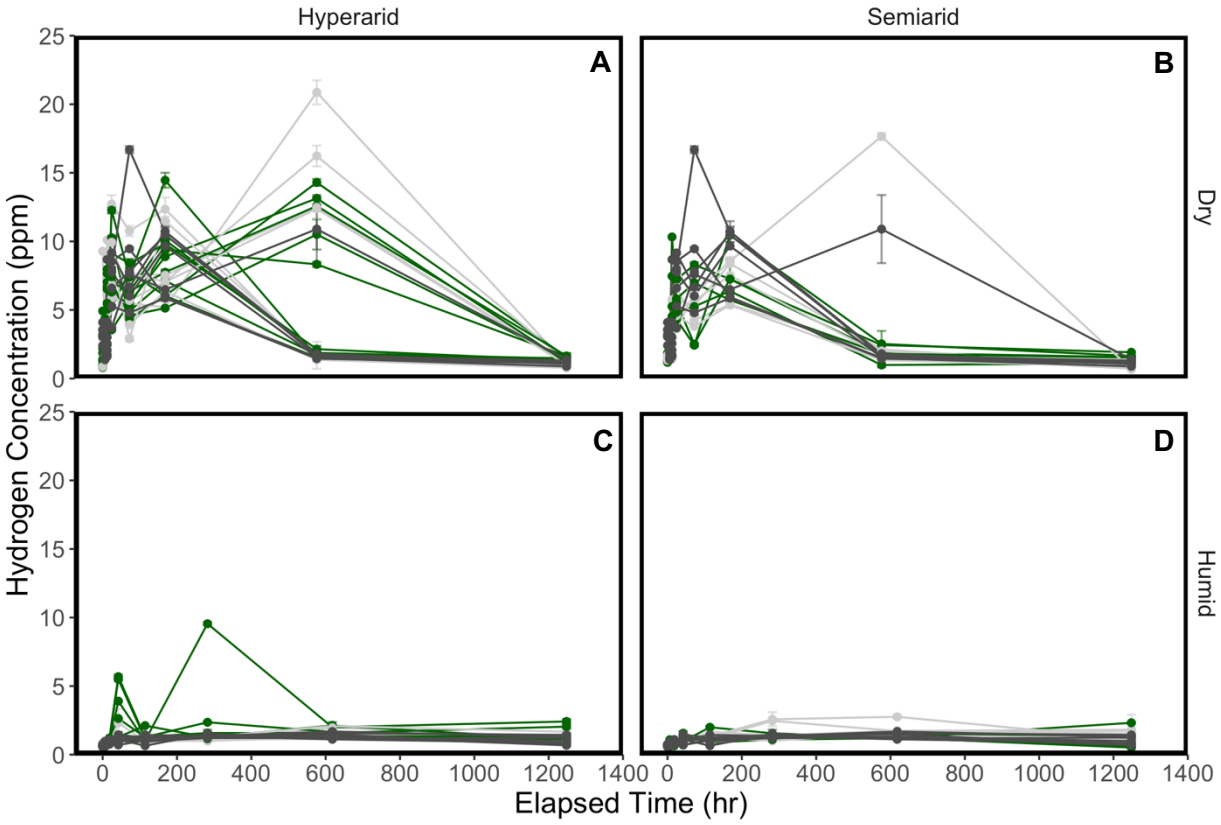

Figure 4.2. Hydrogen concentration timeseries in both experiments. Panels A and B show hydrogen concentration during the dry experiment for the **A)** hyperarid and **B)** semiarid soils. Panels C and D show hydrogen concentration during the humid experiment for the **C)** hyperarid and **D)** semiarid soils. Bottle treatments are distinguished by color: live (green), sterile (light grey), and negative (dark grey). Error bars are 1σ of 3 replicate injections.

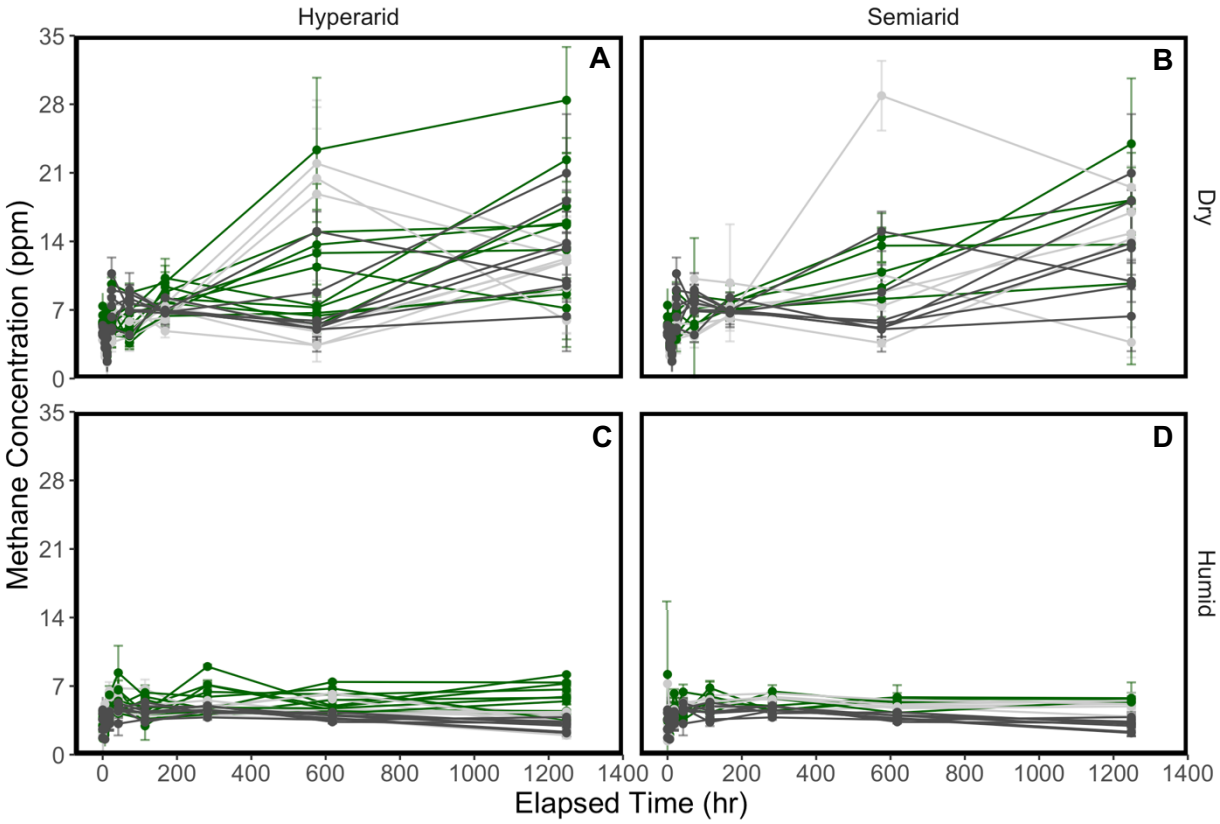

Figure 4.3. Methane concentration timeseries in both experiments. Panels A and B show methane concentration during the dry experiment for the **A)** hyperarid and **B)** semiarid soils. Panels C and D show methane concentration during the humid experiment for the **C)** hyperarid and **D)** semiarid soils. Bottle treatments are distinguished by color: live (green), sterile (light grey), and negative (dark grey). Error bars are 1σ of 3 replicate injections.

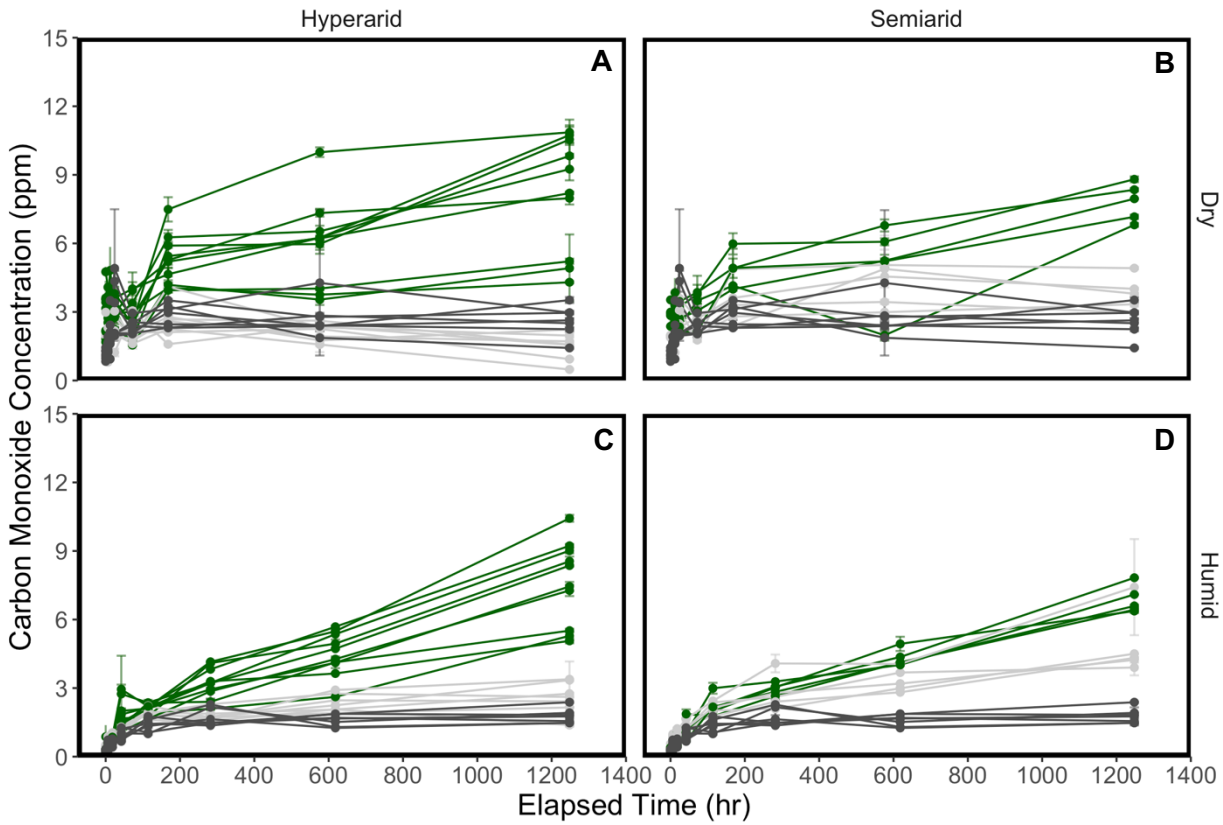

Figure 4.4. Carbon monoxide concentration timeseries in both experiments. Panels A and B show carbon monoxide concentration during the dry experiment for the **A)** hyperarid and **B)** semiarid soils. Panels C and D show carbon monoxide concentration during the humid experiment for the **C)** hyperarid and **D)** semiarid soils. Bottle treatments are distinguished by color: live (green), sterile (light grey), and negative (dark grey). Error bars are 1σ of 3 replicate injections.

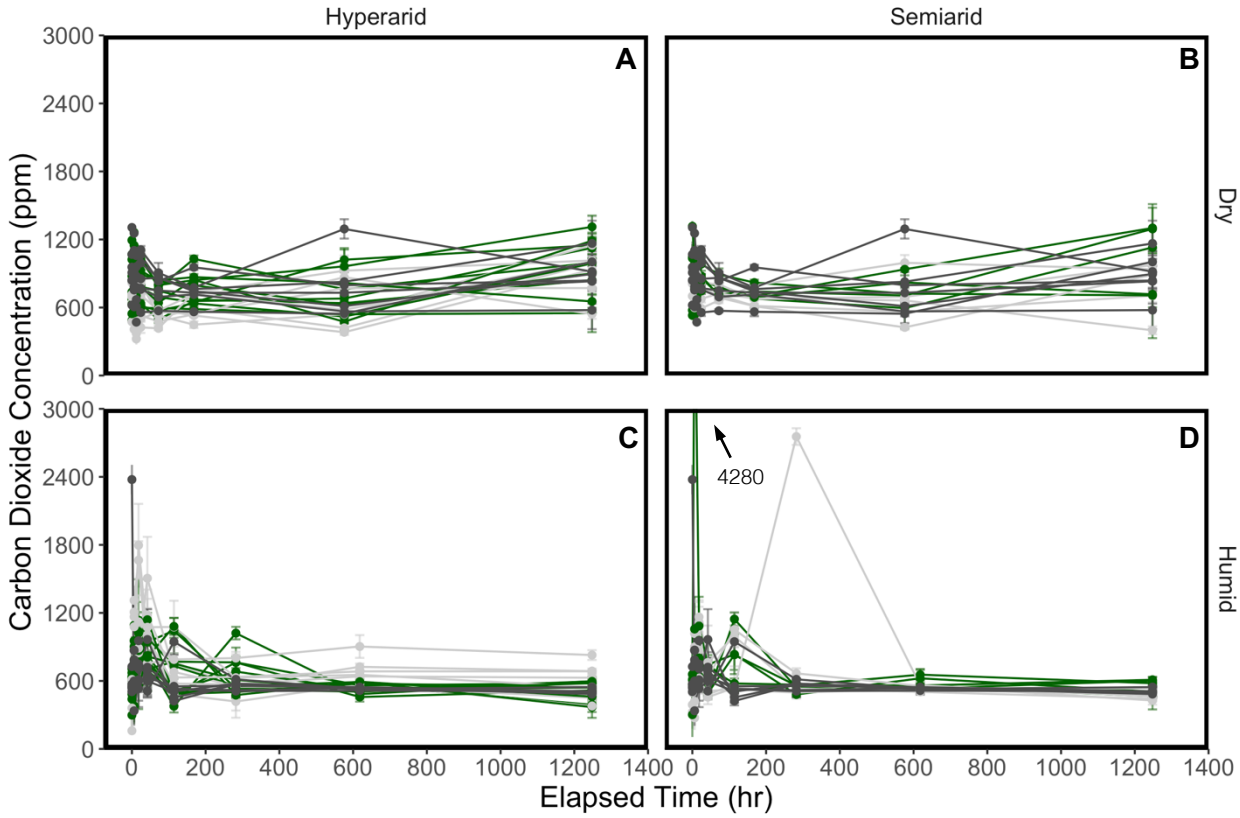

Figure 4.5. Carbon dioxide concentration timeseries in both experiments. Panels A and B show carbon dioxide concentration during the dry experiment for the **A)** hyperarid and **B)** semiarid soils. Panels C and D show carbon dioxide concentration during the humid experiment for the **C)** hyperarid and **D)** semiarid soils. Bottle treatments are distinguished by color: live (green), sterile (light grey), and negative (dark grey). Error bars are 1σ of 3 replicate injections. Note the annotation in panel D showing there is one outlier data point at t = 6 hr with carbon dioxide concentration of 4280 ppm.

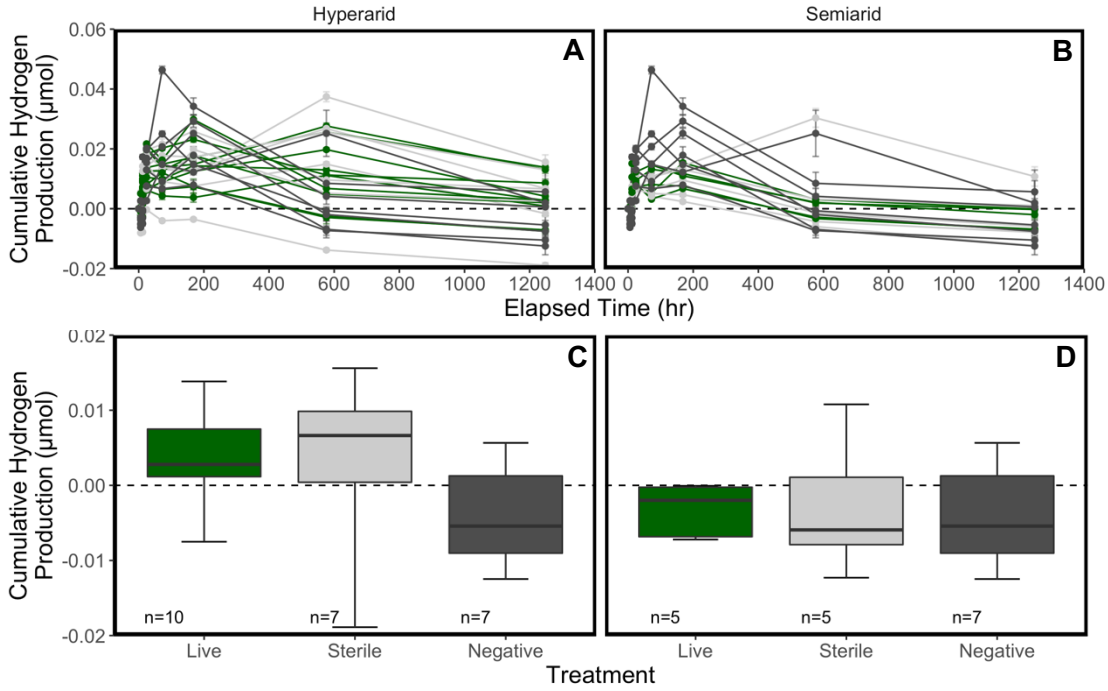

Figure 4.6. Cumulative hydrogen production over the dry experiment duration. Panels A and B show the entire time series for the **A)** hyperarid and **B)** semiarid soils. Bottle treatments are distinguished by color: live (green), sterile (light grey), and negative (dark grey). Error bars are 1σ of 3 replicate injections. Panels C and D show box and whisker plots of cumulative hydrogen at the end of the experiment (t = 1248 hr) for the **C)** hyperarid and **D)** semiarid soils. The box represents the 25th, 50th (median), and 75th percentiles (from bottom to top) and the lower and upper whiskers represent the minimum and maximum of the data, respectively. Numbers at the bottom of the panel are the number of observations in each treatment category.

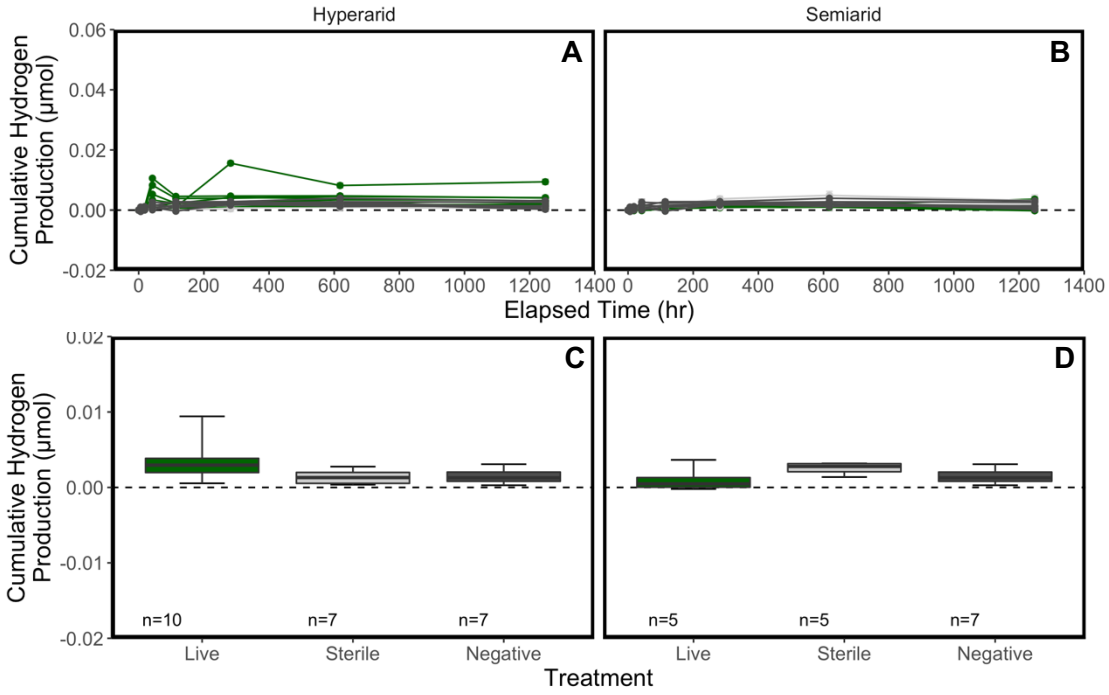

Figure 4.7. Cumulative hydrogen production over the humid experiment duration. Panels A and B show the entire time series for the **A)** hyperarid and **B)** semiarid soils. Bottle treatments are distinguished by color: live (green), sterile (light grey), and negative (dark grey). Error bars are 1σ of 3 replicate injections. Panels C and D show box and whisker plots of cumulative hydrogen at the end of the experiment (t = 1248 hr) for the **C)** hyperarid and **D)** semiarid soils. The box represents the 25th, 50th (median), and 75th percentiles (from bottom to top) and the lower and upper whiskers represent the minimum and maximum of the data, respectively. Numbers at the bottom of the panel are the number of observations in each treatment category.

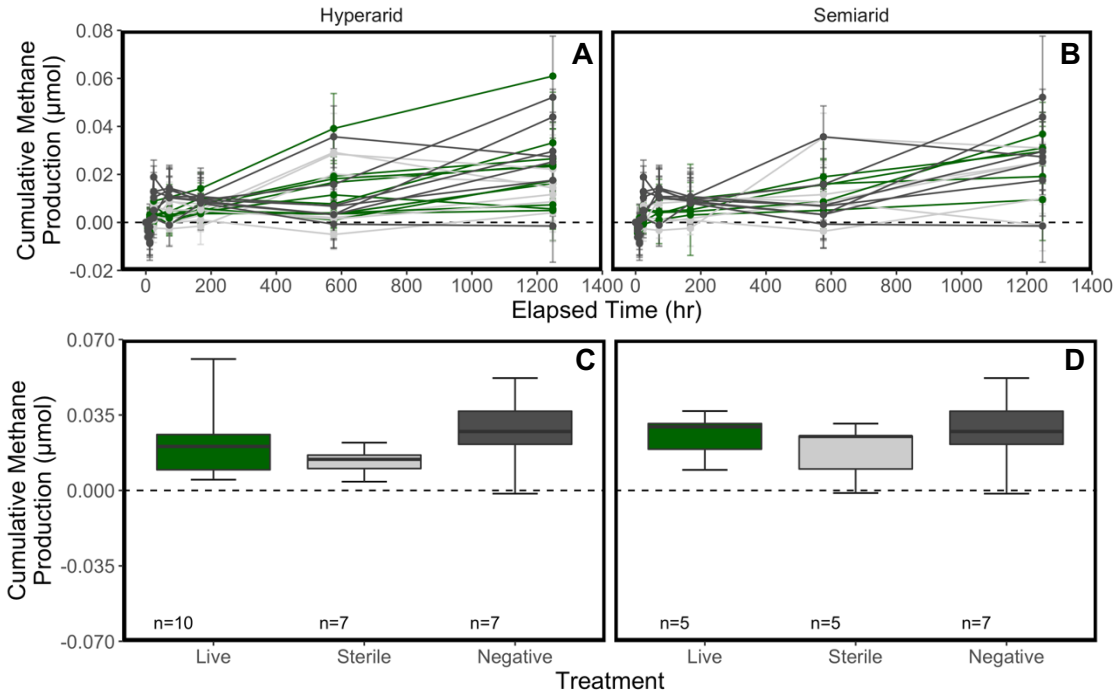

Figure 4.8. Cumulative methane production over the dry experiment duration. Panels A and B show the entire time series for the **A)** hyperarid and **B)** semiarid soils. Bottle treatments are distinguished by color: live (green), sterile (light grey), and negative (dark grey). Error bars are 1σ of 3 replicate injections. Panels C and D show box and whisker plots of cumulative hydrogen at the end of the experiment (t = 1248 hr) for the **C)** hyperarid and **D)** semiarid soils. The box represents the 25th, 50th (median), and 75th percentiles (from bottom to top) and the lower and upper whiskers represent the minimum and maximum of the data, respectively. Numbers at the bottom of the panel are the number of observations in each treatment category.

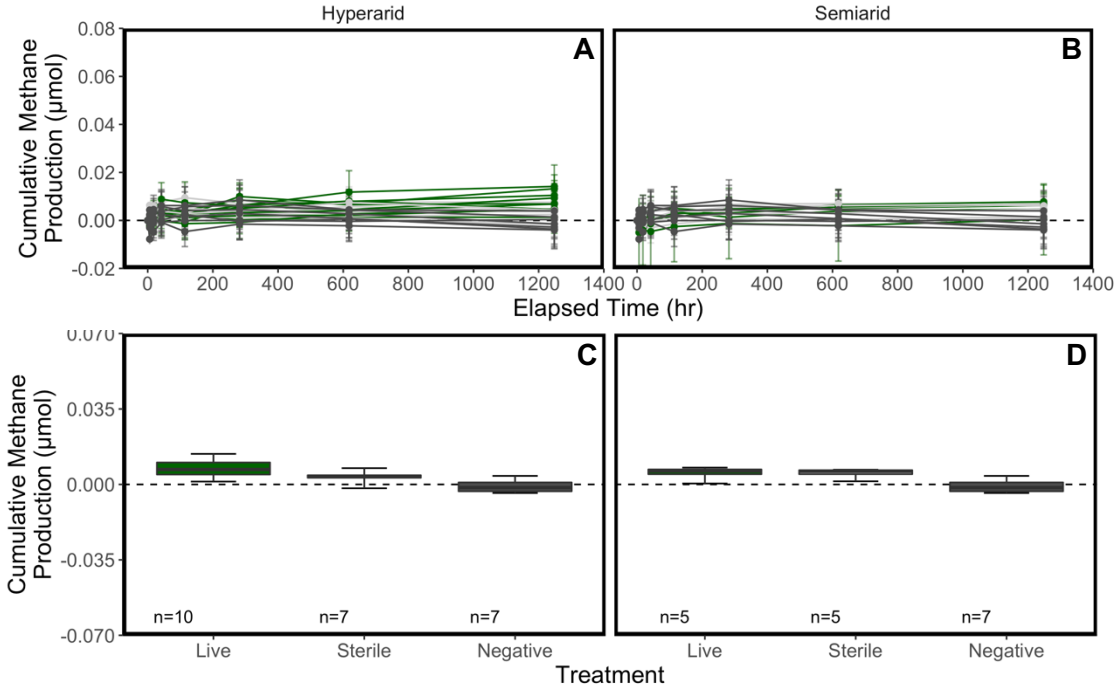

Figure 4.9. Cumulative methane production over the humid experiment duration. Panels A and B show the entire time series for the **A)** hyperarid and **B)** semiarid soils. Bottle treatments are distinguished by color: live (green), sterile (light grey), and negative (dark grey). Error bars are 1σ of 3 replicate injections. Panels C and D show box and whisker plots of cumulative hydrogen at the end of the experiment (1248 hr) for the **C)** hyperarid and **D)** semiarid soils. The box represents the 25th, 50th (median), and 75th percentiles (from bottom to top) and the lower and upper whiskers represent the minimum and maximum of the data, respectively. Numbers at the bottom of the panel are the number of observations in each treatment category.

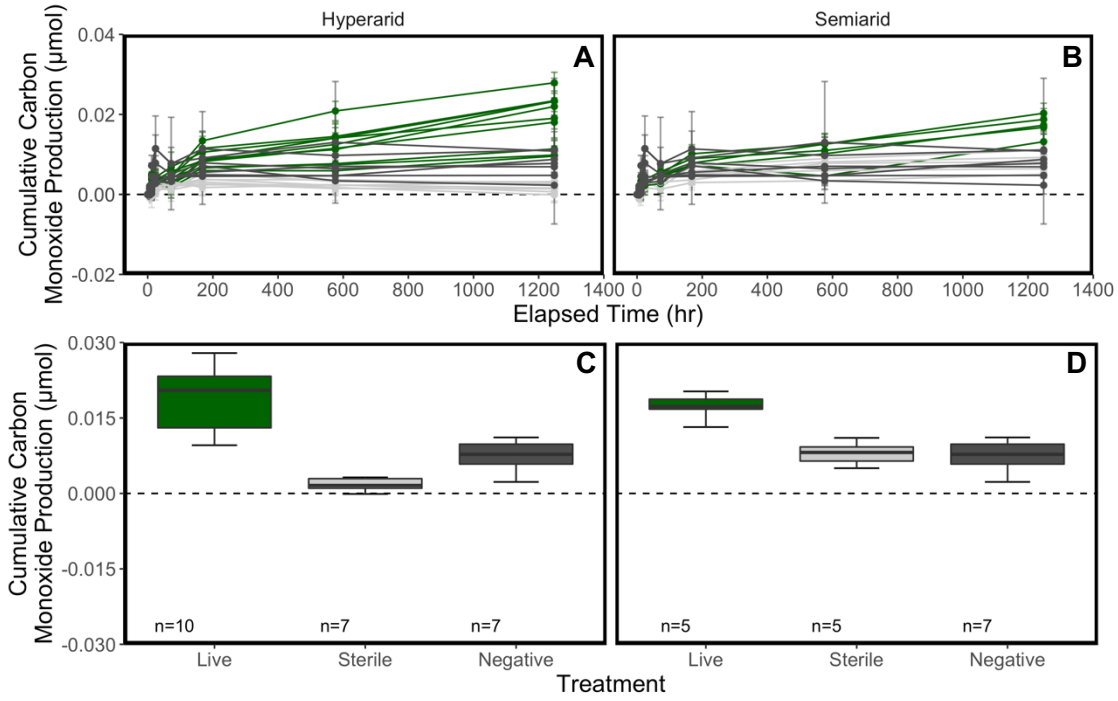

Figure 4.10. Cumulative carbon monoxide production over the dry experiment duration. Panels A and B show the entire time series for the **A)** hyperarid and **B)** semiarid soils. Bottle treatments are distinguished by color: live (green), sterile (light grey), and negative (dark grey). Error bars are 1σ of 3 replicate injections. Panels C and D show box and whisker plots of cumulative hydrogen at the end of the experiment (1248 hr) for the **C)** hyperarid and **D)** semiarid soils. The box represents the 25th, 50th (median), and 75th percentiles (from bottom to top) and the lower and upper whiskers represent the minimum and maximum of the data, respectively. Numbers at the bottom of the panel are the number of observations in each treatment category.

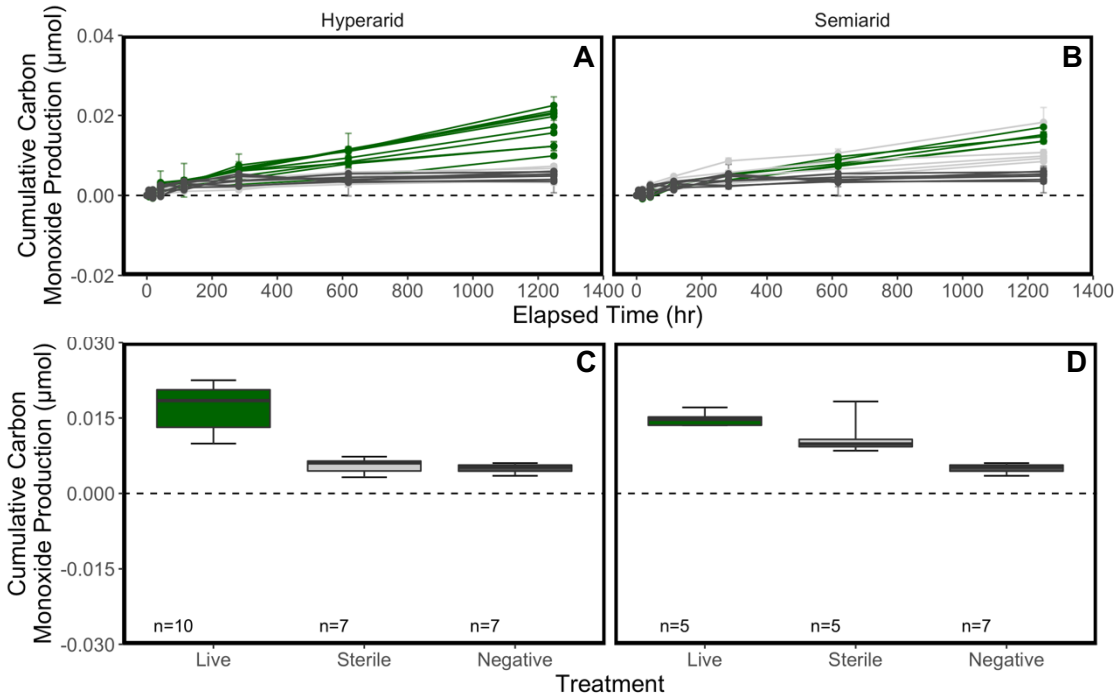

Figure 4.11. Cumulative carbon monoxide production over the humid experiment duration. Panels A and B show the entire time series for the **A)** hyperarid and **B)** semiarid soils. Bottle treatments are distinguished by color: live (green), sterile (light grey), and negative (dark grey). Error bars are 1σ of 3 replicate injections. Panels C and D show box and whisker plots of cumulative hydrogen at the end of the experiment (t = 1248 hr) for the **C)** hyperarid and **D)** semiarid soils. The box represents the 25th, 50th (median), and 75th percentiles (from bottom to top) and the lower and upper whiskers represent the minimum and maximum of the data, respectively. Numbers at the bottom of the panel are the number of observations in each treatment category.

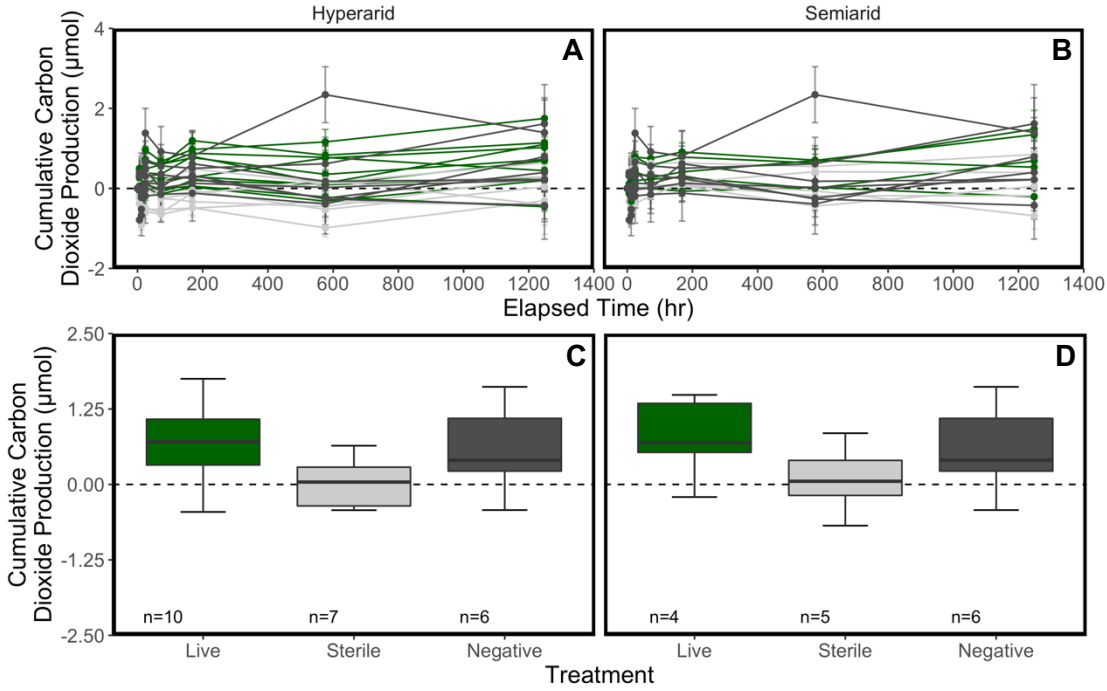

Figure 4.12. Cumulative carbon dioxide production over the dry experiment duration. Panels A and B show the entire time series for the **A)** hyperarid and **B)** semiarid soils. Bottle treatments are distinguished by color: live (green), sterile (light grey), and negative (dark grey). Error bars are 1σ of 3 replicate injections. Panels C and D show box and whisker plots of cumulative hydrogen at the end of the experiment (t = 1248 hr) for the **C)** hyperarid and **D)** semiarid soils. The box represents the 25th, 50th (median), and 75th percentiles (from bottom to top) and the lower and upper whiskers represent the minimum and maximum of the data, respectively. Numbers at the bottom of the panel are the number of observations in each treatment category.

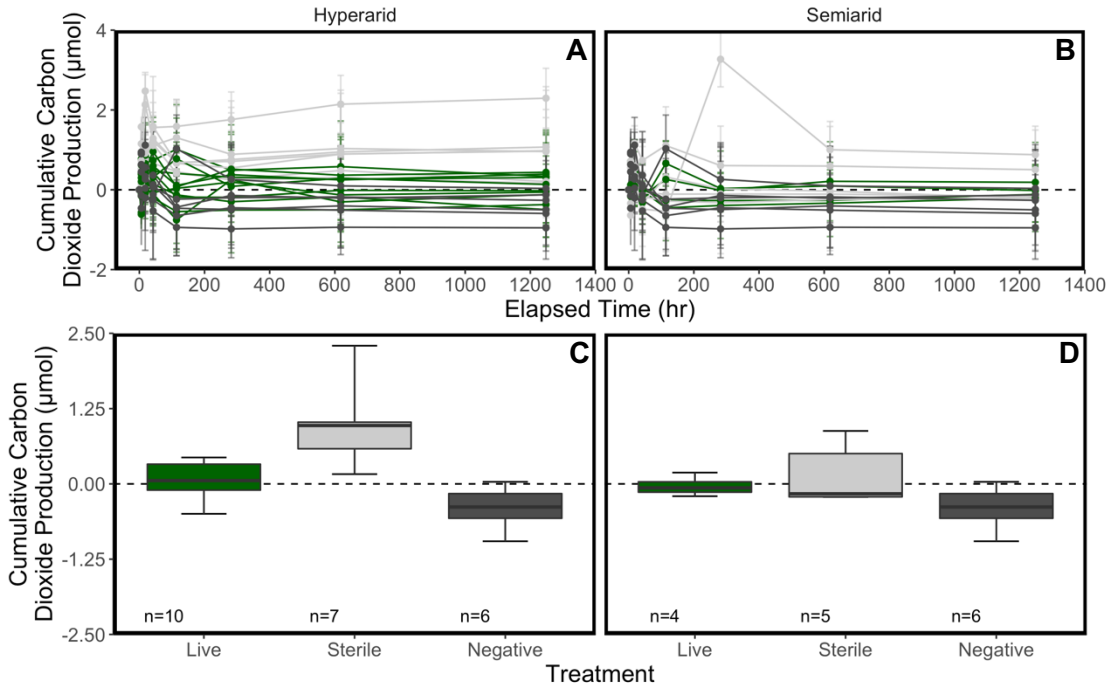

Figure 4.13. Cumulative carbon dioxide production over the humid experiment duration. Panels A and B show the entire time series for the **A)** hyperarid and **B)** semiarid soils. Bottle treatments are distinguished by color: live (green), sterile (light grey), and negative (dark grey). Error bars are 1σ of 3 replicate injections. Panels C and D show box and whisker plots of cumulative hydrogen at the end of the experiment (t = 1248 hr) for the **C)** hyperarid and **D)** semiarid soils. The box represents the 25th, 50th (median), and 75th percentiles (from bottom to top) and the lower and upper whiskers represent the minimum and maximum of the data, respectively. Numbers at the bottom of the panel are the number of observations in each treatment category.

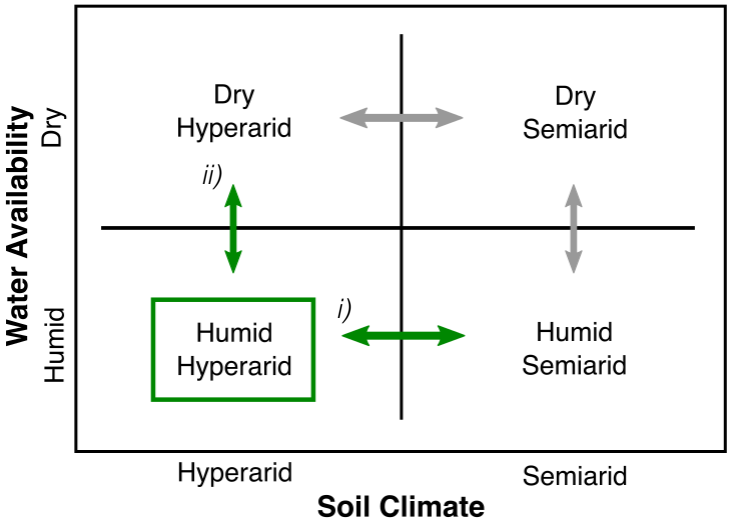

Figure 4.14. Treatment matrix diagram showing the two categorical variables of soil climate and water availability. In the case of methane, there was only one treatment that showed a statistically significant difference between the live and control bottles: humid hyperarid (highlighted by the green square). In this case, there are two informative comparisons I can make (green arrows): *i)* compare between soil climates and *ii)* compare between water availabilities. In the case of the grey arrows, the comparisons represented are not informative as each of the treatments showed no statistically significant difference between the live and control bottles (i.e., I am unable to infer any biological activity). For the three other analytes (hydrogen, carbon monoxide, and carbon dioxide), there were no cases of plausible, statistically significant biological activity in the live bottles.

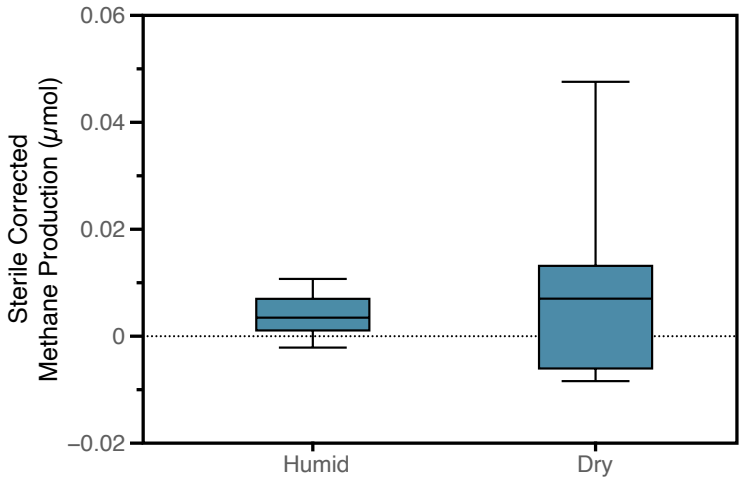

Figure 4.15. Comparison of sterile-corrected methane production in the hyperarid site for the dry and humid experiments (comparison *i* from figure 4.14). The results of a student's t test show that the two populations of values are not significantly different ($p \geq 0.05$).

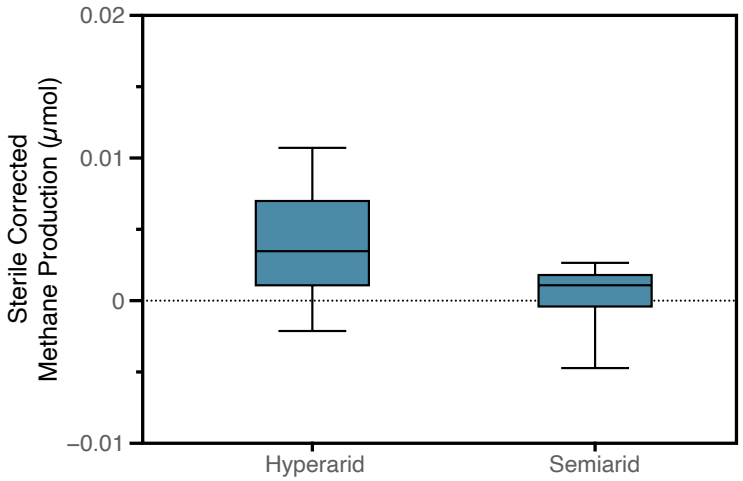

Figure 4.16. Comparison of sterile-corrected metabolic methane production of the hyperarid and semiarid sites in the humid experiment (comparison *ii* from figure 4.14). The results of a student's t test show that the two populations of values are significant ($p < 0.05$).

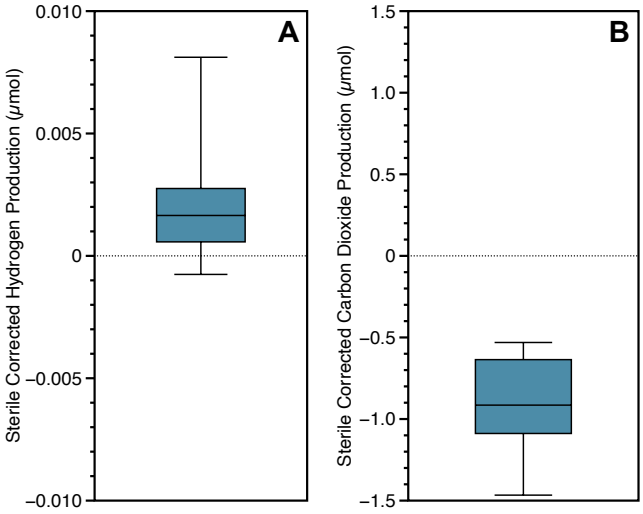

Figure 4.17. Sterile-corrected **A)** hydrogen and **B)** carbon dioxide production in the humid experiment.

Angel, R., Matthies, D., and Conrad, R. (**2011**). Activation of methanogenesis in arid biological soil crusts despite the presence of oxygen. *PLOS ONE*, *6*(5), e20453. DOI: 10.1371/journal.pone.0020453

Azua-Bustos, A., Fairén, A. G., González-Silva, C., Ascaso, C., Carrizo, D., Fernández-Martínez, M. Á., Fernández-Sampedro, M., García-Descalzo, L., García-Villadangos, M., Martin-Redondo, M. P., Sánchez-García, L., Wierzchos, J., and Parro, V. (**2018**). Unprecedented rains decimate surface microbial communities in the hyperarid core of the Atacama Desert. *Scientific Reports*, *8*(1). DOI: 10.1038/s41598-018-35051-w

Azúa-Bustos, A., González-Silva, C., Mancilla, R. A., Salas, L., Gómez-Silva, B., McKay, C. P., and Vicuña, R. (**2011**). Hypolithic cyanobacteria supported mainly by fog in the coastal range of the Atacama Desert. *Microbial Ecology*, *61*(3), 568–581. DOI: 10.1007/s00248-010-9784-5

Azua-Bustos, A., Urrejola, C., and Vicuña, R. (**2012**). Life at the dry edge: Microorganisms of the Atacama Desert. *FEBS Letters*, *586*(18), 2939–2945. DOI: 10.1016/j.febslet.2012.07.025

Belilla, J., Moreira, D., Jardillier, L., Reboul, G., Benzerara, K., López-García, J. M., Bertolino, P., López-Archilla, A. I., and López-García, P. (**2019**). Hyperdiverse archaea near life limits at the polyextreme geothermal Dallol area. *Nature Ecology & Evolution*, *3*(11), 1552–1561. DOI: 10.1038/s41559-019-1005-0

Bendia, A. G., Araujo, G. G., Pulschen, A. A., Contro, B., Duarte, R. T. D., Rodrigues, F., Galante, D., and Pellizari, V. H. (**2018**). Surviving in hot and cold: Psychrophiles and thermophiles from Deception Island volcano, Antarctica. *Extremophiles*, *22*(6), 917–929. DOI: 10.1007/s00792-018-1048-1

Berghuis, B. A., Yu, F. B., Schulz, F., Blainey, P. C., Woyke, T., and Quake, S. R. (**2019**). Hydrogenotrophic methanogenesis in archaeal phylum Verstraetearchaeota reveals the shared ancestry of all methanogens. *Proceedings of the National Academy of Sciences*, *116*(11), 5037–5044. DOI: 10.1073/pnas.1815631116

Borch, T., Kretzschmar, R., Kappler, A., Cappellen, P. V., Ginder-Vogel, M., Voegelin, A., and Campbell, K. (**2010**). Biogeochemical redox processes and their impact on contaminant dynamics. *Environmental Science & Technology*, *44*(1), 15–23. DOI: 10.1021/es9026248

Chan-Yam, K., Goordial, J., Greer, C., Davila, A., McKay, C. P., and Whyte, L. G. (**2019**). Microbial activity and habitability of an Antarctic dry valley water track. *Astrobiology*, ast.2018.1884. DOI: 10.1089/ast.2018.1884

Chiquoine, L. P., Abella, S. R., and Bowker, M. A. (**2016**). Rapidly restoring biological soil crusts and ecosystem functions in a severely disturbed desert ecosystem. *Ecological Applications*, *26*(4), 1260–1272. DOI: 10.1002/15-0973

Conrad, R. (**1996**). Soil microorganisms as controllers of atmospheric trace gases (H_2, CO, CH_4, OCS, N_2O, and NO). *Microbiological Reviews*, *60*(4), 609.

Conrad, R., and Seiler, W. (**1985**). Characteristics of abiological carbon monoxide formation from soil organic matter, humic acids, and phenolic compounds. *Environmental Science & Technology*, *19*(12), 1165–1169. DOI: 10.1021/es00142a004

Day, P. R. (**1965**). Hydrometer method of particle size analysis. *Methods of Soil Analysis. Agronomy*, *9*, 562–566.

Dose, K., Bieger-Dose, A., Ernst, B., Feister, U., Gómez-Silva, B., Klein, A., Risi, S., and Stridde, C. (**2001**). Survival of microorganisms under the extreme conditions of the Atacama Desert. *Origins of Life and Evolution of Biospheres*, *31*(3), 287–303. DOI: 10.1023/A:1010788829265

Douglas, P. M. J., Stolper, D. A., Eiler, J. M., Sessions, A. L., Lawson, M., Shuai, Y., Bishop, A., Podlaha, O. G., Ferreira, A. A., Santos Neto, E. V., Niemann, M., Steen, A. S., Huang, L., Chimiak, L., Valentine, D. L., Fiebig, J., Luhmann, A. J., Seyfried, W. E., Etiope, G., … Kitchen, N. (**2017**). Methane clumped isotopes: Progress and potential for a new isotopic tracer. *Organic Geochemistry*, *113*, 262–282. DOI: 10.1016/j.orggeochem.2017.07.016

Fernández-Martínez, M. Á., dos Santos Severino, R., Moreno-Paz, M., Gallardo-Carreño, I., Blanco, Y., Warren-Rhodes, K., García-Villadangos, M., Ruiz-Bermejo, M., Barberán, A., Wettergreen, D., Cabrol, N., and Parro, V. (**2019**). Prokaryotic community structure and metabolisms in shallow subsurface of Atacama Desert playas and alluvial fans after heavy rains: Repairing and preparing for next dry period. *Frontiers in Microbiology*, *10*, 1641. DOI: 10.3389/fmicb.2019.01641

Garcia-Pichel, F., Johnson, S. L., Youngkin, D., and Belnap, J. (**2003**). Small-scale vertical distribution of bacterial biomass and diversity in biological soil crusts from arid lands in the Colorado Plateau. *Microbial Ecology*, *46*(3), 312–321. DOI: 10.1007/s00248-003-1004-0

Glaser, D. M., Hartnett, H. E., Finn, D. R., Perez-Montaño, S., Cadillo-Quiroz, H., and Desch, S. (**2022**). Water Vapor Adsorption Provides Daily, Sustainable Water to Soils of the Hyperarid Atacama Desert. *Astrobiology*, *22*(10), 1222–1238. DOI: 10.1089/ast.2021.0171

Gödde, M., Meuser, K., and Conrad, R. (**2000**). Hydrogen consumption and carbon monoxide production in soils with different properties. *Biology and Fertility of Soils*, *32*(2), 129–134. DOI: 10.1007/s003740000226

Hall, S. J., Silver, W. L., and Amundson, R. (**2012**). Greenhouse gas fluxes from Atacama Desert soils: A test of biogeochemical potential at the Earth's arid extreme. *Biogeochemistry*, *111*(1–3), 303–315. DOI: 10.1007/s10533-011-9650-7

Hedges, J. I., and Stern, J. H. (**1984**). Carbon and nitrogen determinations of carbonate-containing solids. *Limnology and Oceanography*, *29*(3), 657–663. DOI: 10.4319/lo.1984.29.3.0657

Jacobson, K., van Diepeningen, A., Evans, S., Fritts, R., Gemmel, P., Marsho, C., Seely, M., Wenndt, A., Yang, X., and Jacobson, P. (**2015**). Non-rainfall moisture activates fungal

decomposition of surface litter in the Namib sand sea. *PLOS ONE*, *10*(5). DOI: 10.1371/journal.pone.0126977

Ji, M., Greening, C., Vanwonterghem, I., Carere, C. R., Bay, S. K., Steen, J. A., Montgomery, K., Lines, T., Beardall, J., van Dorst, J., Snape, I., Stott, M. B., Hugenholtz, P., and Ferrari, B. C. (**2017**). Atmospheric trace gases support primary production in Antarctic desert surface soil. *Nature*, *552*(7685), 400–403. DOI: 10.1038/nature25014

Jones, D. L., Olivera-Ardid, S., Klumpp, E., Knief, C., Hill, P. W., Lehndorff, E., and Bol, R. (**2018**). Moisture activation and carbon use efficiency of soil microbial communities along an aridity gradient in the Atacama Desert. *Soil Biology and Biochemistry*, *117*, 68–71. DOI: 10.1016/j.soilbio.2017.10.026

Lynch, R. C., Darcy, J. L., Kane, N. C., Nemergut, D. R., and Schmidt, S. K. (**2014**). Metagenomic evidence for metabolism of trace atmospheric gases by high-elevation desert Actinobacteria. *Frontiers in Microbiology*, *5*. DOI: 10.3389/fmicb.2014.00698

Lyu, Z., Shao, N., Akinyemi, T., and Whitman, W. B. (**2018**). Methanogenesis. *Current Biology*, *28*(13), R727–R732. DOI: 10.1016/j.cub.2018.05.021

McKay, C. P., Friedmann, E. I., Gómez-Silva, B., Cáceres-Villanueva, L., Andersen, D. T., and Landheim, R. (**2003**). Temperature and moisture conditions for life in the extreme arid region of the Atacama Desert: Four years of observations including the El Niño of 1997–1998. *Astrobiology*, *3*(2), 393–406. DOI: 10.1089/153110703769016460

Nanni, E. J., Stallings, M. D., and Sawyer, D. T. (**1980**). Does superoxide ion oxidize catechol, α-tocopherol, and ascorbic acid by direct electron transfer? *Journal of the American Chemical Society*, *102*(13), 4481–4485. DOI: 10.1021/ja00533a029

Navarro-Gonzalez, R., Rainey, F., Molina, P., Bagaley, D., Hollen, B., de la Rosa, J., Small, A., Quinn, R., Grunthaner, F., Caceres, L., Gomez-Silva, B., and McKay, C. (**2003**). Mars-like soils in the Atacama Desert, Chile, and the dry limit of microbial life. *Science*, *302*(5647), 1018–1021. DOI: 10.1126/science.1089143

O'Connor, F. M., Boucher, O., Gedney, N., Jones, C. D., Folberth, G. A., Coppell, R., Friedlingstein, P., Collins, W. J., Chappellaz, J., Ridley, J., and Johnson, C. E. (**2010**). Possible role of wetlands, permafrost, and methane hydrates in the methane cycle under future climate change: A review. *Reviews of Geophysics*, *48*(4). DOI: 10.1029/2010RG000326

Pan, X., Angelidaki, I., Alvarado-Morales, M., Liu, H., Liu, Y., Huang, X., and Zhu, G. (**2016**). Methane production from formate, acetate and H_2/CO_2; focusing on kinetics and microbial characterization. *Bioresource Technology*, *218*, 796–806. DOI: 10.1016/j.biortech.2016.07.032

Penning, H., and Conrad, R. (**2006**). Effect of inhibition of acetoclastic methanogenesis on growth of archaeal populations in an anoxic model environment. *Applied and Environmental Microbiology*, *72*(1), 178–184. DOI: 10.1128/AEM.72.1.178-184.2006

Safriel, U., Adeel, Z., Niemeijer, D., Puigdefabregas, J., White, R., Lal, R., Winslow, M., Ziedler, J., Prince, S., and Archer, E. (**2005**). Dryland Systems. In *Ecosystems and human well-being: Current state and trends* (pp. 623–662). Island Press.

Schulze-Makuch, D., Wagner, D., Kounaves, S. P., Mangelsdorf, K., Devine, K. G., de Vera, J.-P., Schmitt-Kopplin, P., Grossart, H.-P., Parro, V., Kaupenjohann, M., Galy, A., Schneider, B., Airo, A., Frösler, J., Davila, A. F., Arens, F. L., Cáceres, L., Cornejo, F. S., Carrizo, D., … Zamorano, P. (**2018**). Transitory microbial habitat in the hyperarid Atacama Desert. *Proceedings of the National Academy of Sciences*, *115*(11), 2670–2675. DOI: 10.1073/pnas.1714341115

Serrano-Silva, N., Sarria-Guzmán, Y., Dendooven, L., and Luna-Guido, M. (**2014**). Methanogenesis and methanotrophy in soil: A review. *Pedosphere*, *24*(3), 291–307. DOI: 10.1016/S1002-0160(14)60016-3

Shock, E. L., Holland, M., Meyer-Dombard, D., Amend, J. P., Osburn, G. R., and Fischer, T. P. (**2010**). Quantifying inorganic sources of geochemical energy in hydrothermal ecosystems, Yellowstone National Park, USA. *Geochimica et Cosmochimica Acta*, *74*(14), 4005–4043. DOI: 10.1016/j.gca.2009.08.036

Singh, J. S., Raghubanshi, A. S., Reddy, V. S., Singh, S., and Kashyap, A. K. (**1998**). Methane flux from irrigated paddy and dryland rice fields, and from seasonally dry tropical forest and Savanna soils of India. *Soil Biology and Biochemistry*, *30*(2), 135–139. DOI: 10.1016/S0038-0717(97)00112-0

Trembath-Reichert, E., Morono, Y., Ijiri, A., Hoshino, T., Dawson, K. S., Inagaki, F., and Orphan, V. J. (**2017**). Methyl-compound use and slow growth characterize microbial life in 2-km-deep subseafloor coal and shale beds. *Proceedings of the National Academy of Sciences*, *114*(44), E9206–E9215. DOI: 10.1073/pnas.1707525114

Valdivia-Silva, J. E., Navarro-González, R., Fletcher, L., Pérez-Montaño, S., Condori-Apaza, R., Ortega-Gutiérrez, F., and McKay, C. (**2012**). Climatological characteristics in the extreme hyper-arid region of Pampas de La Joya, Peru. Astrobiological approach in four years of observation: 2004–2008. *International Journal of Astrobiology*, *11*(01), 25–35. DOI: 10.1017/S1473550411000292

Vítek, P., Ascaso, C., Artieda, O., and Wierzchos, J. (**2016**). Raman imaging in geomicrobiology: Endolithic phototrophic microorganisms in gypsum from the extreme sun irradiation area in the Atacama Desert. *Analytical and Bioanalytical Chemistry*, *408*(15), 4083–4092. DOI: 10.1007/s00216-016-9497-9

Wendlandt, K.-D., Stottmeister, U., Helm, J., Soltmann, B., Jechorek, M., and Beck, M. (**2010**). The potential of methane-oxidizing bacteria for applications in environmental biotechnology. *Engineering in Life Sciences*, *10*(2), 87–102. DOI: 10.1002/elsc.200900093

Wilhelm, M. B., Davila, A. F., Parenteau, M. N., Jahnke, L. L., Abate, M., Cooper, G., Kelly, E. T., Parro García, V., Villadangos, M. G., Blanco, Y., Glass, B., Wray, J. J., Eigenbrode, J. L., Summons, R. E., and Warren-Rhodes, K. (**2018**). Constraints on the metabolic activity of microorganisms in Atacama surface soils inferred from Rrefractory biomarkers: Implications for Martian habitability and biomarker detection. *Astrobiology*, *18*(7), 955–966. DOI: 10.1089/ast.2017.1705

Zomer, R. J., Trabucco, A., Bossio, D. A., and Verchot, L. V. (**2008**). Climate change mitigation: A spatial analysis of global land suitability for clean development mechanism

afforestation and reforestation. *Agriculture, Ecosystems & Environment*, *126*(1–2), 67–80. DOI: 10.1016/j.agee.2008.01.014

Chapter 5

CONCLUSION

5.1. Summary

The work described in this dissertation characterizes the physico-chemical environment that promotes daily water vapor adsorption in hyperarid soils in the context of habitability of arid environments. I observed and measured water vapor adsorption in the field in one of the driest environments on Earth. Using these observations, I developed a model to quantify water vapor adsorption using only soil temperature and relative humidity profile measurements. In doing so, I developed a novel measurement and modeling technique that can be employed by other researchers across a diverse range of environments. The outcomes of this work highlighted differences in water vapor adsorption between two sites that could not be explained using existing water vapor adsorption models. The discrepancy in water vapor adsorption between the two sites raised a new set of questions about water vapor adsorption and its possible dependence on the mineral composition of the soil.

I designed and executed a set of experiments to measure water vapor adsorption of a set of representative minerals across a matrix of temperature, relative humidity, and surface area. Using this large data set of equilibrium water vapor adsorption measurements; I was able to build five mineral-specific models to predict water vapor adsorption. These results show that there are measurable differences in water vapor adsorption across mineral types when controlling for temperature, relative humidity, and surface area. My work up to this point is

centered on the physico-chemical environment of the Atacama Desert, particularly with regards to water availability in the form of water vapor adsorption. Sentence here about predicting water on Mars and Luna. I hypothesized that this exceedingly small amount of water is bioavailable; and that the typical environmental conditions of the hyperarid Atacama Desert are sufficient to promote biological activity.

I tested this hypothesis using a set of 52-day incubation experiments using soil collected from the Atacama Desert. I show evidence of possible methane-based metabolism in hyperarid soils under high humidity, no fog conditions. This result hints at the highly adapted capabilities of the xerotolerent microorganisms in these soils, capable of utilizing water vapor adsorption as a source of bioavailable water. In addition, these results highlight the difficulty of collecting interpretable data from extremely low-biomass soils. The aggregation of these results suggests the typical water conditions present in the Atacama may be sufficient for highly-adapted microorganisms to exploit. Much more work is necessary to investigate and provide further robust evidence of microbial activity under typical water conditions.

5.2. Implications

The work described here to quantify water vapor adsorption and describe the factors controlling water vapor adsorption hint at the importance of understanding the impact of soil heterogeneity on microbial colonization and biological activity. The macroscale environment of the Atacama Desert is harsh; there is little water and an intense UV radiation flux. However, at the microscale, many of these harsh factors can be attenuated or eliminated. For example, the UV radiation may be harsh, but a location just 1 or 2 cm below the surface of the soil is sufficient to completely block UV from the sun (Dose et al., 2001).

Similarly, there is very little water on the macroscale, but in a microscale fissure of a soil grain there may be enough water to partially or completely engulf a cell. In addition, if the soil grain is of a particular mineral composition; under the right temperature and relative humidity conditions there could be even more favorable water availability.

The results of this dissertation also suggest there are water vapor adsorption heterogeneities, similar to mineral heterogeneities, within a bulk soil. It is likely that soil heterogeneities with higher water vapor adsorption are host to more microorganisms (higher cell density) than soils with lower water vapor adsorption. In this framework, the largest hurdle is the scale of any favorable heterogeneity. The chemical characterization instrumentation on NASA's Perseverance rover (SHERLOC and PIXL) have impressive spatial resolution with ~50 μm per pixel (Razzell Hollis et al., 2022). This may be sufficient to identify a favorable heterogeneity with cell or organics concentrations high enough for detection, but we may ultimately need to identify favorable heterogeneities on the order of cm to m or larger.

There are still many questions regarding the capability of microorganisms to utilize this adsorbed water in hyperarid conditions. The results of chapter 4 suggest a high humidity event (≥95%RH) may provide bioavailable water in hyperarid environments, but the limitations of the methodology prevent me from making more definitive conclusions. However, the mere suggestion of biological activity in these soils is rationale for continued research. The Atacama Desert may be the best natural laboratory to investigate the extreme limits of life due to the extraordinarily dry conditions that have persisted over tens of millions of years. The timescale of pronounced aridity provides ample time for evolutionary adaptation and specialization. The microorganisms that have been observed in the Atacama

are the results of, at least, millions of generations of survival and adaptation to an extremely dry environment. Could these microorganisms survive in drier conditions? What is the longest period of time these microorganisms can go without condensed water? What is the microscale distribution of microorganisms in these soils? Is there evidence of primary producers (particularly chemolithoautotrophs)? Are these microorganisms able to create global-scale atmospheric biosignatures? These are many of the questions that my work has sparked which I hope to pursue over the course of my career.

5.3. Future Work

The principal and most tractable application of this work, particularly chapter 3, is to quantify adsorbed water content in the bulk regolith of Mars. Current models of Martian adsorbed regolith water rely on atmospheric water concentrations and temperature alone (e.g., Böttger et al., 2005; Savijärvi and Harri, 2021). The models described in chapter 3 can estimate Martian adsorbed regolith water with the additional context of mineral abundance and surface area. This independent quantification of Martian adsorbed regolith water will provide crucial context to previous estimates and will serve as an additional reference point for Martian regolith water. Good agreement between previous estimates and estimates using the chapter 3 models will provide additional validation of the accuracy of my models.

The models developed in chapter 3 can also be used to speculate and investigate the potential for microenvironments of water vapor adsorption, and thus potential habitability in the regolith of Mars. Mars is our nearest neighbor and is an exceedingly arid planet, but we are fortunate to have environments on Earth that approximate certain Martian conditions such as aridity (i.e., Figure 5.1). Perhaps the results described in this dissertation could serve to inform current and future NASA missions of targets of interest with regard to higher

potential for water content (i.e., favorable water vapor adsorption heterogeneities). NASA's Perseverance rover is currently operational and searching for high value targets in Jezero Crater on Mars. Perseverance has a large suite of instruments with the capabilities to do some of the analyses described in this dissertation (mineral composition, temperature, and relative humidity). However, a future mission equipped with a soil temperature and relative humidity array (as described in chapter 2), providing information on the temperature and humidity conditions in the near subsurface of the Martian regolith. There have been no similar measurements in Martian soils; all the temperature and relative humidity data obtained to date are collected at a height of 1.6 m on the Mastcam boom. These data would provide crucial data necessary to understand the global water cycle of Mars and potentially help to identify targets of astrobiological interest.

Finding signs of life - extinct or extant - on Mars is exceedingly difficult, especially for a rover with a limited arsenal of tools and techniques. Therefore, the planned Mars sample return mission is likely the best chance to identify biosignatures on Mars. However, the mission is limited by *i)* the total number of samples (43) and *ii)* the information used to select the sampling site. I hope that the results and analysis provided by this dissertation may help to identify targets with the highest potential for signs of life. I would postulate that this would be sedimentary material with high clay or evaporite abundance and low olivine abundance. This type of sediment showed relatively high amounts of water vapor adsorption in my experiments. Therefore, I expect this type of environment to have a higher probability of potential for life due to its higher capability to adsorb water. Without the luxury of an unlimited number and amount of return samples from Mars, it is necessary to ensure that

each sample - intended to measure biosignatures - provides the highest possible potential for detection.

Finally, I hope to use the knowledge gained here to characterize exoplanets with the objective to detect a robust biosignature on an arid exoplanet. Outside our solar system, there is likely to be a plethora of arid worlds and I may be able to extrapolate the results and analysis from this dissertation to putative arid exoplanets. A planet with little surface water, similar to Mars, may be habitable and indeed inhabited. I may be able to use the information gained during my dissertation to hypothesize putative biospheres on these planets and predict potential global-scale atmospheric biosignatures that may be detected by JWST or LUVOIR. The information in this dissertation will be critical to understanding the water cycle and climate of an arid planet and may constrain the potential metabolic reactions of such a planet.

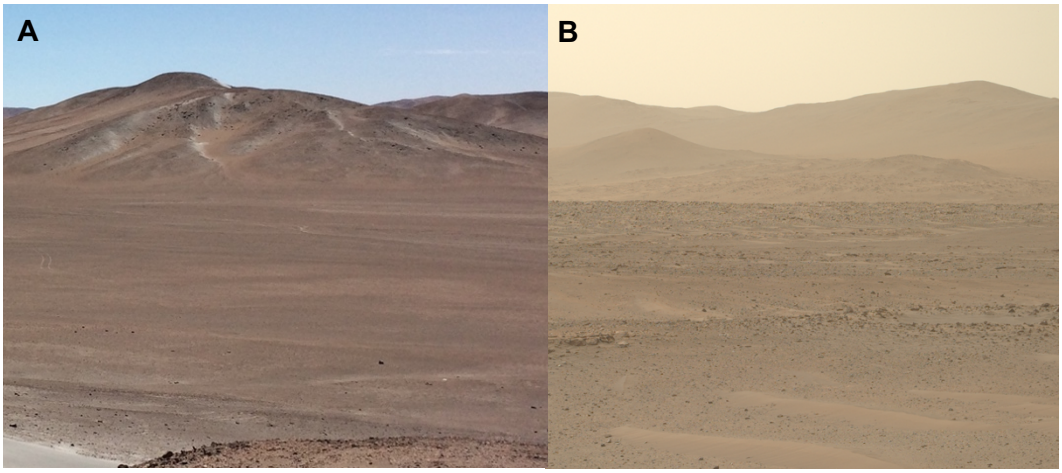

Figure 5.1: Images of hyperarid environments. **A)** The hyperarid region of *Pampas de la Joya* in the Atacama Desert taken on Sep 30, 2017, by Donald Glaser using an iPhone 5s. **B)** Inside Jezero Crater on Mars, looking toward the ancient delta outcrop taken on Aug 21, 2022, by NASA's Perseverance rover using Mastcam-Z. These two sites are similar in several ways, including visual appearance.

CHAPTER 5 REFERENCES

Böttger, H. M., Lewis, S. R., Read, P. L., and Forget, F. (**2005**). The effects of the martian regolith on GCM water cycle simulations. *Icarus*, *177*(1), 174–189. DOI: 10.1016/j.icarus.2005.02.024

Dose, K., Bieger-Dose, A., Ernst, B., Feister, U., Gómez-Silva, B., Klein, A., Risi, S., and Stridde, C. (**2001**). Survival of microorganisms under the extreme conditions of the Atacama Desert. *Origins of Life and Evolution of Biospheres*, *31*(3), 287–303. DOI: 10.1023/A:1010788829265

Razzell Hollis, J., Moore, K. R., Sharma, S., Beegle, L., Grotzinger, J. P., Allwood, A., Abbey, W., Bhartia, R., Brown, A. J., Clark, B., Cloutis, E., Corpolongo, A., Henneke, J., Hickman-Lewis, K., Hurowitz, J. A., Jones, M. W. M., Liu, Y., Martinez-Frías, J., Murphy, A., Pedersen, D. A. K., Shkolyar, S., Siljeström, S., Steele, A., Tice, M., Treiman, A., Uckert, K., VanBommel, S., and Yanchilina, A. (**2022**). The power of paired proximity science observations: Co-located data from SHERLOC and PIXL on Mars. *Icarus*, *387*, 115179. DOI: 10.1016/j.icarus.2022.115179

Savijärvi, H. I., and Harri, A.-M. (**2021**). Water vapor adsorption on Mars. *Icarus*, *357*, 114270. DOI: 10.1016/j.icarus.2020.114270

REFERENCES

AbdulHalim, R. G., Bhatt, P. M., Belmabkhout, Y., Shkurenko, A., Adil, K., Barbour, L. J., and Eddaoudi, M. (**2017**). A fine-tuned metal–organic framework for autonomous indoor moisture control. *Journal of the American Chemical Society*, *139*(31), 10715–10722. DOI: 10.1021/jacs.7b04132

Agam, N., and Berliner, P. R. (**2004**). Diurnal water content changes in the bare soil of a coastal desert. *Journal of Hydrometeorology*, *5*(5), 922–933. DOI: 10.1175/1525-7541(2004)005<0922:DWCCIT>2.0.CO;2

Agam, N., and Berliner, P. R. (**2006**). Dew formation and water vapor adsorption in semi-arid environments—A review. *Journal of Arid Environments*, *65*(4), 572–590. DOI: 10.1016/j.jaridenv.2005.09.004

Alduchov, O. A., and Eskridge, R. E. (**1996**). Improved magnus form approximation of saturation vapor pressure. *Journal of Applied Meteorology*, *35*(4), 601–609. DOI: 10.1175/1520-0450(1996)035<0601:IMFAOS>2.0.CO;2

Allan, M., Taylor, L. S., and Mauer, L. J. (**2016**). Common-ion effects on the deliquescence lowering of crystalline ingredient blends. *Food Chemistry*, *195*(15), 2–10. DOI: 10.1016/j.foodchem.2015.04.063

Allen, T. (**2013**). *Particle size measurement*. Springer.

Amer, A. M. (**2019**). Soil moisture adsorption capacity and specific surface area in relation to water vapor pressure in arid and tropical soils. *Eurasian Journal of Soil Science*, *8*(4), 289–297. DOI: 10.18393/ejss.580889

Anbazhagan, S., and Arivazhagan, S. (**2010**). Reflectance spectra of analog anorthosites: Implications for lunar highland mapping. *Planetary and Space Science*, *58*(5), 752–760. DOI: 10.1016/j.pss.2009.12.002

Angel, R., Matthies, D., and Conrad, R. (**2011**). Activation of methanogenesis in arid biological soil crusts despite the presence of oxygen. *PLOS ONE*, *6*(5), e20453. DOI: 10.1371/journal.pone.0020453

Arthur, E., Tuller, M., Moldrup, P., Jensen, D. K., and De Jonge, L. W. (**2015**). Prediction of clay content from water vapour sorption isotherms considering hysteresis and soil organic matter content: Clay content prediction from water vapour sorption. *European Journal of Soil Science*, *66*(1), 206–217. DOI: 10.1111/ejss.12191

Azua-Bustos, A., Fairén, A. G., González-Silva, C., Ascaso, C., Carrizo, D., Fernández-Martínez, M. Á., Fernández-Sampedro, M., García-Descalzo, L., García-Villadangos, M., Martin-Redondo, M. P., Sánchez-García, L., Wierzchos, J., and Parro, V. (**2018**). Unprecedented rains decimate surface microbial communities in the hyperarid core of the Atacama Desert. *Scientific Reports*, *8*(1). DOI: 10.1038/s41598-018-35051-w

Azúa-Bustos, A., González-Silva, C., Mancilla, R. A., Salas, L., Gómez-Silva, B., McKay, C. P., and Vicuña, R. (**2011**). Hypolithic cyanobacteria supported mainly by fog in the coastal range of the Atacama Desert. *Microbial Ecology*, *61*(3), 568–581. DOI: 10.1007/s00248-010-9784-5

cAzua-Bustos, A., Urrejola, C., and Vicuña, R. (**2012**). Life at the dry edge: Microorganisms of the Atacama Desert. *FEBS Letters*, *586*(18), 2939–2945. DOI: 10.1016/j.febslet.2012.07.025

Bastin, J.-F., Berrahmouni, N., Grainger, A., Maniatis, D., Mollicone, D., Moore, R., Patriarca, C., Picard, N., Sparrow, B., Abraham, E. M., Aloui, K., Atesoglu, A., Attore, F., Bassüllü, Ç., Bey, A., Garzuglia, M., García-Montero, L. G., Groot, N., Guerin, G., Laestadius, L., Lowe, A. J., Mamane, B., Marchi, G., Patterson, P., Rezende, M., Ricci, S., Salcedo, I., Diaz, A. S.-P., Stolle, F., Surappaeva, V., and Castro, R. (**2017**). The extent of forest in dryland biomes. *Science*, *356*(6338), 635–638. DOI: 10.1126/science.aam6527

Beck, P., Pommerol, A., Schmitt, B., and Brissaud, O. (**2010**). Kinetics of water adsorption on minerals and the breathing of the Martian regolith. *Journal of Geophysical Research*, *115*(E10), E10011. DOI: 10.1029/2009JE003539

Belilla, J., Moreira, D., Jardillier, L., Reboul, G., Benzerara, K., López-García, J. M., Bertolino, P., López-Archilla, A. I., and López-García, P. (**2019**). Hyperdiverse archaea near life limits at the polyextreme geothermal Dallol area. *Nature Ecology & Evolution*, *3*(11), 1552–1561. DOI: 10.1038/s41559-019-1005-0

Bendia, A. G., Araujo, G. G., Pulschen, A. A., Contro, B., Duarte, R. T. D., Rodrigues, F., Galante, D., and Pellizari, V. H. (**2018**). Surviving in hot and cold: Psychrophiles and thermophiles from Deception Island volcano, Antarctica. *Extremophiles*, *22*(6), 917–929. DOI: 10.1007/s00792-018-1048-1

Berghuis, B. A., Yu, F. B., Schulz, F., Blainey, P. C., Woyke, T., and Quake, S. R. (**2019**). Hydrogenotrophic methanogenesis in archaeal phylum Verstraetearchaeota reveals the shared ancestry of all methanogens. *Proceedings of the National Academy of Sciences*, *116*(11), 5037–5044. DOI: 10.1073/pnas.1815631116

Bhambhani, M. R., Cutting, P. A., Sing, K. S. W., and Turk, D. H. (**1972**). Analysis of nitrogen adsorption isotherms on porous and nonporous silicas by the BET and αs methods. *Journal of Colloid and Interface Science*, *38*(1), 109–117. DOI: 10.1016/0021-9797(72)90226-3

Borch, T., Kretzschmar, R., Kappler, A., Cappellen, P. V., Ginder-Vogel, M., Voegelin, A., and Campbell, K. (**2010**). Biogeochemical redox processes and their impact on contaminant dynamics. *Environmental Science & Technology*, *44*(1), 15–23. DOI: 10.1021/es9026248

Böttger, H. M., Lewis, S. R., Read, P. L., and Forget, F. (**2005**). The effects of the martian regolith on GCM water cycle simulations. *Icarus*, *177*(1), 174–189. DOI: 10.1016/j.icarus.2005.02.024

Butler, B. M., and Hillier, S. (**2021**). powdR: An R package for quantitative mineralogy using full pattern summation of X-ray powder diffraction data. *Computers & Geosciences*, *147*, 104662. DOI: 10.1016/j.cageo.2020.104662

Campbell, G., and Shiozawa, S. (**1992**). Prediction of hydraulic properties of soils using particle-size distribution and bulk density data. *Indirect Methods for Estimating the Hydraulic Properties of Unsaturated Soils*, 317–328.

Chan-Yam, K., Goordial, J., Greer, C., Davila, A., McKay, C. P., and Whyte, L. G. (**2019**). Microbial activity and habitability of an Antarctic dry valley water track. *Astrobiology*, ast.2018.1884. DOI: 10.1089/ast.2018.1884

Chen, Y., Han, X., Wang, Y., and Lu, J. (**2020**). Precipitation of calcite veins in serpentinized harzburgite at Tianxiu hydrothermal field on Carlsberg ridge (3.67°N), northwest Indian ocean: Implications for fluid circulation. *Journal of Earth Science*, *31*(1), 91–101. DOI: 10.1007/s12583-020-0876-y

Chiquoine, L. P., Abella, S. R., and Bowker, M. A. (**2016**). Rapidly restoring biological soil crusts and ecosystem functions in a severely disturbed desert ecosystem. *Ecological Applications*, *26*(4), 1260–1272. DOI: 10.1002/15-0973

Conrad, R. (**1996**). Soil microorganisms as controllers of atmospheric trace gases (H_2, CO, CH_4, OCS, N_2O, and NO). *Microbiological Reviews*, *60*(4), 609.

Conrad, R., and Seiler, W. (**1985**). Characteristics of abiological carbon monoxide formation from soil organic matter, humic acids, and phenolic compounds. *Environmental Science & Technology*, *19*(12), 1165–1169. DOI: 10.1021/es00142a004

Dashora, P., Gupta, G., and Dashora, J. (**2005**). Thermal conductivity, diffusivity and heat capacity of plasticized polyvinyl chloride. *Indian Journal of Pure and Applied Physics*, *43*(2), 132–136.

Davila, A. F., Gómez-Silva, B., de los Rios, A., Ascaso, C., Olivares, H., McKay, C. P., and Wierzchos, J. (**2008**). Facilitation of endolithic microbial survival in the hyperarid core of the Atacama Desert by mineral deliquescence: Deliquescence and microbial survival. *Journal of Geophysical Research: Biogeosciences*, *113*(G1). DOI: 10.1029/2007JG000561

Day, P. R. (**1965**). Hydrometer method of particle size analysis. *Methods of Soil Analysis. Agronomy*, *9*, 562–566.

Domagal-Goldman, S. D., Wright, K. E., Adamala, K., Arina de la Rubia, L., Bond, J., Dartnell, L. R., Goldman, A. D., Lynch, K., Naud, M.-E., Paulino-Lima, I. G., Singer, K., Walter-Antonio, M., Abrevaya, X. C., Anderson, R., Arney, G., Atri, D., Azúa-Bustos, A., Bowman, J. S., Brazelton, W. J., Brennecka, G. A., Carns, R., Chopra, A., Colangelo-Lillis, J., Crockett, C. J., DeMarines, J., Frank, E. A., Frantz, C., de la Fuente, E., Galante, D., Glass, J., Gleeson, D., Glein, C. R., Goldblatt, C., Horak, R., Horodyskyj, L., Kaçar, B., Kereszturi, A., Knowles, E., Mayeur, P., McGlynn, S., Miguel, Y., Montgomery, M., Neish, C., Noack, L., Rugheimer, S., Stüeken, E. E., Tamez-Hidalgo, P., Walker, S. I., and Wong, T. (**2016**). The astrobiology primer v2.0. *Astrobiology*, *16*(8), 561–653. DOI: 10.1089/ast.2015.1460

Dong, J., Fischer, R. A., Stixrude, L. P., Lithgow-Bertelloni, C. R., Eriksen, Z. T., and Brennan, M. C. (**2022**). Water storage capacity of the martian mantle through time. *Icarus*, *385*, 115113. DOI: 10.1016/j.icarus.2022.115113

Dose, K., Bieger-Dose, A., Ernst, B., Feister, U., Gómez-Silva, B., Klein, A., Risi, S., and Stridde, C. (**2001**). Survival of microorganisms under the extreme conditions of the Atacama Desert. *Origins of Life and Evolution of Biospheres*, *31*(3), 287–303. DOI: 10.1023/A:1010788829265

Douglas, P. M. J., Stolper, D. A., Eiler, J. M., Sessions, A. L., Lawson, M., Shuai, Y., Bishop, A., Podlaha, O. G., Ferreira, A. A., Santos Neto, E. V., Niemann, M., Steen, A. S., Huang, L., Chimiak, L., Valentine, D. L., Fiebig, J., Luhmann, A. J., Seyfried, W. E., Etiope, G., Schoell, M., Inskeep, W. P., Moran, J. J., and Kitchen, N. (**2017**). Methane clumped isotopes: Progress and potential for a new isotopic tracer. *Organic Geochemistry*, *113*, 262–282. DOI: 10.1016/j.orggeochem.2017.07.016

Dupas-Langlet, M., Benali, M., Pezron, I., Saleh, K., and Metlas-Komunjer, L. (**2013**). Deliquescence lowering in mixtures of NaCl and sucrose powders elucidated by modeling the water activity of corresponding solutions. *Journal of Food Engineering*, *115*(3), 391–397. DOI: 10.1016/j.jfoodeng.2012.10.042

Eberl, D. (**2003**). *User guide to RockJock-A program for determining quantitative mineralogy from X-ray diffraction data* (No. 2331–1258). US Geological Survey.

El Fadli, K. I., Cerveny, R. S., Burt, C. C., Eden, P., Parker, D., Brunet, M., Peterson, T. C., Mordacchini, G., Pelino, V., Bessemoulin, P., Stella, J. L., Driouech, F., Wahab, M. M. A., and Pace, M. B. (**2013**). World Meteorological Organization assessment of the purported world record 58°C temperature extreme at El Azizia, Libya (13 September 1922). *Bulletin of the American Meteorological Society*, *94*(2), 199–204. DOI: 10.1175/BAMS-D-12-00093.1

Fedorova, A., Montmessin, F., Korablev, O., Lefèvre, F., Trokhimovskiy, A., and Bertaux, J. (**2021**). Multi-annual monitoring of the water vapor vertical distribution on Mars by SPICAM on Mars express. *Journal of Geophysical Research: Planets*, *126*(1). DOI: 10.1029/2020JE006616

Fernández-Martínez, M. Á., dos Santos Severino, R., Moreno-Paz, M., Gallardo-Carreño, I., Blanco, Y., Warren-Rhodes, K., García-Villadangos, M., Ruiz-Bermejo, M., Barberán, A., Wettergreen, D., Cabrol, N., and Parro, V. (**2019**). Prokaryotic community structure and metabolisms in shallow subsurface of Atacama Desert playas and alluvial fans after heavy rains: Repairing and preparing for next dry period. *Frontiers in Microbiology*, *10*, 1641. DOI: 10.3389/fmicb.2019.01641

Fischer, E., Martínez, G. M., Rennó, N. O., Tamppari, L. K., and Zent, A. P. (**2019**). Relative humidity on Mars: New results from the Phoenix TECP sensor. *Journal of Geophysical Research: Planets*, 2019JE006080. DOI: 10.1029/2019JE006080

Fletcher, A. J., Uygur, Y., and Thomas, K. M. (**2007**). Role of surface functional groups in the adsorption kinetics of water vapor on microporous activated carbons. *The Journal of Physical Chemistry C*, *111*(23), 8349–8359. DOI: 10.1021/jp070815v

Frost, C. D., Frost, B. R., and Beard, J. S. (**2016**). On silica-rich granitoids and their eruptive equivalents. *American Mineralogist*, *101*(6), 1268–1284. DOI: 10.2138/am-2016-5307

Gao, Z., Horton, R., and Liu, H. P. (**2010**). Impact of wave phase difference between soil surface heat flux and soil surface temperature on soil surface energy balance closure. *Journal of Geophysical Research*, *115*(D16), D16112. DOI: 10.1029/2009JD013278

Garcia-Pichel, F., Johnson, S. L., Youngkin, D., and Belnap, J. (**2003**). Small-scale vertical distribution of bacterial biomass and diversity in biological soil crusts from arid lands in

the Colorado Plateau. *Microbial Ecology*, *46*(3), 312–321. DOI: 10.1007/s00248-003-1004-0

Glaser, D. M., Hartnett, H. E., Finn, D. R., Perez-Montaño, S., Cadillo-Quiroz, H., and Desch, S. (**2022**). Water Vapor Adsorption Provides Daily, Sustainable Water to Soils of the Hyperarid Atacama Desert. *Astrobiology*, *22*(10), 1222–1238. DOI: 10.1089/ast.2021.0171

Gödde, M., Meuser, K., and Conrad, R. (**2000**). Hydrogen consumption and carbon monoxide production in soils with different properties. *Biology and Fertility of Soils*, *32*(2), 129–134. DOI: 10.1007/s003740000226

Gough, R. V., Chevrier, V. F., and Tolbert, M. A. (**2014**). Formation of aqueous solutions on Mars via deliquescence of chloride–perchlorate binary mixtures. *Earth and Planetary Science Letters*, *393*, 73–82. DOI: 10.1016/j.epsl.2014.02.002

Gough, R. V., Chevrier, V. F., and Tolbert, M. A. (**2016**). Formation of liquid water at low temperatures via the deliquescence of calcium chloride: Implications for Antarctica and Mars. *Planetary and Space Science*, *131*, 79–87. DOI: 10.1016/j.pss.2016.07.006

Graber, A., Santi, P., and Meza Arestegui, P. (**2021**). Constraining the critical groundwater conditions for initiation of large, irrigation-induced landslides, Siguas River Valley, Peru. *Landslides*, *18*(12), 3753–3767. DOI: 10.1007/s10346-021-01767-6

Graf, D. L. (**1961**). Crystallographic tables for the rhombohedral carbonates. *American Mineralogist*, *46*(11–12), 1283–1316. DOI: 10.1007/BF03176144

Grasset, O., Castillo-Rogez, J., Guillot, T., Fletcher, L. N., and Tosi, F. (**2017**). Water and volatiles in the outer solar system. *Space Science Reviews*, *212*(1–2), 835–875. DOI: 10.1007/s11214-017-0407-z

Green, D. H., and Ringwood, A. E. (**1967**). The genesis of basaltic magmas. *Contributions to Mineralogy and Petrology*, *15*(2), 103–190. DOI: 10.1007/BF00372052

Guo, L., Gu, W., Peng, C., Wang, W., Li, Y. J., Zong, T., Tang, Y., Wu, Z., Lin, Q., Ge, M., Zhang, G., Hu, M., Bi, X., Wang, X., and Tang, M. (**2019**). A comprehensive study of hygroscopic properties of calcium- and magnesium-containing salts: Implication for hygroscopicity of mineral dust and sea salt aerosols. *Atmospheric Chemistry and Physics*, *19*(4), 2115–2133. DOI: 10.5194/acp-19-2115-2019

Hall, S. J., Silver, W. L., and Amundson, R. (**2012**). Greenhouse gas fluxes from Atacama Desert soils: A test of biogeochemical potential at the Earth's arid extreme. *Biogeochemistry*, *111*(1–3), 303–315. DOI: 10.1007/s10533-011-9650-7

Hamilton, V. E., and Christensen, P. R. (**2005**). Evidence for extensive, olivine-rich bedrock on Mars. *Geology*, *33*(6), 433. DOI: 10.1130/G21258.1

Hartmann, L., Ciesla, F., Gressel, O., and Alexander, R. (**2017**). Disk evolution and the fate of water. *Space Science Reviews*, *212*(1–2), 813–834. DOI: 10.1007/s11214-017-0406-0

Hecker, C., der Meijde, M. van, and van der Meer, F. D. (**2010**). Thermal infrared spectroscopy on feldspars—Successes, limitations and their implications for remote sensing. *Earth Science Reviews*, *103*(1–2), 60–70. DOI: 10.1016/j.earscirev.2010.07.005

Hedges, J. I., and Stern, J. H. (**1984**). Carbon and nitrogen determinations of carbonate-containing solids. *Limnology and Oceanography*, *29*(3), 657–663. DOI: 10.4319/lo.1984.29.3.0657

Heinz, J., Rambags, V., and Schulze-Makuch, D. (**2021**). Physicochemical parameters limiting growth of Debaryomyces hansenii in solutions of hygroscopic compounds and their effects on the habitability of Martian brines. *Life*, *11*(11), 1194. DOI: 10.3390/life11111194

Hickman-Lewis, K., Moore, K. R., Hollis, J. J. R., Tuite, M. L., Beegle, L. W., Bhartia, R., Grotzinger, J. P., Brown, A. J., Shkolyar, S., Cavalazzi, B., and Smith, C. L. (**2022**). *In situ* Identification of paleoarchean biosignatures using colocated perseverance rover analyses: Perspectives for *in situ* Mars science and sample return. *Astrobiology*, *22*(9), 1143–1163. DOI: 10.1089/ast.2022.0018

Houben, H. (**1999**). The martian diurnal water cycle. *Advances in Space Research*, *23*(9), 1587–1590. DOI: 10.1016/S0273-1177(99)00174-X

Houston, J., and Hartley, A. J. (**2003**). The central Andean west-slope rainshadow and its potential contribution to the origin of hyper-aridity in the Atacama Desert. *International Journal of Climatology*, *23*(12), 1453–1464. DOI: 10.1002/joc.938

Izidoro, A., de Souza Torres, K., Winter, O. C., and Haghighipour, N. (**2013**). A compound model for the origin of Earth's water. *The Astrophysical Journal*, *767*(1), 54. DOI: 10.1088/0004-637X/767/1/54

Jabro, J. D. (**2009**). Water vapor diffusion through soil as affected by temperature and aggregate size. *Transport in Porous Media*, *77*(3), 417–428. DOI: 10.1007/s11242-008-9267-z

Jacobs, A. F. G., Heusinkveld, B. G., and Berkowicz, S. M. (**2002**). A simple model for potential dewfall in an arid region. *Atmospheric Research*, *64*(1–4), 285–295. DOI: 10.1016/S0169-8095(02)00099-6

Jacobson, K., van Diepeningen, A., Evans, S., Fritts, R., Gemmel, P., Marsho, C., Seely, M., Wenndt, A., Yang, X., and Jacobson, P. (**2015**). Non-rainfall moisture activates fungal decomposition of surface litter in the Namib sand sea. *PLOS ONE*, *10*(5). DOI: 10.1371/journal.pone.0126977

Ji, M., Greening, C., Vanwonterghem, I., Carere, C. R., Bay, S. K., Steen, J. A., Montgomery, K., Lines, T., Beardall, J., van Dorst, J., Snape, I., Stott, M. B., Hugenholtz, P., and Ferrari, B. C. (**2017**). Atmospheric trace gases support primary production in Antarctic desert surface soil. *Nature*, *552*(7685), 400–403. DOI: 10.1038/nature25014

Jones, D. L., Olivera-Ardid, S., Klumpp, E., Knief, C., Hill, P. W., Lehndorff, E., and Bol, R. (**2018**). Moisture activation and carbon use efficiency of soil microbial communities along an aridity gradient in the Atacama Desert. *Soil Biology and Biochemistry*, *117*, 68–71. DOI: 10.1016/j.soilbio.2017.10.026

Kaiser, K., and Guggenberger, G. (**2003**). Mineral surfaces and soil organic matter. *European Journal of Soil Science*, *54*(2), 219–236. DOI: 10.1046/j.1365-2389.2003.00544.x

Kaseke, K. F., Mills, A. J., Brown, R., Esler, K. J., Henschel, J. R., and Seely, M. K. (**2012**a). A method for direct assessment of the "non rainfall" atmospheric water cycle: Input and evaporation from the soil. *Pure and Applied Geophysics*, *169*(5–6), 847–857. DOI: 10.1007/s00024-011-0328-9

Kaseke, K. F., Mills, A. J., Esler, K., Henschel, J., Seely, M. K., and Brown, R. (**2012**b). Spatial variation of "non-rainfall" water input and the effect of mechanical soil crusts on input and evaporation. *Pure and Applied Geophysics*, *169*(12), 2217–2229. DOI: 10.1007/s00024-012-0469-5

Kite, E. S. (**2019**). Geologic Constraints on Early Mars Climate. *Space Science Reviews*, *215*(1), 10. DOI: 10.1007/s11214-018-0575-5

Koeniger, P., Marshall, J. D., Link, T., and Mulch, A. (**2011**). An inexpensive, fast, and reliable method for vacuum extraction of soil and plant water for stable isotope analyses by mass spectrometry: Vacuum extraction of soil and plant water for stable isotope analyses. *Rapid Communications in Mass Spectrometry*, *25*(20), 3041–3048. DOI: 10.1002/rcm.5198

Kool, D., Agra, E., Drabkin, A., Duncan, A., Fendinat, P. P., Leduc, S., Lupovitch, G., Nambwandja, A. N., Ndilenga, N. S., Nguyễn Thị, T., Poodiack, B., Sagi, L., Shmuel, Y., Maggs-Kölling, G., Marais, E., Pinshow, B., Turner, J. S., and Agam, N. (**2021**). The overlooked non-rainfall water input sibling of fog and dew: Daily water vapor adsorption on a !Nara hummock in the Namib Sand Sea. *Journal of Hydrology*, *598*, 126420. DOI: 10.1016/j.jhydrol.2021.126420

Kosmas, C., Danalatos, N. G., Poesen, J., and van Wesemael, B. (**1998**). The effect of water vapour adsorption on soil moisture content under Mediterranean climatic conditions. *Agricultural Water Management*, *36*(2), 157–168. DOI: 10.1016/S0378-3774(97)00050-4

Kosmas, C., Marathianou, M., Gerontidis, S., Detsis, V., Tsara, M., and Poesen, J. (**2001**). Parameters affecting water vapor adsorption by the soil under semi-arid climatic conditions. *Agricultural Water Management*, *48*(1), 61–78. DOI: 10.1016/S0378-3774(00)00113-X

Koutsoyiannis, D. (**2012**). Clausius–Clapeyron equation and saturation vapour pressure: Simple theory reconciled with practice. *European Journal of Physics*, *33*(2), 295–305. DOI: 10.1088/0143-0807/33/2/295

Lane, M. D., and Christensen, P. R. (**2013**). Determining olivine composition of basaltic dunes in Gale Crater, Mars, from orbit: Awaiting ground truth from Curiosity. *Geophysical Research Letters*, *40*(14), 3517–3521. DOI: 10.1002/grl.50621

Latosińska, J. N., Latosińska, M., and Bielak, J. (**2015**). Towards analysis and predicting maps of ultraviolet index from experimental astronomical parameters (solar elevation, total ozone level, aerosol index, reflectivity). Artificial neural networks global scale approach. *Aerospace Science and Technology*, *43*, 301–313. DOI: 10.1016/j.ast.2015.03.011

Lauro, S. E., Pettinelli, E., Caprarelli, G., Guallini, L., Rossi, A. P., Mattei, E., Cosciotti, B., Cicchetti, A., Soldovieri, F., Cartacci, M., Di Paolo, F., Noschese, R., and Orosei, R.

(**2021**). Multiple subglacial water bodies below the south pole of Mars unveiled by new MARSIS data. *Nature Astronomy*, *5*(1), 63–70. DOI: 10.1038/s41550-020-1200-6

Lawrence, M. G. (**2005**). The relationship between relative humidity and the dewpoint temperature in moist air: A simple conversion and applications. *Bulletin of the American Meteorological Society*, *86*(2), 225–234. DOI: 10.1175/BAMS-86-2-225

Leão, T. P., and Tuller, M. (**2014**). Relating soil specific surface area, water film thickness, and water vapor adsorption. *Water Resources Research*, *50*(10), 7873–7885. DOI: 10.1002/2013WR014941

Levien, L., Prewitt, C. T., and Weidner, D. J. (**1980**). Structure and elastic properties of quartz at pressure. *American Mineralogist*, *65*(9–10), 920–930.

Levin, G. V., and Straat, P. A. (**1976**). Labeled release—An experiment in radiorespirometry. *Origins of Life*, *7*(3), 293–311. DOI: 10.1007/BF00926948

Li, L., Zhang, X., Luan, Z., Du, Z., Xi, S., Wang, B., Cao, L., Lian, C., and Yan, J. (**2018**). *In situ* quantitative raman detection of dissolved carbon dioxide and sulfate in deep-sea high-temperature hydrothermal vent fluids. *Geochemistry, Geophysics, Geosystems*, *19*(6), 1809–1823. DOI: 10.1029/2018GC007445

Liu, L., Tan, S. (Johnathan), Horikawa, T., Do, D. D., Nicholson, D., and Liu, J. (**2017**). Water adsorption on carbon—A review. *Advances in Colloid and Interface Science*, *250*, 64–78. DOI: 10.1016/j.cis.2017.10.002

Lynch, R. C., Darcy, J. L., Kane, N. C., Nemergut, D. R., and Schmidt, S. K. (**2014**). Metagenomic evidence for metabolism of trace atmospheric gases by high-elevation desert Actinobacteria. *Frontiers in Microbiology*, *5*. DOI: 10.3389/fmicb.2014.00698

Lyu, Z., Shao, N., Akinyemi, T., and Whitman, W. B. (**2018**). Methanogenesis. *Current Biology*, *28*(13), R727–R732. DOI: 10.1016/j.cub.2018.05.021

Mason, B. (**1963**). Olivine composition in chondrites. *Geochimica et Cosmochimica Acta*, *27*(10), 1011–1023. DOI: 10.1016/0016-7037(63)90062-0

McCaskey, J. P. (**2020**). History of 'temperature': Maturation of a measurement concept. *Annals of Science*, *77*(4), 399–444. DOI: 10.1080/00033790.2020.1817980

McHugh, T. A., Morrissey, E. M., Reed, S. C., Hungate, B. A., and Schwartz, E. (**2015**). Water from air: An overlooked source of moisture in arid and semiarid regions. *Scientific Reports*, *5*(1). DOI: 10.1038/srep13767

McKay, C. P., Friedmann, E. I., Gómez-Silva, B., Cáceres-Villanueva, L., Andersen, D. T., and Landheim, R. (**2003**). Temperature and moisture conditions for life in the extreme arid region of the Atacama Desert: Four years of observations including the El Niño of 1997–1998. *Astrobiology*, *3*(2), 393–406. DOI: 10.1089/153110703769016460

Mellini, M. (**1982**). The crystal structure of lizardite 1T: hydrogen bonds and polytypism. *American Mineralogist*, *67*(5–6), 587–598.

Nádudvari, Á., Abramowicz, A., Maniscalco, R., and Viccaro, M. (**2020**). The estimation of lava flow temperatures using landsat night-time Images: Case studies from eruptions of

Mt. Etna and Stromboli (Sicily, Italy), Kīlauea (Hawaii Island), and Eyjafjallajökull and Holuhraun (Iceland). *Remote Sensing*, *12*(16), 2537. DOI: 10.3390/rs12162537

Nanni, E. J., Stallings, M. D., and Sawyer, D. T. (**1980**). Does superoxide ion oxidize catechol, α-tocopherol, and ascorbic acid by direct electron transfer? *Journal of the American Chemical Society*, *102*(13), 4481–4485. DOI: 10.1021/ja00533a029

Narvaez-Montoya, C., Torres-Martínez, J. A., Pino-Vargas, E., Cabrera-Olivera, F., Loge, F. J., and Mahlknecht, J. (**2022**). Predicting adverse scenarios for a transboundary coastal aquifer system in the Atacama Desert (Peru/Chile). *Science of The Total Environment*, *806*, 150386. DOI: 10.1016/j.scitotenv.2021.150386

Navarro-González, R., McKay, C. P., and Mvondo, D. N. (**2001**). A possible nitrogen crisis for Archaean life due to reduced nitrogen fixation by lightning. *Nature*, *412*(6842), 61–64. DOI: 10.1038/35083537

Navarro-Gonzalez, R., Rainey, F., Molina, P., Bagaley, D., Hollen, B., de la Rosa, J., Small, A., Quinn, R., Grunthaner, F., Caceres, L., Gomez-Silva, B., and McKay, C. (**2003**). Mars-like soils in the Atacama Desert, Chile, and the dry limit of microbial life. *Science*, *302*(5647), 1018–1021. DOI: 10.1126/science.1089143

Nelson Eby, G. (**2016**). *Principles of environmental geochemistry*. Waveland Press, Inc.

Nord, A. G., Annersten, H., and Filippidis, A. (**1982**). The cation distribution in synthetic Mg–Fe–Ni olivines. *American Mineralogist*, *67*(11–12), 1206–1211.

O'Brien, D. P., Izidoro, A., Jacobson, S. A., Raymond, S. N., and Rubie, D. C. (**2018**). The delivery of water during terrestrial planet formation. *Space Science Reviews*, *214*(1), 47. DOI: 10.1007/s11214-018-0475-8

O'Connor, F. M., Boucher, O., Gedney, N., Jones, C. D., Folberth, G. A., Coppell, R., Friedlingstein, P., Collins, W. J., Chappellaz, J., Ridley, J., and Johnson, C. E. (**2010**). Possible role of wetlands, permafrost, and methane hydrates in the methane cycle under future climate change: A review. *Reviews of Geophysics*, *48*(4). DOI: 10.1029/2010RG000326

Ohtani, E. (**1983**). Formation of olivine textures in pallasites and thermal history of pallasites in their parent body. *Physics of the Earth and Planetary Interiors*, *32*(2), 182–192. DOI: 10.1016/0031-9201(83)90138-3

Pan, X., Angelidaki, I., Alvarado-Morales, M., Liu, H., Liu, Y., Huang, X., and Zhu, G. (**2016**). Methane production from formate, acetate and H_2/CO_2; focusing on kinetics and microbial characterization. *Bioresource Technology*, *218*, 796–806. DOI: 10.1016/j.biortech.2016.07.032

Pei, L., Min, Q., Du, Y., Wang, Z., Yin, B., Yang, K., Disterhoft, P., Pongetti, T., and Zhu, L. (**2019**). Water vapor near-UV absorption: Laboratory spectrum, field evidence, and atmospheric impacts. *Journal of Geophysical Research: Atmospheres*, *124*(24), 14310–14324. DOI: 10.1029/2019JD030724

Penning, H., and Conrad, R. (**2006**). Effect of inhibition of acetoclastic methanogenesis on growth of archaeal populations in an anoxic model environment. *Applied and Environmental Microbiology*, *72*(1), 178–184. DOI: 10.1128/AEM.72.1.178-184.2006

Peslier, A. H., and Bizimis, M. (**2015**). Water in Hawaiian peridotite minerals: A case for a dry metasomatized oceanic mantle lithosphere. *Geochemistry, Geophysics, Geosystems*, *16*(4), 1211–1232. DOI: 10.1002/2015GC005780

Piqueux, S., Buz, J., Edwards, C. S., Bandfield, J. L., Kleinböhl, A., Kass, D. M., Hayne, P. O., The MCS, and THEMIS Teams. (**2019**). Widespread shallow water ice on Mars at high latitudes and midlatitudes. *Geophysical Research Letters*, *46*(24), 14290–14298. DOI: 10.1029/2019GL083947

Pointing, S. B., and Belnap, J. (**2012**). Microbial colonization and controls in dryland systems. *Nature Reviews Microbiology*, *10*(8), 551–562. DOI: 10.1038/nrmicro2831

Pyle, L. A., Hall, L. M., and Bork, E. W. (**2019**). Soil properties in northern temperate pastures do not vary with management practices and are independent of rangeland health. *Canadian Journal of Soil Science*, *99*(4), 495–507. DOI: 10.1139/cjss-2019-0076

Razzell Hollis, J., Moore, K. R., Sharma, S., Beegle, L., Grotzinger, J. P., Allwood, A., Abbey, W., Bhartia, R., Brown, A. J., Clark, B., Cloutis, E., Corpolongo, A., Henneke, J., Hickman-Lewis, K., Hurowitz, J. A., Jones, M. W. M., Liu, Y., Martinez-Frías, J., Murphy, A., Pedersen, D. A. K., Shkolyar, S., Siljeström, S., Steele, A., Tice, M., Treiman, A., Uckert, K., VanBommel, S., and Yanchilina, A. (**2022**). The power of paired proximity science observations: Co-located data from SHERLOC and PIXL on Mars. *Icarus*, *387*, 115179. DOI: 10.1016/j.icarus.2022.115179

Rennó, N. O., Bos, B. J., Catling, D., Clark, B. C., Drube, L., Fisher, D., Goetz, W., Hviid, S. F., Keller, H. U., Kok, J. F., Kounaves, S. P., Leer, K., Lemmon, M., Madsen, M. B., Markiewicz, W. J., Marshall, J., McKay, C., Mehta, M., Smith, M., Zorzano, M. P., Smith, P. H., Stoker, C., and Young, S. M. M. (**2009**). Possible physical and thermodynamical evidence for liquid water at the Phoenix landing site. *Journal of Geophysical Research*, *114*. DOI: 10.1029/2009JE003362

Resurreccion, A. C., Moldrup, P., Tuller, M., Ferré, T. P. A., Kawamoto, K., Komatsu, T., and de Jonge, L. W. (**2011**). Relationship between specific surface area and the dry end of the water retention curve for soils with varying clay and organic carbon contents: SOIL WATER CHARACTERISTIC CURVE. *Water Resources Research*, *47*(6). DOI: 10.1029/2010WR010229

Robertson, E. C. (**1988**). Thermal properties of rocks. *USGS Open-File Report 88-441*, 106. DOI: 10.3133/ofr88441

Rockland, L. B. (**1960**). Saturated salt solutions for static control of relative humidity between 5° and 40°C. *Analytical Chemistry*, *32*(10), 1375–1376. DOI: 10.1021/ac60166a055

Saethre, E. (**2007**). Close encounters: UFO beliefs in a remote Australian Aboriginal community. *Journal of the Royal Anthropological Institute*, *13*(4), 901–915. DOI: 10.1111/j.1467-9655.2007.00463.x

Safriel, U., Adeel, Z., Niemeijer, D., Puigdefabregas, J., White, R., Lal, R., Winslow, M., Ziedler, J., Prince, S., and Archer, E. (**2005**). Dryland Systems. In *Ecosystems and human well-being: Current state and trends* (pp. 623–662). Island Press.

Savijärvi, H. I., and Harri, A.-M. (**2021**). Water vapor adsorption on Mars. *Icarus*, *357*, 114270. DOI: 10.1016/j.icarus.2020.114270

Savijärvi, H. I., Harri, A.-M., and Kemppinen, O. (**2015**). Mars science laboratory diurnal moisture observations and column simulations: MSL diurnal moisture. *Journal of Geophysical Research: Planets*, *120*(5), 1011–1021. DOI: 10.1002/2014JE004732

Scambos, T. A., Campbell, G. G., Pope, A., Haran, T., Muto, A., Lazzara, M., Reijmer, C. H., and van den Broeke, M. R. (**2018**). Ultralow surface temperatures in east Antarctica from satellite thermal infrared mapping: The coldest places on Earth. *Geophysical Research Letters*, *45*(12), 6124–6133. DOI: 10.1029/2018GL078133

Schulze-Makuch, D., Wagner, D., Kounaves, S. P., Mangelsdorf, K., Devine, K. G., de Vera, J.-P., Schmitt-Kopplin, P., Grossart, H.-P., Parro, V., Kaupenjohann, M., Galy, A., Schneider, B., Airo, A., Frösler, J., Davila, A. F., Arens, F. L., Cáceres, L., Cornejo, F. S., Carrizo, D., Dartnell, L., DiRuggiero, J., Flury, M., Ganzert, L., Gessner, M. O., Grathwohl, P., Guan, L., Heinz, J., Hess, M., Keppler, F., Maus, D., McKay, C. P., Meckenstock, R. U., Montgomery, W., Oberlin, E. A., Probst, A. J., Sáenz, J. S., Sattler, T., Schirmack, J., Sephton, M. A., Schloter, M., Uhl, J., Valenzuela, B., Vestergaard, G., Wörmer, L., and Zamorano, P. (**2018**). Transitory microbial habitat in the hyperarid Atacama Desert. *Proceedings of the National Academy of Sciences*, *115*(11), 2670–2675. DOI: 10.1073/pnas.1714341115

Schumacher, B. A., Shines, K. C., Burton, J. V., and Papp, M. L. (**1990**). Comparison of Three Methods for Soil Homogenization. *Soil Science Society of America Journal*, *54*(4), 1187–1190. DOI: 10.2136/sssaj1990.03615995005400040046x

Seiff, A., Kirk, D. B., Knight, T. C. D., Young, R. E., Mihalov, J. D., Young, L. A., Milos, F. S., Schubert, G., Blanchard, R. C., and Atkinson, D. (**1998**). Thermal structure of Jupiter's atmosphere near the edge of a 5-μm hot spot in the north equatorial belt. *Journal of Geophysical Research: Planets*, *103*(E10), 22857–22889. DOI: 10.1029/98JE01766

Serrano-Silva, N., Sarria-Guzmán, Y., Dendooven, L., and Luna-Guido, M. (**2014**). Methanogenesis and methanotrophy in soil: A review. *Pedosphere*, *24*(3), 291–307. DOI: 10.1016/S1002-0160(14)60016-3

Shen, J. (**2020**). Phospholipid biomarkers in Mars-analogous soils of the Atacama Desert. *International Journal of Astrobiology*, *19*(6), 505–514. DOI: 10.1017/S1473550420000294

Shock, E. L., Holland, M., Meyer-Dombard, D., Amend, J. P., Osburn, G. R., and Fischer, T. P. (**2010**). Quantifying inorganic sources of geochemical energy in hydrothermal ecosystems, Yellowstone National Park, USA. *Geochimica et Cosmochimica Acta*, *74*(14), 4005–4043. DOI: 10.1016/j.gca.2009.08.036

Singh, J. S., Raghubanshi, A. S., Reddy, V. S., Singh, S., and Kashyap, A. K. (**1998**). Methane flux from irrigated paddy and dryland rice fields, and from seasonally dry tropical forest

and Savanna soils of India. *Soil Biology and Biochemistry*, *30*(2), 135–139. DOI: 10.1016/S0038-0717(97)00112-0

Smith, I. B., Lalich, D. E., Rezza, C., Horgan, B. H. N., Whitten, J. L., Nerozzi, S., and Holt, J. W. (**2021**). A solid interpretation of bright radar reflectors under the Mars south polar ice. *Geophysical Research Letters*, *48*(15). DOI: 10.1029/2021GL093618

Soil Survey Staff. (**2014**). *Kellogg soil survey laboratory methods manual* (42 version 5). US Department of Agriculture, Natural Resources Conservation Service.

Srodoń, J., Drits, V. A., McCarty, D. K., Hsieh, J. C. C., and Eberl, D. D. (**2001**). Quantitative X-Ray diffraction analysis of clay-bearing rocks from random preparations. *Clays and Clay Minerals*, *49*(6), 514–528. DOI: 10.1346/CCMN.2001.0490604

Steele, L. J., Balme, M. R., and Lewis, S. R. (**2017**). Regolith-atmosphere exchange of water in Mars' recent past. *Icarus*, *284*, 233–248. DOI: 10.1016/j.icarus.2016.11.023

Stern, S. A., Bagenal, F., Ennico, K., Gladstone, G. R., Grundy, W. M., McKinnon, W. B., Moore, J. M., Olkin, C. B., Spencer, J. R., Weaver, H. A., Young, L. A., Andert, T., Andrews, J., Banks, M., Bauer, B., Bauman, J., Barnouin, O. S., Bedini, P., Beisser, K., Beyer, R. A., Bhaskaran, S., Binzel, R. P., Birath, E., Bird, M., Bogan, D. J., Bowman, A., Bray, V. J., Brozovic, M., Bryan, C., Buckley, M. R., Buie, M. W., Buratti, B. J., Bushman, S. S., Calloway, A., Carcich, B., Cheng, A. F., Conard, S., Conrad, C. A., Cook, J. C., Cruikshank, D. P., Custodio, O. S., Dalle Ore, C. M., Deboy, C., Dischner, Z. J. B., Dumont, P., Earle, A. M., Elliott, H. A., Ercol, J., Ernst, C. M., Finley, T., Flanigan, S. H., Fountain, G., Freeze, M. J., Greathouse, T., Green, J. L., Guo, Y., Hahn, M., Hamilton, D. P., Hamilton, S. A., Hanley, J., Harch, A., Hart, H. M., Hersman, C. B., Hill, A., Hill, M. E., Hinson, D. P., Holdridge, M. E., Horanyi, M., Howard, A. D., Howett, C. J. A., Jackman, C., Jacobson, R. A., Jennings, D. E., Kammer, J. A., Kang, H. K., Kaufmann, D. E., Kollmann, P., Krimigis, S. M., Kusnierkiewicz, D., Lauer, T. R., Lee, J. E., Lindstrom, K. L., Linscott, I. R., Lisse, C. M., Lunsford, A. W., Mallder, V. A., Martin, N., McComas, D. J., McNutt, R. L., Mehoke, D., Mehoke, T., Melin, E. D., Mutchler, M., Nelson, D., Nimmo, F., Nunez, J. I., Ocampo, A., Owen, W. M., Paetzold, M., Page, B., Parker, A. H., Parker, J. W., Pelletier, F., Peterson, J., Pinkine, N., Piquette, M., Porter, S. B., Protopapa, S., Redfern, J., Reitsema, H. J., Reuter, D. C., Roberts, J. H., Robbins, S. J., Rogers, G., Rose, D., Runyon, K., Retherford, K. D., Ryschkewitsch, M. G., Schenk, P., Schindhelm, E., Sepan, B., Showalter, M. R., Singer, K. N., Soluri, M., Stanbridge, D., Steffl, A. J., Strobel, D. F., Stryk, T., Summers, M. E., Szalay, J. R., Tapley, M., Taylor, A., Taylor, H., Throop, H. B., Tsang, C. C. C., Tyler, G. L., Umurhan, O. M., Verbiscer, A. J., Versteeg, M. H., Vincent, M., Webbert, R., Weidner, S., Weigle, G. E., White, O. L., Whittenburg, K., Williams, B. G., Williams, K., Williams, S., Woods, W. W., Zangari, A. M., and Zirnstein, E. (**2015**). The Pluto system: Initial results from its exploration by New Horizons. *Science*, *350*(6258), aad1815. DOI: 10.1126/science.aad1815

Strydom, C. A., Hudson-Lamb, D. L., Potgieter, J. H., and Dagg, E. (**1995**). The thermal dehydration of synthetic gypsum. *Thermochimica Acta*, *269–270*, 631–638. DOI: 10.1016/0040-6031(95)02521-9

Stull, R. (**2015**). *Practical Meteorology: An algebra-based survey of atmospheric science*. University of British Columbia. https://doi.library.ubc.ca/10.14288/1.0300441

Sun, S. -s., and McDonough, W. F. (**1989**). Chemical and isotopic systematics of oceanic basalts: Implications for mantle composition and processes. *Geological Society, London, Special Publications*, *42*(1), 313–345. DOI: 10.1144/GSL.SP.1989.042.01.19

Tait, K. T., McCubbin, F. M., Smith, C. L., Agee, C. B., Busemann, H., Cavalazzi, B., Debaille, V., Hutzler, A., Usui, T., Kminek, G., Meyer, M. A., Beaty, D. W., Carrier, B. L., Haltigin, T., Hays, L. E., Cockell, C. S., Glavin, D. P., Grady, M. M., Hauber, E., Marty, B., Pratt, L. M., Regberg, A. B., Smith, A. L., Summons, R. E., Swindle, T. D., Tosca, N. J., Udry, A., Velbel, M. A., Wadhwa, M., Westall, F., and Zorzano, M.-P. (**2022**). Preliminary planning for Mars sample return (MSR) curation activities in a sample receiving facility (SRF). *Astrobiology*, *22*(S1), S-57-S-80. DOI: 10.1089/ast.2021.0105

Tamari, S. (**2004**). Optimum design of the constant-volume gas pycnometer for determining the volume of solid particles. *Measurement Science and Technology*, *15*(3), 549–558. DOI: 10.1088/0957-0233/15/3/007

Taubner, R.-S., Olsson-Francis, K., Vance, S. D., Ramkissoon, N. K., Postberg, F., de Vera, J.-P., Antunes, A., Camprubi Casas, E., Sekine, Y., Noack, L., Barge, L., Goodman, J., Jebbar, M., Journaux, B., Karatekin, Ö., Klenner, F., Rabbow, E., Rettberg, P., Rückriemen-Bez, T., Saur, J., Shibuya, T., and Soderlund, K. M. (**2020**). Experimental and simulation efforts in the astrobiological exploration of exooceans. *Space Science Reviews*, *216*(1), 9. DOI: 10.1007/s11214-020-0635-5

Terada, N., Kulikov, Y. N., Lammer, H., Lichtenegger, H. I. M., Tanaka, T., Shinagawa, H., and Zhang, T. (**2009**). Atmosphere and water loss from early Mars under extreme solar wind and extreme ultraviolet conditions. *Astrobiology*, *9*(1), 55–70. DOI: 10.1089/ast.2008.0250

Tomaszkiewicz, M., Abou Najm, M., Beysens, D., Alameddine, I., and El-Fadel, M. (**2015**). Dew as a sustainable non-conventional water resource: A critical review. *Environmental Reviews*, *23*(4), 425–442. DOI: 10.1139/er-2015-0035

Toner, J. D., and Catling, D. C. (**2018**). Chlorate brines on Mars: Implications for the occurrence of liquid water and deliquescence. *Earth and Planetary Science Letters*, *497*, 161–168. DOI: 10.1016/j.epsl.2018.06.011

Trembath-Reichert, E., Morono, Y., Ijiri, A., Hoshino, T., Dawson, K. S., Inagaki, F., and Orphan, V. J. (**2017**). Methyl-compound use and slow growth characterize microbial life in 2-km-deep subseafloor coal and shale beds. *Proceedings of the National Academy of Sciences*, *114*(44), E9206–E9215. DOI: 10.1073/pnas.1707525114

Troeh, F. R., Jabro, J. D., and Kirkham, D. (**1982**). Gaseous diffusion equations for porous materials. *Geoderma*, *27*(3), 239–253. DOI: 10.1016/0016-7061(82)90033-7

Tuller, M., and Or, D. (**2005**). Water films and scaling of soil characteristic curves at low water contents: Scaling of characteristic curves. *Water Resources Research*, *41*(9). DOI: 10.1029/2005WR004142

Valdivia-Silva, J. E., Navarro-González, R., Fletcher, L., Pérez-Montaño, S., Condori-Apaza, R., Ortega-Gutiérrez, F., and McKay, C. (**2012**a). Climatological characteristics in the extreme hyper-arid region of Pampas de La Joya, Peru. Astrobiological approach in four years of observation: 2004–2008. *International Journal of Astrobiology*, *11*(01), 25–35. DOI: 10.1017/S1473550411000292

Valdivia-Silva, J. E., Navarro-González, R., Ortega-Gutierrez, F., Fletcher, L. E., Perez-Montaño, S., Condori-Apaza, R., and McKay, C. P. (**2011**). Multidisciplinary approach of the hyperarid desert of Pampas de La Joya in southern Peru as a new Mars-like soil analog. *Geochimica et Cosmochimica Acta*, *75*(7), 1975–1991. DOI: 10.1016/j.gca.2011.01.017

Valdivia-Silva, J. E., Navarro-González, R., Rosa, J. de la, and McKay, C. P. (**2012**b). Decomposition of sodium formate and L- and D-alanine in the Pampas de La Joya soils: Implications as a new geochemical analogue to Martian regolith. *Advances in Space Research*, *49*(5), 821–833. DOI: 10.1016/j.asr.2011.12.012

Vera, A., Pino-Vargas, E., Verma, M. P., Chucuya, S., Chávarri, E., Canales, M., Torres-Martínez, J. A., Mora, A., and Mahlknecht, J. (**2021**). Hydrodynamics, hydrochemistry, and stable isotope geochemistry to assess temporal behavior of seawater intrusion in the La Yarada aquifer in the vicinity of Atacama Desert, Tacna, Peru. *Water*, *13*(22), 3161. DOI: 10.3390/w13223161

Verhoef, A., Diaz-Espejo, A., Knight, J. R., Villagarcía, L., and Fernández, J. E. (**2006**). Adsorption of water vapor by bare soil in an olive grove in southern Spain. *Journal of Hydrometeorology*, *7*(5), 1011–1027. DOI: 10.1175/JHM556.1

Viglas, K. (**2016**). The placement of Lucian's novel true history in the genre of science fiction. *Interlitteraria*, *21*(1), 158. DOI: 10.12697/IL.2016.21.1.13

Vítek, P., Ascaso, C., Artieda, O., and Wierzchos, J. (**2016**). Raman imaging in geomicrobiology: Endolithic phototrophic microorganisms in gypsum from the extreme sun irradiation area in the Atacama Desert. *Analytical and Bioanalytical Chemistry*, *408*(15), 4083–4092. DOI: 10.1007/s00216-016-9497-9

Wendlandt, K.-D., Stottmeister, U., Helm, J., Soltmann, B., Jechorek, M., and Beck, M. (**2010**). The potential of methane-oxidizing bacteria for applications in environmental biotechnology. *Engineering in Life Sciences*, *10*(2), 87–102. DOI: 10.1002/elsc.200900093

Wenk, H. R., Joswig, W., Tagai, T., Korekawa, M., and Smith, B. K. (**1980**). The average structure of An 62–66 labradorite. *American Mineralogist*, *65*(1–2), 81–95.

Wierzchos, J., Casero, M. C., Artieda, O., and Ascaso, C. (**2018**). Endolithic microbial habitats as refuges for life in polyextreme environment of the Atacama Desert. *Current Opinion in Microbiology*, *43*, 124–131. DOI: 10.1016/j.mib.2018.01.003

Wilhelm, M. B., Davila, A. F., Parenteau, M. N., Jahnke, L. L., Abate, M., Cooper, G., Kelly, E. T., Parro García, V., Villadangos, M. G., Blanco, Y., Glass, B., Wray, J. J., Eigenbrode, J. L., Summons, R. E., and Warren-Rhodes, K. (**2018**). Constraints on the metabolic activity of microorganisms in Atacama surface soils inferred from Rrefractory

biomarkers: Implications for Martian habitability and biomarker detection. *Astrobiology*, *18*(7), 955–966. DOI: 10.1089/ast.2017.1705

Zhang, X., Sun, P., Yan, T., Huang, Y., Ma, Z., Zou, B., Zheng, W., Zhou, J., Gong, Y., and Sun, C. Q. (**2015**). Water's phase diagram: From the notion of thermodynamics to hydrogen-bond cooperativity. *Progress in Solid State Chemistry*, *43*(3), 71–81. DOI: 10.1016/j.progsolidstchem.2015.03.001

Zomer, R. J., Trabucco, A., Bossio, D. A., and Verchot, L. V. (**2008**). Climate change mitigation: A spatial analysis of global land suitability for clean development mechanism afforestation and reforestation. *Agriculture, Ecosystems & Environment*, *126*(1–2), 67–80. DOI: 10.1016/j.agee.2008.01.014

APPENDIX A

CHAPTER 2 SUPPLEMENTAL INFORMATION

A.1. Water Concentration Profile Identification

In order to determine water concentration gradients for each of the ~700 soil T & $[H_2O_{(g)}]$ depth profiles collected in the field; we developed a procedure to classify the shape of the $[H_2O_{(g)}]$ profile as a function of depth into one of three profile types: *i)* $[H_2O_{(g)}]$ minimum, *ii)* $[H_2O_{(g)}]$ maximum, and *iii)* constant profiles (Figure 2.7). In brief, the two determining factors for profile categorization are *i)* the $[H_2O_{(g)}]$ slope between 0 and 2.5 cm ($m_{1\text{-}2}$; Figure A.16) and *ii)* the $[H_2O_{(g)}]$ slope between depth 2.5 and 30 cm ($m_{2\text{-}6}$; Figure A.16). The $m_{1\text{-}2}$ slope is the primary determinant for profile type with the threshold set at <-15 μM cm^{-1} for a $[H_2O_{(g)}]$ minimum profile and >15 μM cm^{-1} for a $[H_2O_{(g)}]$ maximum profile. In addition, the $m_{2\text{-}6}$ slope must be >0 μM cm^{-1} for $[H_2O_{(g)}]$ minimum profiles, and <0 μM cm^{-1} for $[H_2O_{(g)}]$ maximum profiles. The combination of these two factors allows an accurate identification of profile type that is much faster than manual (human) determination of the profile type.

A.1.1. Upper Profile Region Approximation

The upper region of the profile always includes the surface value (z = 0) and is determined by iterative linear regression, each eliminating the deepest data point starting at 20 cm until the regression achieves an $r^2 \geq 0.9$ or until the region contains exactly 2 data points (Figure A.17).

A.1.2. Lower Profile Region Approximation

Approximating the lower region of the profile is more complex as there may be a no flux boundary in the lower portion of the profile and these points should be excluded. The 'no flux boundary' and the lower region are determined using two different algorithms. The 'no

flux boundary' is identified by calculating the $[H_2O_{(g)}]$ slope between 20 and 10 cm ($m_{4\text{-}5}$ in Figure A.18). The 20 cm depth data are considered no-flux and removed if $m_{4\text{-}5}$ is between -10 and 10 μM cm^{-1}. With the 'no flux boundary' identified, we use the second algorithm to identify the top and the bottom of the lower region. Linear regressions are calculated starting from the lowest point in the upper region (upperMaxDep) to the deepest non-excluded point and then iterating by excluding the lowest point until n = 3. This process is repeated starting from the highest point not included in the upper region (upperMaxDep + 1) to the deepest non-excluded point and iterating by excluding the lowest point until n = 3 (Figure A.18 A&B). If the highest r^2 value for the resulting linear regression is ≥ 0.9, then that subset of points is identified as the lower region. If none of the profiles meet the r^2-threshold, then an n = 2 regression must be used. The n = 2 regression is selected by first drawing the line between highest point not included in the upper sub-profile and the next lower point (Figure A.19C). To validate this line, we solve for the $[H_2O_{(g)}]$ at the lowest point in the upper region. If this value is greater than 1.1 times the $[H_2O_{(g)}]$ of the lowest point of the upper region (in the case of an $[H_2O_{(g)}]$ minimum profile) or is less than 0.9 times the $[H_2O_{(g)}]$ of the lowest point of the upper profile (in the case of an $[H_2O_{(g)}]$ maximum profile), then this line is invalid. The next n = 2 line is drawn between the lowest point of the upper region and the next point. This line is validated by comparing its slope to the slope of the upper region. If the slopes are of the same sign, then this line is invalid. With the upper and lower profiles identified, ∂z is calculated as the depth of the lowest included point (Figure A.10).

A.1.3. Profile Identification Quality Control

The profile identification algorithm was built iteratively and benchmarked against manual identification of $[H_2O_{(g)}]$ minimum, $[H_2O_{(g)}]$ maximum, and constant profiles. Identification

parameters were adjusted until the algorithm was able to correctly identify all profiles as one of the three types.

A.2. Simulation Results: Water Content Plateau over Time

Figure A.11 shows the water content over time for both soil samples; additionally, the results of four linear regressions are plotted. Here we find that for all regressions, except one, the slope is not significantly different from zero. The exception being the regression for the MDQ soil sample including intervals 2, 4, and 6. This is most likely since the soil is still equilibrating to the chamber conditions, hence the low water content at the end of interval 2 (point n_1), resulting in a positive slope. However, the linear regression including all points from n_1 to d_4 is not significantly different from zero.

A.3. Other Water Inputs

A.3.1. Dew

Dewpoint temperature is the temperature at which water will condense on surfaces and has been described previously by Lawrence (2005) as

$$t_d = \frac{B\left[ln\left(\frac{RH}{100}\right)+\frac{At}{B+t}\right]}{A-ln\left(\frac{RH}{100}\right)-\frac{At}{B+t}}, ; \quad \text{(A.1)}$$

where t_d is dewpoint temperature, RH is relative humidity, and t is temperature. The constants A = 17.625 and B = 243.04°C are empirically derived by Aduchov & Eskridge (1996). Figure A.15 shows the difference between the surface air temperature (T at 0 cm) and the dewpoint temperature for both sites, calculated as

$$Air - Dewpoint\ Difference = t - t_d, ; \quad \text{(A.2)}$$

where if Air – Dewpoint Difference equals 0, there is dew deposition on the surface.

A.3.2. Deliquescence

Figure A.22 shows surface RH over time at both sites and the right Y-axis shows the DRH of several relevant deliquescent minerals. There are five naturally occurring minerals with DRH within the surface RH range observed in the field: $CaCl_2$, KF, $MgCl_2$, $CaNO_3$, and $MgNO_3$. However, both the RockJock XRD model as well as the MDI® Jade software were unable to fit the spectra of any of these minerals to the MDQ or LH spectra.

Table A.1: Soil extractable major ions for MDQ. Mass values are normalized to dry soil weight. The fraction of extracted ions is the proportion of an individual ion relative to the sum of all extracted ions. Ions are sorted from highest to lowest fraction. Values are the average of two replicate samples and the uncertainties are one standard deviation of the average. Calcium and sulfate (**bold**) are the dominant ion pair.

Extractable Ion	*Mass per gram dry soil ($mg\ kg^{-1}$)*	*Fraction of Extracted Ions (%)*
Total Ions	104.6 ± 14.27	- -
Calcium (+)	38.6 ± 3.82	37 ± 3.7
Sulfate (-)	38.1 ± 0.46	36 ± 0.4
Sodium (+)	12.7 ± 8.68	12 ± 8.3
Chloride (-)	7.1 ± 5.41	7 ± 5.2
Nitrate (-)	4.2 ± 2.64	4 ± 2.5
Magnesium (+)	1.6 ± 1.01	2 ± 1.0
Potassium (+)	1.3 ± 0.23	1 ± 0.2
Ammonium (+)	0.8 ± 0.23	1 ± 0.2
Fluoride (-)	0.1 ± 0.01	< 1 ± 0.1
Phosphate (-)	0.1 ± 0.01	< 1 ± 0.1

Table A.2: Soil extractable major ions for LH. Mass values are normalized to dry soil weight. The fraction of extracted ions is the proportion of an individual ion relative to the sum of all extracted ions. Ions are sorted from highest to lowest fraction. Values are the average of two replicate samples and the uncertainties are one standard deviation of the average. Sodium and chloride (**bold**) are the dominant ion pair.

Extractable Ion	*Mass per gram dry soil ($mg\ kg^{-1}$)*	*Fraction of Extracted Ions (%)*
Total Ions	232.3 ± 7.78	- -
Sodium (+)	64.3 ± 1.95	28 ± 0.8
Chloride (-)	57.0 ± 3.50	25 ± 1.5
Sulfate (-)	39.6 ± 1.94	17 ± 0.8
Calcium (+)	37.6 ± 1.85	16 ± 0.8
Nitrate (-)	21.7 ± 0.33	9 ± 0.1
Magnesium (+)	6.6 ± 1.06	3 ± 0.5
Potassium (+)	4.6 ± 0.10	2 ± 0.1
Fluoride (-)	0.5 ± 0.06	< 1 ± 0.1
Ammonium (+)	0.5 ± 0.11	< 1 ± 0.1
Phosphate (-)	ND ND	ND ND

Table A.3: Temperature replicate measurement precision. The mean and maximum standard deviation (SD) is reported for several ranges of temperature measurements. For all temperatures the mean SD is less than 0.01ºC and the maximum SD is less than 0.08ºC. There is no correlation between temperature and the SD of measurements, indicating that the sensors are equally precise from 0 to 50ºC and the sensor is behaving nominally.

Temperature Range (ºC)	*Mean SD (ºC)*	*Maximum SD (ºC)*
0 – 50 (All)	0.0089	0.079
0 – 10	0.0092	0.022
10 – 20	0.0087	0.037
20 – 30	0.0086	0.042
30 – 40	0.0100	0.079
40 – 50	0.0091	0.045

Table A.4: Relative humidity replicate measurement precision. The mean and maximum standard deviation (SD) is reported for several ranges of relative humidity measurements. For all relative humidity values the mean SD is less than 0.03%RH and the maximum SD is roughly 0.1%RH. There is a slight trend between relative humidity and the SD of measurements, indicating that the sensors are somewhat less precise at higher RH. However, the maximum observed SD (± 0.1%RH) is similar to the manufacturer reported resolution of ± 0.04%RH, indicating that the sensor is behaving nominally.

Relative Humidity Range (%RH)	*Mean SD (%RH)*	*Maximum SD (%RH)*
0 – 100 (All)	0.0086	0.1050
0 – 20	0.0076	0.0480
20 – 40	0.0081	0.0970
40 – 60	0.0169	0.1050
60 – 80	0.0143	0.0940
80 – 100	0.0270	0.0390

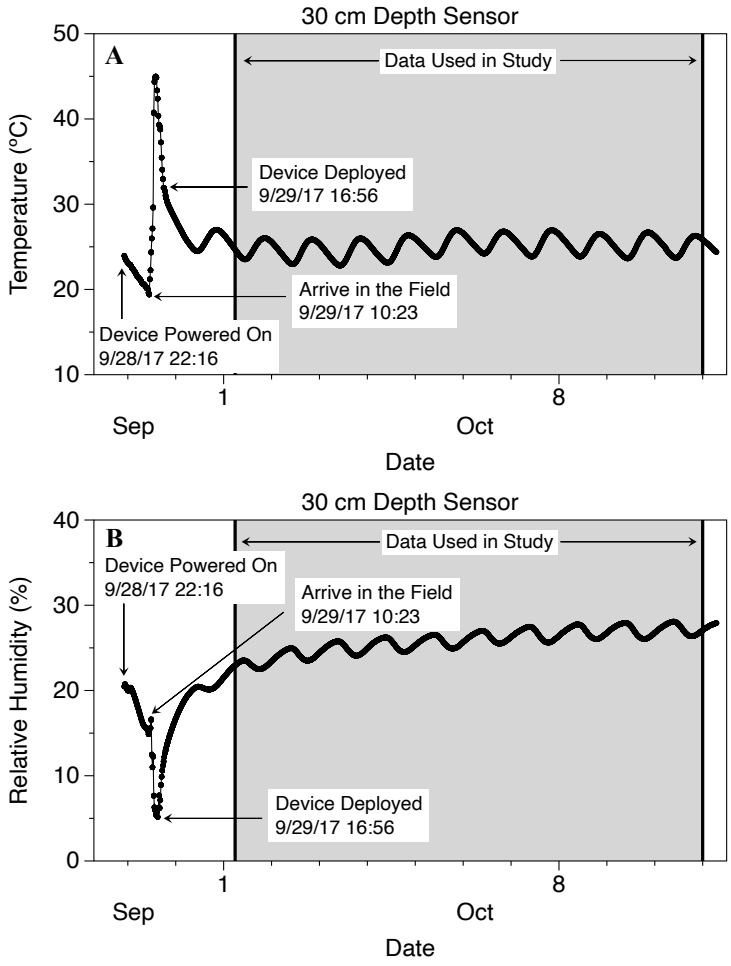

Figure A.1: Temperature and Humidity data collected at 30 cm depth; **A)** temperature and **B)** relative humidity data from the MDQ sensor array. Figure annotations show notable, pre-deployment events. Grey shaded area shows the portion of the of data after the sensors had stabilized that was used in this study.

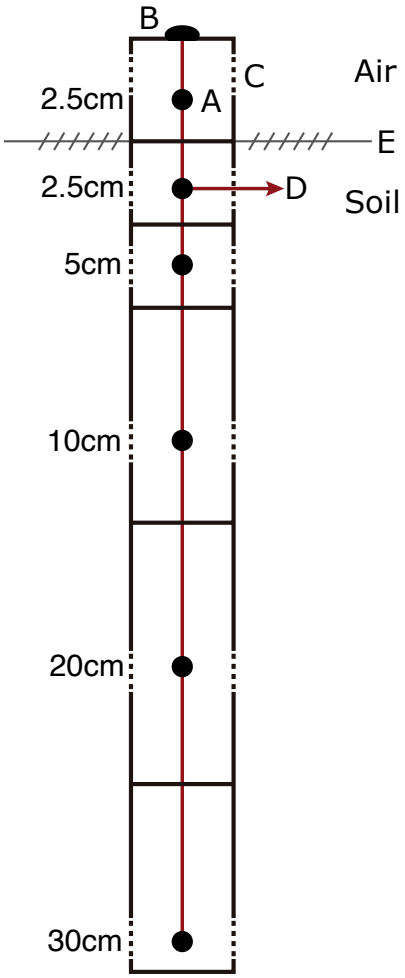

Figure A.2: Schematic diagram of the soil temperature and humidity sensor array. Outer shell is PVC tubing
and chambers are separated by plastic weld putty to produce an airtight seal. Red lines are signal wires. **A:** location of the temperature and relative humidity sensor (HIH7000), **B:** location of the light sensor (photoresistor), **C:** opening to surrounding soil, covered with a Tyvek® membrane, **D:** hardwire connection to an arduino datalogger (located ~10 cm from array). The hashed line at **E** represents the location of the soil/air interface.

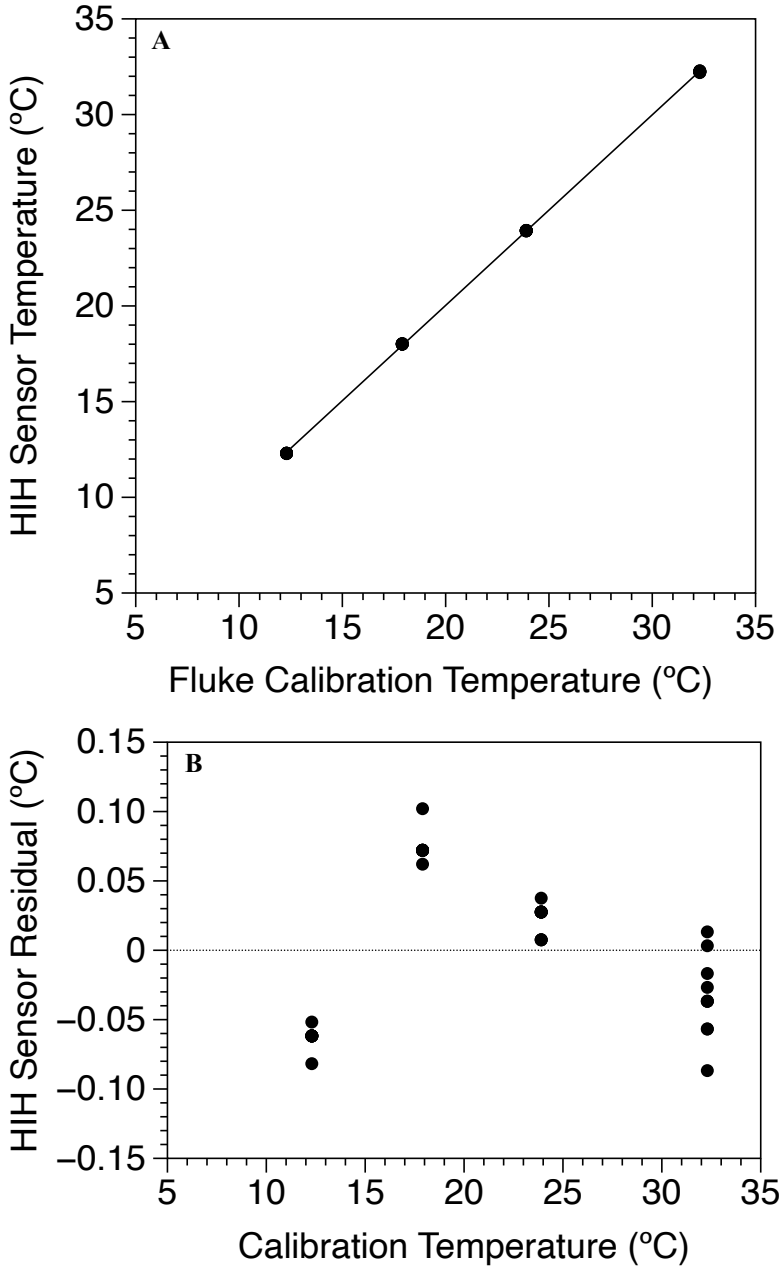

Figure A.3: HIH Sensor calibration for temperature. A four-point calibration was performed to assess the accuracy of the HIH sensors. **A)** HIH temperature and calibration temperature have a correlation coefficient of $R^2 = 0.99994$ and a slope of 0.99575. **B)** Residuals of HIH temperature are < 0.15ºC over the calibration range.

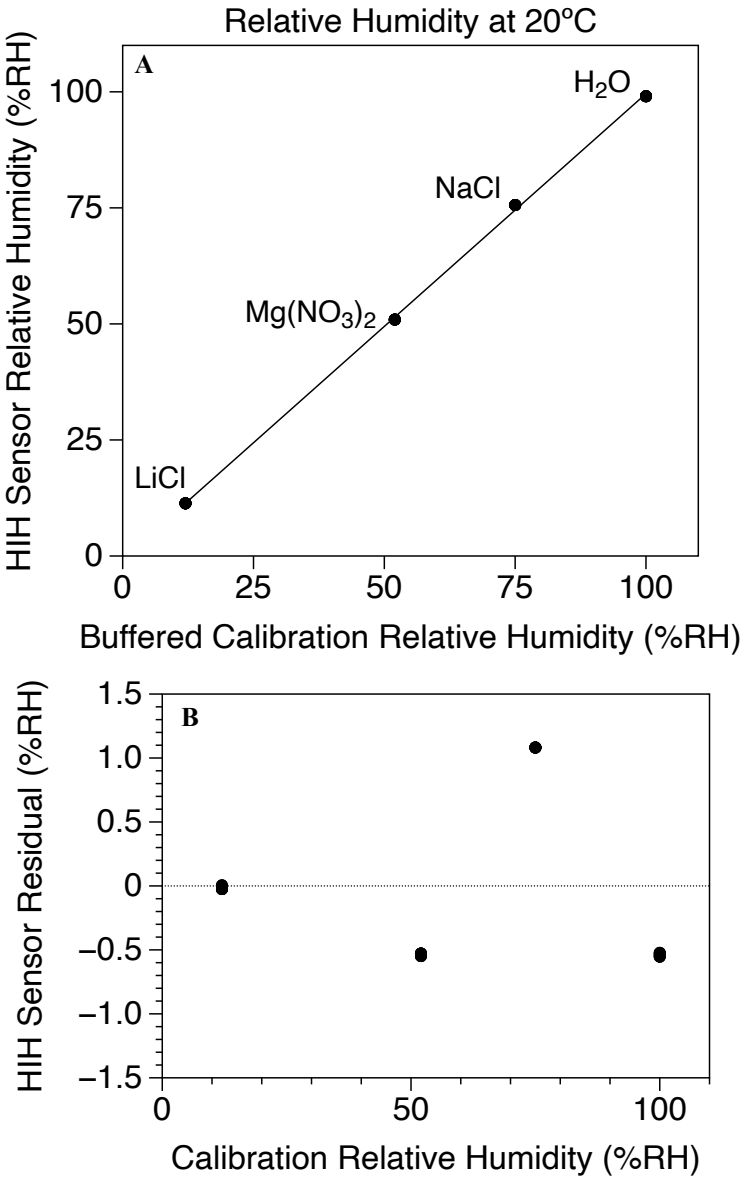

Figure A.4: HIH Sensor calibration for relative humidity. A four-point calibration was performed at 20ºC to assess the accuracy of the HIH sensors. **A)** HIH relative humidity and calibration relative humidity have a correlation coefficient of $R^2 = 0.99959$ and a slope of 1.0026. **B)** Residuals of HIH relative humidity are < 1.5%RH over the calibration range.

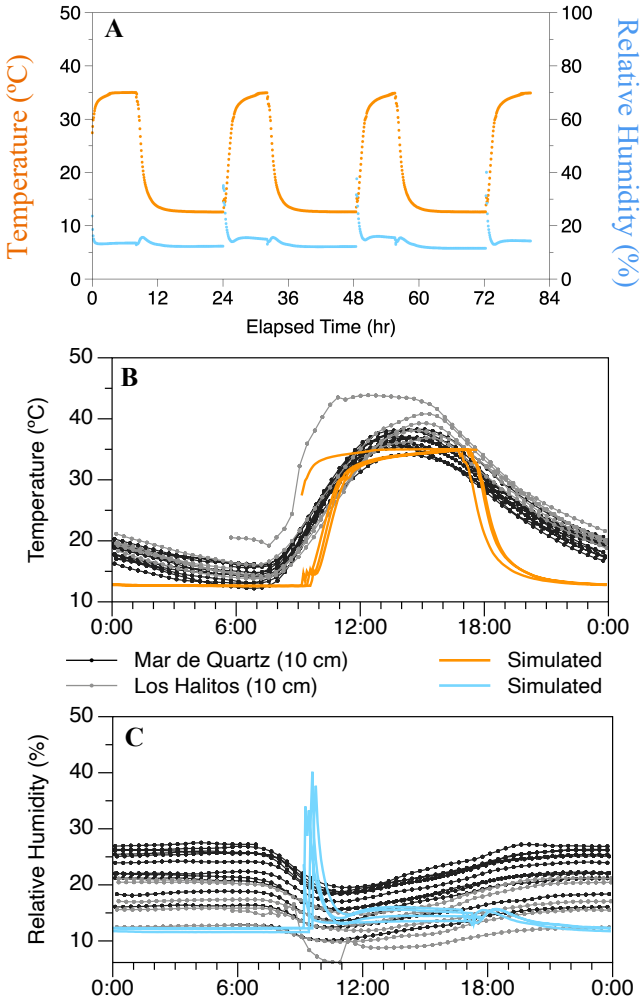

Figure A.5: A) Simulation enclosure temperature (orange) and relative humidity (cyan) over the duration of the experiment. **B)** Simulation enclosure temperature (orange) and field temperature at 10 cm depth at MDQ (black) and LH (grey). **C)** Simulation enclosure relative humidity (cyan) and field relative humidity at 10 cm depth at MDQ (black) and LH (grey). Our simulation experiment reasonably replicates the T and RH conditions observed at 10cm depth in the field.

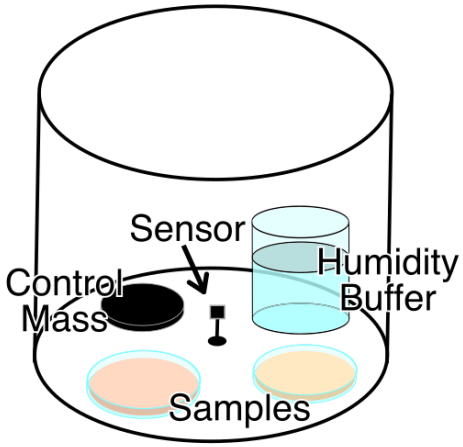

Figure A.6: Schematic diagram of humidity enclosure setup for laboratory simulations. All simulation components are sealed within an air-tight polymethylmethacrylate container.

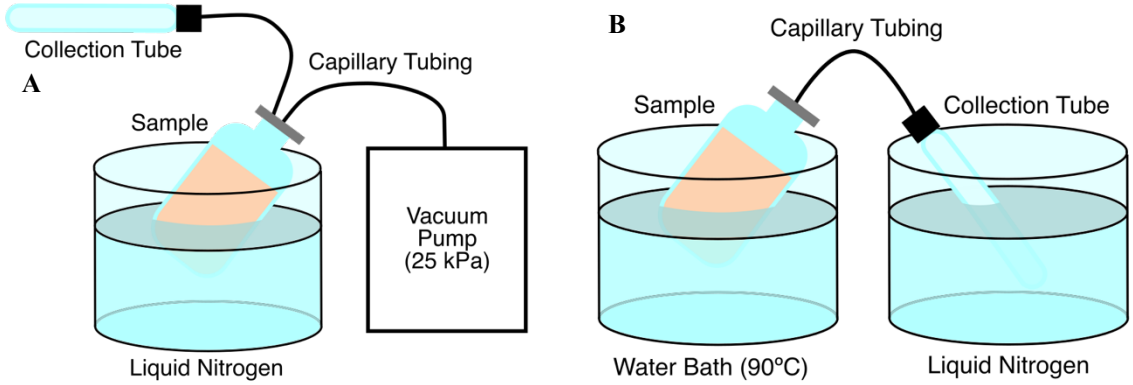

Figure A.7: Schematic Diagram of soil water extraction method. This two-step process was adapted from Koeniger et al. 2011. **A)** Sample bottle (a crimp top serum vial) and collection tube (an Exetainer™ with a thick septum) are connected by stainless steel capillary tubing and both are evacuated for 15 min, to 25 kPa gauge while sample sits in liquid nitrogen. **B)** Sample bottle is then placed in a 90°C water bath and collection tube is moved to the liquid nitrogen bath for 2 hours.

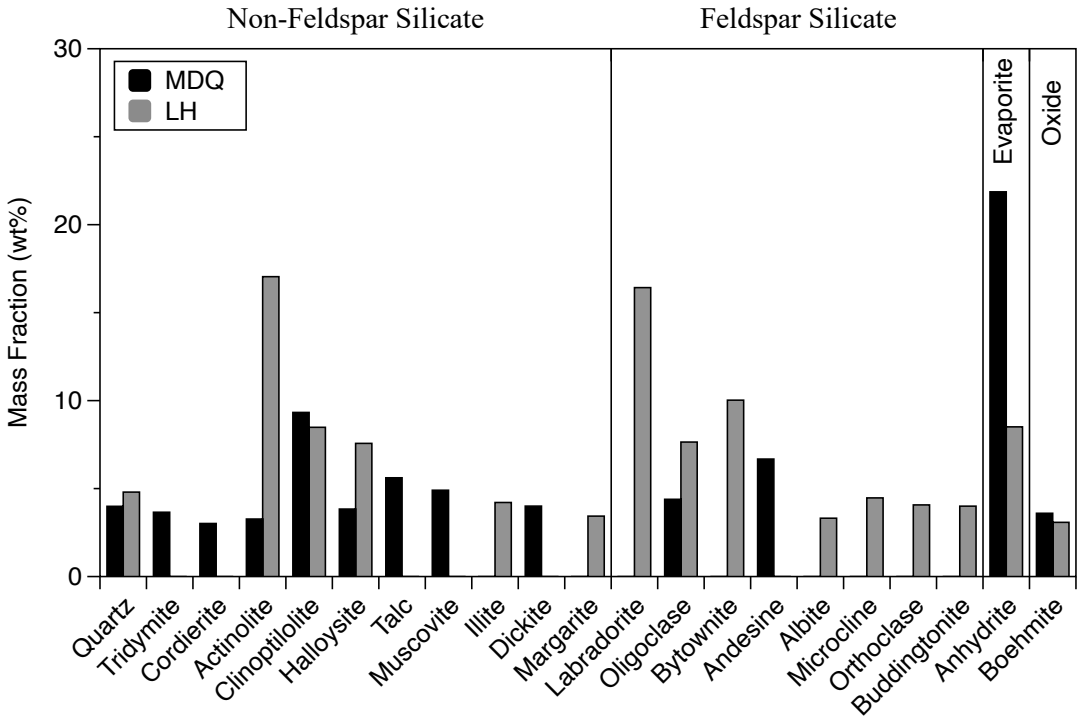

Figure A.8: Mineral abundance for MDQ (black) and LH (grey). Minerals are organized into broad categories of non-feldspar silicates, feldspar silicates, evaporites, and oxides. Anhydrite is the most abundant mineral at MDQ, while actinolite is the most abundant mineral at LH. MDQ contains less feldspar silicates compared to LH.

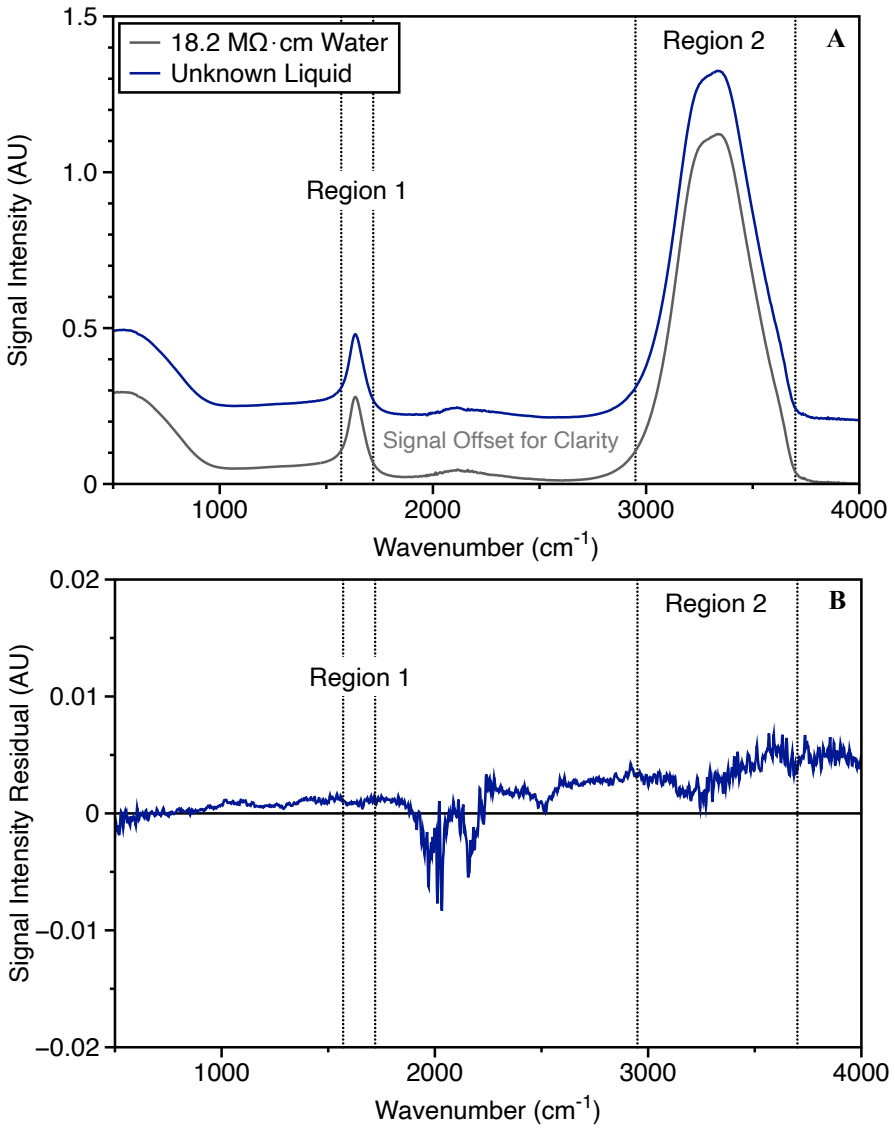

Figure A.9: FTIR spectrum **A)** of the unknown liquid extracted from MDQ soil after 48 h incubation at 12ºC and 12%RH. Signal intensity vs. wavenumber for the sample (dark blue line) is compared to a deionized water standard (grey line); signal for the sample is offset by +0.2 AU (absorbance units) for clarity. **B)** Signal intensity residual (i.e., unknown sample – deionized water). The regions with high signal absorption (indicated as region 1 and 2) are marked by dotted lines for comparison between plots. Note the residuals are quite low in the region of the water peaks. The similarity in the two FTIR spectra is strong evidence that the extracted liquid is water.

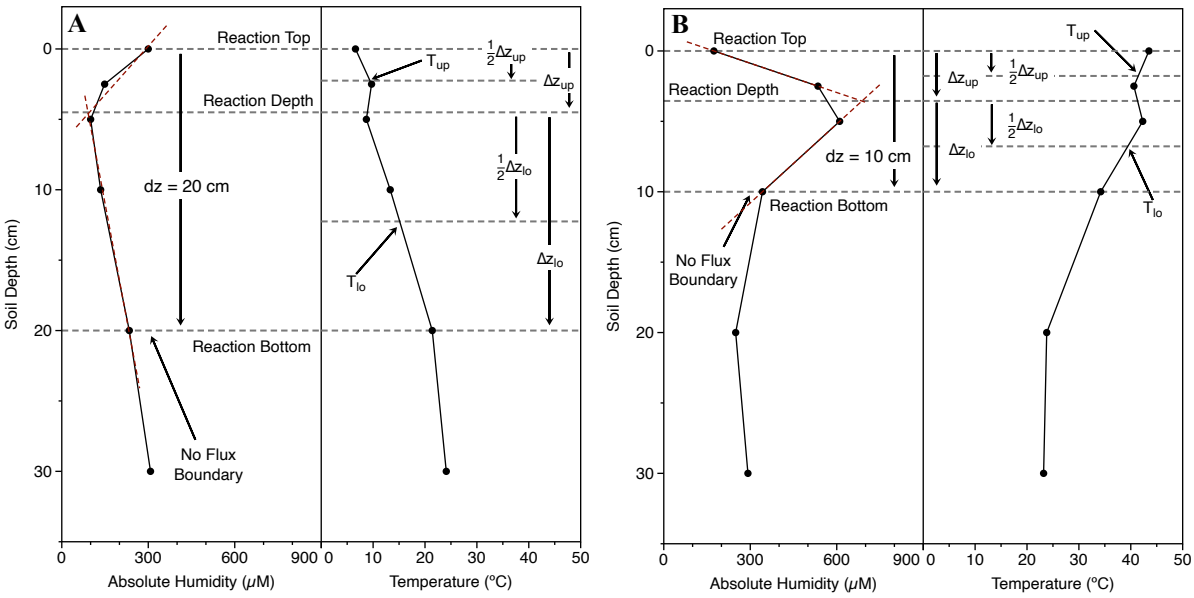

Figure A.10: Algorithm of upper and lower sub-profile temperature determination for **A)** $[H_2O_{(g)}]$ minimum and **B)** $[H_2O_{(g)}]$ maximum profile types. The upper and lower temperatures are used to calculate the diffusion coefficient. The total depth (dz) is used in equations 2.3 & 2.6.

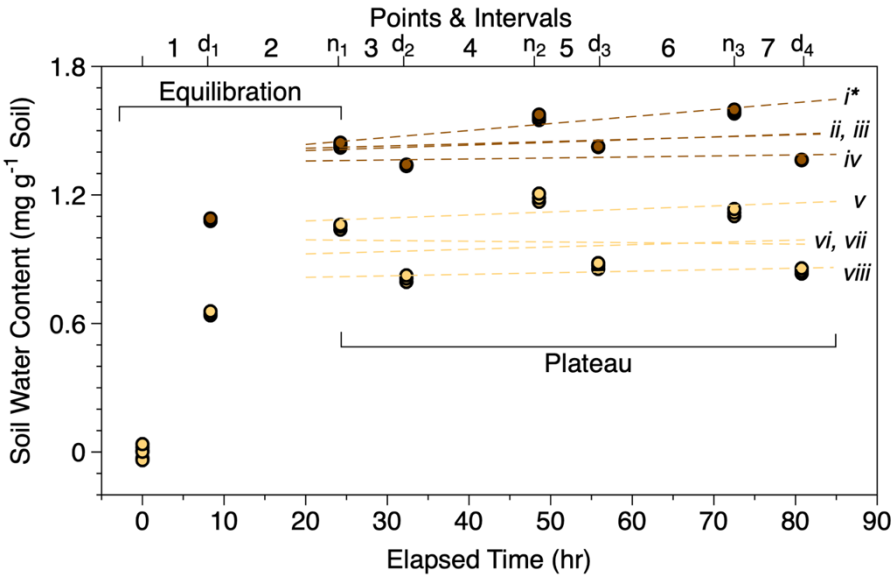

Figure A.11: Water content vs. elapsed time for MDQ (brown) and LH (tan) soils during the simulation experiment. Points are labeled according to a measurement taken after a daytime period (d), or after a nighttime period (n). Subscripts to d and n correspond to the number of measurements in the sequence. Intervals between measurements are numbered 1 through 7, where even intervals are nighttime conditions and odd intervals are daytime conditions. Dashed lines with roman numeral labels (*i* – *viii*) are linear regression lines on various sections of the plateau data where i) MDQ(n_1, n_2, n_3), ii) MDQ(n_1, d_2, n_2, d_3, n_3, d_4), iii) MDQ(d_2, n_2, d_3, n_3, d_4), iv) MDQ(d_2, d_3, d_4), v) LH(n_1, n_2, n_3), vi) LH(n_1, d_2, n_2, d_3, n_3, d_4), vii) LH(d_2, n_2, d_3, n_3, d_4), and viii) LH(d_2, d_3, d_4). The regression slopes of sections ii, iii, iv, v, vi, vii, viii are not significantly different from zero. This indicates that both soils reached an equilibrium-like state for the last 4 intervals. The asterisk indicates that the slope of linear regression i is significantly different from zero. However, there is strong evidence that the soils have reached an equilibrium-like state with positive and negative oscillations in response to changes in T.

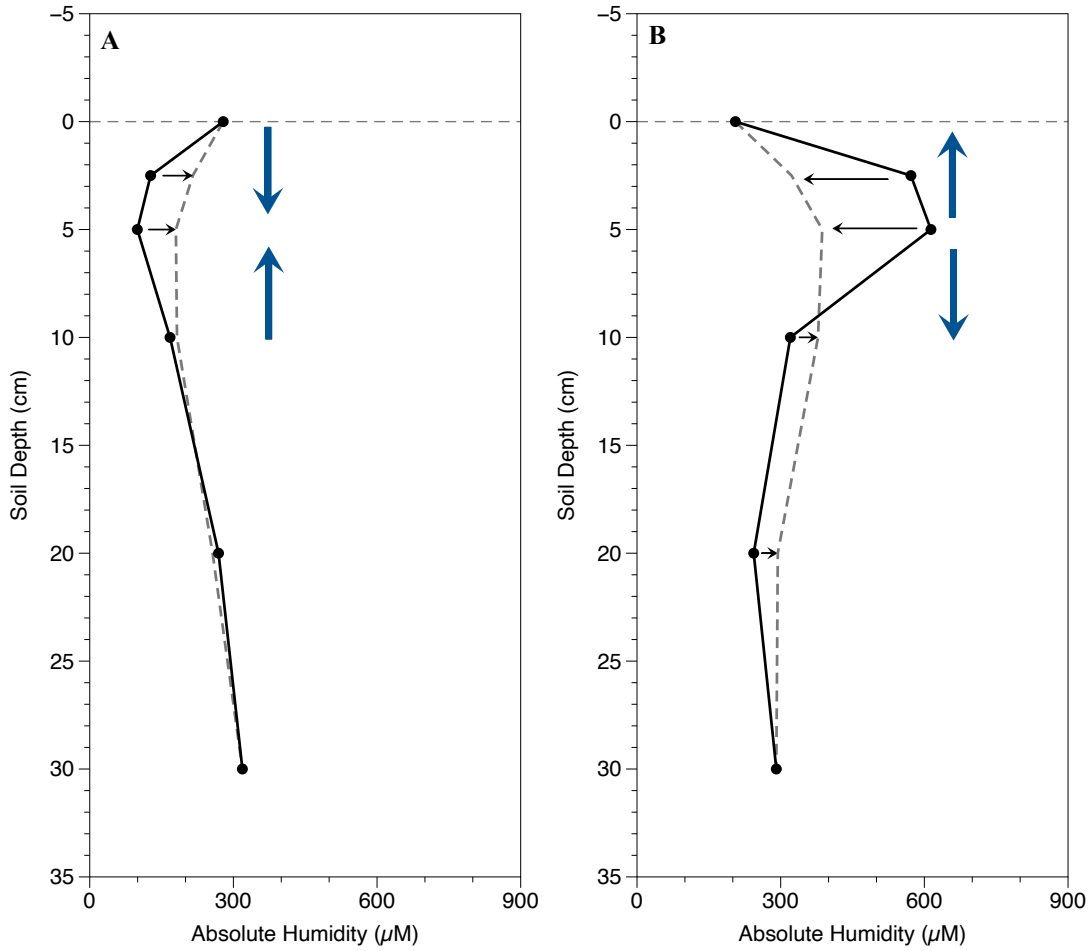

Figure A.12: Representative A) [$H_2O_{(g)}$] minimum-type and B) [$H_2O_{(g)}$] maximum-type profiles. Observed [$H_2O_{(g)}$] values are shown with black circles and solid lines. Grey dashed line shows the expected profile if diffusion were the only process acting on [$H_2O_{(g)}$] over 20 minutes. However, the observed profile shapes are stable on the order of hours, indicating another active process changing [$H_2O_{(g)}$]. Blue lines show the direction of [$H_2O_{(g)}$] diffusion based on the profile. Panel A shows [$H_2O_{(g)}$] moving to 5 cm from above and below; this profile needs an active process that remove [$H_2O_{(g)}$] from the pore space if it is to remain stable on timescales of the order of hours. Panel B is analogous for conditions requiring that water be added to the pore space to maintain the profile with a maximum in [$H_2O_{(g)}$].

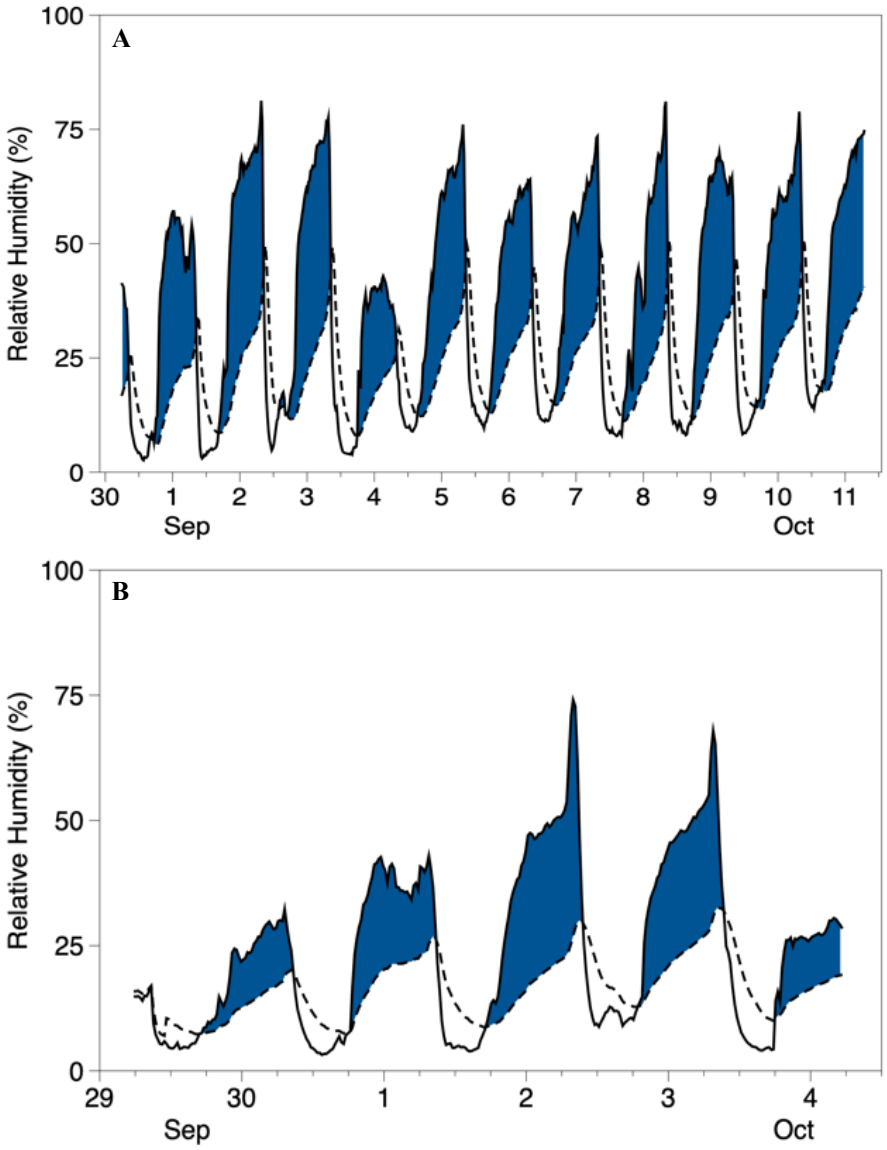

Figure A.13. Surface (solid line) and 2.5 cm (dashed line) relative humidity at **A)** Mar de Quartz and **B)** Los Halitos. Blue filled areas indicate time periods where the surface relative humidity is greater than the relative humidity at 2.5 cm. This indicates favorable conditions for WVA from ~18:00 in the afternoon to 9:00 the following morning.

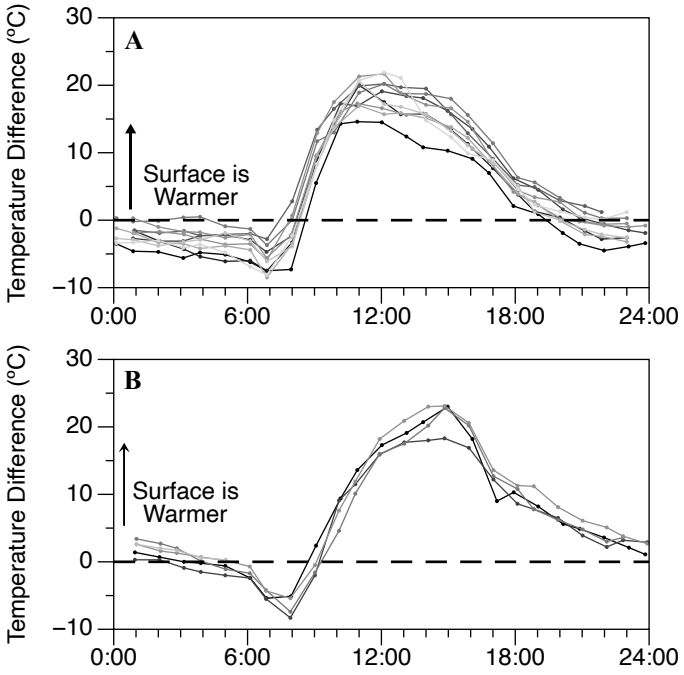

Figure A.14: Temperature difference over time where temperature difference is calculated as surface T(our measurement) – Air T(meteorological measurement). Positive values indicate a warmer surface compared to air. **A)** Surface-Air temperature difference at Mar de Quartz. The gray-scale gradient distinguishes different days from the earliest date (black line, Oct 1) to the latest date (lightest gray, Oct 11). **B)** Surface-Air temperature difference at Los Halitos. The gray-scale gradient distinguishes different days from the earliest date (black line, Sep 30) to the latest date (lightest gray, Oct 4). The positive temperature difference peak around 12:00 indicates a large influence of conductive warming from the soil surface. We interpret this as evidence that our surface sensor is a reasonable proxy for surface temperature.

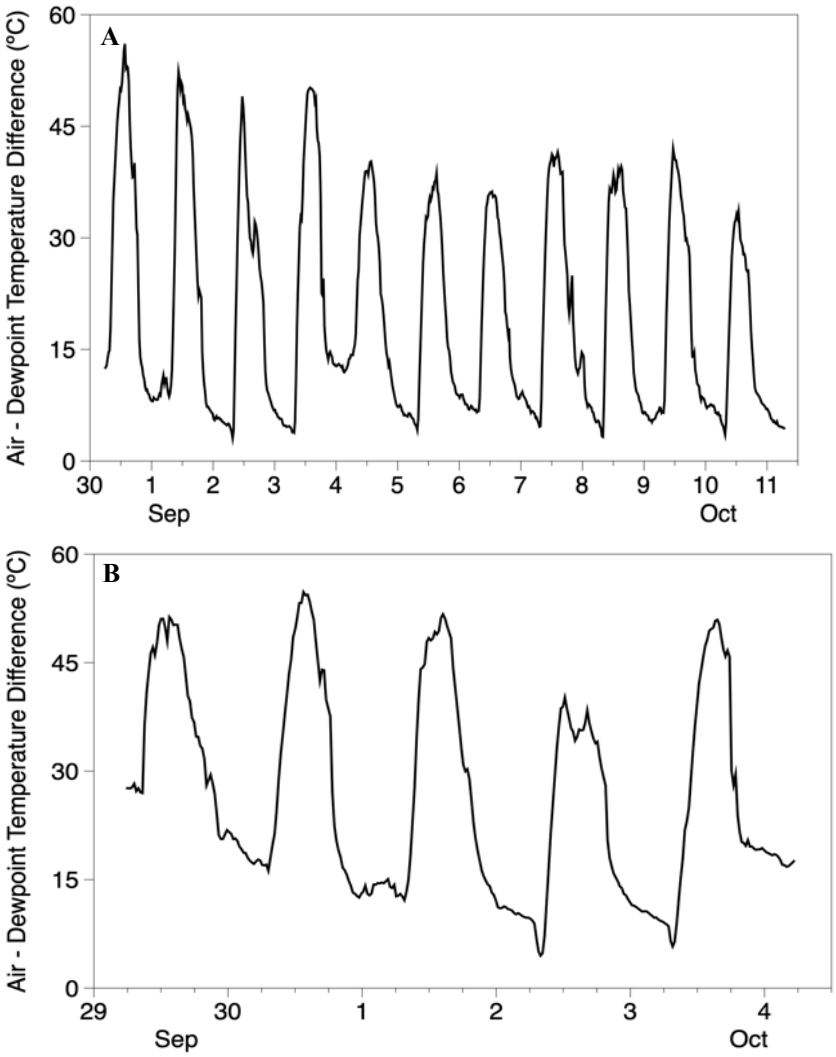

Figure A.15: Air – Dewpoint temperature difference over time at **A)** Mar de Quartz and **B)** Los Halitos during the field measurement. Air – Dewpoint temperature difference is calculated as surface air temperature minus the dewpoint temperature. This evidence supports our interpretation that no dew deposition occurred during our observations as the temperature is generally > 5ºC above the dewpoint.

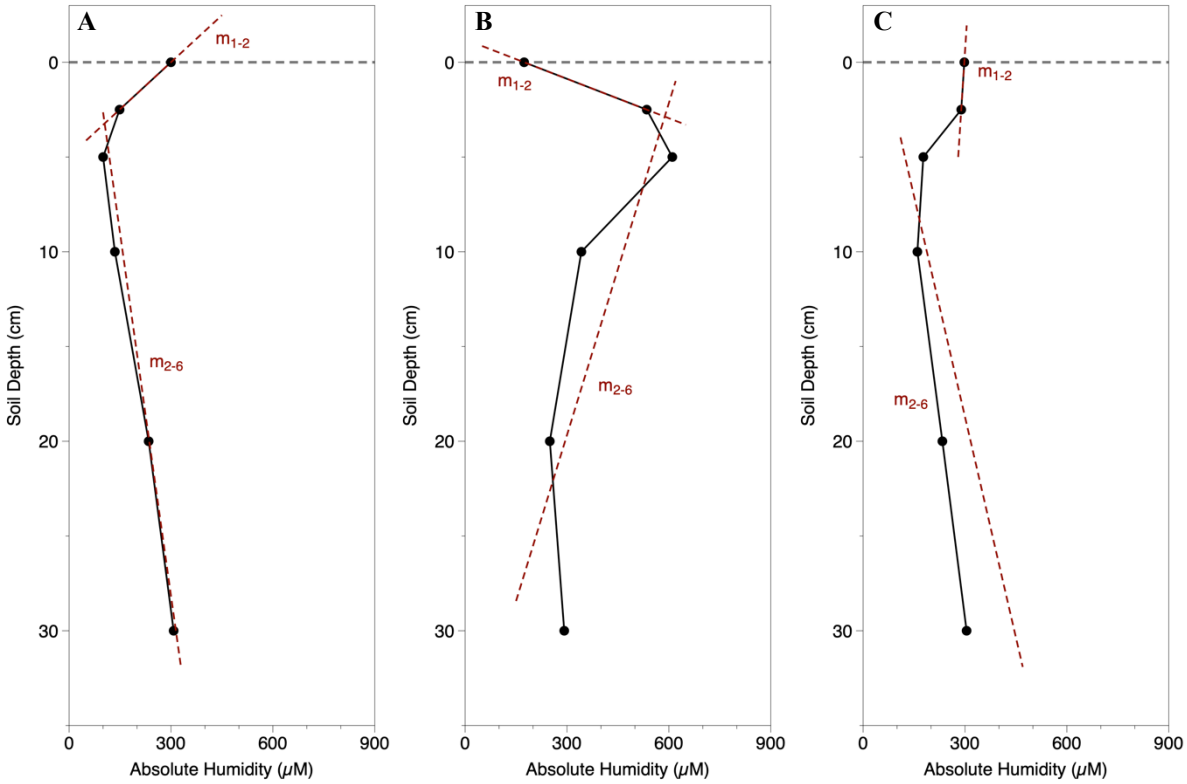

Figure A.16: Examples of the regression slopes used to identify profile type in the case of **A)** [$H_2O_{(g)}$] minimum, **B)** [$H_2O_{(g)}$] maximum, and **C)** constant. We use the m1-2 slope to identify the profile type.

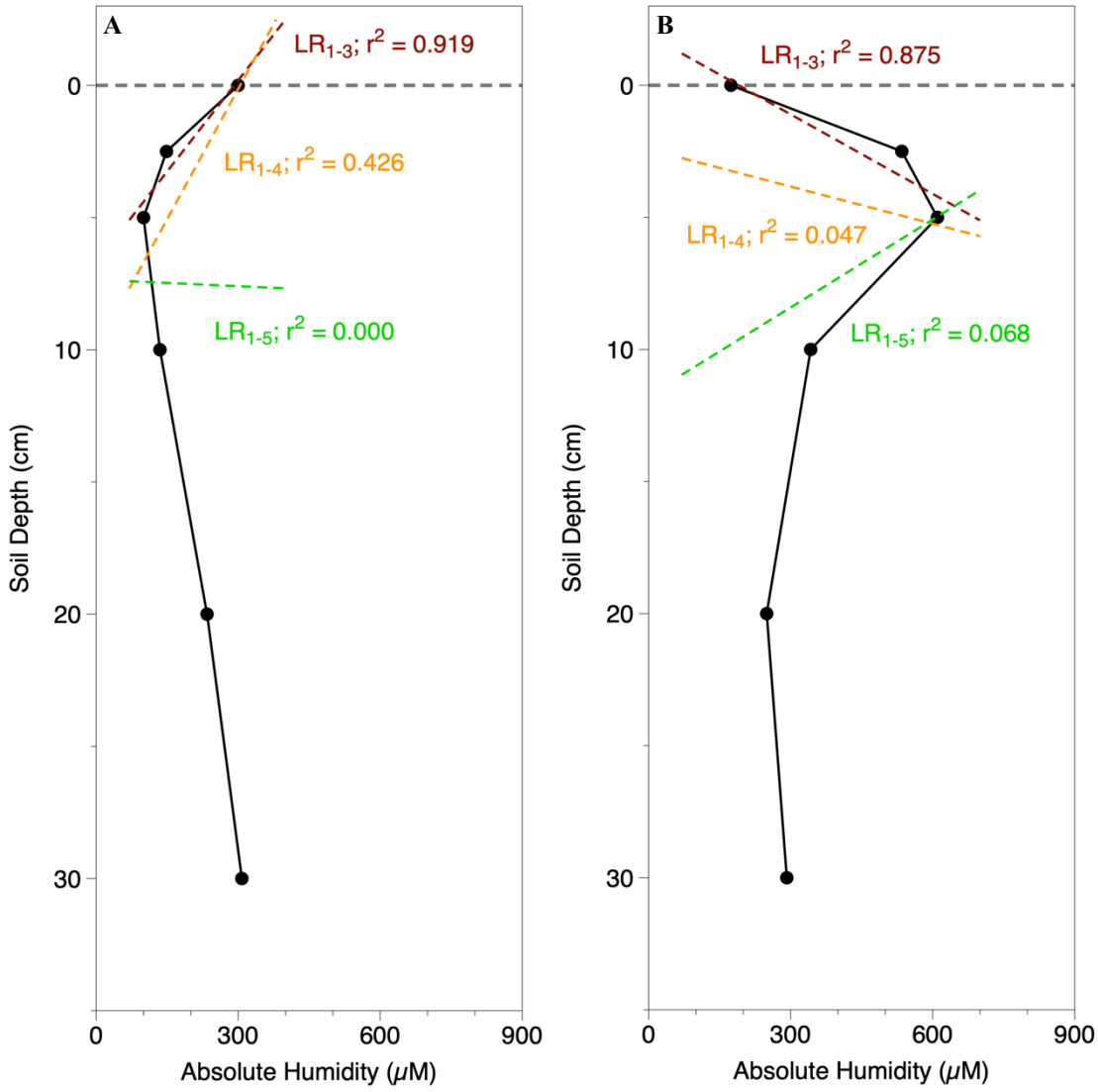

Figure A.17: Upper profile identification process for **A)** [$H_2O_{(g)}$] minimum and **B)** [$H_2O_{(g)}$] maximum profile types. Slopes of $m_{1\text{-}2}$ < -15 μM cm^{-1} are labeled as [$H_2O_{(g)}$] minimum-type profiles and $m_{1\text{-}2}$ slopes > 15 μM cm^{-1} are labeled as [$H_2O_{(g)}$] maximum-type profiles.

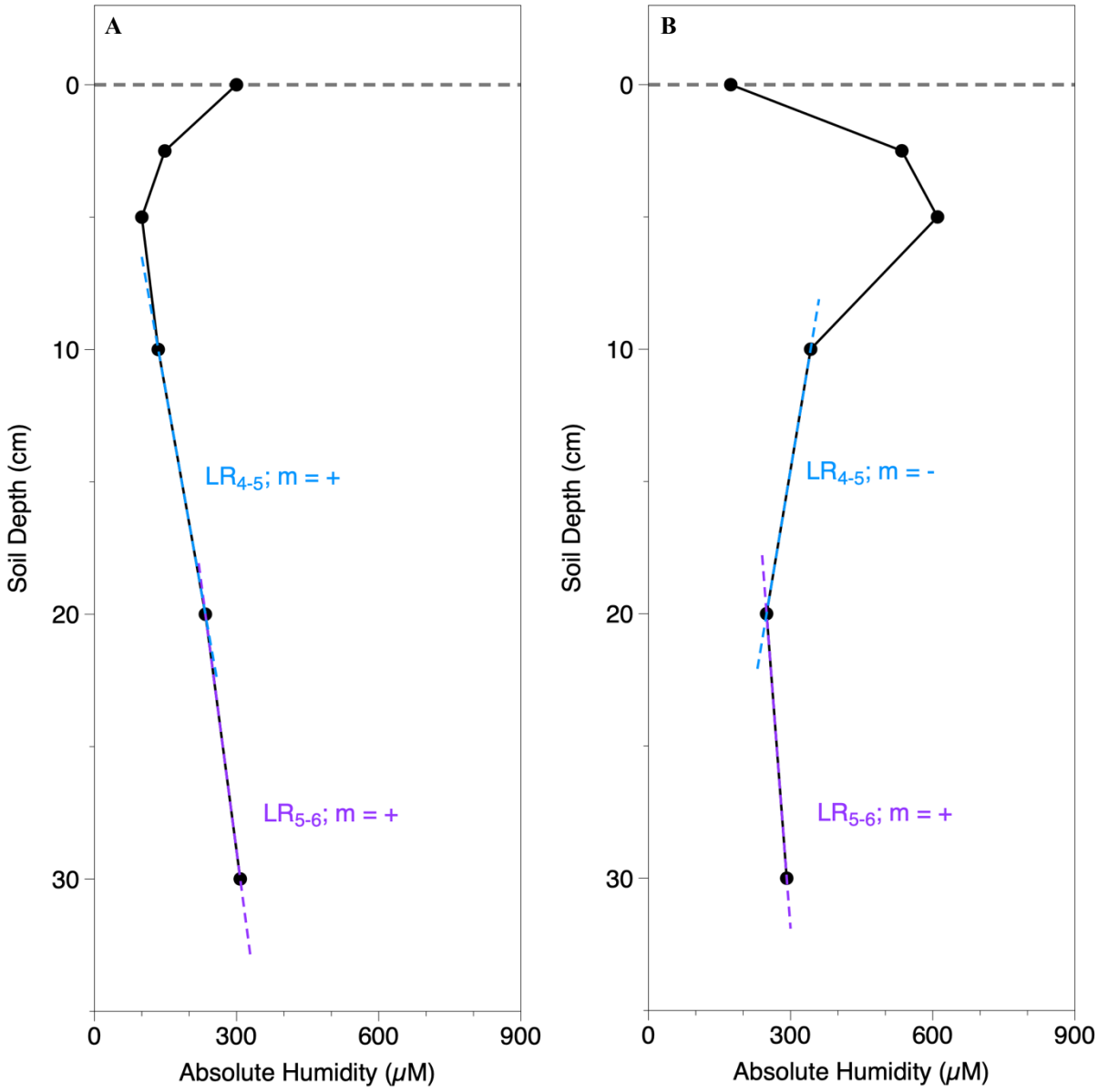

Figure A.18: Reaction 'bottom' identification for **A)** [$H_2O_{(g)}$] minimum and **B)** [$H_2O_{(g)}$] maximum profile types. This algorithm identifies points to be excluded from the lower profile regression.

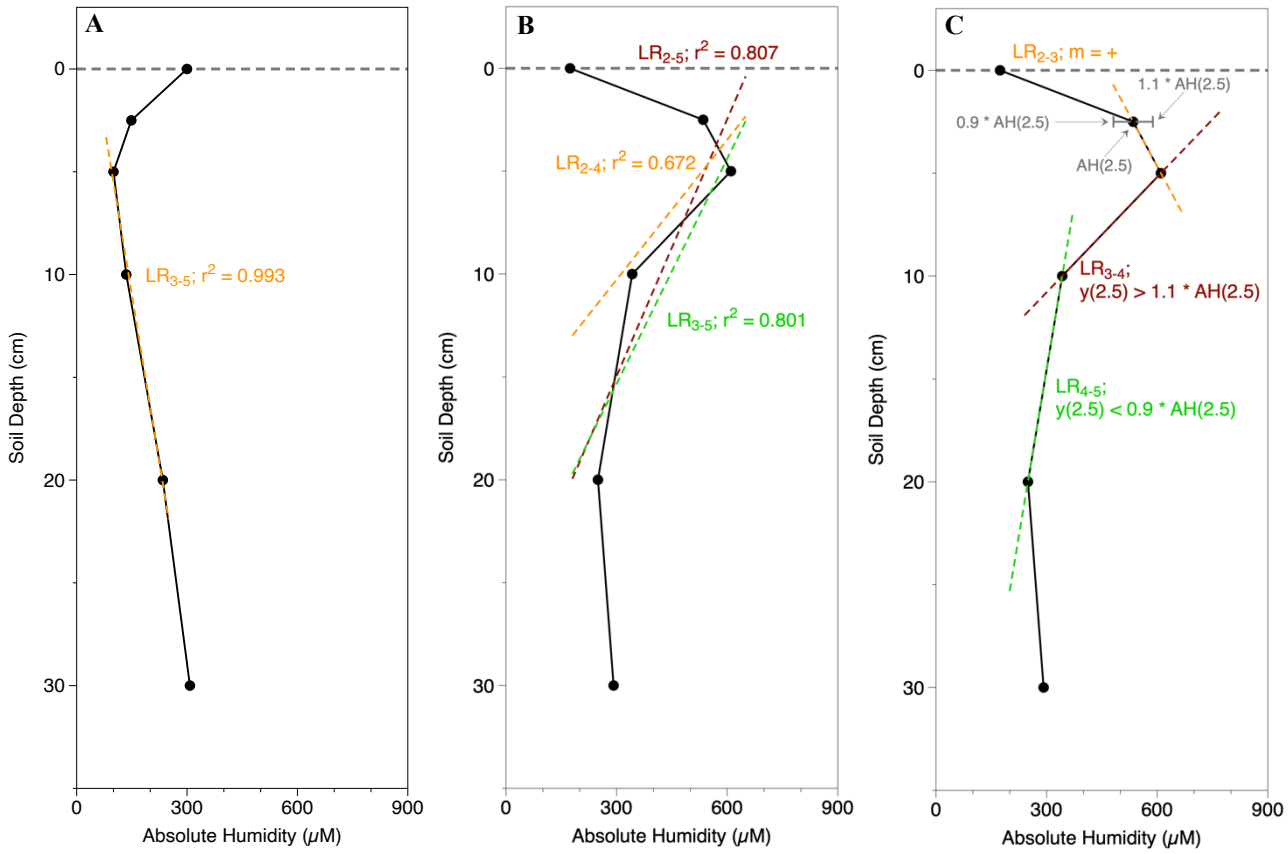

Figure A.19: Lower profile identification process for **A)** [$H_2O_{(g)}$] minimum, **B)** [$H_2O_{(g)}$] maximum profile types with linear regressions of n ≥ 3, and **C)** [$H_2O_{(g)}$] maximum profile types with lower profile linear regressions of n =2.

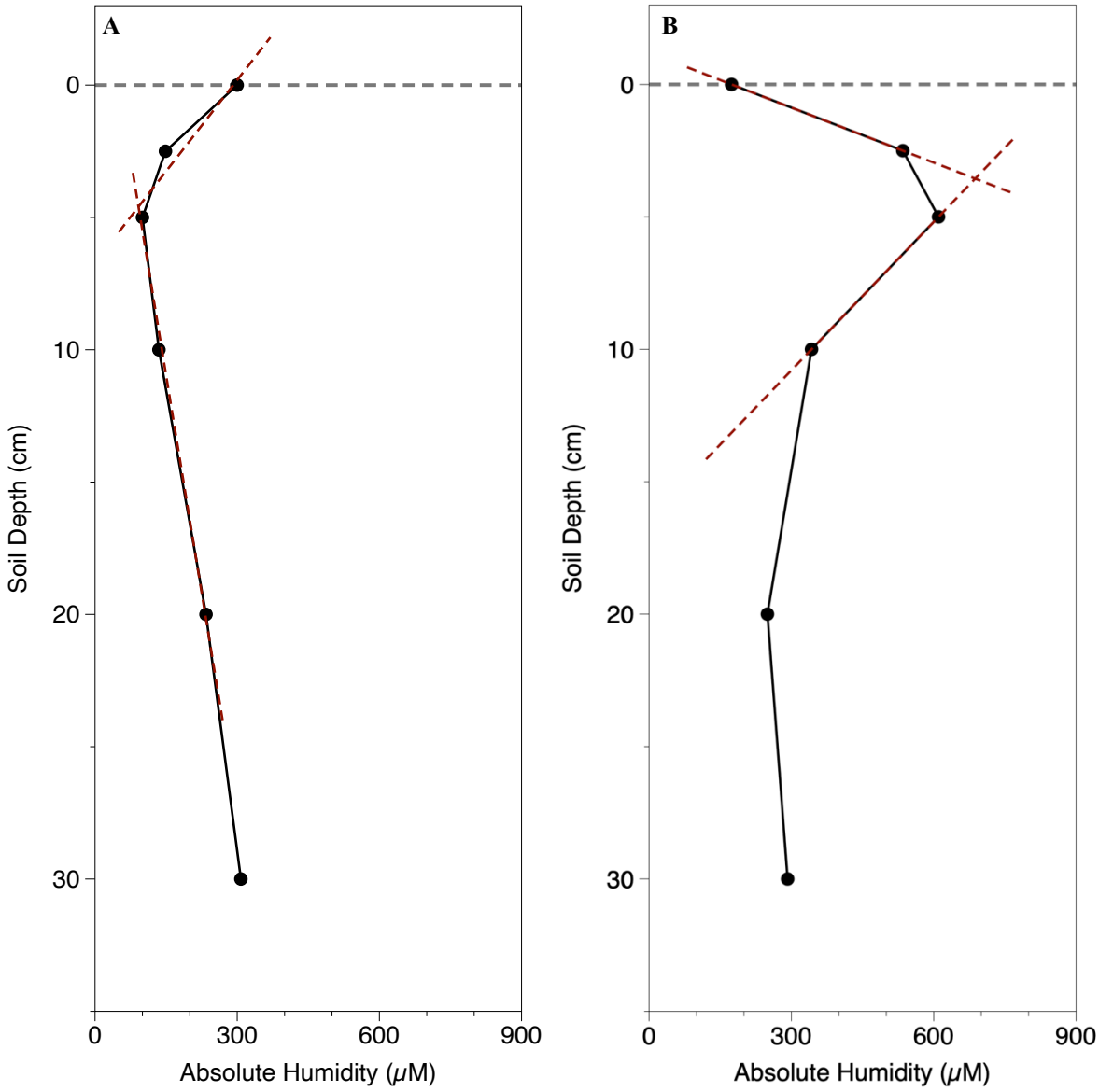

Figure A.20: Final linear approximations for **A)** [$H_2O_{(g)}$] minimum and **B)** [$H_2O_{(g)}$] maximum profile types. The black dots are the field-measured [$H_2O_{(g)}$] values and the red dashed lines are the linear approximation of the data using the algorithms described in detail in section A.1.

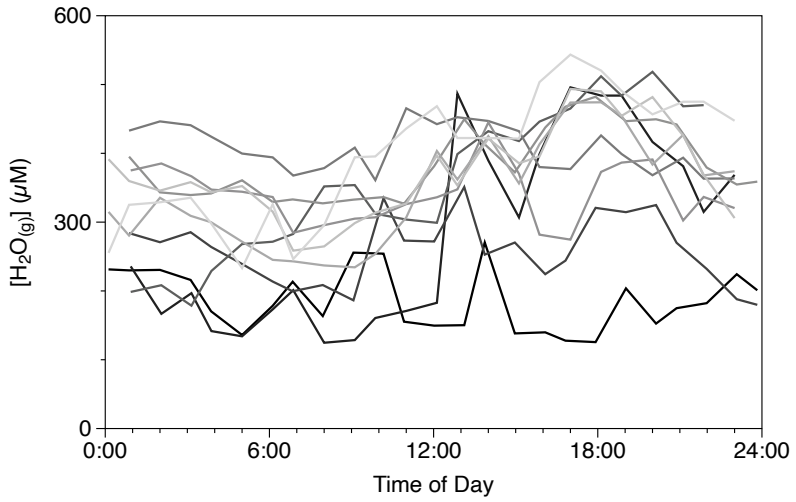

Figure A.21: $[H_2O_{(g)}]$ from the 10 m meteorological station during the field observations from Oct. 1 (black) to Oct 10 (light grey). There is no discernable diurnal pattern in $[H_2O_{(g)}]$ from the 10 m meteorological data. This indicates the diurnal pattern observed in figure 10 is not influenced by the overlying atmospheric $[H_2O_{(g)}]$.

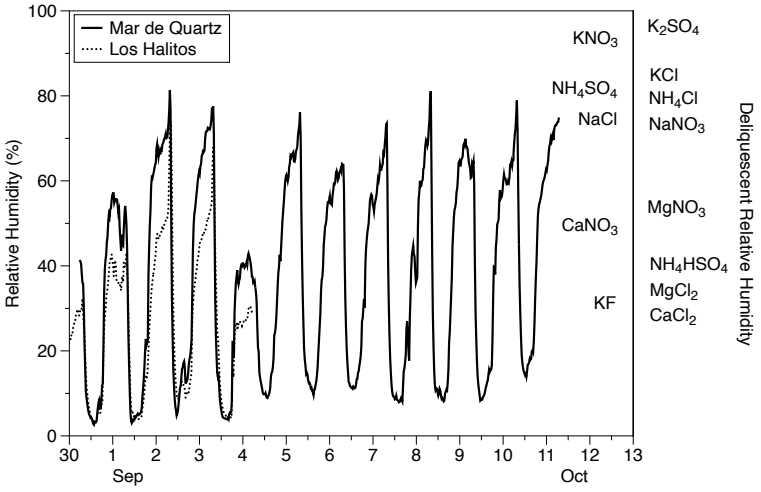

Figure A.22 Surface relative humidity at MDQ (solid line) and LH (dashed line) over the observational period. The deliquescent relative humidity (at 25ºC) of several environmentally relevant minerals are shown on the right y axis. All minerals with DRH below the maximum observed RH were unable to be identified via powder XRD in MDQ and LH soils. This provides reasonable evidence that the soils of MDQ and LH did not deliquesce over the observational period.

APPENDIX A REFERENCES

Alduchov, O. A., and Eskridge, R. E. (**1996**). Improved magnus form approximation of saturation vapor pressure. *Journal of Applied Meteorology*, *35*(4), 601–609. DOI: 10.1175/1520-0450(1996)035<0601:IMFAOS>2.0.CO;2

Lawrence, M. G. (**2005**). The relationship between relative humidity and the dewpoint temperature in moist air: A simple conversion and applications. *Bulletin of the American Meteorological Society*, *86*(2), 225–234. DOI: 10.1175/BAMS-86-2-225

APPENDIX B

PUBLICATION CITATION

Chapter 2 titled "Water Vapor Adsorption Provides Daily, Sustainable Water to Soils of The Hyperarid Atacama Desert" is reprinted in this dissertation with permission from co-authors: Damien Finn, Saul Perez-Montaño, Hinsby Cadillo-Quiroz, Hilairy Hartnett and Steve Desch. The original article was published in the October 2022 issue (volume 22, number 10) of Astrobiology (Glaser et al., 2022). DOI: 10.1089/ast.2021.0171

APPENDIX C

CHAPTER 3 SUPPLEMENTAL INFORMATION

Table C.1: Dry mass values for each sample.

Mineral	Grain Size	Replicate	n	Mass (g)
Olivine	Large	1	3	40.4565 ± 0.00268
		2	8	42.632 ± 0.00099
		3	6	41.7429 ± 0.00196
	Small	1	6	25.5914 ± 0.00236
		2	6	24.8038 ± 0.00186
		3	7	23.9261 ± 0.00253
Anorthite	Large	1	8	32.4405 ± 0.00135
		2	6	35.7268 ± 0.00124
		3	8	39.4254 ± 0.00161
	Small	1	6	17.7325 ± 0.00118
		2	6	18.8552 ± 0.00108
		3	6	13.5637 ± 0.00146
Quartz	Large	1	8	33.8453 ± 0.00574
		2	8	37.7141 ± 0.00509
		3	8	35.6539 ± 0.00504
	Small	1	6	14.3456 ± 0.0031
		2	6	16.9543 ± 0.00288
		3	6	18.7327 ± 0.00303
Serpentine	Large	1	7	23.8108 ± 0.00502
		2	7	24.3046 ± 0.00424
		3	7	24.6257 ± 0.00427
	Small	1	6	13.7629 ± 0.00349
		2	8	14.002 ± 0.00471
		3	6	15.5328 ± 0.0049
Calcite	Large	2	6	12.8216 ± 0.00313
		3	6	11.5942 ± 0.00325
	Small	2	6	19.4892 ± 0.00518
		3	6	22.6218 ± 0.00636

Table C.2: Experimental mass measurements of composite mineral mixture samples.

Incubation	Relative Humidity		Temperature		Mixture 1 Mass		Mixture 2 Mass		Mixture 3 Mass	
	Mean (%)	SD (%)	Mean (ºC)	SD (ºC)	Mean (g)	SD (g)	Mean (g)	SD (g)	Mean (g)	SD (g)
1	51	0.1	24.7	0.04	22.5086	0.00029	28.3931	0.00012	27.2988	0.00033
2	46	0.1	24.7	0.06	22.5060	0.00012	28.3907	0.00012	27.2960	0.00017
3	48	0.1	24.8	0.05	22.5077	0.00012	28.3916	0.00016	27.2977	0.00012
4	54	0.1	24.8	0.07	22.5106	0.00026	28.3955	0.00034	27.3018	0.00025
5	56	0.1	24.8	0.05	22.5121	0.00021	28.3978	0.00024	27.3024	0.00037
6	58	0.1	24.8	0.04	22.5154	0.00036	28.4016	0.00042	27.3078	0.00024

SD: standard deviation

Table C.3: Experimental mass measurements of complex natural soil samples: MDQ and LH.

Water Availability	Replicate	Relative Humidity		Temperature		MDQ Mass		LH Mass	
		Mean (%)	SD (%)	Mean (ºC)	SD (ºC)	Mean (g)	SD (g)	Mean (g)	SD (g)
High	1	56	0.1	24.8	0.05	159.4289	0.00069	107.7470	0.00054
	2	58	0.1	24.8	0.04	159.4667	0.00054	107.7636	0.00090
Medium	1	12	0.1	12.6	0.07	159.3961	0.00131	107.6778	0.00106
	2	12	0.1	12.6	0.05	159.3994	0.00094	107.6729	0.00094
Low	1	16	0.1	33.6	0.07	159.3790	0.00016	107.6556	0.00078
	2	16	0.1	33.6	0.06	159.3713	0.00012	107.6539	0.00069

SD: standard deviation

Table C.4: Preliminary model coefficients and RMSE for each mineral. This table helps to decide which model to use: equation 3.4 or 3.5. Here I decide that the models are similar enough to use the least complex model (equation 3.5).

Mineral	Model	a	b	d	c	RMSE	Mean Residual at Low Water Content
olivine	with c	0.000188	-0.0173	0.715		0.435	0.501
	without c	0.000190	-0.0153	0.732	-0.0807	0.434	0.507
anorthite	with c	0.000195	-0.0061	0.783		0.511	0.402
	without c	0.000179	-0.0171	0.705	0.4033	0.493	0.389
serpentine	with c	0.001453	-0.0707	0.357		1.685	1.290
	without c	0.001486	-0.0470	0.534	-2.0402	1.628	1.559
quartz	with c	0.000685	-0.0582	0.926		1.215	0.815
	without c	0.000716	-0.0361	1.239	-1.5872	1.157	1.025
calcite	with c	0.000810	-0.0365	0.735		0.623	-0.326
	without c	0.000804	-0.0407	0.232	1.8697	0.597	-0.144

Table C.5: Final model coefficients fit to each mineral using equation 3.7.

Mineral	r^2	RMSE	a	b	d	f
Olivine	0.9481	0.222	0.0002	-0.0070	0.4809	6.33E-07
Anorthite	0.9195	0.281	0.0002	0.0033	0.4362	2.59E-07
Serpentine	0.9880	0.555	0.0011	-0.0395	0.3273	1.19E-06
Quartz	0.9776	0.489	0.0006	-0.0286	0.6796	7.85E-07
Calcite	0.9877	0.532	0.0007	-0.0391	0.8071	-1.44E-06

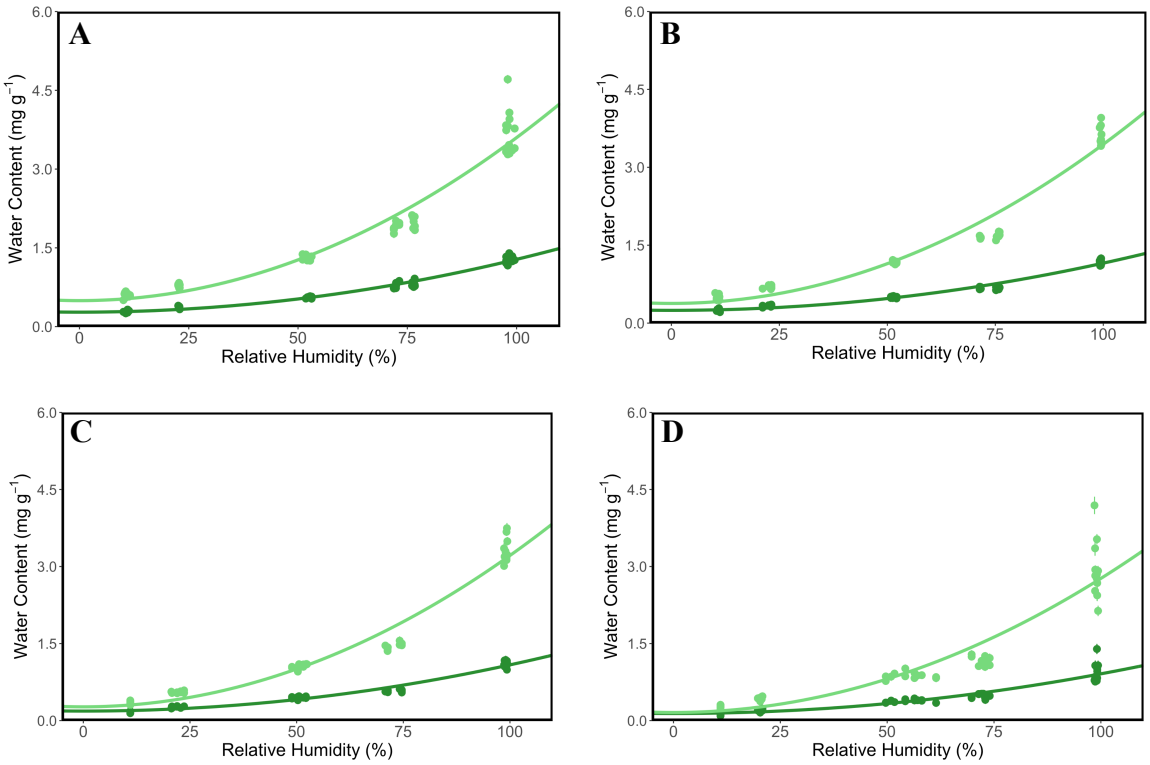

Figure C.1: Olivine water content as a function of relative humidity at fixed T = **A)** 10, **B)** 18, **C)** 26, and **D)** 35°C. Data (points) and linear regression (line) are separated by categorical variable grain size (large, dark green; small, light green).

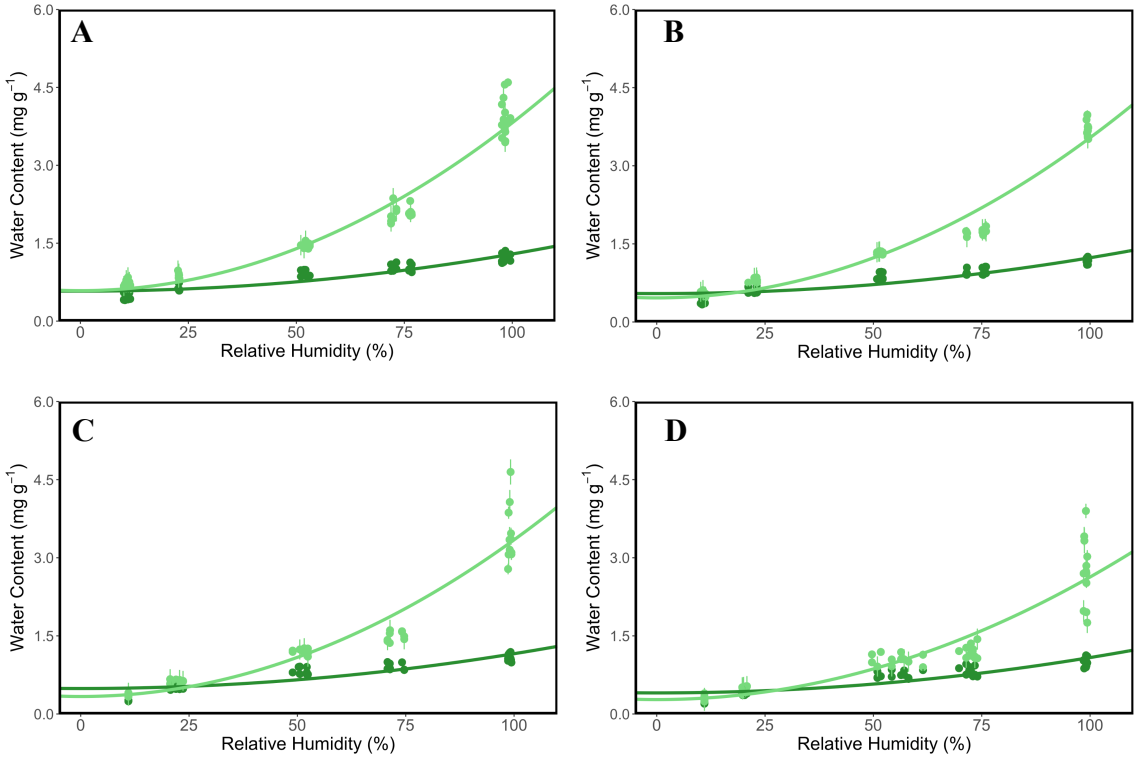

Figure C.2: Anorthite water content as a function of relative humidity at fixed T = **A)** 10, **B)** 18, **C)** 26, and **D)** 35ºC. Data (points) and linear regression (line) are separated by categorical variable grain size (large, dark green; small, light green).

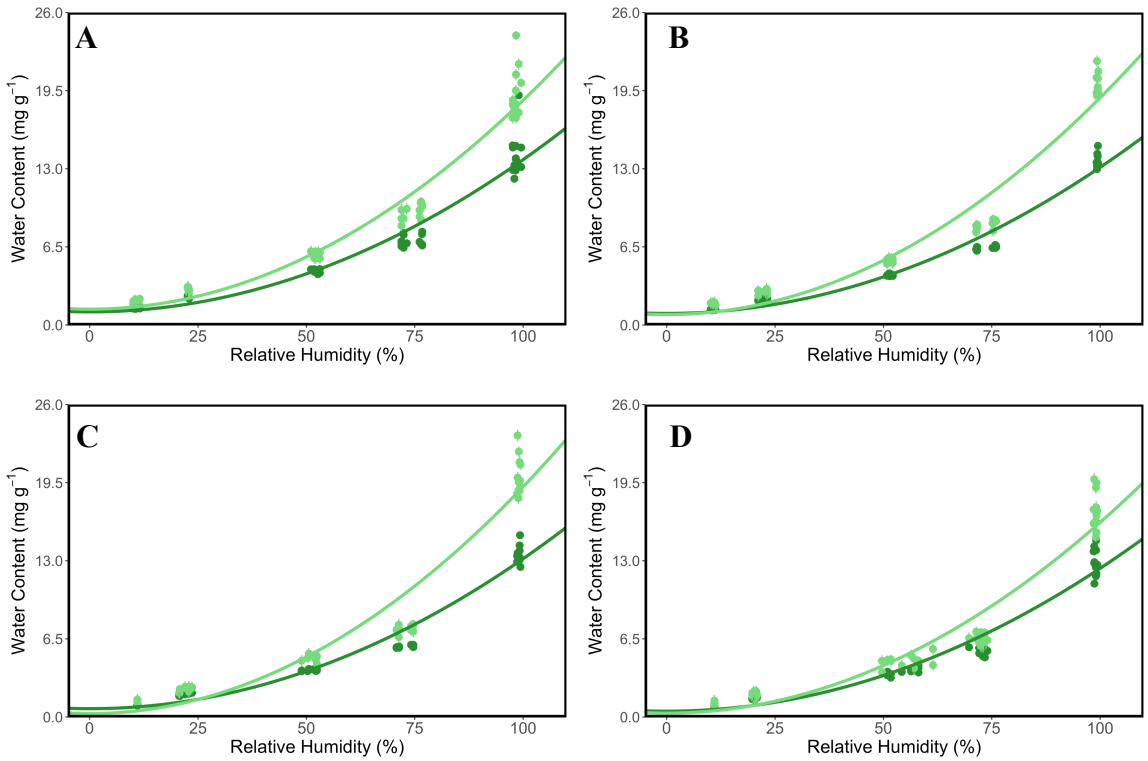

Figure C.3: Serpentine water content as a function of relative humidity at fixed T = **A)** 10, **B)** 18, **C)** 26, and **D)** 35ºC. Data (points) and linear regression (line) are separated by categorical variable grain size (large, dark green; small, light green).

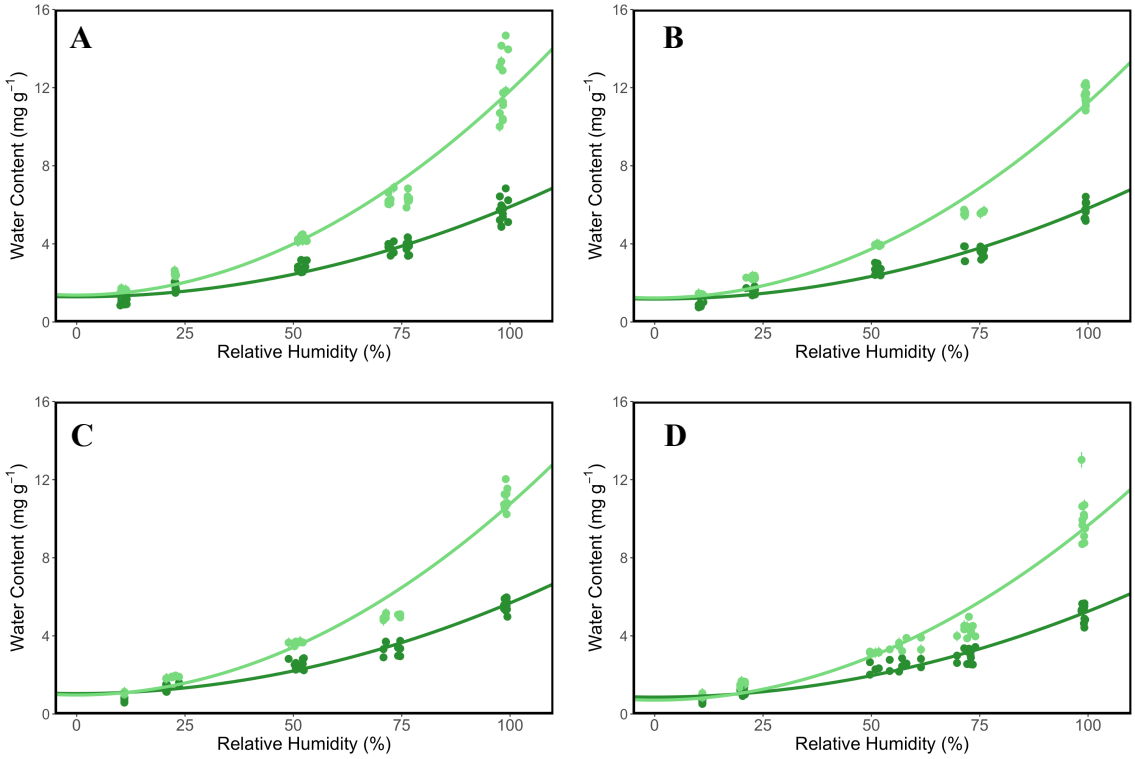

Figure C.4: Quartz water content as a function of relative humidity at fixed T = **A)** 10, **B)** 18, **C)** 26, and **D)** 35°C. Data (points) and linear regression (line) are separated by categorical variable grain size (large, dark green; small, light green).

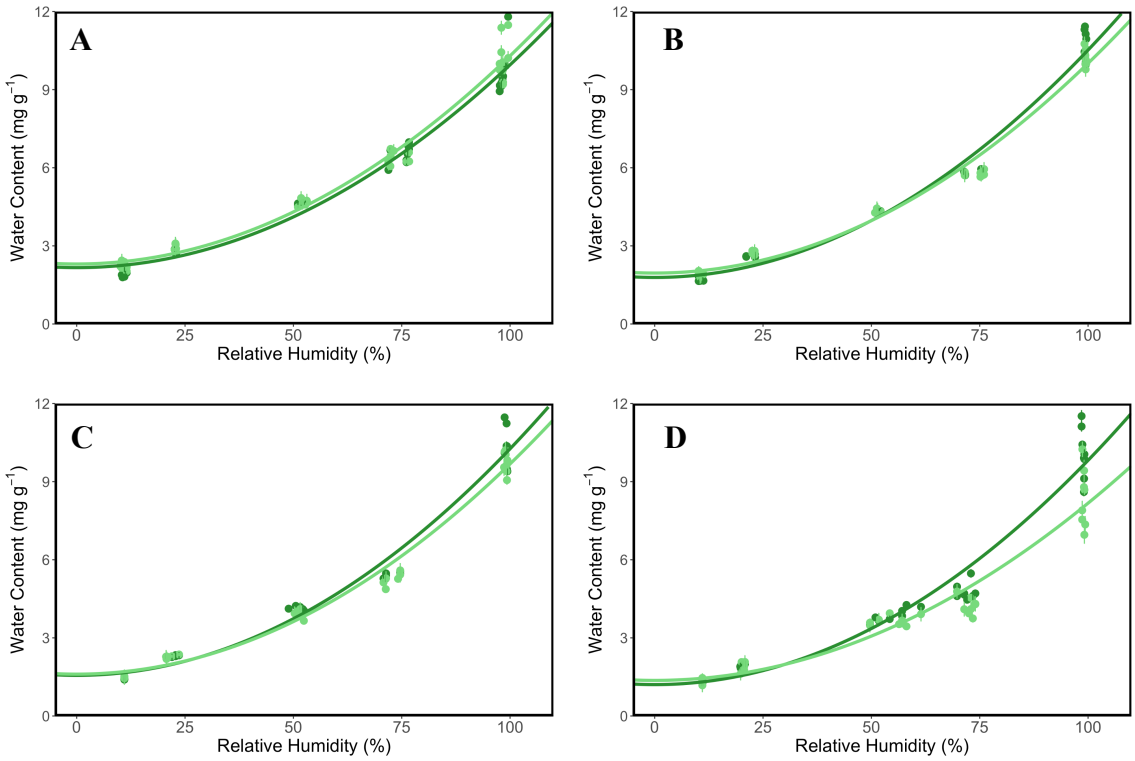

Figure C.5: Calcite water content as a function of relative humidity at fixed T = **A)** 10, **B)** 18, **C)** 26, and **D)** 35°C. Data (points) and linear regression (line) are separated by categorical variable grain size (large, dark green; small, light green).

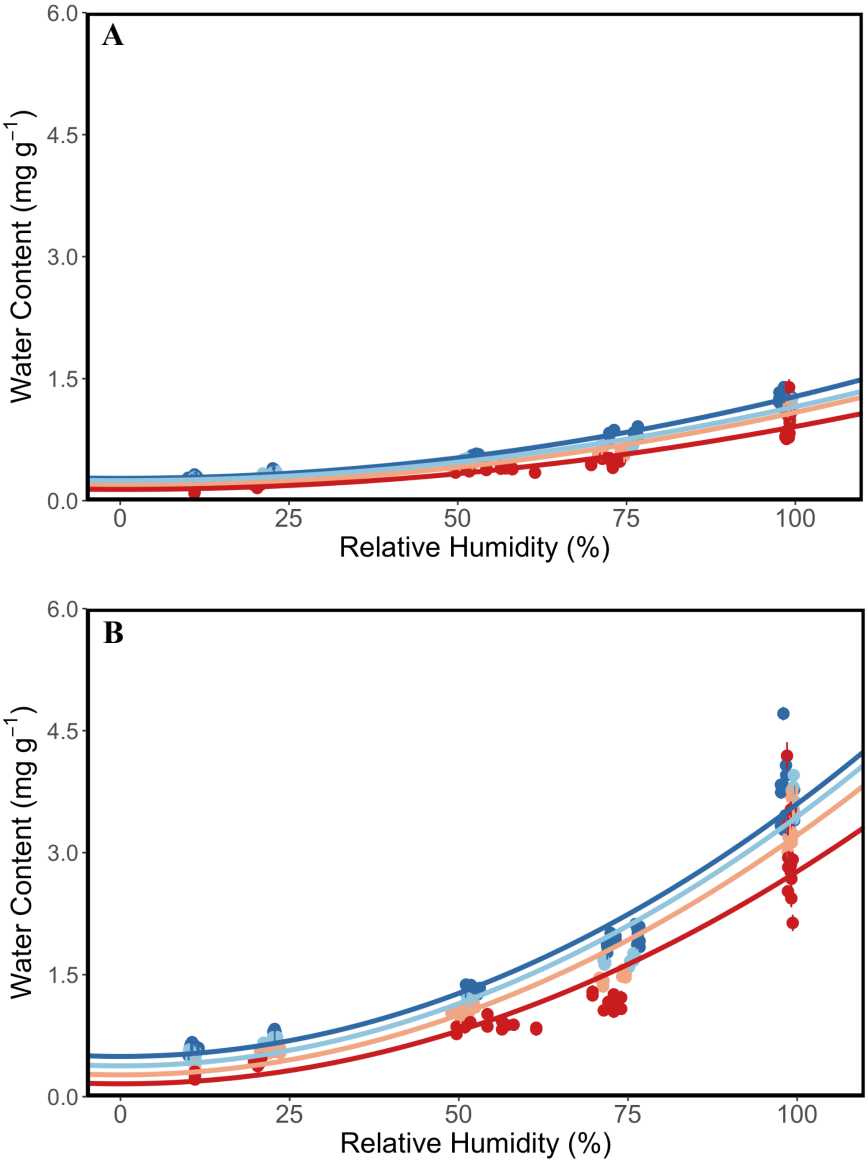

Figure C.6: Olivine water content as a function of relative humidity at fixed grain size: **A)** large and **B)** small. Data (points) and linear regression (line) are separated by categorical variable temperature (10°C, navy blue; 18°C, light blue; 26°C orange; 35°C red).

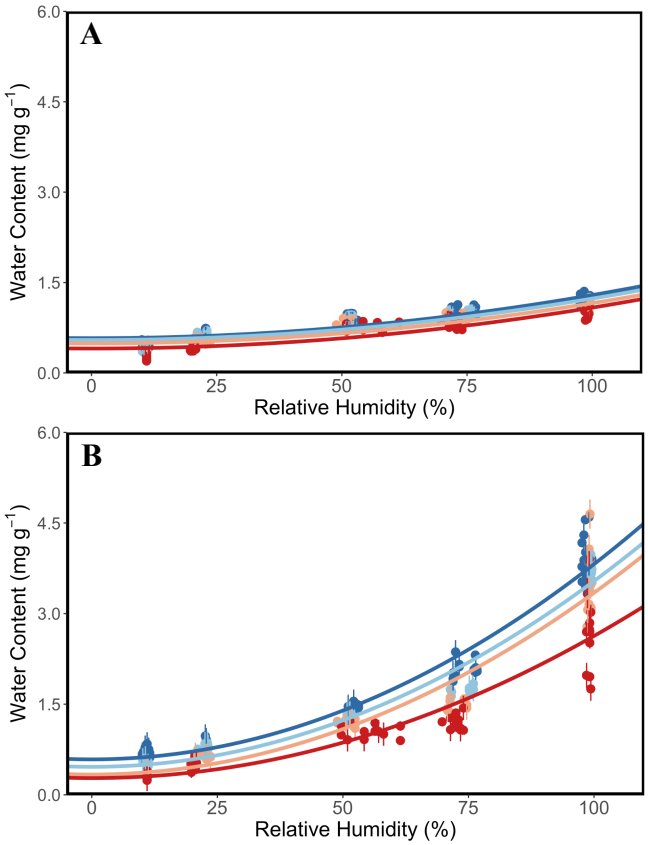

Figure C.7: Anorthite water content as a function of relative humidity at fixed grain size: **A)** large and **B)** small. Data (points) and linear regression (line) are separated by categorical variable temperature (10ºC, navy blue; 18ºC, light blue; 26ºC orange; 35ºC red).

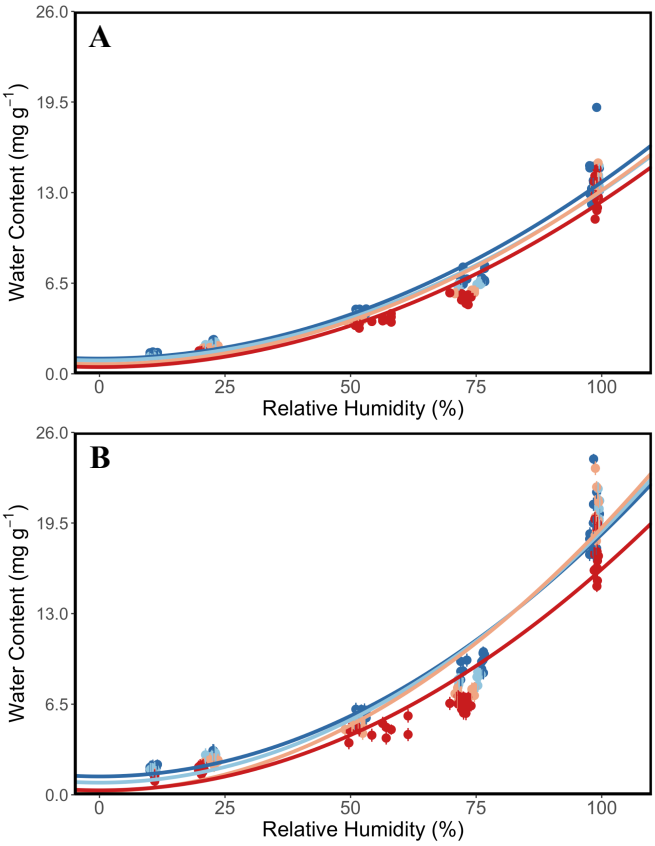

Figure C.8: Serpentine water content as a function of relative humidity at fixed grain size: **A)** large and **B)** small. Data (points) and linear regression (line) are separated by categorical variable temperature (10ºC, navy blue; 18ºC, light blue; 26ºC orange; 35ºC red).

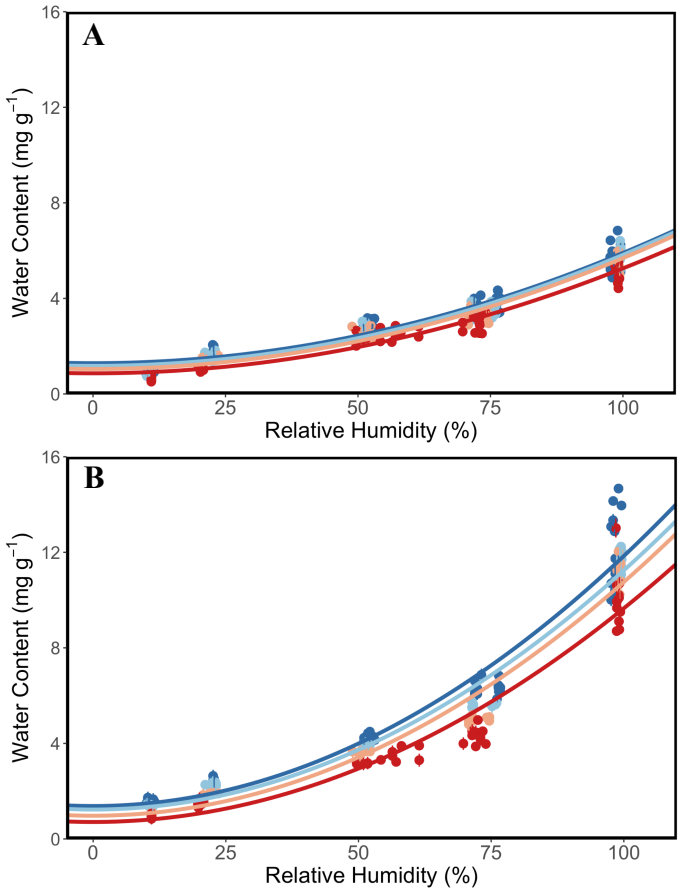

Figure C.9 Quartz water content as a function of relative humidity at fixed grain size: **A)** large and **B)** small. Data (points) and linear regression (line) are separated by categorical variable temperature (10ºC, navy blue; 18ºC, light blue; 26ºC orange; 35ºC red).

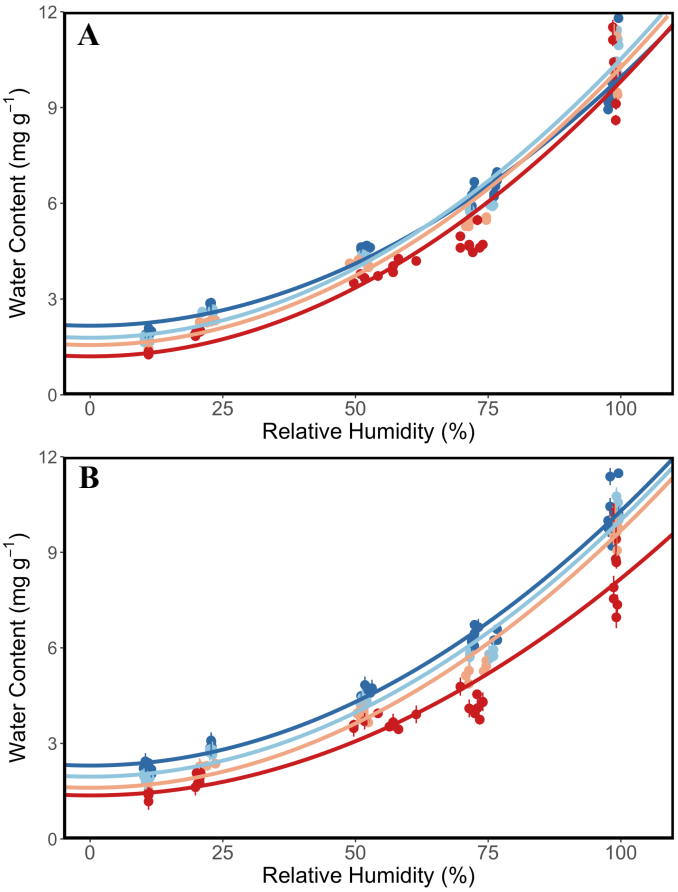

Figure C.10: Calcite water content as a function of relative humidity at fixed grain size: **A)** large and **B)** small. Data (points) and linear regression (line) are separated by categorical variable temperature (10ºC, navy blue; 18ºC, light blue; 26ºC orange; 35ºC red).

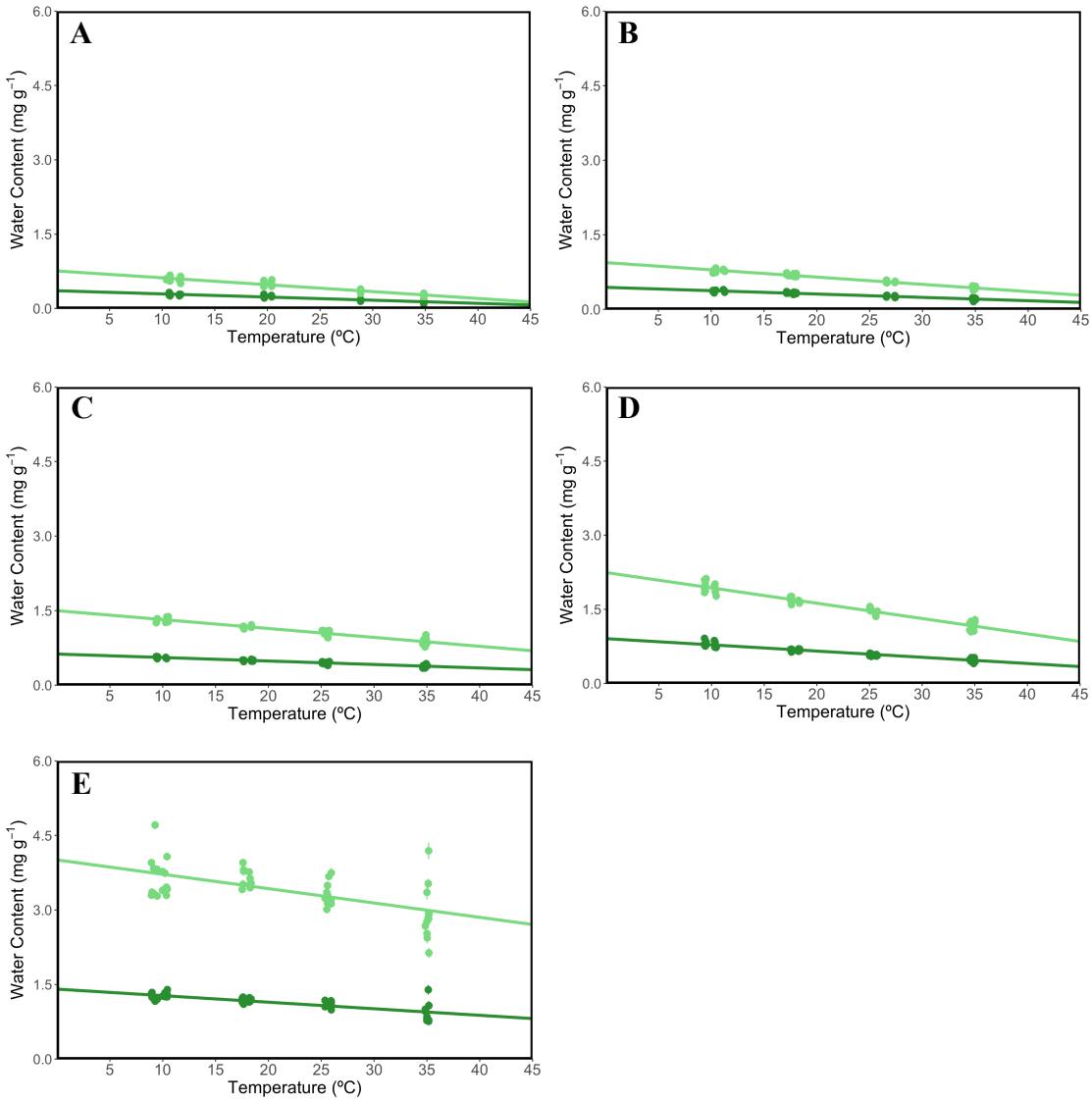

Figure C.11: Olivine water content as a function of temperature at fixed RH buffer: **A)** LiCl (11%), **B)** KCH_3COO (24%), **C)** $Mg(NO_3)_2$ (52%), **D)** NaCl (75%), and **E)** H_2O (100%). Data (points) and linear regression (line) are separated by categorical variable grain size (large, dark green; small, light green).

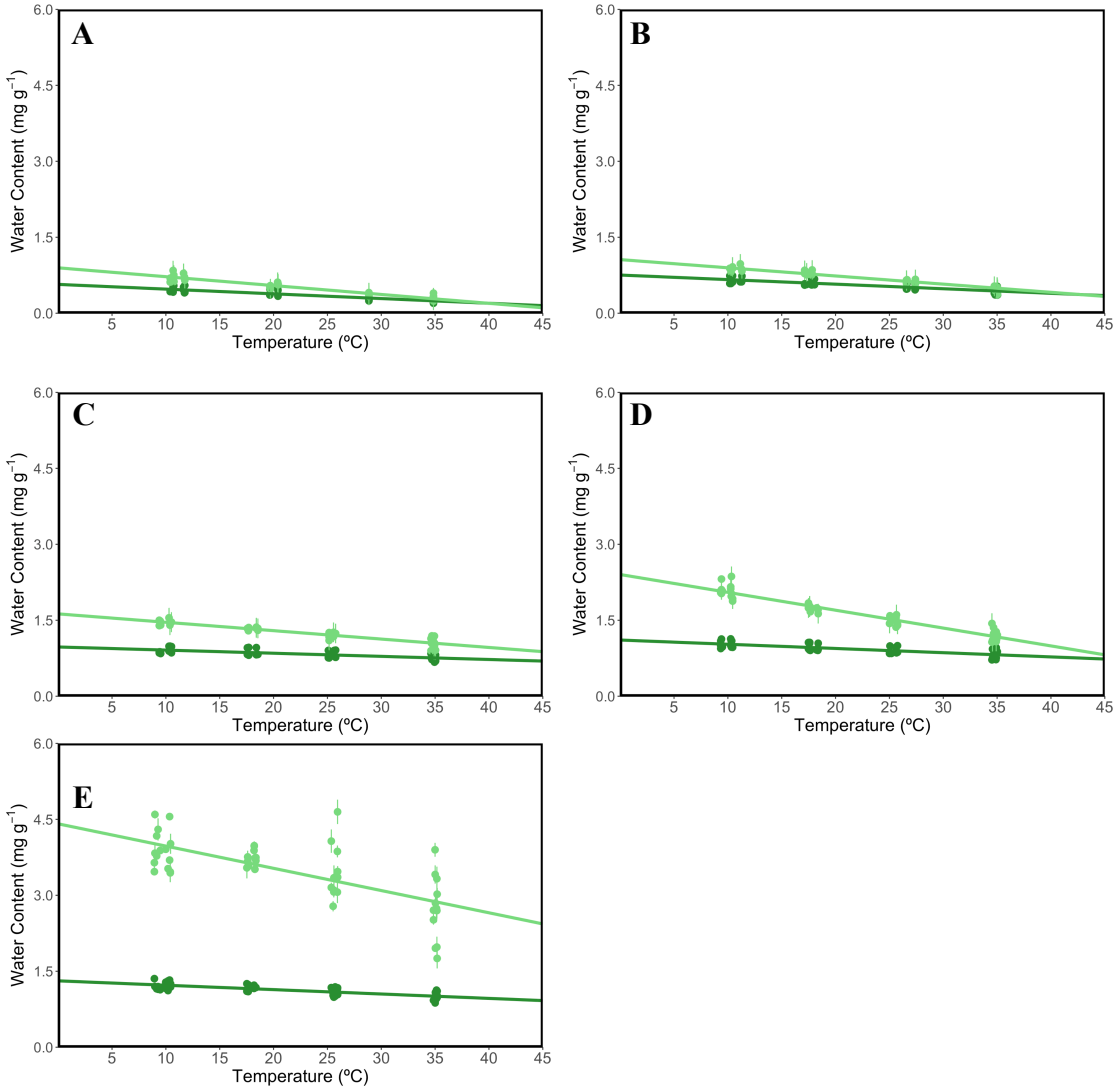

Figure C.12: Anorthite water content as a function of temperature at fixed RH buffer: **A)** LiCl (11%), **B)** KCH_3COO (24%), **C)** $Mg(NO_3)_2$ (52%), **D)** NaCl (75%), and **E)** H_2O (100%). Data (points) and linear regression (line) are separated by categorical variable grain size (large, dark green; small, light green).

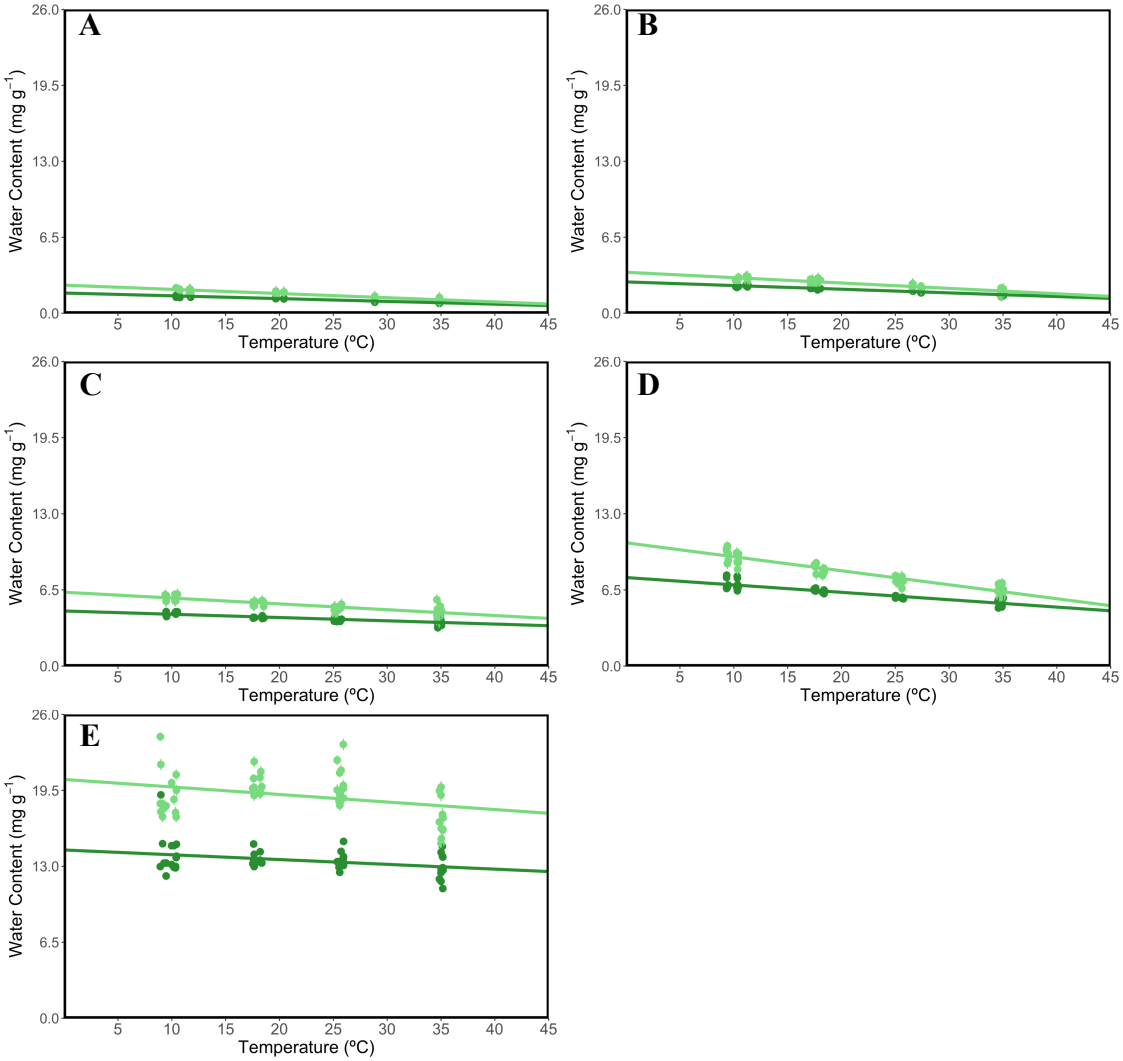

Figure C.13: Serpentine water content as a function of temperature at fixed RH buffer: **A)** LiCl (11%), **B)** KCH_3COO (24%), **C)** $Mg(NO_3)_2$ (52%), **D)** NaCl (75%), and **E)** H_2O (100%). Data (points) and linear regression (line) are separated by categorical variable grain size (large, dark green; small, light green).

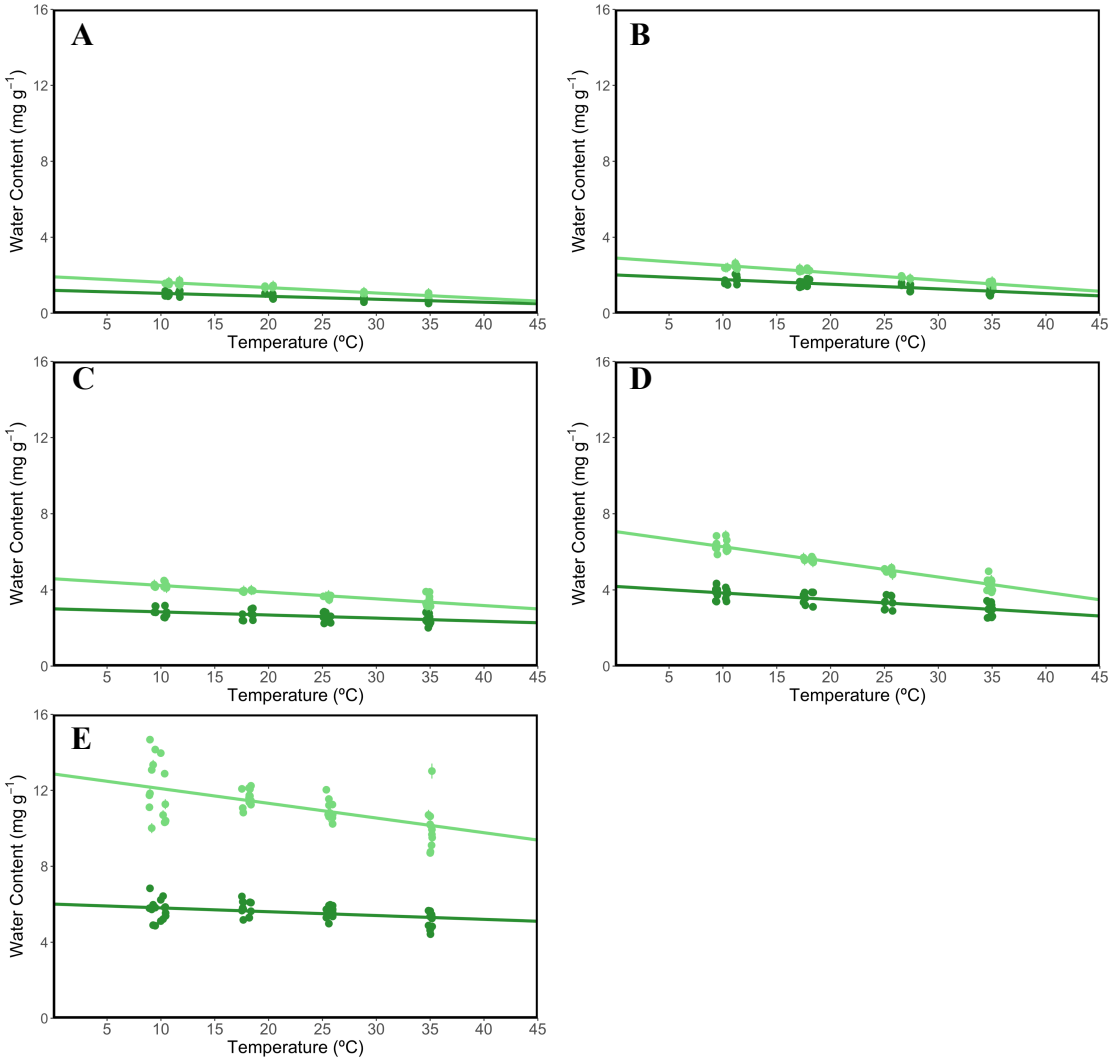

Figure C.14: Quartz water content as a function of temperature at fixed RH buffer: **A)** LiCl (11%), **B)** KCH_3COO (24%), **C)** $Mg(NO_3)_2$ (52%), **D)** NaCl (75%), and **E)** H_2O (100%). Data (points) and linear regression (line) are separated by categorical variable grain size (large, dark green; small, light green).

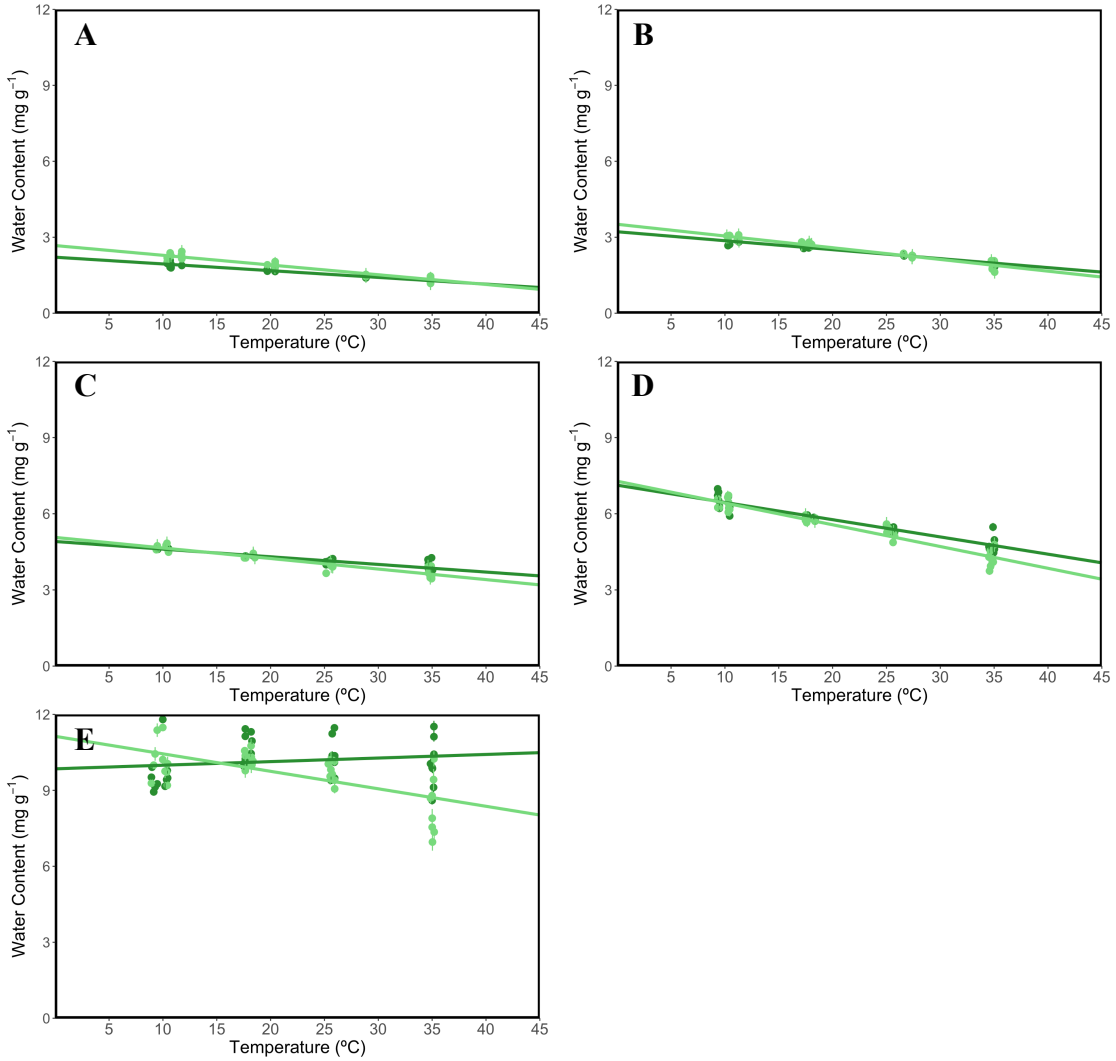

Figure C.15: Calcite water content as a function of temperature at fixed RH buffer: **A)** LiCl (11%), **B)** KCH_3COO (24%), **C)** $Mg(NO_3)_2$ (52%), **D)** NaCl (75%), and **E)** H_2O (100%). Data (points) and linear regression (line) are separated by categorical variable grain size (large, dark green; small, light green).

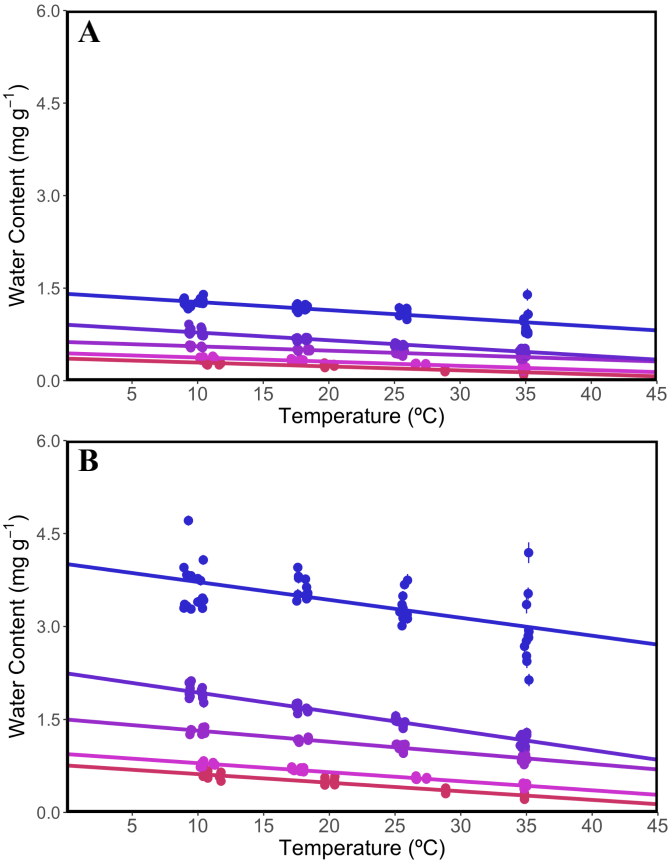

Figure C.16: Olivine water content as a function of temperature at fixed grain size: **A)** large and **B)** small. Data (points) and linear regression (line) are separated by categorical variable RH buffer (LiCl, red; KCH_3COO, pink; $Mg(NO_3)_2$, magenta; NaCl, violet; H_2O, blue).

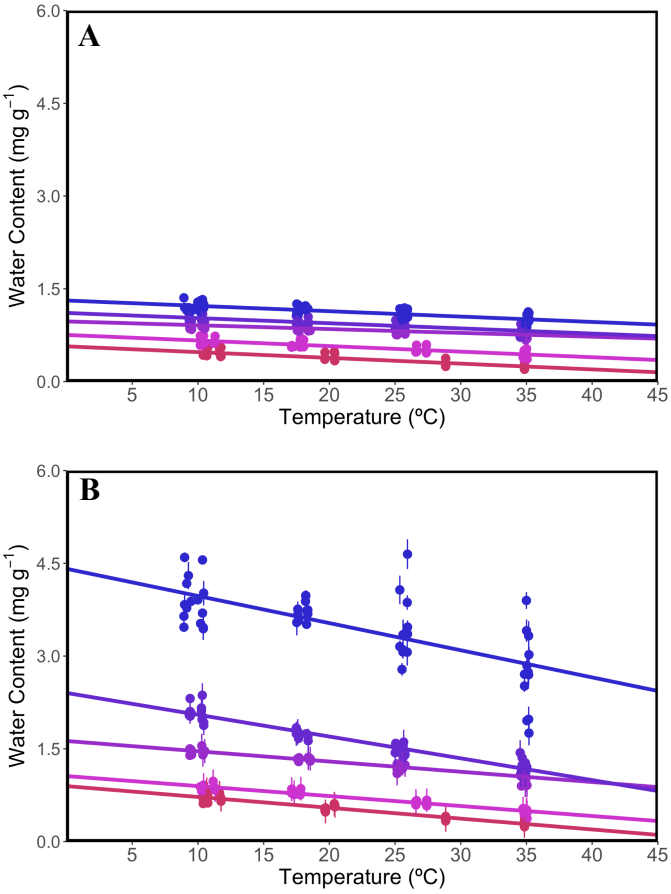

Figure C.17: Anorthite water content as a function of temperature at fixed grain size: **A)** large and **B)** small. Data (points) and linear regression (line) are separated by categorical variable RH buffer (LiCl, red; KCH_3COO, pink; $Mg(NO_3)_2$, magenta; NaCl, violet; H_2O, blue).

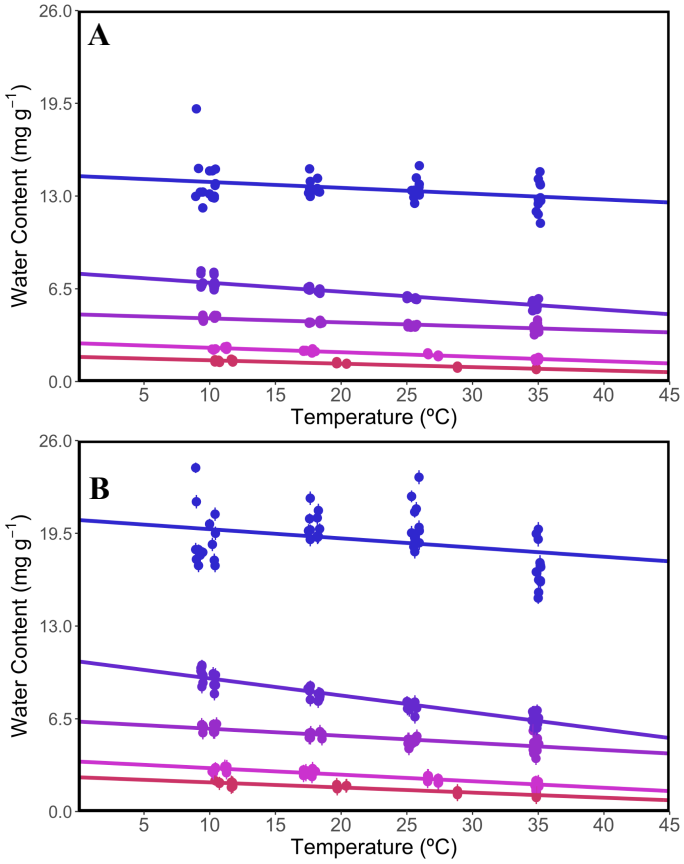

Figure C.18: Serpentine water content as a function of temperature at fixed grain size: **A)** large and **B)** small. Data (points) and linear regression (line) are separated by categorical variable RH buffer (LiCl, red; KCH_3COO, pink; $Mg(NO_3)_2$, magenta; NaCl, violet; H_2O, blue).

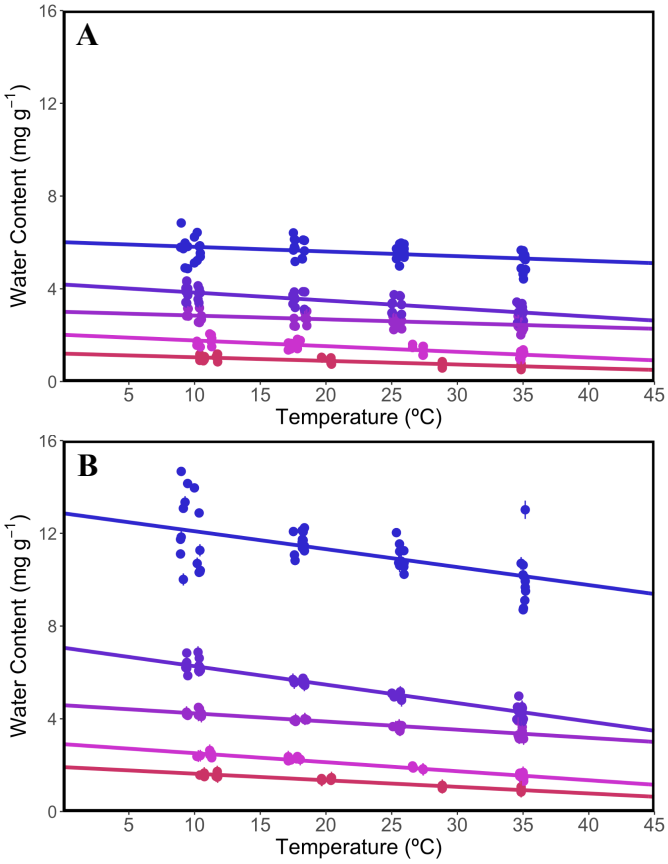

Figure C.19: Quartz water content as a function of temperature at fixed grain size: **A)** large and **B)** small. Data (points) and linear regression (line) are separated by categorical variable RH buffer (LiCl, red; KCH_3COO, pink; $Mg(NO_3)_2$, magenta; NaCl, violet; H_2O, blue).

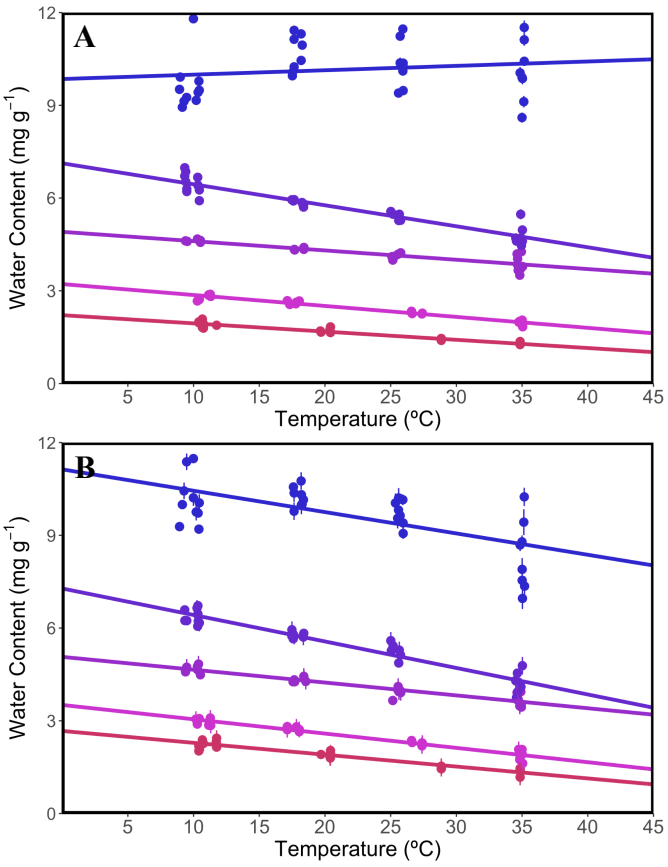

Figure C.20: Calcite water content as a function of temperature at fixed grain size: **A)** large and **B)** small. Data (points) and linear regression (line) are separated by categorical variable RH buffer (LiCl, red; KCH_3COO, pink; $Mg(NO_3)_2$, magenta; NaCl, violet; H_2O, blue).

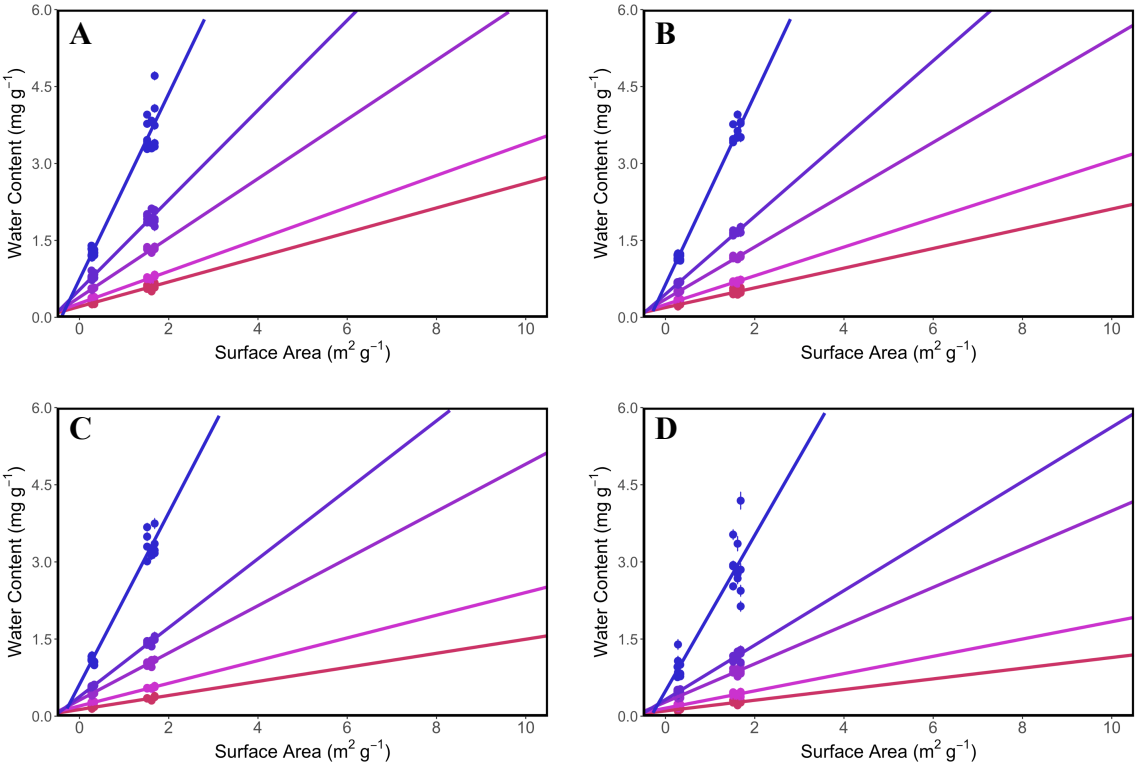

Figure C.21: Olivine water content as a function of surface area at fixed T = **A)** 10, **B)** 18, **C)** 26, and **D)** 35°C. Data (points) and linear regression (line) are separated by categorical variable RH buffer (LiCl, red; KCH_3COO, pink; $Mg(NO_3)_2$, magenta; NaCl, violet; H_2O, blue).

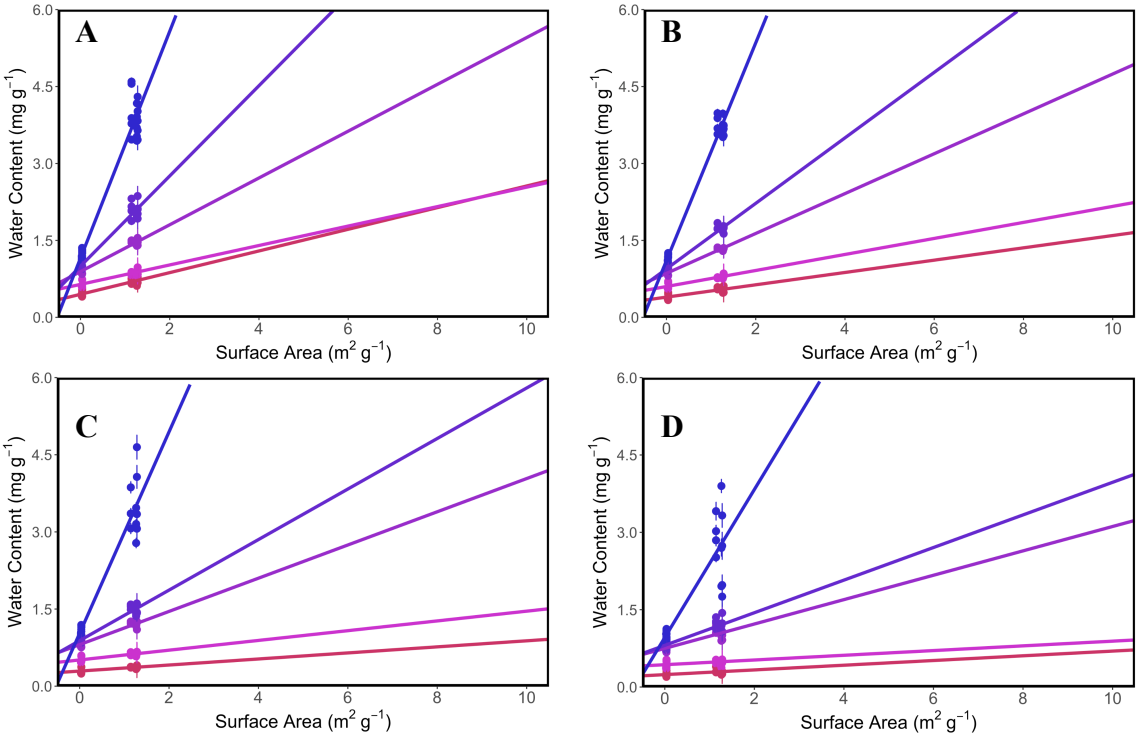

Figure C.22:. Anorthite water content as a function of surface area at fixed T = **A)** 10, **B)** 18, **C)** 26, and **D)** 35°C. Data (points) and linear regression (line) are separated by categorical variable RH buffer (LiCl, red; KCH_3COO, pink; $Mg(NO_3)_2$, magenta; NaCl, violet; H_2O, blue).

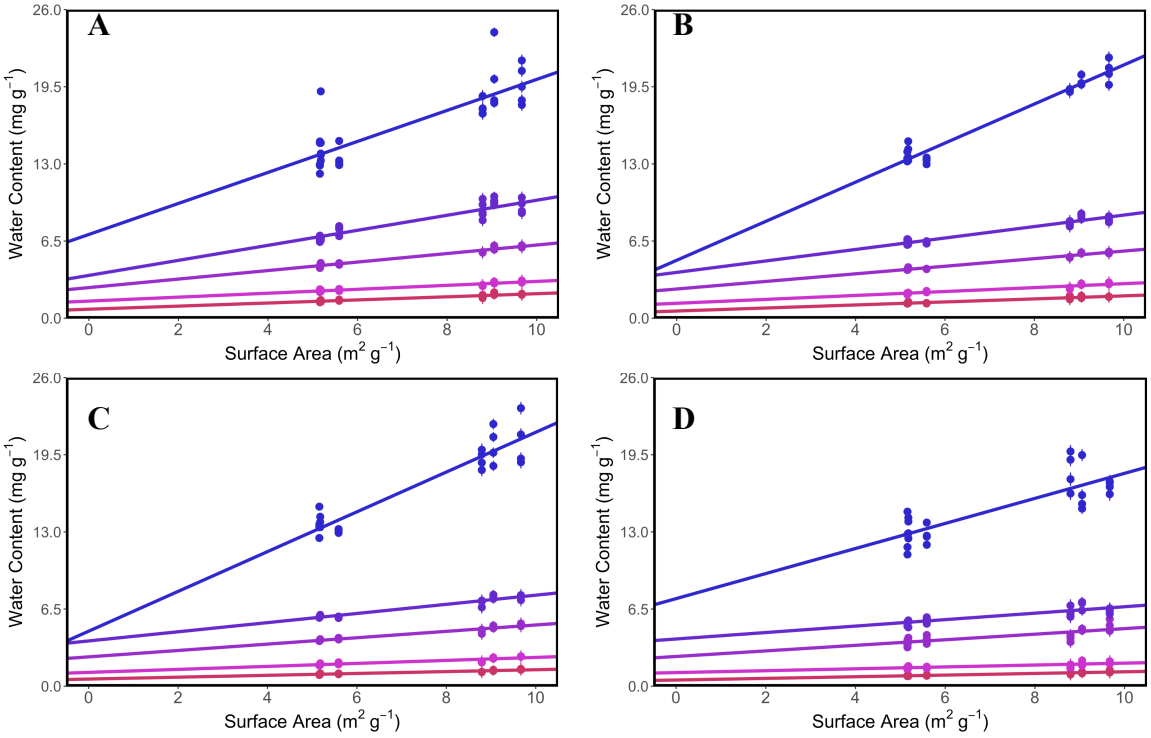

Figure C.23: Serpentine water content as a function of surface area at fixed T = **A)** 10, **B)** 18, **C)** 26, and **D)** 35°C. Data (points) and linear regression (line) are separated by categorical variable RH buffer (LiCl, red; KCH_3COO, pink; $Mg(NO_3)_2$, magenta; NaCl, violet; H_2O, blue).

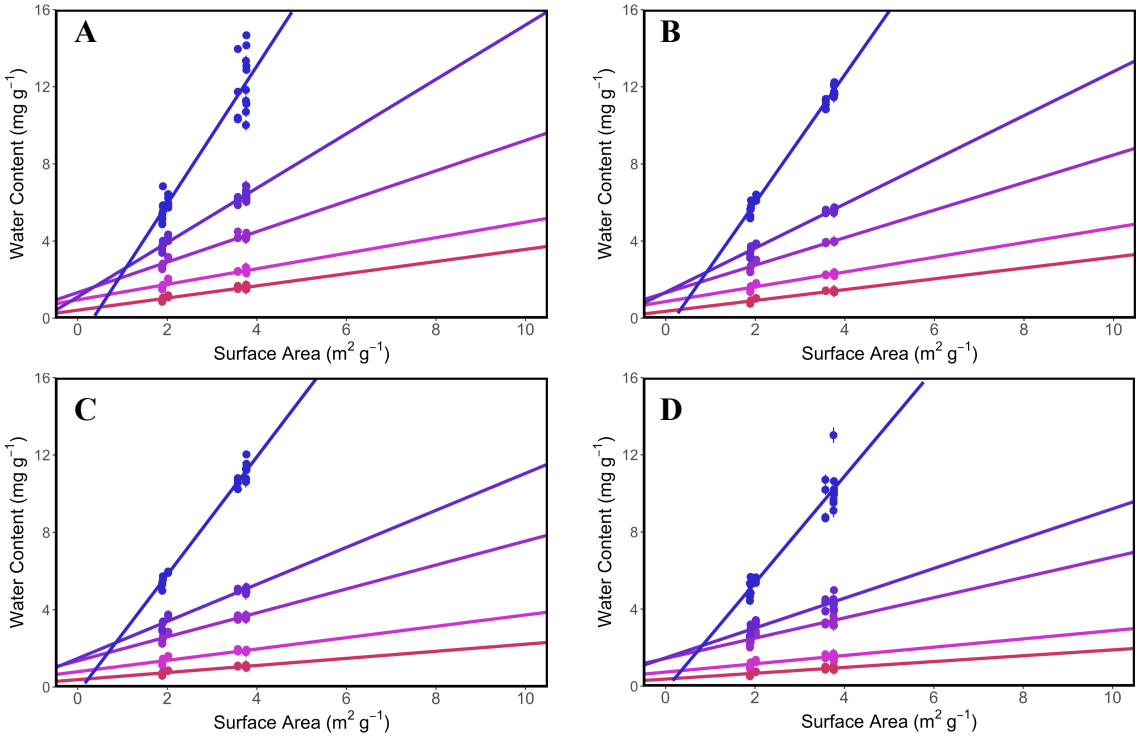

Figure C.24: Quartz water content as a function of surface area at fixed T = **A)** 10, **B)** 18, **C)** 26, and **D)** 35°C. Data (points) and linear regression (line) are separated by categorical variable RH buffer (LiCl, red; KCH_3COO, pink; $Mg(NO_3)_2$, magenta; NaCl, violet; H_2O, blue).

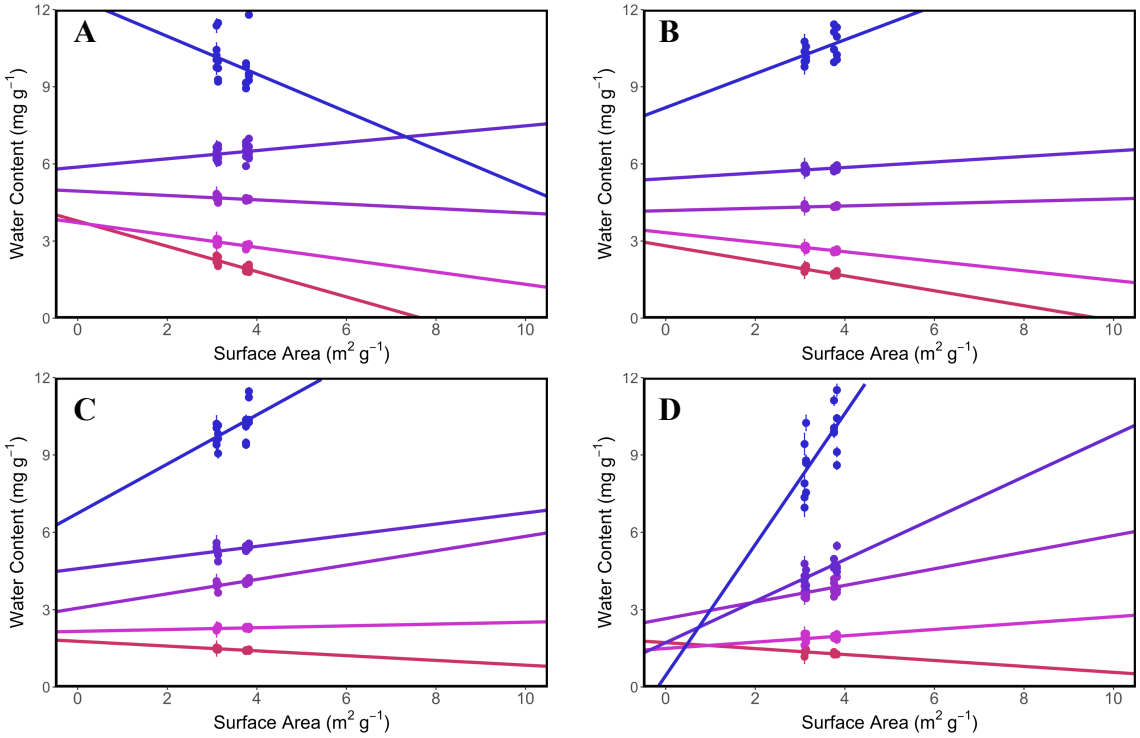

Figure C.25: Calcite water content as a function of surface area at fixed T = **A)** 10, **B)** 18, **C)** 26, and **D)** 35°C. Data (points) and linear regression (line) are separated by categorical variable RH buffer (LiCl, red; KCH_3COO, pink; $Mg(NO_3)_2$, magenta; NaCl, violet; H_2O, blue).

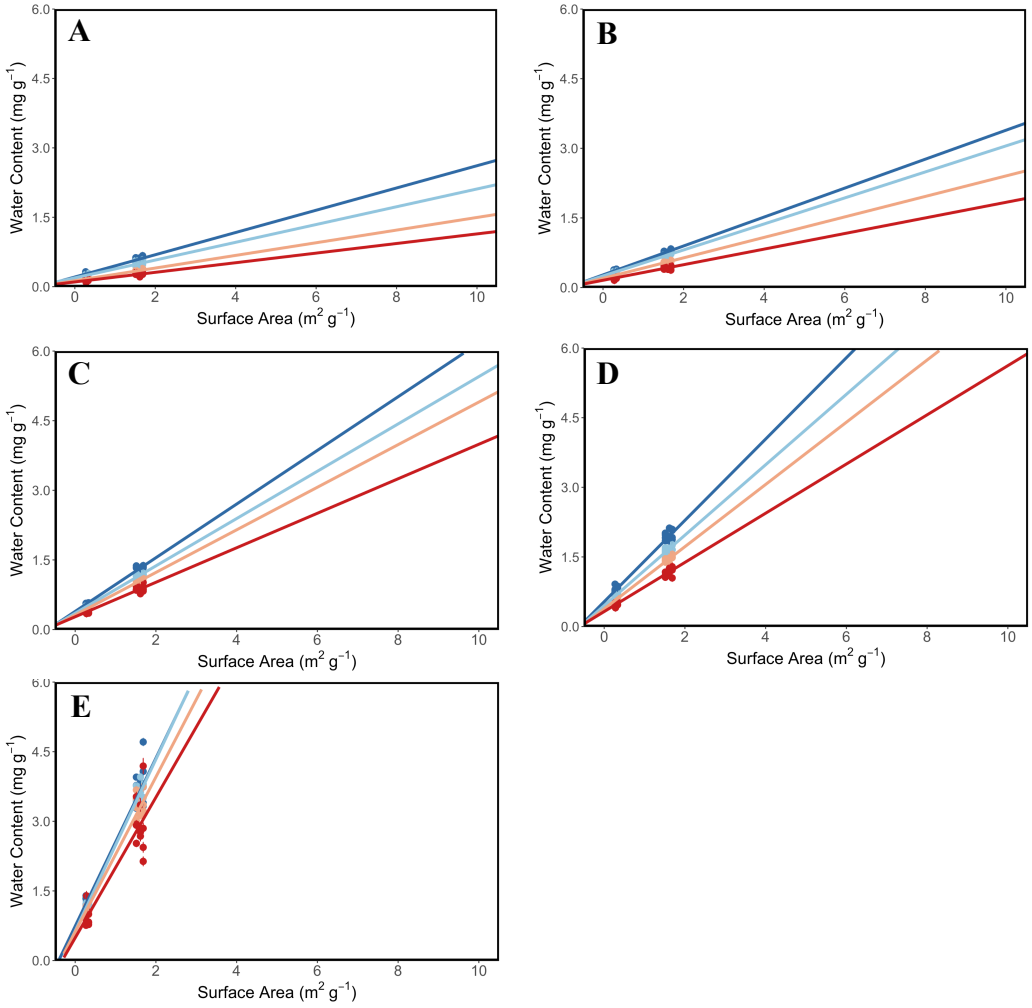

Figure C.26: Olivine water content as a function of surface area at RH buffer: **A)** LiCl (11%), **B)** KCH_3COO (24%), **C)** $Mg(NO_3)_2$ (52%), **D)** NaCl (75%), and **E)** H_2O (100%). Data (points) and linear regression (line) are separated by categorical variable temperature (10ºC, navy blue; 18ºC, light blue; 26ºC orange; 35ºC red).

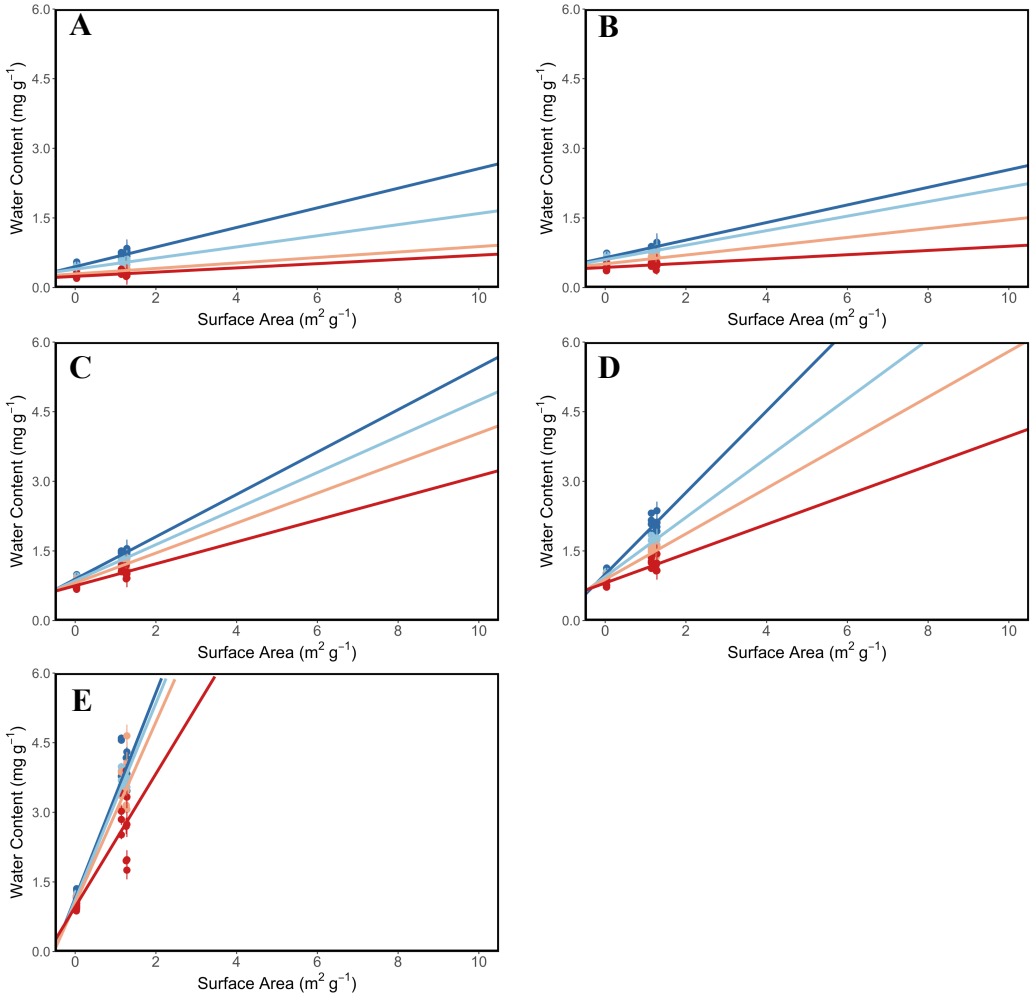

Figure C.27: Anorthite water content as a function of surface area at RH buffer: **A)** LiCl (11%), **B)** KCH_3COO (24%), **C)** $Mg(NO_3)_2$ (52%), **D)** NaCl (75%), and **E)** H_2O (100%). Data (points) and linear regression (line) are separated by categorical variable temperature (10ºC, navy blue; 18ºC, light blue; 26ºC orange; 35ºC red).

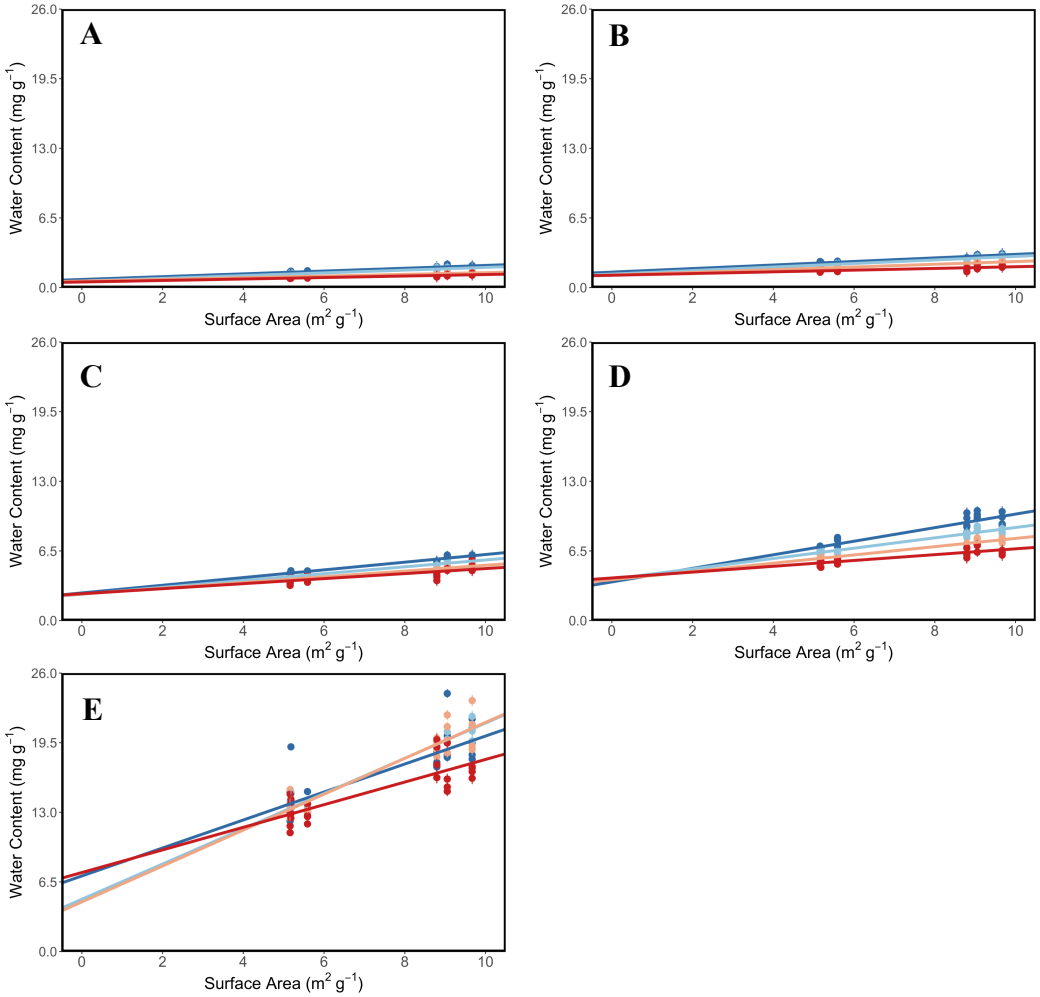

Figure C.28: Serpentine water content as a function of surface area at RH buffer: **A)** LiCl (11%), **B)** KCH_3COO (24%), **C)** $Mg(NO_3)_2$ (52%), **D)** NaCl (75%), and **E)** H_2O (100%). Data (points) and linear regression (line) are separated by categorical variable temperature (10ºC, navy blue; 18ºC, light blue; 26ºC orange; 35ºC red).

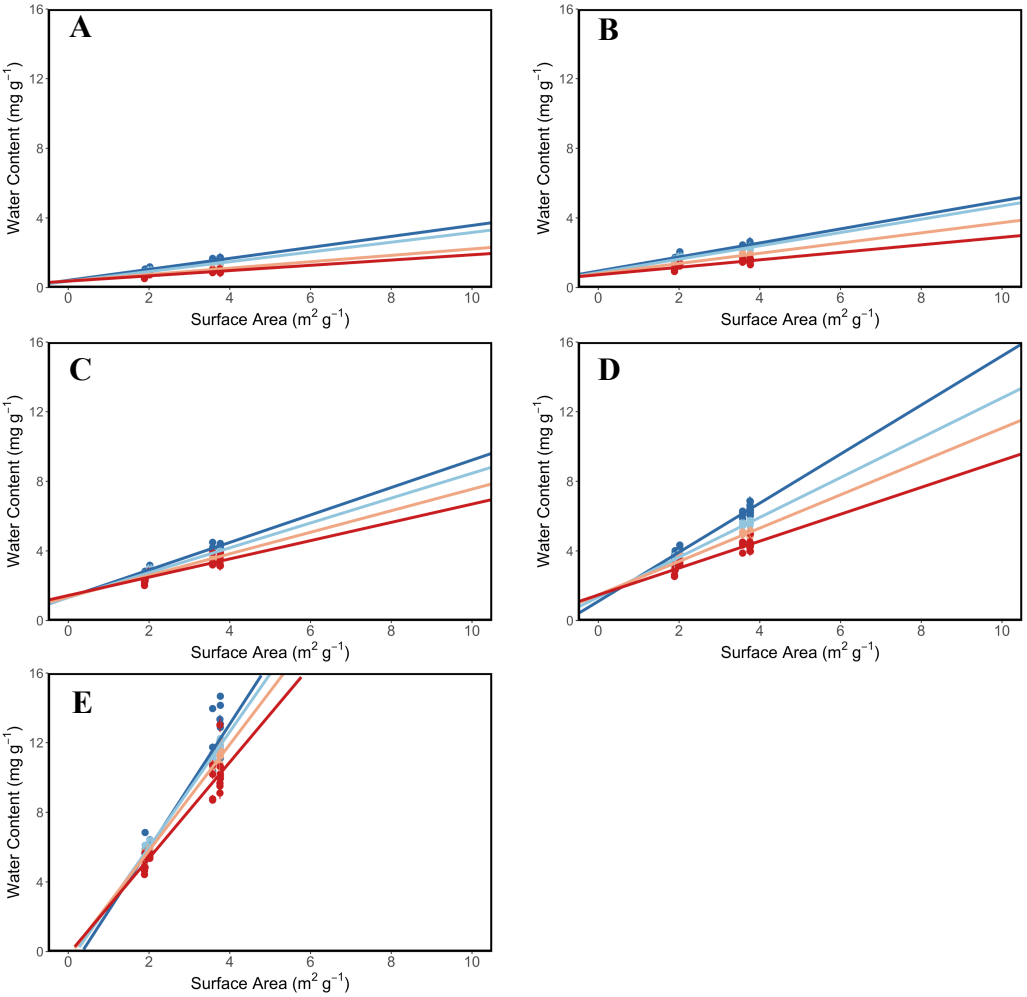

Figure C.29: Quartz water content as a function of surface area at RH buffer: **A)** LiCl (11%), **B)** KCH_3COO (24%), **C)** $Mg(NO_3)_2$ (52%), **D)** NaCl (75%), and **E)** H_2O (100%). Data (points) and linear regression (line) are separated by categorical variable temperature (10ºC, navy blue; 18ºC, light blue; 26ºC orange; 35ºC red).

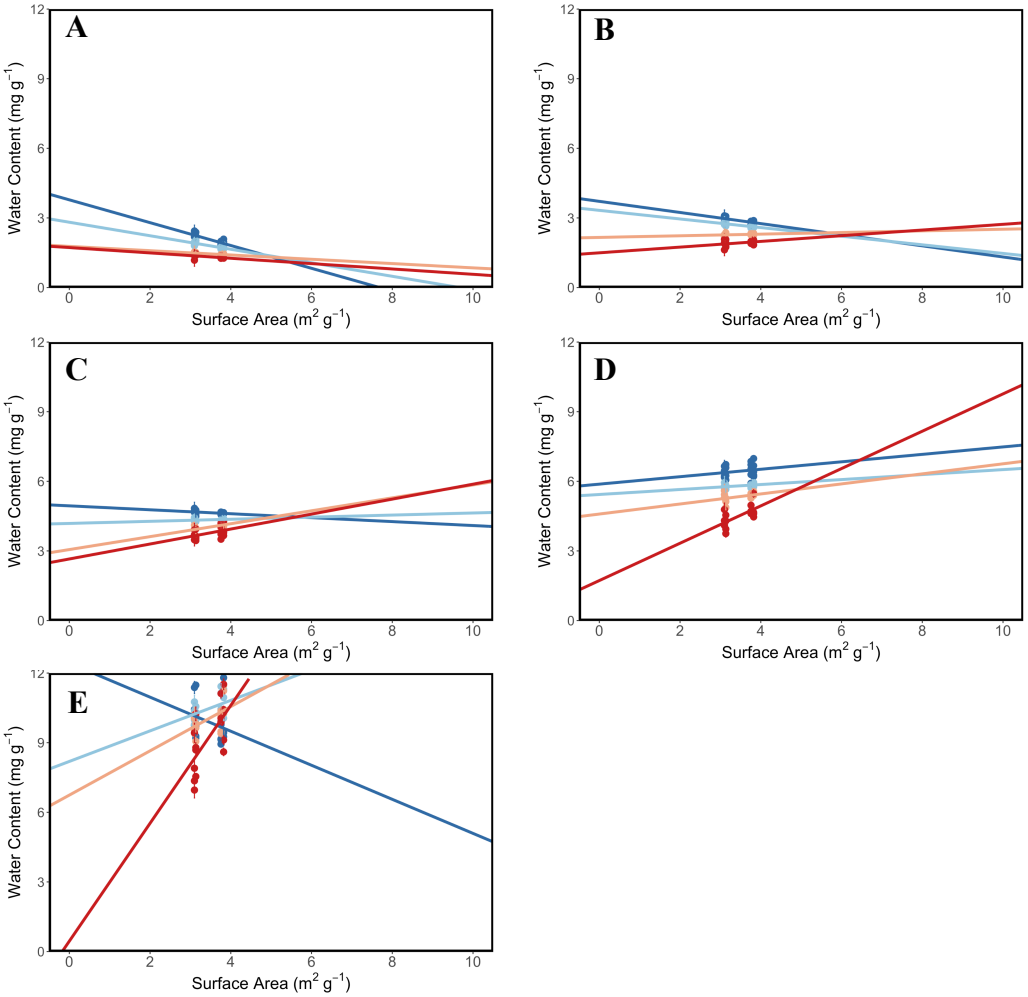

Figure C.30: Calcite water content as a function of surface area at RH buffer: **A)** LiCl (11%), **B)** KCH_3COO (24%), **C)** $Mg(NO_3)_2$ (52%), **D)** NaCl (75%), and **E)** H_2O (100%). Data (points) and linear regression (line) are separated by categorical variable temperature (10ºC, navy blue; 18ºC, light blue; 26ºC orange; 35ºC red).

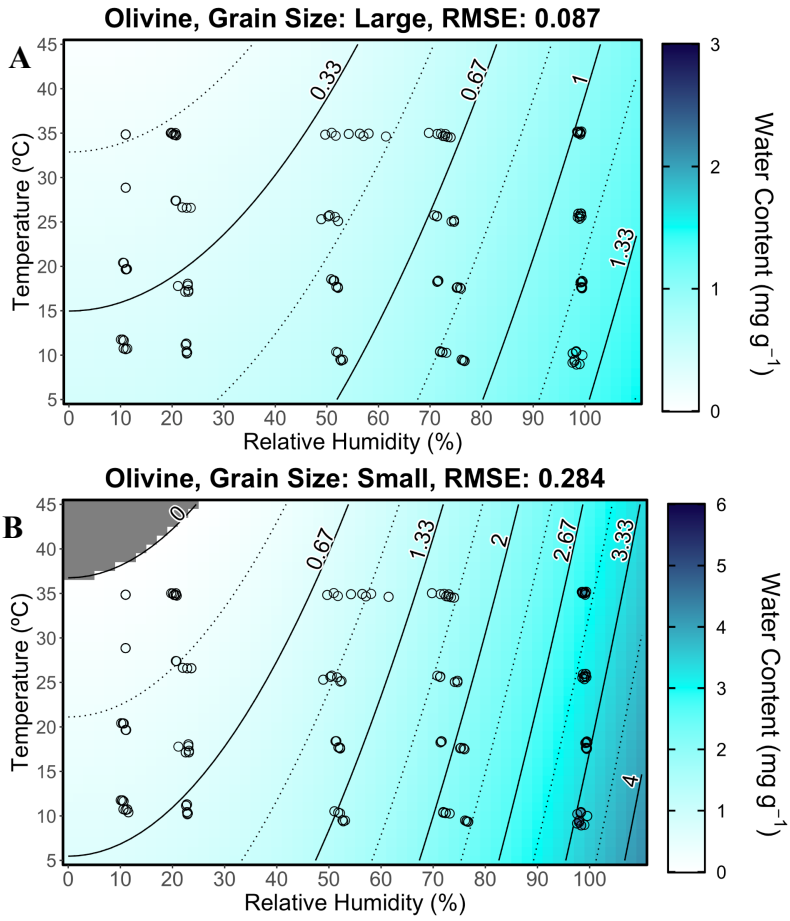

Figure C.31: Olivine experimental (points) and modeled (contours) water content as a function of relative humidity and temperature (2D fixed surface area model). **A)** low surface area (large grain size) and **B)** high surface area (small grain size).

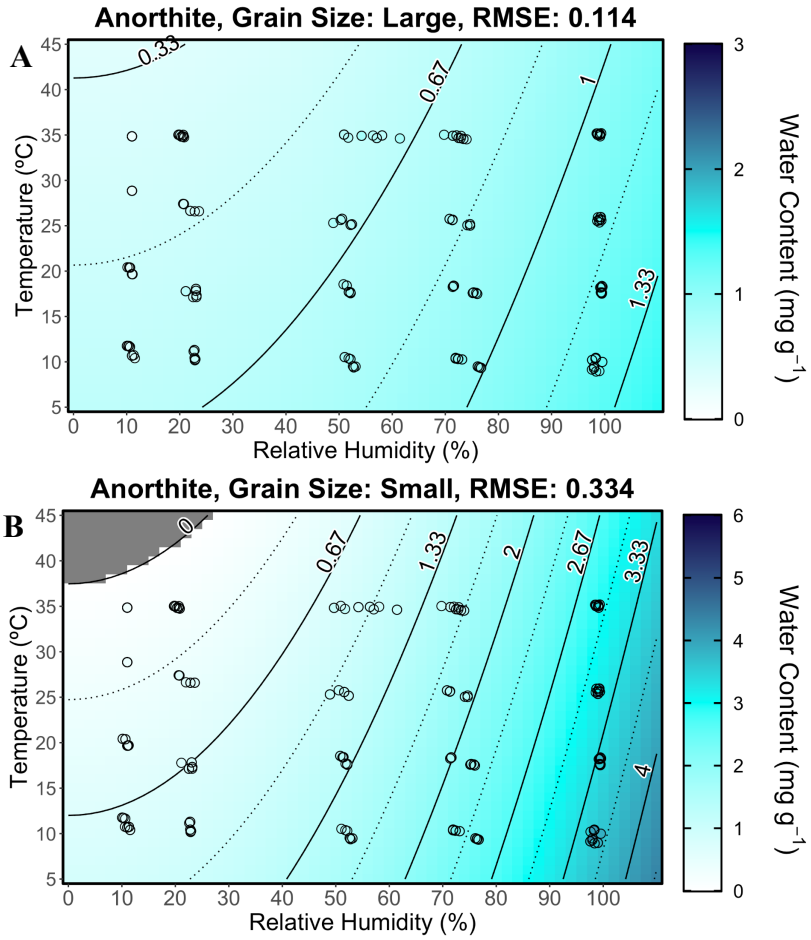

Figure C.32: Anorthite experimental (points) and modeled (contours) water content as a function of relative humidity and temperature (2D fixed surface area model). **A)** low surface area (large grain size) and **B)** high surface area (small grain size).

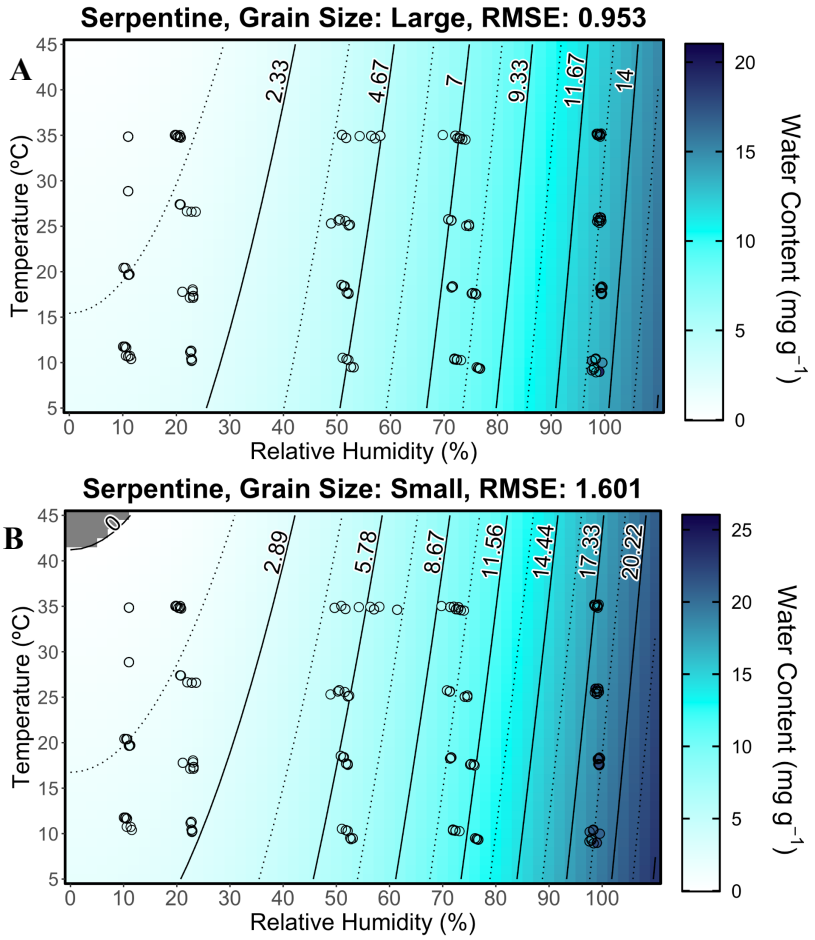

Figure C.33: Serpentine experimental (points) and modeled (contours) water content as a function of relative humidity and temperature (2D fixed surface area model). **A)** low surface area (large grain size) and **B)** high surface area (small grain size).

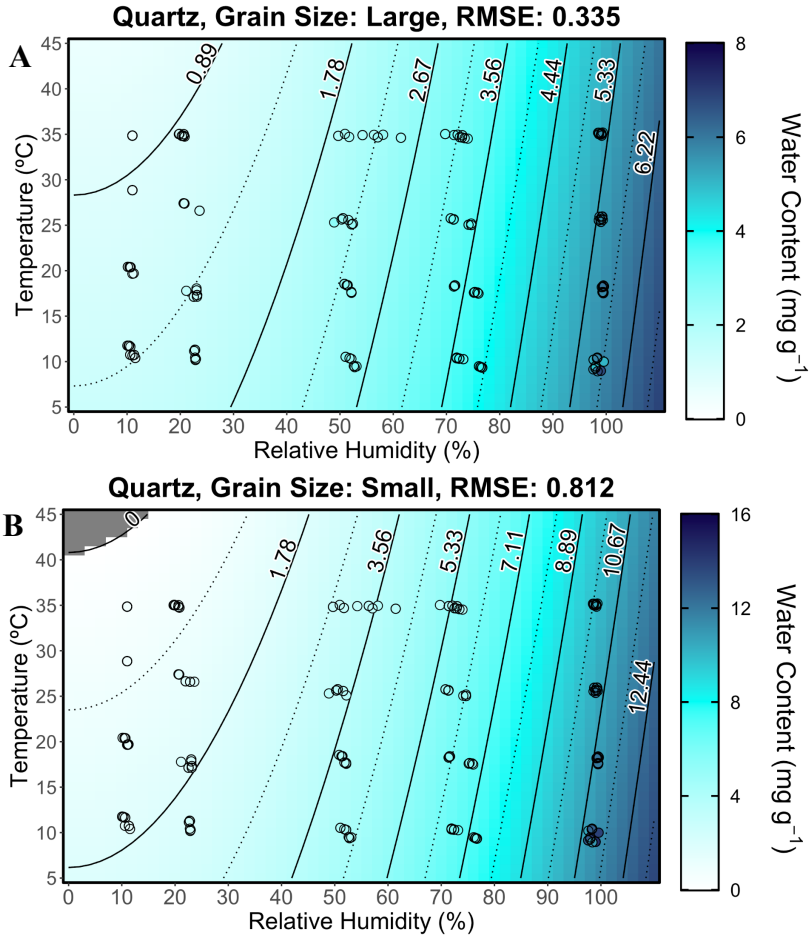

Figure C.34: Quartz experimental (points) and modeled (contours) water content as a function of relative humidity and temperature (2D fixed surface area model). **A)** low surface area (large grain size) and **B)** high surface area (small grain size).

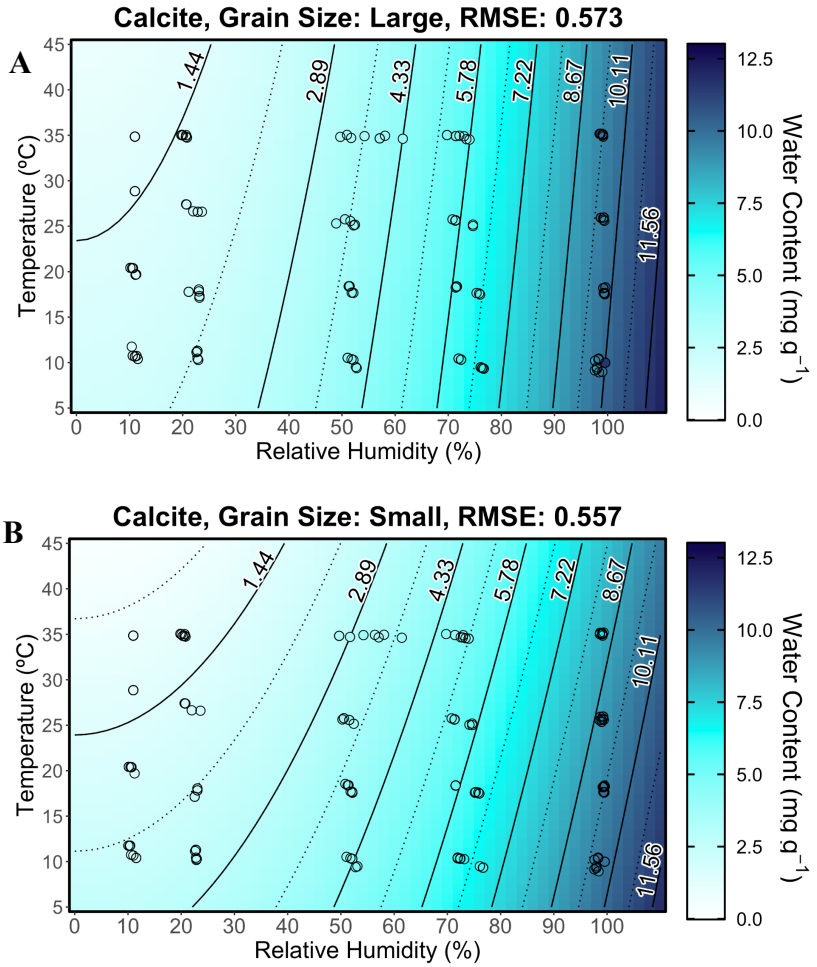

Figure C.35: Calcite experimental (points) and modeled (contours) water content as a function of relative humidity and temperature (2D fixed surface area model). **A)** low surface area (large grain size) and **B)** high surface area (small grain size).

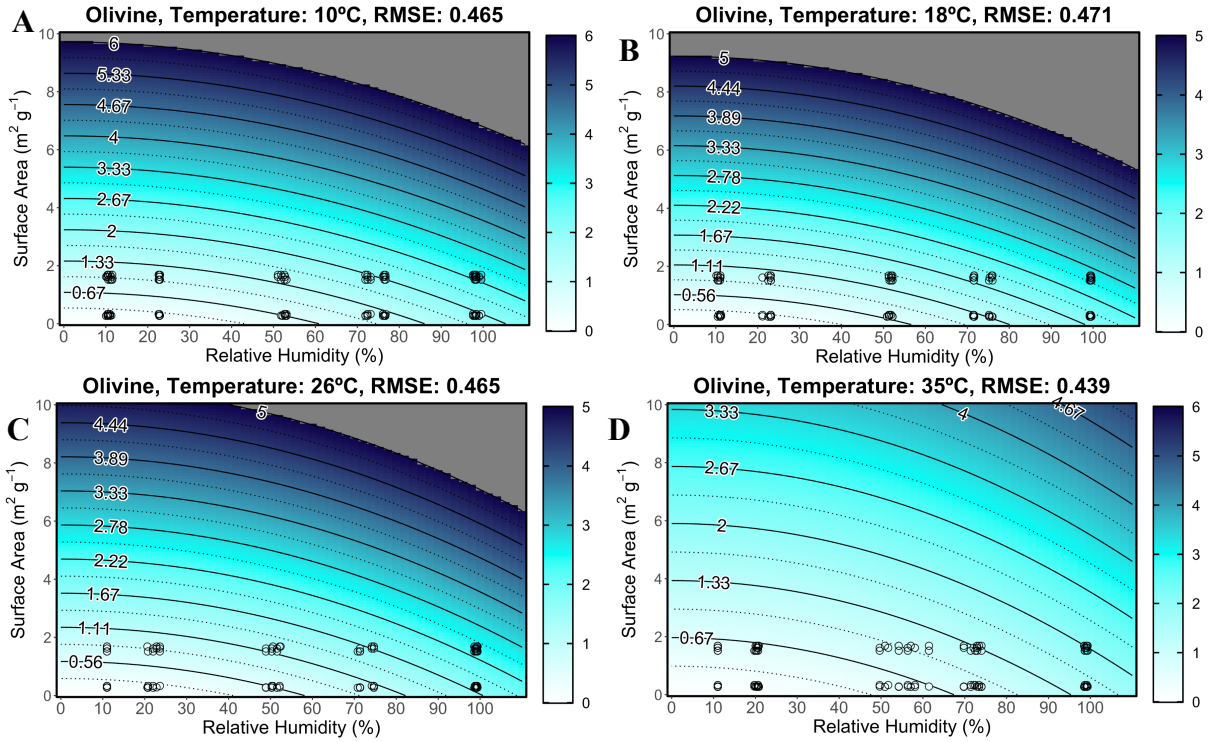

Figure C.36: Olivine experimental (points) and modeled (contours) water content as a function of relative humidity and surface area (2D fixed temperature model). **A)** 10ºC, **B)** 18ºC, **C)** 26ºC, and **D)** 35ºC.

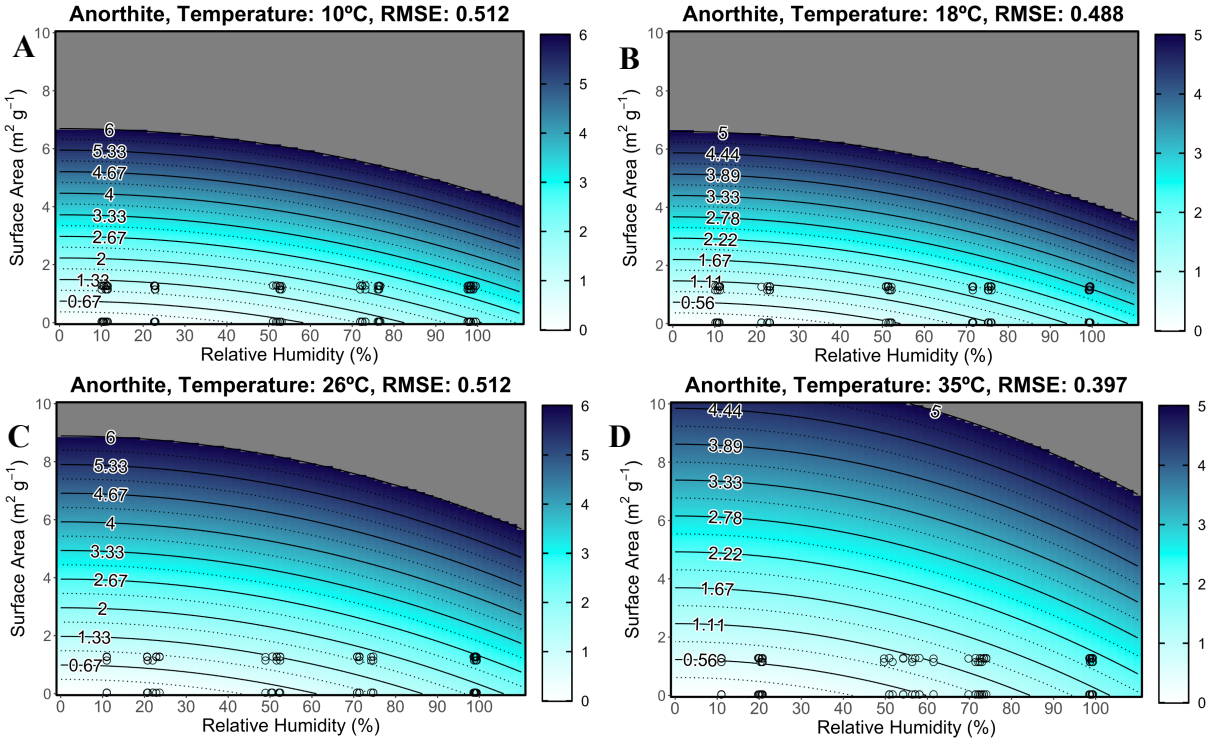

Figure C.37: Anorthite experimental (points) and modeled (contours) water content as a function of relative humidity and surface area (2D fixed temperature model). **A)** 10ºC, **B)** 18ºC, **C)** 26ºC, and **D)** 35ºC.

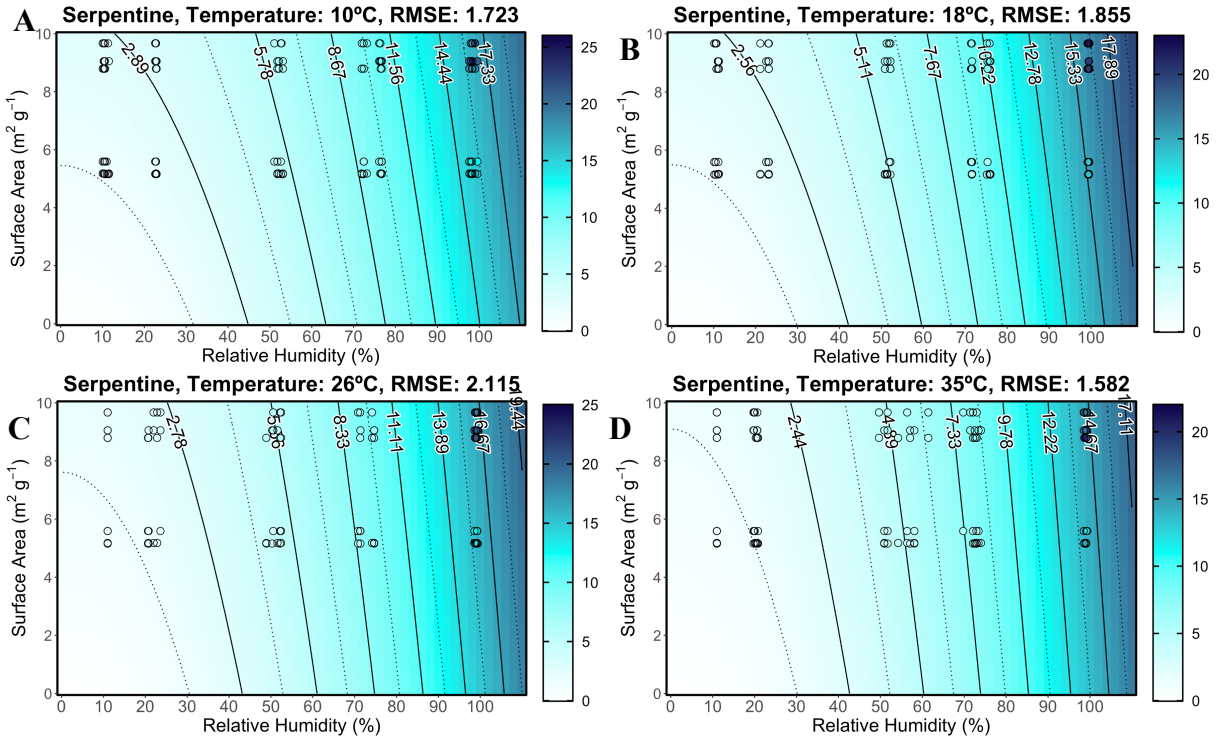

Figure C.38: Serpentine experimental (points) and modeled (contours) water content as a function of relative humidity and surface area (2D fixed temperature model). **A)** 10ºC, **B)** 18ºC, **C)** 26ºC, and **D)** 35ºC.

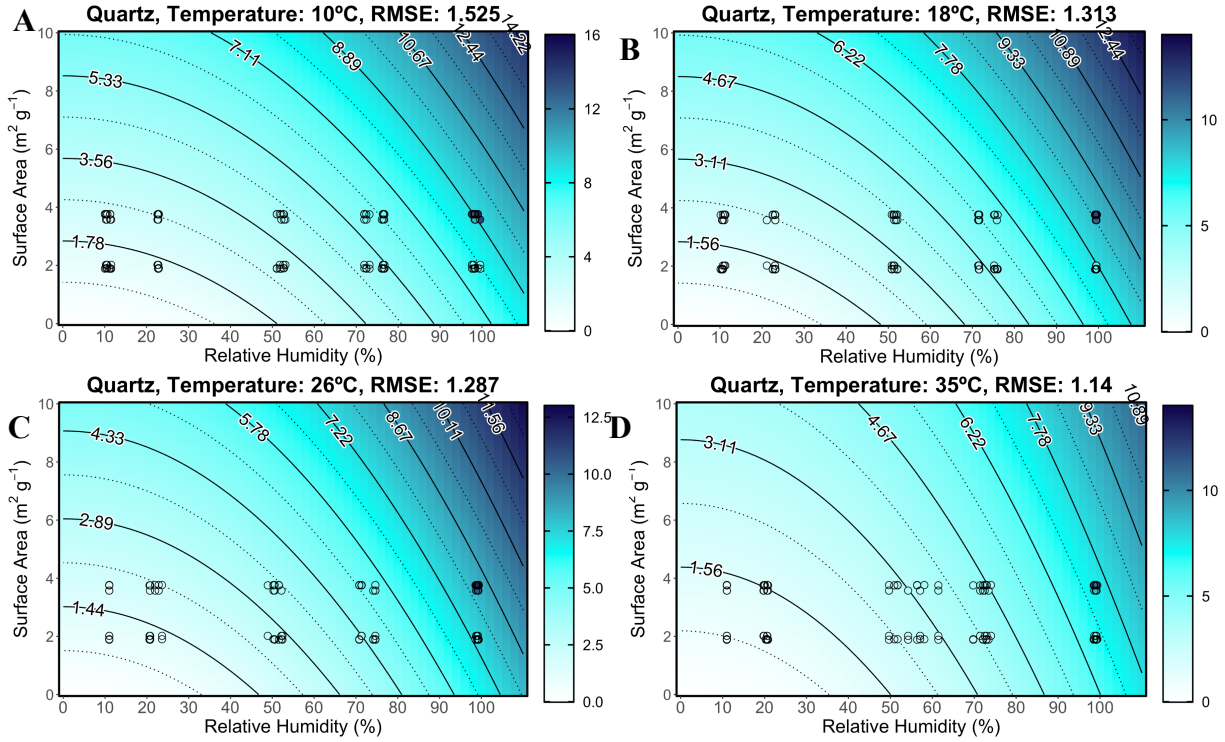

Figure C.39: Quartz experimental (points) and modeled (contours) water content as a function of relative humidity and surface area (2D fixed temperature model). **A)** 10ºC, **B)** 18ºC, **C)** 26ºC, and **D)** 35ºC.

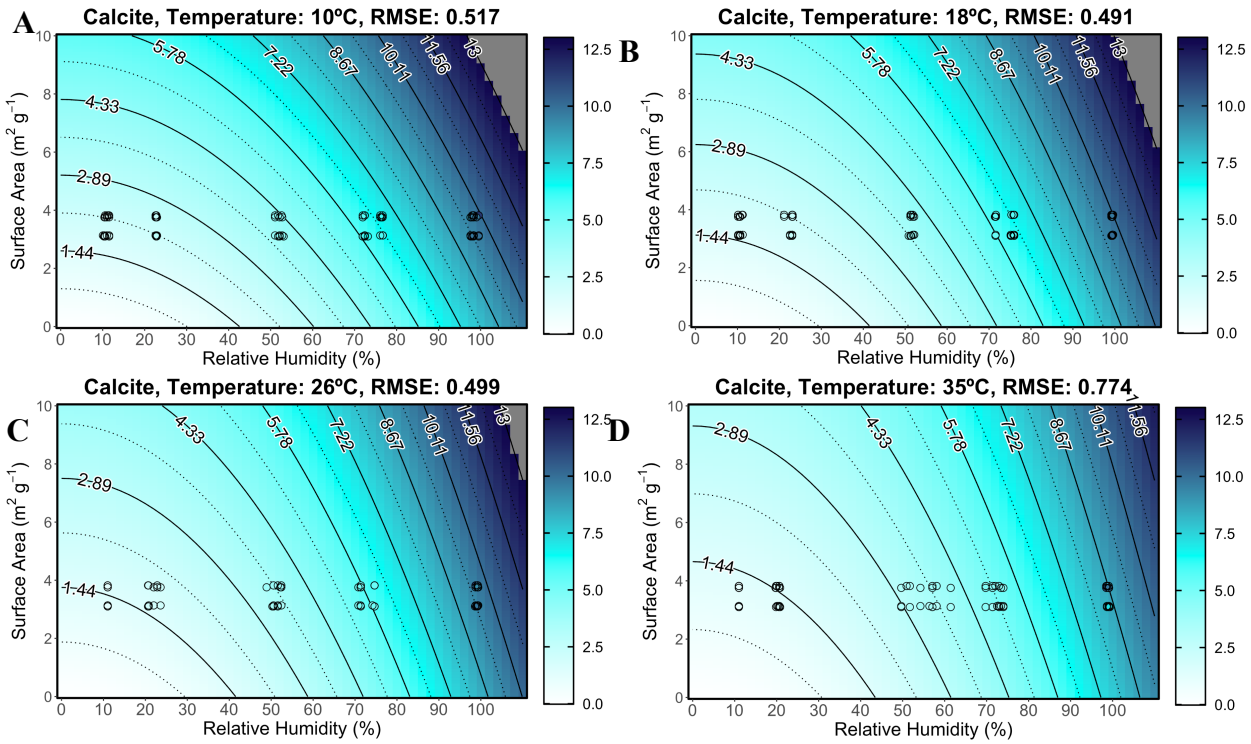

Figure C.40: Calcite experimental (points) and modeled (contours) water content as a function of relative humidity and surface area (2D fixed temperature model). **A)** 10ºC, **B)** 18ºC, **C)** 26ºC, and **D)** 35ºC.

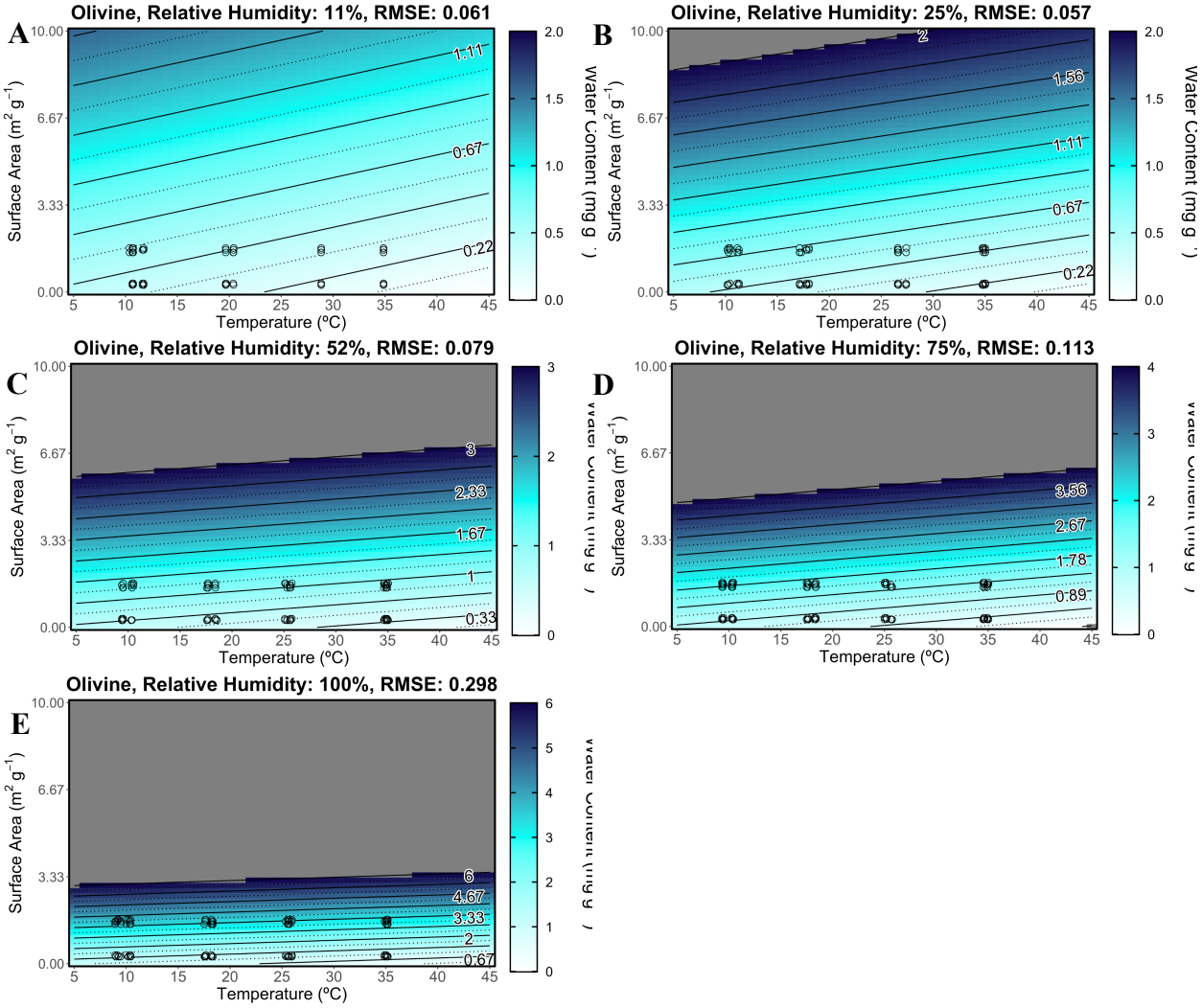

Figure C.41: Olivine experimental (points) and modeled (contours) water content as a function of temperature and surface area (2D fixed relative humidity model). **A)** LiCl (11%RH), **B)** KCH_3COO (23%RH), **C)** $Mg(NO_3)_2$ (52%RH), **D)** NaCl (75%RH), and **E)** H_2O (100%RH).

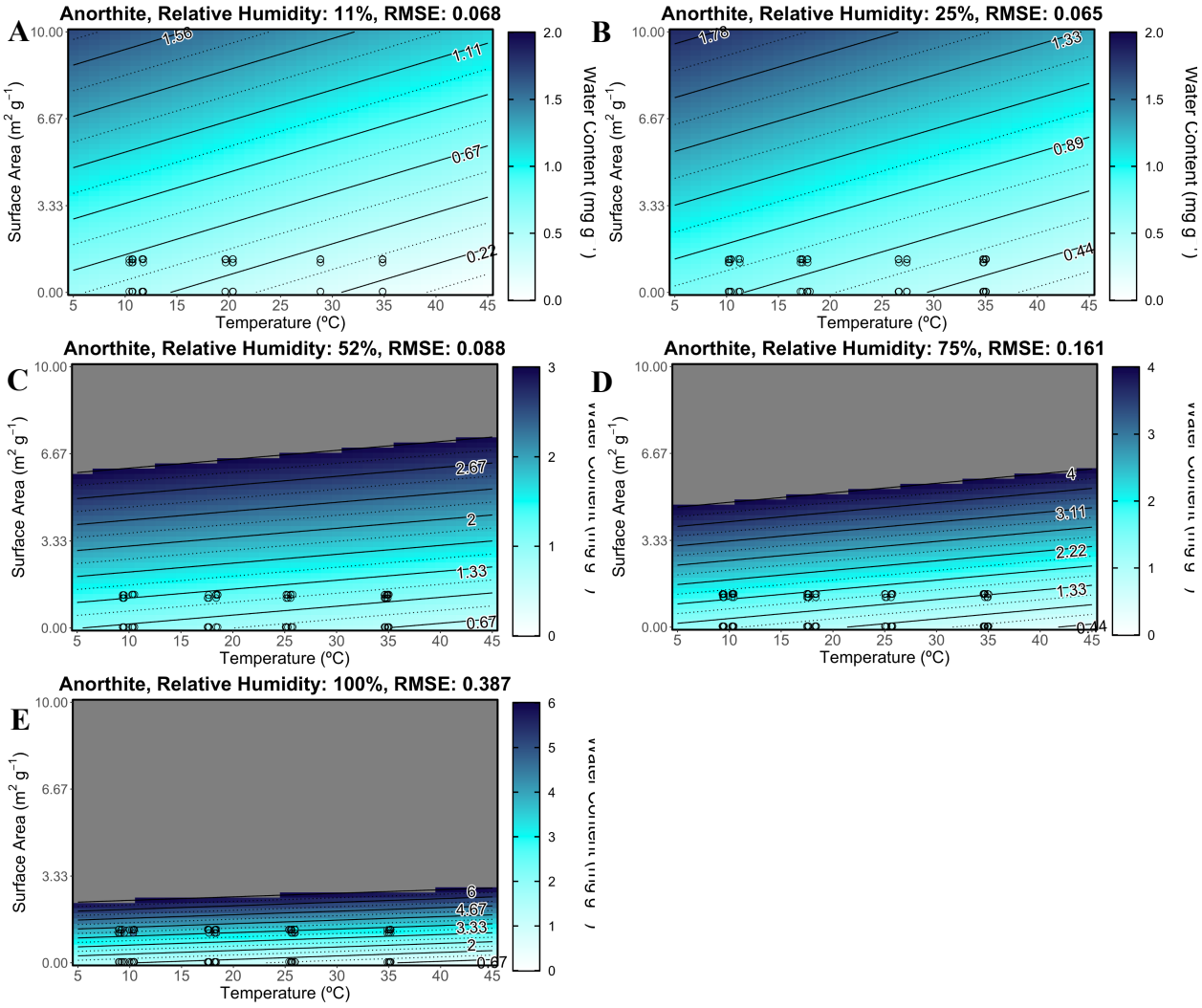

Figure C.42: Anorthite experimental (points) and modeled (contours) water content as a function of temperature and surface area (2D fixed relative humidity model). **A)** LiCl (11%RH), **B)** KCH_3COO (23%RH), **C)** $Mg(NO_3)_2$ (52%RH), **D)** NaCl (75%RH), and **E)** H_2O (100%RH).

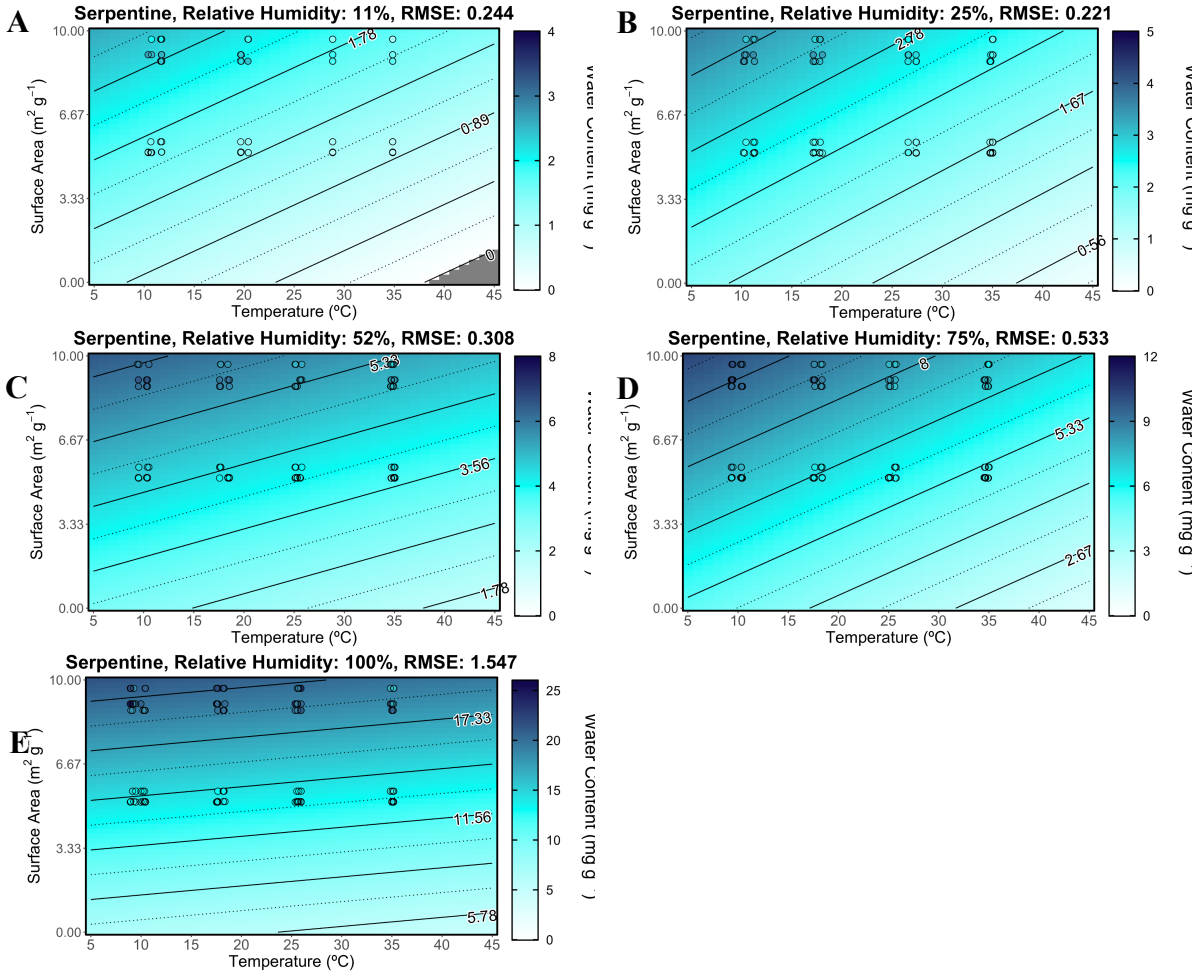

Figure C.43: Serpentine experimental (points) and modeled (contours) water content as a function of temperature and surface area (2D fixed relative humidity model). **A)** LiCl (11%RH), **B)** KCH_3COO (23%RH), **C)** $Mg(NO_3)_2$ (52%RH), **D)** NaCl (75%RH), and **E)** H_2O (100%RH).

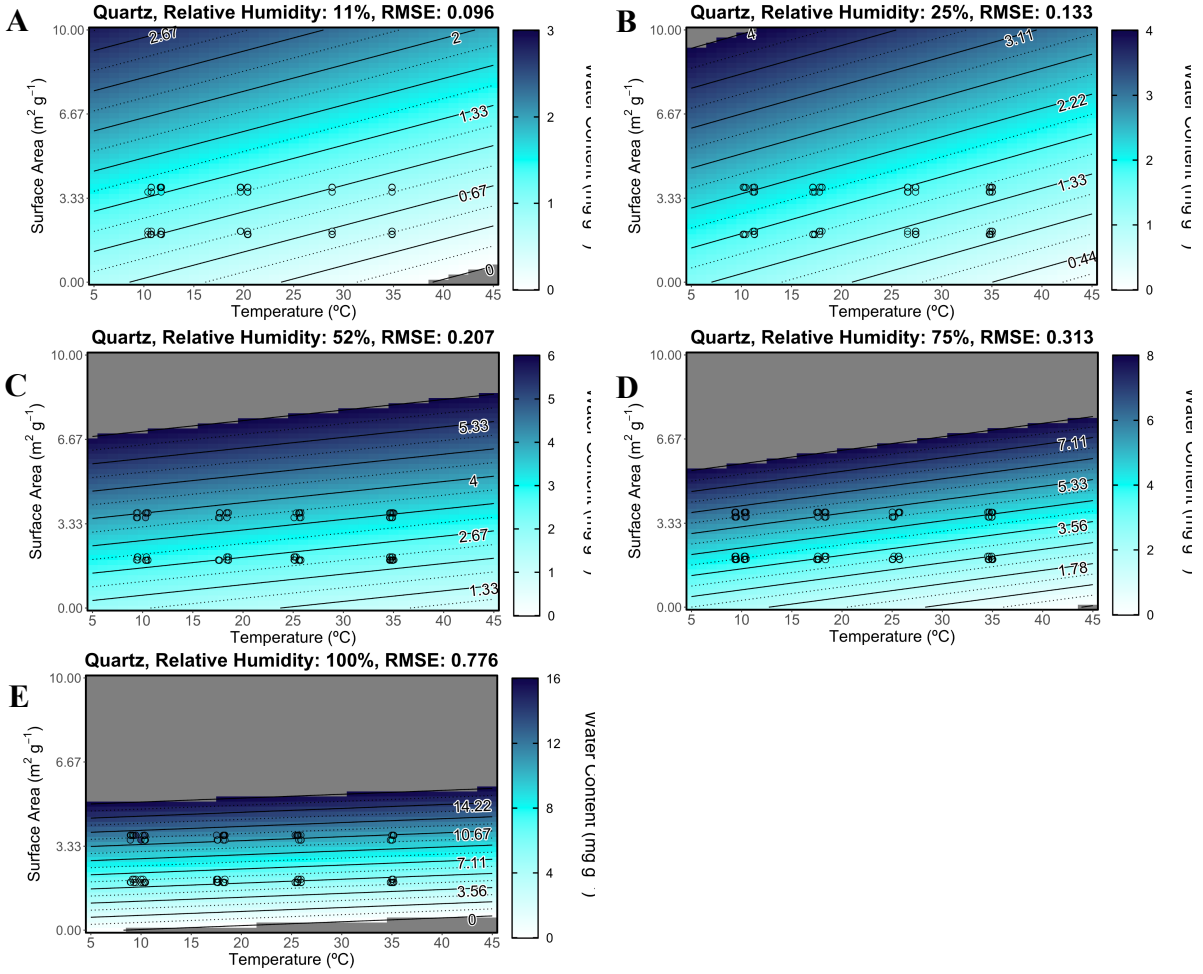

Figure C.44: Quartz experimental (points) and modeled (contours) water content as a function of temperature and surface area (2D fixed relative humidity model). **A)** LiCl (11%RH), **B)** KCH_3COO (23%RH), **C)** $Mg(NO_3)_2$ (52%RH), **D)** NaCl (75%RH), and **E)** H_2O (100%RH).

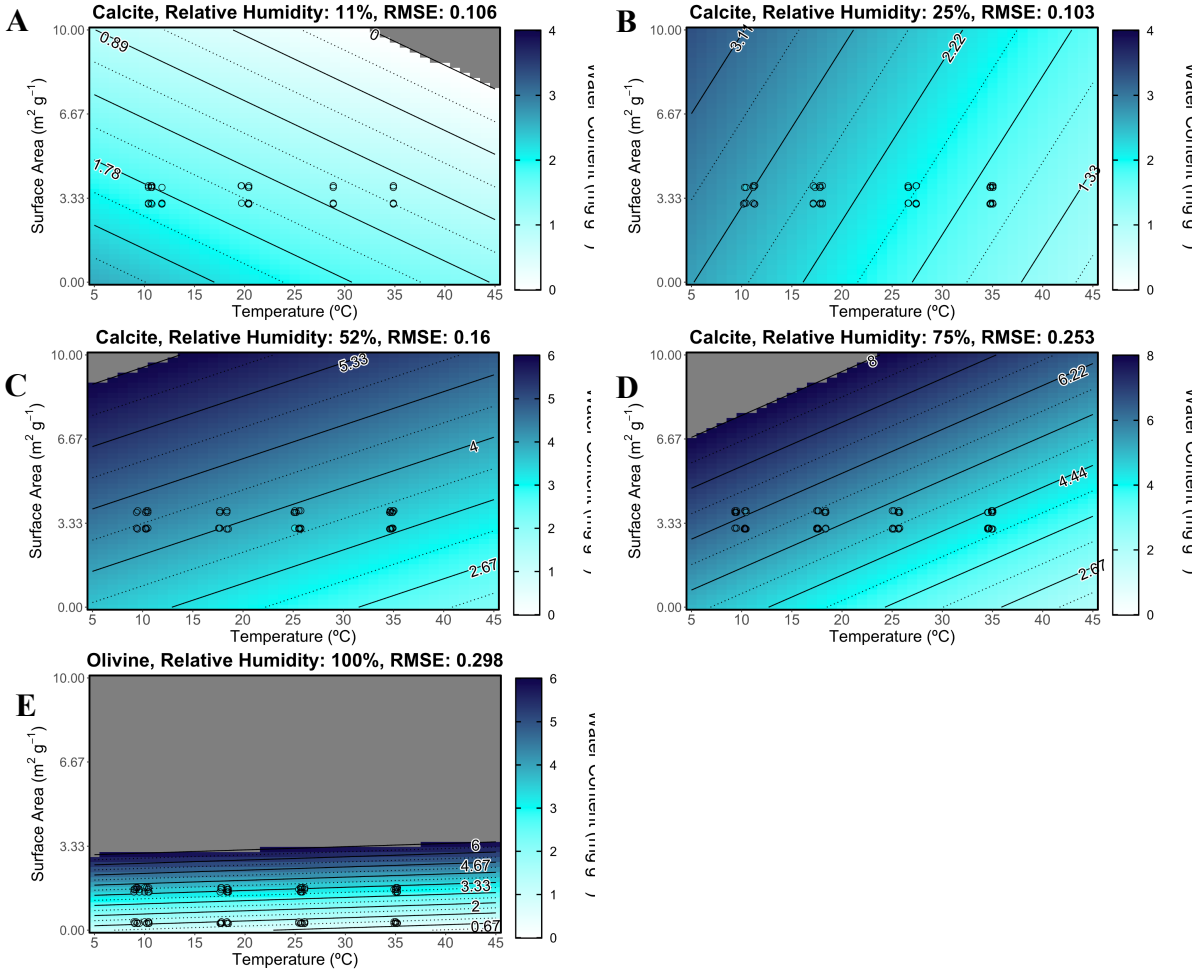

Figure C.45: Calcite experimental (points) and modeled (contours) water content as a function of temperature and surface area (2D fixed relative humidity model). **A)** LiCl (11%RH), **B)** KCH_3COO (23%RH), **C)** $Mg(NO_3)_2$ (52%RH), **D)** NaCl (75%RH), and **E)** H_2O (100%RH).

APPENDIX D

PUBLICATION CITATION

Chapter 3 titled "Mineral Composition Affects Water Vapor Adsorption in Unsaturated Soils" is reprinted in this dissertation with permission from co-author Hilairy Hartnett. The original article has been submitted to ACS Earth and Space Chemistry.

APPENDIX E

CHAPTER 4 SUPPLEMENTAL INFORMATION

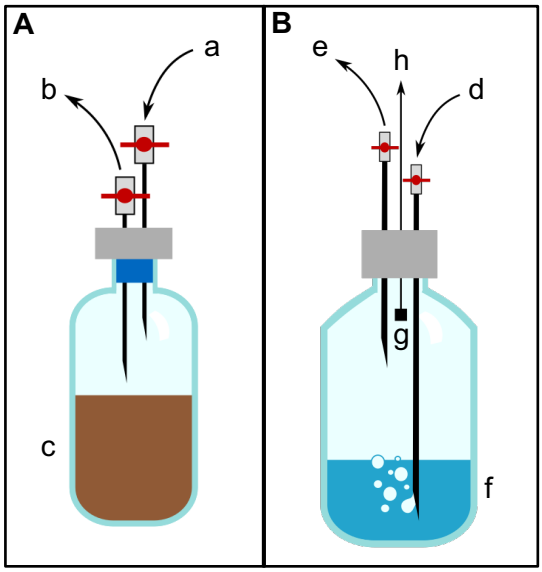

Figure E.1: Diagram of sample bottle (60 mL; panel A) and atmospheric source jar (5 L; panel B). Sample bottle is fitted with two stopcock valves and two needles; valve a is the atmospheric input (from source jar [0 hr] or 60 mL syringe [all other times]) and valve b is gas sample output (to foil bag). Soil is brown area at bottom of jar labeled as c; note that negative controls did not contain soil. Source jar is fitted with two stopcock valves and needles; valve d is input from pump (1 L min^{-1}) and valve e is output to sample (valve a). Substrate at bottom of jar (f) is shown here as water for the humid experiment; for the dry experiment the jar was similarly filled with drierite desiccant. Black square (g) is a temperature and relative humidity sensor to maintain target relative humidity of source air. Label h notes the output of temperature and relative humidity data to a live readout. Note: objects are not to scale.

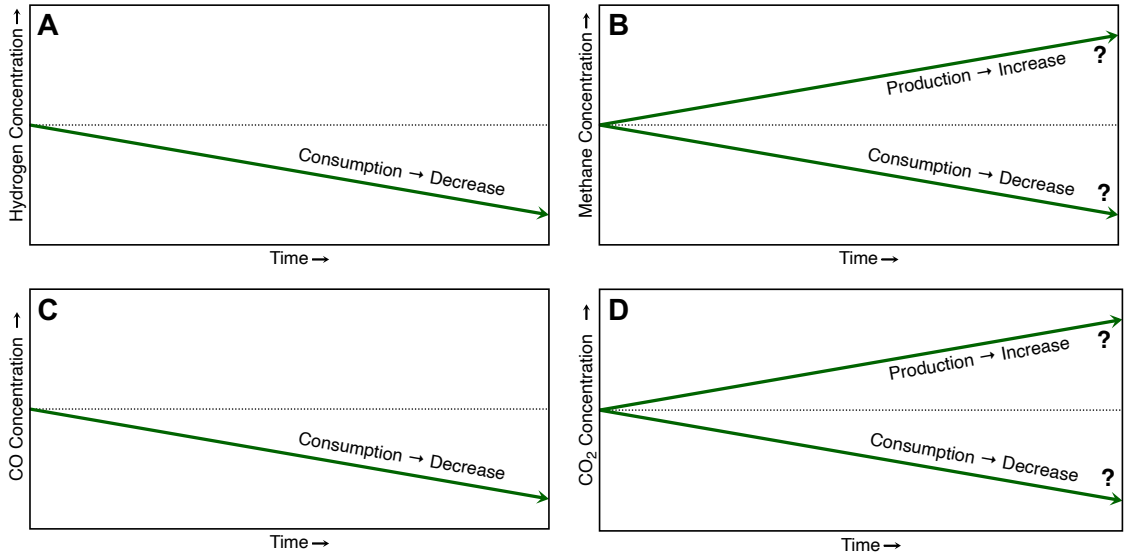

Figure E.2: Diagram of my hypothesis of changes in analyte concentrations over time with the start of the experiment on the left and the end on the right. **A)** Hypothesis of hydrogen concentrations over the experiment duration if there is active hydrogen-based metabolism. Trace gas scavenging consumes hydrogen leading to a decrease in concentration. **B)** Hypothesis of methane concentrations over the experiment duration if there are active methane-based metabolisms. Methane-based metabolisms can both produce and consume methane, therefore it will be necessary to consider methane in the context of other analytes. **C)** Hypothesis of carbon monoxide concentrations over the experiment duration if there is active carbon monoxide-based metabolism. Similar to hydrogen, carbon monoxide is consumed through trace gas scavenging. **D)** Hypothesis of carbon dioxide concentrations over the experiment duration if there are active carbon dioxide-based metabolisms. Similar to methane, carbon dioxide can be both produced and consumed in metabolic reactions, so it will be necessary to consider carbon dioxide along with other analytes.

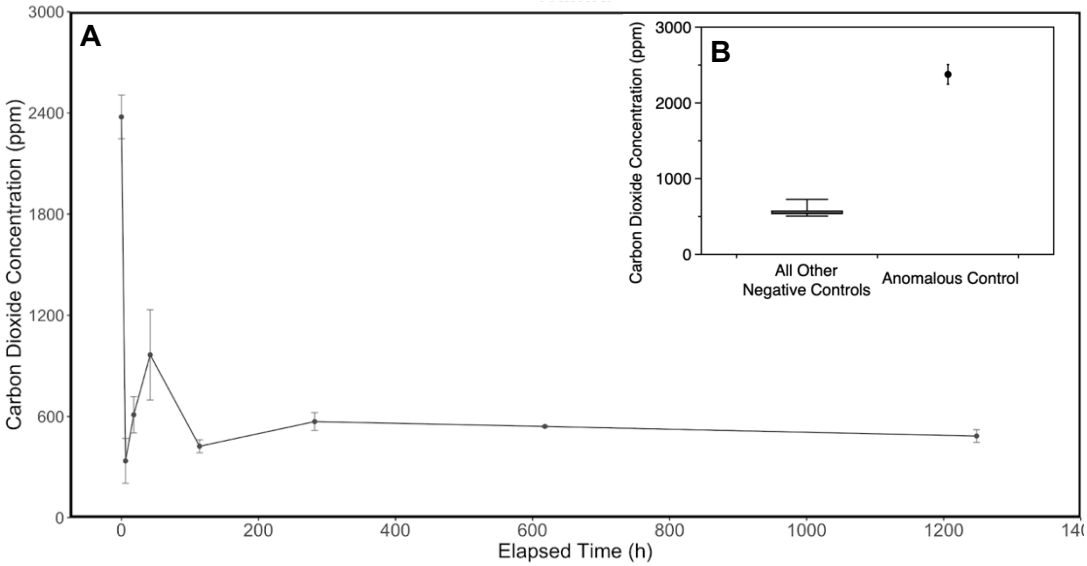

Figure E.3: Carbon dioxide concentration in the anomalous negative control bottle. Panel **A** shows the concentration over the entire experiment duration and panel **B** compares the 0 hr concentration of the anomalous control to all other negative controls at 0 hr (both experiments). The anomalous control has a 0 hr concentration roughly 3 times higher than the next most concentrated negative control bottle.

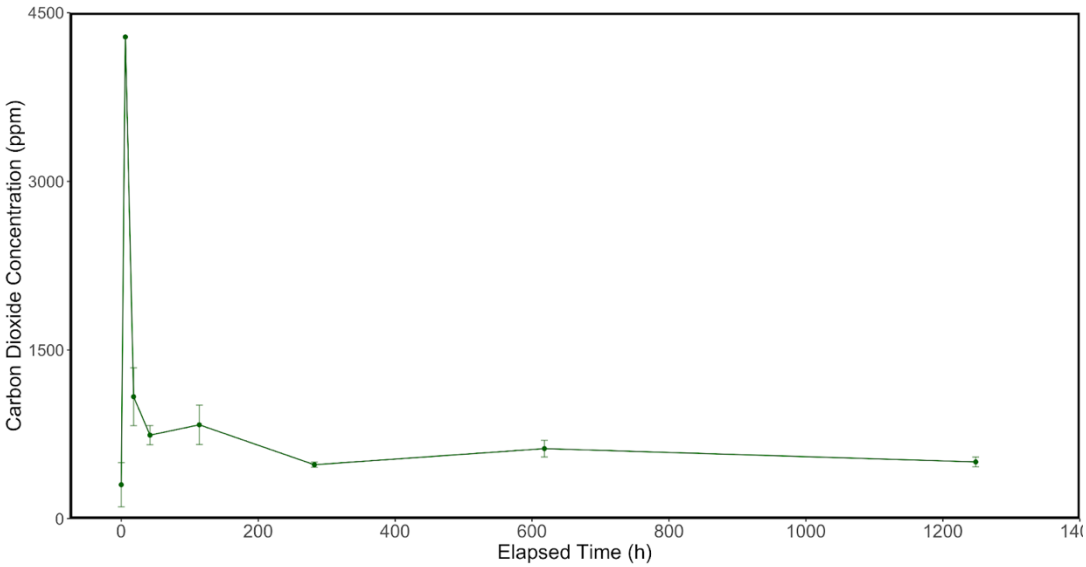

Figure E.4: Carbon dioxide concentration of the anomalous live sample bottle over the duration of the experiment. The concentration at 6 hr is the highest concentration measured in both experiments, and is roughly 50% higher than the next most concentrated measurement.

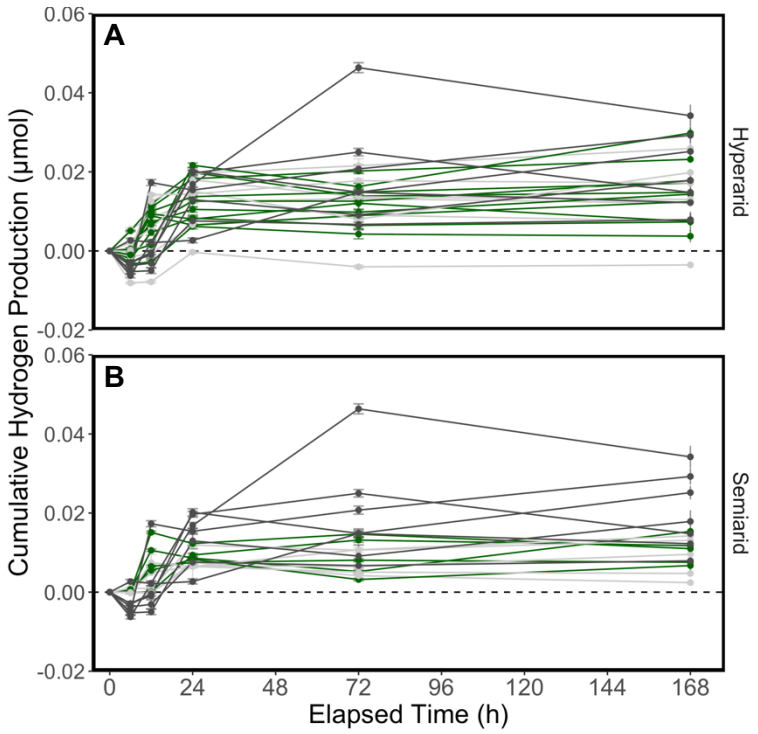

Figure E.5: Cumulative hydrogen production in the dry experiment over the first 168 hr (~1 week) in the **A)** hyperarid and **B)** semiarid soils.

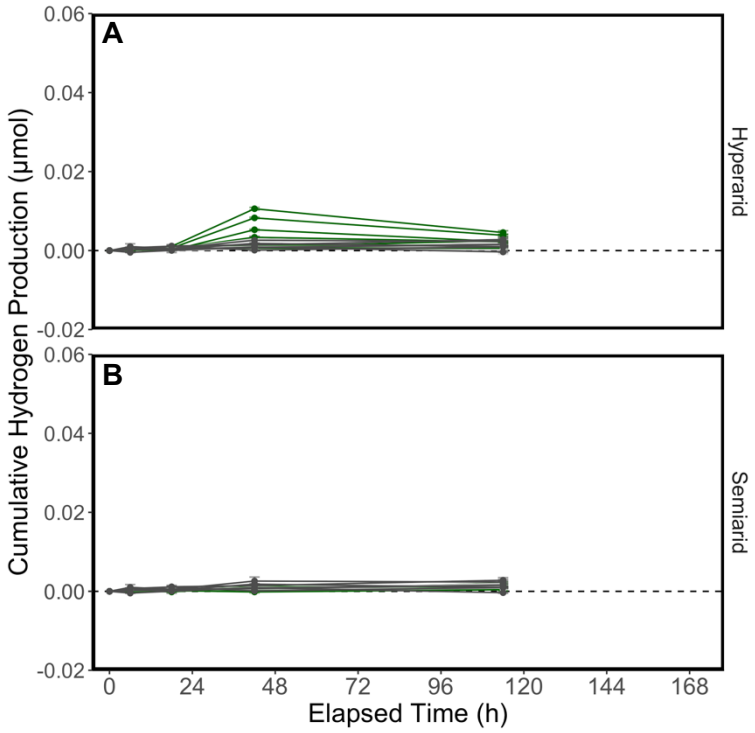

Figure E.6: Cumulative hydrogen production in the humid experiment over the first 168 hr (~1 week) in the **A)** hyperarid and **B)** semiarid soils.

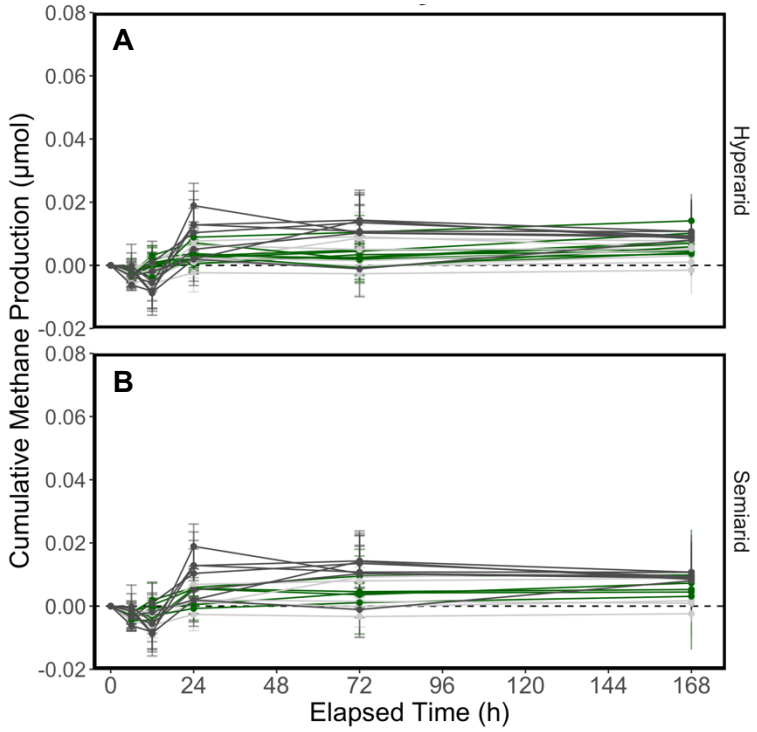

Figure E.7 Cumulative methane production in the dry experiment over the first 168 hr (~1 week) in the **A)** hyperarid and **B)** semiarid soils.

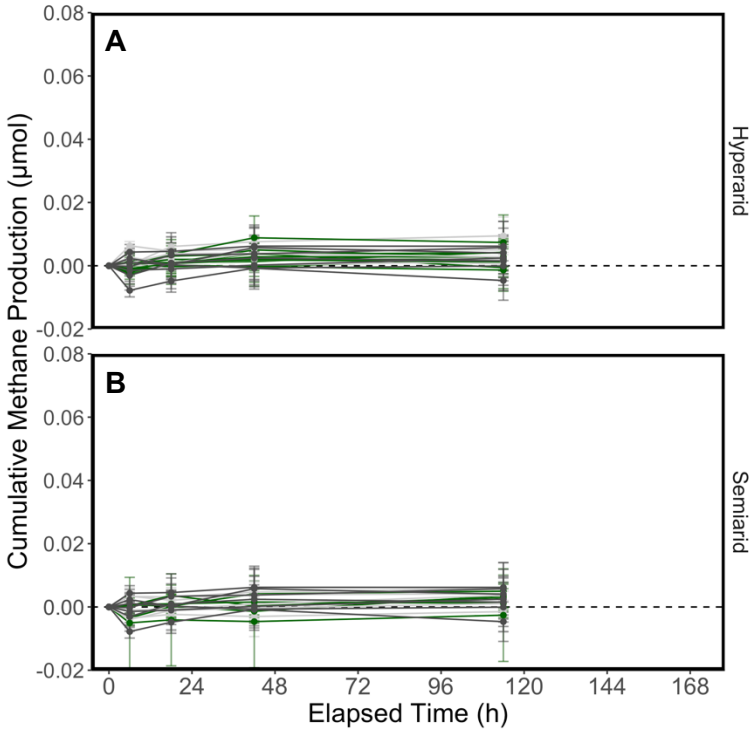

Figure E.8: Cumulative methane production in the humid experiment over the first 168 hr (~1 week) in the **A)** hyperarid and **B)** semiarid soils.

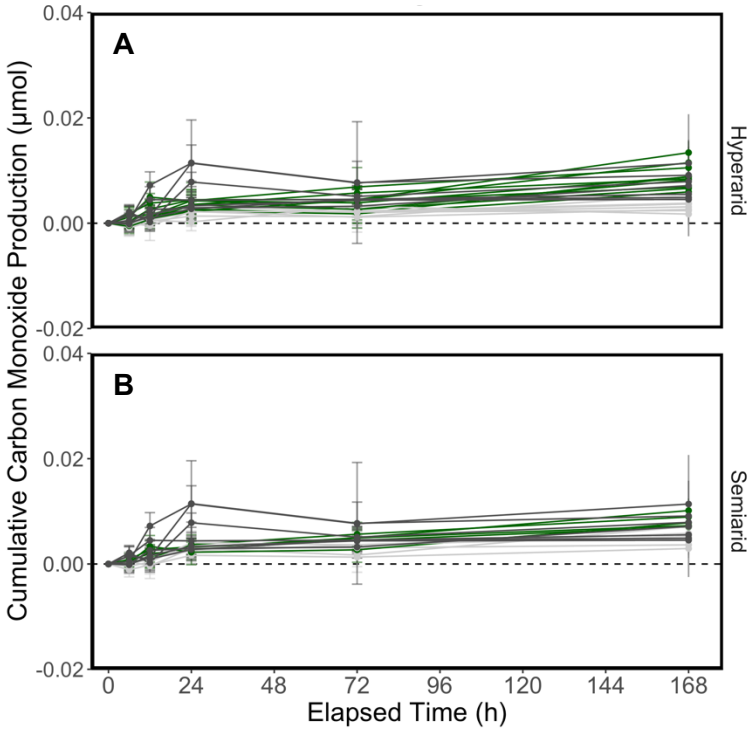

Figure E.9: Cumulative carbon monoxide production in the dry experiment over the first 168 hr (~1 week) in the **A)** hyperarid and **B)** semiarid soils.

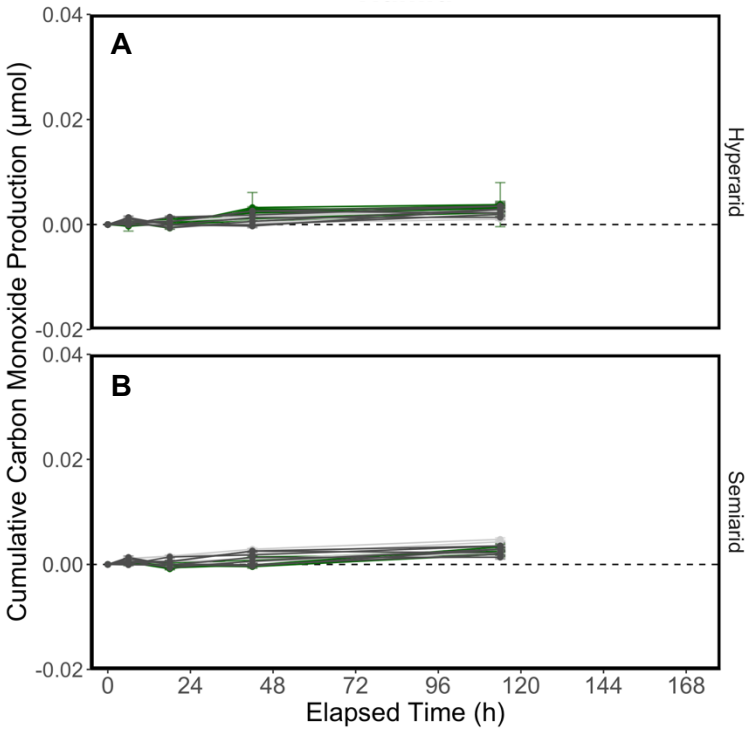

Figure E.10: Cumulative carbon monoxide production in the humid experiment over the first 168 hr (~1 week) in the **A)** hyperarid and **B)** semiarid soils.

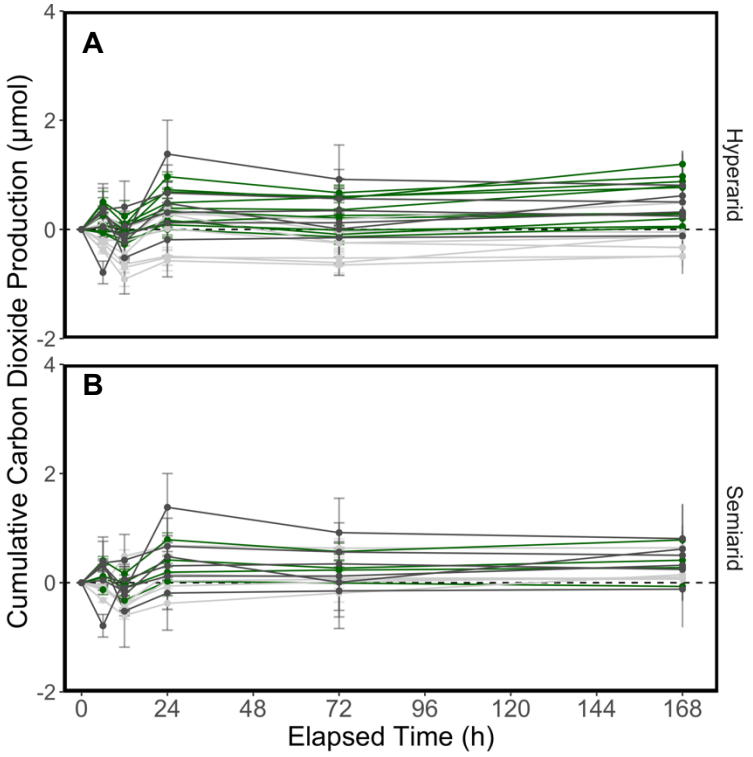

Figure E.11: Cumulative carbon dioxide production in the dry experiment over the first 168 hr (~1 week) in the **A)** hyperarid and **B)** semiarid soils.

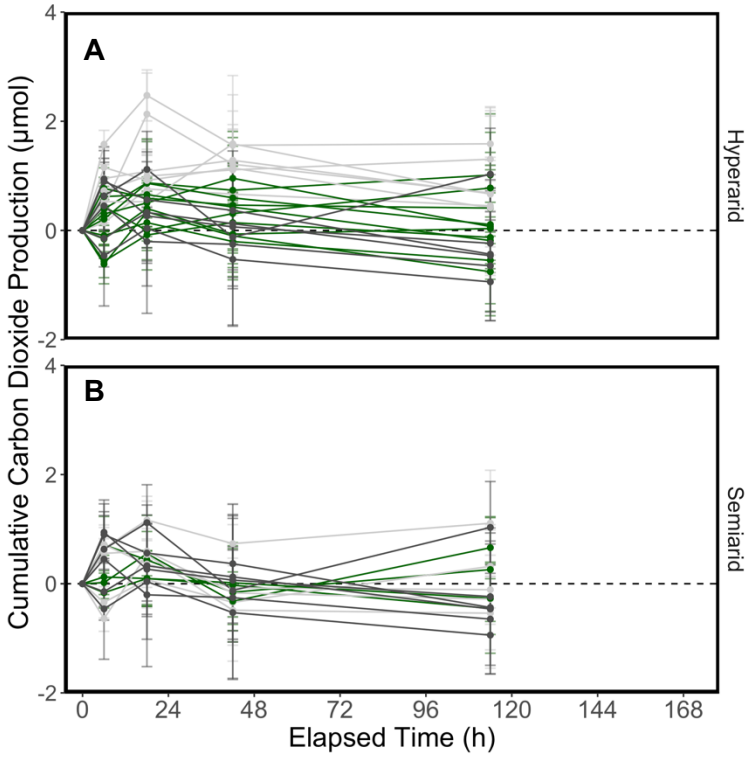

Figure E.12: Cumulative carbon dioxide production in the humid experiment over the first 168 hr (~1 week) in the **A)** hyperarid and **B)** semiarid soils.